



## 저작자표시-비영리-변경금지 2.0 대한민국

이용자는 아래의 조건을 따르는 경우에 한하여 자유롭게

- 이 저작물을 복제, 배포, 전송, 전시, 공연 및 방송할 수 있습니다.

다음과 같은 조건을 따라야 합니다:



저작자표시. 귀하는 원저작자를 표시하여야 합니다.



비영리. 귀하는 이 저작물을 영리 목적으로 이용할 수 없습니다.



변경금지. 귀하는 이 저작물을 개작, 변형 또는 가공할 수 없습니다.

- 귀하는, 이 저작물의 재이용이나 배포의 경우, 이 저작물에 적용된 이용허락조건을 명확하게 나타내어야 합니다.
- 저작권자로부터 별도의 허가를 받으면 이러한 조건들은 적용되지 않습니다.

저작권법에 따른 이용자의 권리는 위의 내용에 의하여 영향을 받지 않습니다.

이것은 [이용허락규약\(Legal Code\)](#)을 이해하기 쉽게 요약한 것입니다.

[Disclaimer](#)

공학박사 학위논문

**A Multiscale Design for Opto-Mechanical Behavior of  
Photo-Responsive Polymer Nanocomposites Induced  
by an Isomerization Reaction**

이성질화 반응에 의한 광반응 고분자 나노복합재의  
빛-기계 연성거동의 멀티스케일 설계

2016 년 8 월

서울대학교 대학원

기계항공공학부

최 준 명

**A Multiscale Design for Opto-Mechanical Behavior of  
Photo-Responsive Polymer Nanocomposites Induced  
by an Isomerization Reaction**

이성질화 반응에 의한 광반응 고분자 나노복합재의  
빛-기계 연성거동의 멀티스케일 설계

지도교수 조 맹 효  
이 논문을 공학박사 학위논문으로 제출함  
2016 년 4 월

서울대학교 대학원  
기계항공공학부  
최 준 명

최준명의 공학박사 학위논문을 인준함  
2016 년 6 월

위 원 장

김 윤 영



(인)

부위원장

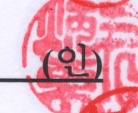
조 맹 효



(인)

위 원

윤 병 등



(인)

위 원

김 도 년



(인)

위 원

양 승 화



(인)

# Abstract

In this dissertation, the optical and thermal actuation behaviors of glassy photo-responsive polymer (PRP) and polymer nanocomposites containing gold nanoparticles were investigated using a multiscale model which integrates all-atom molecular dynamics (MD) simulations and continuum mechanics. Primary emphasis is placed on the effective photostrain as well as the elastic properties of PRP and PRP nanocomposites during the trans-to-cis isomerization by UV light. The atomic model consists of azobenzene derivatives aligned with the nematic axis, densely crosslinked side methyl chains, and untreated gold nanoparticles. By implementing a switchable potential formalism for the nitrogen double bonds in the diazene group, the conformational change of the mesogenic side group liquid crystalline polymer is simulated using MD and its structural effect on the photo-mechanical properties of the nanocomposites is quantitatively predicted.

The MD results showed that, as the trans-to-cis isomerization reaction of the azobenzene progresses, the length of the lattice in the nematic direction gradually decreases. Meanwhile, the material changes from transversely isotropic to isotropic with reduced order of orientation of the matrix and with decreased thermal stretching ratio. Regarding the PRP nanocomposites, the linear correlation between the macroscopic shrinkage of the material and the microscopic disorder of the order parameter was clearly observed and thus the photonic actuation of the considered nanocomposite system was certified. Meanwhile, the adsorption characteristics of the side polymer chains in the vicinity of the nanoparticle were maintained during the isomerization reaction and hence the thermo-mechanical stability of the PRP was enhanced regardless of the degree of photo-isomerization. Particularly, the MD results also revealed that a clearance at the interface between the nanoparticle and the



polymer matrix allowed a spatial freedom for shrinkage of the microstructure and thus the photostrain also improved during the reaction. Such unexpected but desired effect appears more remarkably as the embedded nanoparticle size decreases, indicating that the size of the nanoparticle is a key parameter determining the opto-mechanical properties of PRP nanocomposites.

To assess the photo-thermal actuation properties of the bulk material (under stress-free condition) as well as the inherent load transfer mechanism at the interface between the nanoparticle and the matrix (under mechanical loading) via continuum mechanics, we established a multiscale model which provides a design guide for PRP nanocomposites in a multiphysical environment. The orientational order parameter of the liquid crystal phase of the material obtained from MD simulations was curve-fitted with conventional Haller extrapolation. Since the coefficients of the curve showed clear tendency for the size of the nanoparticle as well as the ratio of photo-isomerization, they could be described as functions of the shape parameter which enables the design of the macroscopic photo-bending of the PRP nanocomposites specimen and their applications in view of the mechanics of materials. Furthermore, to explicitly characterize the role of interfacial interactions between the nanoparticle and polymer matrix in strain energy density under mechanical loading, a multi inclusion model was considered for finite element (FE) analysis. The effective stiffness and the spatial range of the interphase layer in the FE model were numerically identified by matching the deformation energy of the with the corresponding deformation energy in the MD model using the energy method and the homogenization theory. It is verified that the equivalent continuum model obtained from the multiscale method satisfactorily predicts not only the overall mechanical properties of nanocomposites, but also the local stress distribution at the interphase along

with their inherent nanoparticle size and photo-isomerization reaction effects.

Lastly, as a practical mechanical application, we suggested a light driven, self-adaptive PRP composite strand which avoids obstacles in a closed system. It was demonstrated that the strand could be deformed multiple times by UV-light irradiations to thread the given maze-like structure, and the strand had a sufficient load carrying capability to sustain substantial tensile stresses without fracture. Therefore, we conclude that the present multiscale model is valuable as a design guide for the mechanical design and analysis of the nanoparticle-reinforced PRP systems and their related mechanical applications.

**Keywords:** Photo-Responsive Polymer, Multiscale Analysis, Polymer Nanocomposites, Interphase, Molecular Dynamics Simulation, Continuum Mechanics

**Student Number:** 2010-24076

# Table of Contents

<b>Table of Contents .....</b>	<b>iv</b>
<b>List of Tables .....</b>	<b>viii</b>
<b>List of Figures .....</b>	<b>xi</b>
<b>1. Introduction .....</b>	<b>1</b>
1.1. Photo-responsive polymer (PRP) .....	1
1.2. PRP reinforced with nanoparticles .....	6
1.3. Characterization of effective interphase formed in polymer nanocomposites .....	8
1.4. Nano-continuum bridged multiscale model .....	10
1.5. Outline of the thesis.....	11
<b>2. Photo-thermal actuation analysis of PRP.....</b>	<b>15</b>
2.1. Model preparation for the MD simulations .....	15
2.1.1. Modeling of nematic liquid crystalline polymer system .....	15
2.1.2. Applying trans-to-cis photoswitching potential.....	18
2.2. Characterization of the material properties during the photo-isomerization reaction .....	26
2.2.1. Macroscopic bulk lattice change with incompressibility .....	26
2.2.2. Mechanical properties .....	27
2.2.3. Microstate order parameter change during heating-up simulation .....	28
2.2.4. Quantification of the photo-thermal deformation of PRP .....	29
2.3. Suggestion of a mechanical application: A light-driven PRP thread .....	34

2.3.1. Motivation .....	34
2.3.2. Experimental section .....	35
2.3.3. Threading the physical maze with a PRP strand.....	38
2.4. Chapter summary and conclusions .....	42
<b>3. An all-atom analysis of PRP nanocomposites .....</b>	<b>43</b>
3.1. Modeling of PRP/gold nanocomposites using MD simulations.....	43
3.2. Characterization of the effective material properties of the PRP/gold nanocomposites .....	49
3.3. Role of the interfacial layer during the photo-isomerization reactions .....	55
3.3.1. Structural characteristics of the PRP molecules around the nanoparticle ...	55
3.3.2. Nanoparticle size effect on photostrain and mechanical properties .....	59
3.3.3. Linear correlation between micro-macro deformation phenomena explained with photo-thermal phase transition .....	62
3.4. Chapter summary and conclusions .....	72
<b>4. Multiscale design model for PRP nanocomposites and their associated interphases .....</b>	<b>74</b>
4.1. Shape parameter under stress-free conditions .....	74
4.1.1. Basic background .....	74
4.1.2. Influence of the nanoparticle and photo-isomerization reaction .....	77
4.1.3. Description of the order parameter and shape parameter under photo-thermal stimuli.....	79
4.2. Characterization of the interfacial behavior during mechanical loading	



condition.....	88
4.2.1. Local stress distributions at the interfacial layer .....	88
4.2.2. Modeling of an equivalent multiscale unit using energy method and homogenization .....	92
4.2.3. Estimation of the obtained interphase models with model validations .....	97
4.3. Chapter summary and conclusions.....	112
 <b>5. Conclusions and recommendations.....</b>	<b>117</b>
 <b>Appendix A. Multiscale analysis for the effective thickness and mechanical properties of the interphase in polymer nanocomposites .....</b>	<b>121</b>
A.1. Overview .....	121
A.2. Revealing strengthened interphase formed in crosslinked epoxy/SiC nanocomposites .....	122
A.2.1. Modeling of crosslinked nanocomposites system in MD.....	122
A.2.2. Global elastic response of the nanocomposites .....	125
A.2.3. Local stress distribution under tensile loading .....	129
A.2.4. Derivation of the equivalent interphase using multiscale model.....	131
A.3. Revealing weakened interphase formed in crosslinked epoxy/carbon nanotube nanocomposites .....	148
A.3.1. Brief review on polymer/carbon nanotube nanocomposites .....	148
A.3.2. MD simulations and results .....	151
A.3.3. Quantification of deformation energy at the epoxy/carbon nanotube interface .....	156

A.3.4. Multiscale mechanical analysis of the nanocomposites and their effective interphase model.....	161
A.3.5. Strain energy and local stress at the interphase .....	163
A.4. Summary of Appendix A .....	181
 <b>Appendix B. Multiscale analysis for the thermoelastic behavior of polymer nanocomposites in a wide range of temperatures.....</b>	<b>184</b>
B.1. Overview .....	184
B.2. MD simulations and results .....	185
B.2.1. Modeling of representative unit cell systems.....	185
B.2.2. Glass transition temperature .....	187
B.2.3. Coefficient of thermal expansion .....	190
B.2.4. Elastic modulus.....	193
B.3. Multi inclusion micromechanics model for thermoelasticity .....	203
B.4. Scale-bridging model for thermoelasticity of the interphase .....	207
B.4.1. Determination of the volume fraction and thermoelastic properties.....	207
B.4.2. Description of the properties as a function of particle size and temperature.....	215
B.4.3. Estimation of the thermoelastic properties of nanocomposites with validation .....	218
B.5. Summary of Appendix B .....	228
 <b>References .....</b>	<b>230</b>
 <b>Abstract .....</b>	<b>252</b>

## List of Tables

<b>Table 2.1</b> Dihedral force field parameters for the diazene group and its photo-isomerization description .....	21
<b>Table 2.2</b> Geometrical properties of trans and cis state azobenzene .....	21
<b>Table 2.3</b> Photo-mechanical properties of the PRP materials. Regarding the partly isomerized models, the photostrain calculation was repeated 4 times and averaged with random selection of isomerization sites. S.D. is standard deviation of the model. ....	33
<b>Table 3.1</b> Neat PRP and PRP/gold nanocomposite systems studied.....	46
<b>Table 4.1</b> Clearance temperature of the neat PRP and the PRP/gold nanocomposites according to the ratio of isomerization reaction .....	83
<b>Table 4.2</b> Temperature-independent characteristic coefficients of the neat PRP and the PRP/gold nanocomposites for Haller's extrapolation model .....	83
<b>Table 4.3</b> Dimensionless fitting coefficients obtained from the MD results.....	84
<b>Table 4.4</b> Effective thickness and properties of the interphase of PRP/gold nanocomposites obtained from the equivalent multiscale model.....	102
<b>Table 4.5</b> Deformation energy density of the effective interphase during the tensile loading (in x-axis). The value predicted by the present multiscale method was reproduced by the remeshed FE model for the model validation.....	103
<b>Table A.1</b> Chemical composition of crosslinked epoxy and crosslinked epoxy/SiC nanocomposites in MD simulation. The effective particle volume fractions and the unit cell densities after equilibration with isothermal-isobaric (NPT) ensemble are also described.....	137
<b>Table A.2</b> The elastic mechanical properties of the molecular models.....	138

<b>Table A.3</b> The effective Young's moduli and volume fractions for the equivalent interphase .....	138
<b>Table A.4</b> Comparison the interphase thickness result with related references .....	139
<b>Table A.5</b> Comparison of the strain energy density at the interphase layer with that of full atomic model .....	140
<b>Table A.6</b> Composition of bulk epoxy and SWNT/epoxy nanocomposite unit cell systems .....	169
<b>Table A.7</b> Elastic properties of zigzag-SWNT according to the tube diameter used for the FE models in this study (units: GPa).....	170
<b>Table A.8</b> Elastic constants of neat epoxy and SWNT/epoxy nanocomposite models derived using MD simulations (units: GPa) .....	170
<b>Table A.9</b> The effective layer thickness and mechanical properties of the equivalent interphase predicted by MD-FE linked multiscale model.....	171
<b>Table A.10</b> Predictions of deformation energy density and their comparison results with the ones derived from the other previous methods.....	172
<b>Table A.11</b> Local stress prediction results for the validation sites (the 'site A' depicted in <b>Figure A.19</b> ).....	173
<b>Table B.1</b> Composition of epoxy and epoxy/SiC nanocomposite unit cell systems. ....	196
<b>Table B.2</b> Results of the analysis of the glass transition temperatures of pure epoxy and nanocomposites .....	197
<b>Table B.3</b> Thermal expansion coefficient (CTE) of the modeled system (units: $10^{-6}/K$ ) .....	198
<b>Table B.4</b> The elastic modulus of the modeled system at various temperature conditions (units: GPa) .....	199



<b>Table B.5</b> Deviation of the elastic modulus of pure epoxy in relation to the simulation time and comparison with the literature (units: GPa).....	199
<b>Table B.6</b> Determining the initial interphase thickness by radial density distribution. ..	221
<b>Table B.7</b> Coefficients of fitted variables .....	221

## List of Figures

<b>Figure 1.1</b> Mechanism of bending of a photoresponsive liquid crystal: (a) Photo-isomerization reaction of azobenzene molecules, (b) change of polymer microstructure during the photo-isomerization, and (c) macroscopic bending deformation of the PRP material.....	5
<b>Figure 2.1</b> Azobenzene derivatives used in this study.....	22
<b>Figure 2.2</b> A two-step crosslinking process to prepare glassy liquid crystalline polymer networks in MD simulations .....	22
<b>Figure 2.3</b> Modeled PRP material using MD simulation. Diazene groups were highlighted to identify that the host liquid crystal molecules were aligned in the x direction of the unit cell. ....	23
<b>Figure 2.4</b> Trans-cis photo-isomerization of azobenzene in MD simulation: (a) schematic of the conformation change of diazene group and (b) dihedral potential energy functions for the reproduction of trans-cis transition of the azobenzene.....	24
<b>Figure 2.5</b> Trans-to-cis photo-isomerization simulation for the modeled PRP unit cell. As the isomerization reaction was progressed, both the disorder of the alignment of polymer molecules and the shrinkage of the system along the x direction were observed. ....	25
<b>Figure 2.6</b> (a) Unit cell lengths along the director axis and (b) densities of the PRP models during the photo-isomerization. Photo-switching potential was applied at 16.4 ns. ....	31
<b>Figure 2.7</b> Elastic stiffness components and their ratio according to the cis-isomerization ratio.....	32
<b>Figure 2.8</b> Scalar orientational order parameter at a wide range of temperature (photo-switching potential was applied at 300 K prior to the heating-up simulation .....	32

<b>Figure 2.9</b> POM images of (a) the neat PRP material coated with cellophane and (b) the PRP immersed in the fusible interfacing under 100X magnification. ....	39
<b>Figure 2.10</b> (a) A maze part modeled in the CAD apparatus and its prototype produced by 3D printer and (b) the experimental setup. ....	40
<b>Figure 2.11</b> (a) A schematic view of passing through the maze with the PRP strand guided by UV-light, and (b) snapshots of path-finding behavior of the PRP strand in a maze. ....	41
<b>Figure 3.1</b> Molecular structure of the components contained in photo-responsive polymer and its nanocomposites. (a) Liquid crystal monomer compound, (b) diacrylate crosslinking agent and (c) gold nanoparticles. ....	47
<b>Figure 3.2</b> Configuration of the modeled PRP/gold nanocomposites periodic unit cell. (a) Front view of the original configuration, (b) highlighted view of crosslinked polymer chains in green, (c) highlighted view of photoactive mesogens as ellipsoidal inclusions and (d) side-view of the configuration of (c) .....	48
<b>Figure 3.3</b> Overall workflow of the present MD simulations for the neat PRP and the PRP/gold nanocomposites models. ....	54
<b>Figure 3.4</b> Length distribution of the azobenzene moieties in the neat PRP unit cell according to the photo-isomerization ratio. ....	65
<b>Figure 3.5</b> Radial density distribution of the polymer backbone constituents according to the size of the nanoparticle: (a) Non-isomerized PRP/gold models and (b) fully isomerized PRP/gold models. ....	65
<b>Figure 3.6</b> (a) Configurations of the additional equilibrated models with larger nanoparticle sizes (alignments of the mesogen fragments are highlighted in green) and (b) averaged order parameters of the PRP matrix of the considered nanocomposites models. ....	66
<b>Figure 3.7</b> Radial distribution of the scalar orientational order parameter of the PRP/gold	

(20Å) nanocomposites according to the photo-isomerization ratio of the azobenzene. (a) Local orientation of the azobenzene was measured from the arbitrarily defined spherical shell around the nanoparticle with given thickness ( $t_{\text{int}}$ ). (b) Obtained distribution of the orientational order of azobenzene molecules along the nematic director..... 67

**Figure 3.8** Calculated photostrain of the neat PRP and the PRP/gold nanocomposites models according to the photo-isomerization ratio. Because the trans-to-cis isomerization simulation induced the shrinkage of the unit cell, we plotted the compressive strain as positive. Error bars for the nanocomposites models represent one standard deviation around the mean value..... 68

**Figure 3.9** Elastic stiffness components of the PRP/gold nanocomposites according to the photo-isomerization of the azobenzene molecules inside of the structure. (a) Normal (x-axis) and (b) transverse (y- and z-axes) stiffness along the nematic axis of the azobenzene. .... 69

**Figure 3.10** Thermal phase transition profile of the PRP/gold nanocomposites according to the photo-isomerization ratio of the azobenzene. We defined the melting point of the material where the averaged orientational order of the microstructure is lower than 0.05..... 70

**Figure 3.11** Linear correlation between the macroscopic deformation of the modeled unit cell and the microscopic orientational order of the internal molecules according to the diameter of gold nanoparticle in the unit cell. The final graph in (e) was obtained from the previous simulation data introduced in **Chapter 2**. We defined the compressive strain as positive. .... 71

**Figure 4.1** Exponent dependence of the characteristic coefficients of the PRP



nanocomposites models and their fitting curves..	85
<b>Figure 4.2</b> The continuous function for orientational order parameter of the PRP/gold nanocomposites according to the nanoparticle size and the photo-isomerization ratio.....	86
<b>Figure 4.3</b> The continuous function for shape parameter of the PRP/gold nanocomposites according to the nanoparticle size and the photo-isomerization ratio .....	87
<b>Figure 4.4</b> The polymer networks in the vicinity of the nanoparticle were selected by the arbitrarily defined local shell group (highlighted in green) to calculate the deformation energy distribution at the interfacial region.....	104
<b>Figure 4.5</b> Deformation energy density distribution in normal (x-axis) direction.....	104
<b>Figure 4.6</b> Deformation energy density distribution in transversal (y- and z-axes) direction. ....	105
<b>Figure 4.7</b> A schematic view of the present multiscale mechanical analysis for the effective interphase formed in PRP/gold nanocomposites considering with the nanoparticle size effect, as well as trans-to-cis photo-isomerization reaction. ....	106
<b>Figure 4.8</b> Flowchart for obtaining the effective thickness and properties of the interphase, integrating the MD simulation with FE analysis. ....	107
<b>Figure 4.9</b> The number of non-bond pairs between the gold nanoparticle and the nearest polymer chain with respect to the size of the nanoparticle. The corresponding value for gold cluster is also drawn as dash line to specify the saturation point. ....	108
<b>Figure 4.10</b> (a) Estimated interphase thickness and (b) the corresponding value of the energy density according to nanoparticle size and photo-isomerization ratio of the system.....	108
<b>Figure 4.11</b> Comparison between the predicted multiscale solution and the MD simulation model in terms of the nanoparticle radius and photo-isomerization ratio. ....	109

<b>Figure 4.12</b> Model validation with the comparison of the local virial stresses of the PRP nanocomposites reinforced with 16 Å-gold nanoparticles obtained from the MD model with the corresponding ones predicted by the equivalent multiscale model. ....	110
<b>Figure 4.13</b> Local stress distribution of the interphase of PRP nanocomposites reinforced with 16 Å-gold nanoparticles during the light irradiation under mechanical loading condition.....	111
<b>Figure A.1</b> Molecular structure images of (a) an epoxy resin (EPON 862®) and (b) a crosslinker (TETA®).....	141
<b>Figure A.2</b> Snapshots of the (a) uncured and (b) cured state of epoxy resin. Force field types change during the crosslinking reaction is also stated. When the epoxide triangular ring-opening occurs, a new covalent bonding is formed with a nitrogen atom in the hardener molecule within the cutoff distance.....	141
<b>Figure A.3</b> (a) Crosslinked epoxy/SiC nanocomposites unit cell model and (b) highlighted view of nanoparticle and crosslinked points .....	142
<b>Figure A.4</b> Linear elastic behaviors of the nanocomposites ( $r_p = 10.00 \text{ Å}$ ) along the three axes.....	142
<b>Figure A.5</b> Arbitrarily defined local group for the observation of effective deformation energy on interphase layer. The distance between the particle surface and the inner boundary of the spherical surface is varied while maintaining the thickness of the local group.....	143
<b>Figure A.6</b> Elastic behavior of the locally isolated polymer matrix domain for (a) nanocomposites ( $r_p = 10.00 \text{ Å}$ ) and (b) pure epoxy systems with respect to the same spherical shell energy group. The legend describes the inner and outer distances of the energy group from the center of the unit cell. ....	143

<b>Figure A.7</b> Local strain energy density distribution of the nanocomposites ( $r_p = 10.00 \text{ \AA}$ ) regarding the kinds of energy groups. ....	144
<b>Figure A.8</b> Strain energy density profile of (a) ‘particle-excluded hollow-sphere group’ and for (b) the interphase in continuum basis obtained by homogenization process under various thickness conditions .....	144
<b>Figure A.9</b> A flowchart for the derivation of interfacial mechanical properties and geometry of the interphase by using the multiscale approach.....	145
<b>Figure A.10</b> Comparison of the strain energy density profiles of the interphase in the FE model and the local energy density profiles of the particle-excluded hollow-sphere group in MD .....	146
<b>Figure A.11</b> Relationship between the nanoparticle curvature and the effective number of non-bond pairs.....	146
<b>Figure A.12</b> Model validation with the comparison of the local stress-strain curves predicted by the equivalent continuum model with the averaged virial stress calculated from the molecular model: (a) validation sites description, (b) comparison result of the site A (adsorbed matrix region), and (c) comparison result of the site B (non-adsorbed matrix region) .....	147
<b>Figure A.13</b> Molecular structure images of (a) an epoxy resin (EPON 862 <sup>®</sup> ), (b) a hardener (TETA <sup>®</sup> ) and (c) a nano-reinforcement (zigzag single-walled carbon nanotube). ....	174
<b>Figure A.14</b> The SWNT/epoxy nanocomposite unit cells modeled in MD simulations. A total of four different sizes of unit cells with the same volume fraction of reinforcement (5.95 vol.%) were prepared. According to the unit cell size, the dispersed zigzag-SWNT model changed its chirality as follows: (a) (9,0) (b) (12,0) (c) (15,0) and (d) (18,0).....	175
<b>Figure A.15</b> Radial density distributions of epoxy matrix in the nanocomposites unit cells.	

Each curve was derived at the room temperature condition after equilibrated by the NPT ensemble. The inset in each subfigure describes the overall density distribution profile of the unit cell including the nanofiber. .... 176

**Figure A.16** Strain energy density curves at the interfacial layer according to the distance from the nanotube surface (solid lines with symbols) derived using MD simulations and the strain energy density of the FE based interphase models under various layer thickness conditions (bold lines without symbols)..... 177

**Figure A.17** (a) A scheme of the MD-FE bridged multiscale method which characterizes the thickness and strain energy density of the effective interphases of the SWNT/epoxy nanocomposite and (b) its flowchart. .... 177

**Figure A.18** The number of non-bond pairs between the nanotube and the adjacent polymer constituents according to the diameter of the nanotube. The corresponding value for single-layered graphite (graphene) is also depicted as dash-dot line to show that the number of non-bond pairs gradually saturates to the value as nanotube diameter increases..... 178

**Figure A.19** Model validation with the comparison of the local stress-strain curves predicted by the equivalent continuum model with the averaged virial stress calculated from the molecular model at the validation site (marked as ‘A’): (a) MD simulation model, (b) FE model obtained by the present analysis. .... 178

**Figure A.20** A schematic comparison of internal force distribution in the nanocomposite structure during the external loading: (a) a real environment where both of the soft interface and the functionally graded polymer region exist and (b) a single interphase model that the adsorbed polymer region interacting with the nanotube is treated as an independent material and perfectly bonded to the two opposing surfaces..... 179

**Figure A.21** Local stress distribution of the effective interphase during the tensile loading



along x direction predicted by the proposed multiscale models: (a) Epoxy + (9,0) SWNT, (b) Epoxy + (12,0) SWNT, (c) Epoxy + (15,0) SWNT, and (d) Epoxy + (18,0) SWNT nanocomposite (colormap units: GPa) ..... 180

**Figure B.1** (a) The cross-linked epoxy unit is formed by reaction between the carbon of EPON862<sup>®</sup> and the nitrogen of TETA<sup>®</sup>. (b) The unit chain of the polymer network, which converges to a ratio to 61%; this has been considered in the present study. .... 200

**Figure B.2** (a) Epoxy/SiC nanocomposites and (b) pure crosslinked epoxy models. A total of five different sizes of unit cells with the same volume fraction regarding nanocomposites were prepared. .... 200

**Figure B.3** The MSD curves of: (a) pure epoxy and (b) the E54 system. .... 201

**Figure B.4** The specific volume-temperature relations of: (a) pure epoxy and (b) the E54 system..... 201

**Figure B.5** The CTEs increase as the measured temperature range broadens within the same phase region because the specific volume-temperature plot is convex. It is worth noting that the size effect on the CTE could be observed regardless of the phase of the nanocomposites. .... 202

**Figure B.6** Comparison of the elastic moduli of the smallest-filler-reinforced, the largest-filler-reinforced, and pure epoxy cells under various temperature conditions. The size effect could be observed clearly both below and above the glass transition..... 202

**Figure B.7** MD results on the thermoelasticity of nanocomposites were linearly regressed for the glass (250K~350K), transition (350K~450K), and rubber (450K~550K) regions. All the cases of nanocomposites showed good linearity in the given temperature ranges of phases. .... 222

<b>Figure B.8</b> Radial density distribution functions (RDFs) of matrix (epoxy) in modeled unit cells were estimated at the 250K condition, after equilibrated by the NPT ensemble. Both the RDF and averaged density line are depicted until the radial distance reaches the PBC boundary. ....	223
<b>Figure B.9</b> Flowchart for deriving interfacial thermoelastic properties, transferring the MD simulation results into micromechanics model. ....	224
<b>Figure B.10</b> Updated interphase thicknesses by temperature condition.....	224
<b>Figure B.11</b> Comparing the CTE between the pure matrix cell and interphase domain in nanocomposite unit cells at room temperature and rubbery state condition. ....	225
<b>Figure B.12</b> Interphase moduli of nanocomposites derived from three phase multi inclusion micromechanics model.....	225
<b>Figure B.13</b> Effective moduli of interphase for a wide range of temperatures.....	226
<b>Figure B.14</b> Comparison between the MD simulation and the current bridging model in terms of the embedded particle radius. Here, the error bar on MD results means one deviation of analyzed results (averaged 6 times). Effective moduli of interphase for a wide range of temperatures .....	226
<b>Figure B.15</b> Finite element model to support the feasibility of the thermoelastic property of interphase in nanocomposites derived from the current bridging methodology. ....	227
<b>Figure B.16</b> Comparison between the MD simulation results and current bridging model in terms of the temperature condition. The solutions of finite element method are depicted in case of that the diameter of interphase does not exceed the modeled unit cell length.	227

# **1. Introduction**

## **1.1. Photo-responsive polymer (PRP)**

Shape memory polymer (SMP) is a promising polymer material which changes its conformation of polymer molecules and their inter- and intramolecular interactions by multiple external stimuli [1,2]. During the past decade, SMPs have received increasing attention not only in polymer science, but also in the mechanical engineering field due to their considerable potential for multifunctional structures [3]. The deformation path and state of the responsive region of the SMP are determined by both of its functional groups in the polymer and by the entanglements of the polymer networks and physical interlocking among them. Hence, the multiple deformation behavior of the material can be designed by applying two or more types of stimuli, by utilizing the chemical reaction of the functional sites and the phase transition of the polymer networks. Some mechanical tuning techniques, such as the pre-stretching and quenching processes [4,5] or the multi-layering process [6,7], are also applicable for the modulation of the deformation field. Because the material can be precisely operated with the user's own environment and preference, it is particularly useful as a mechanical device for the bending actuator [8-10], wireless and implantable drug delivery system [11], three-dimensional (3-D) flexible microchannel [12], and biomimetic artificial muscle [13,14], etc.

Diverse types of SMPs with different functional groups of copolymer and polymer

architecture have been developed to reach the desired deformation of the object [3]. Among these ‘smart’ materials, a photo-responsive polymer (PRP) which consists of a liquid crystalline polymer in the nematic state [15] and photoactive agents such as azobenzene [16-19], azotolane [20], and diarylethene [21,22] shows notable features and provides a new potential for the utilization of SMPs [23]. The characteristics of the SMP implicitly depend on the type of energy source used as a trigger signal. Unlike most of the conventional SMP material requires thermal energy for its operation, the PRP material reversibly changes its molecular phase not only because of the thermal transition of liquid crystalline phases, but also because of the light irradiation.

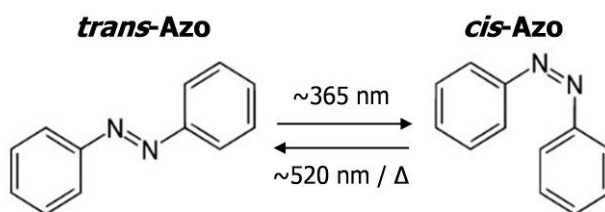
The origin of photo-responsibility of the material is attributed to the conformational isomerization of the photoactive agents of the polymer matrix. When the light is irradiated, the molecular geometry and the associated bonding characteristics are changed, allowing a nematic to isotropic (and *vice versa*) transition in the liquid crystalline polymer [16], as illustrated in **Figure 1.1**. Such photo-mechanical behavior is indeed useful for the design of SMP devices because the light source can be remotely and momentarily delivered to the target locations on the object. Also, the light irradiation can be modulated specifically with high precision – by changing the focus position or by blocking out the rays. The attachment of any additional components (e.g. electric circuit or battery) on the material would not be required for the operation. These characteristics of the PRP material enable the development of optically and thermally responsive structures and hence widen the application fields of optical micro- and nano-devices such as solid-liquid patterning for

photolithographic process[24], tunable focal lens [25-27], and molecular-level switching of nanostructures [23,28,29].

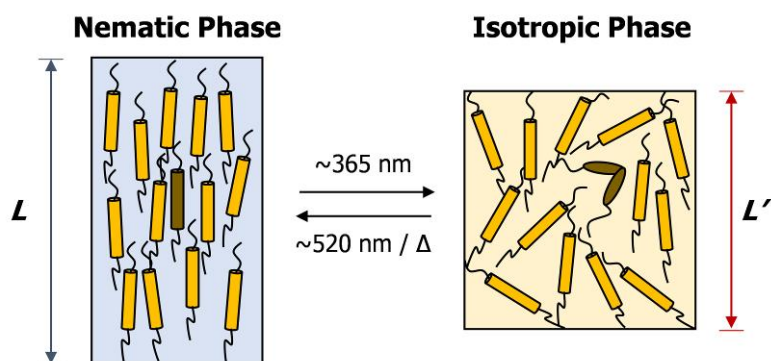
The most important aspect of the PRP is that the atomic scale dislocation and reorientation dynamics induced by the photo-isomerization directly affect the bending and/or stretching behavior of the material and the deformation is large enough to be detected with the naked eye. This shows considerable potential for photoactive liquid crystalline polymer as a user comprehensible, opto-mechanically controlled condensed matter structure. Accordingly, in recent studies, various photo-mechanical devices using the multi-functionality of PRP material have been suggested. Iamsaard et al. [30] developed photo-responsive ribbons which show large but reversible deformation in a variety of shapes. The deformation types between stretching and curvature could be easily selected from the direction in which the layered PRP film was cut. Particularly, they proposed a robust design method for a coiled spring structure in terms of an angular offset between the molecular orientation and cutting direction, and realized mixed-helicity springs by experiment. Yamada et al. [31] developed photo-driven motors by utilizing the photo-induced rolling motion of a continuous ring of laminated film composed of a PRP layer (surface) and a liquid crystalline elastomer (bulk). Because the system can be operated under non-contact and battery-free conditions, the researchers claimed that the minimum operation size of the device could be significantly reduced and hence adaptable to microscale- and nanoscale applications. Liu et al. [32,33] designed a microscale-patterned PRP film with the use of indium tin oxide electrodes and controlled the surface topology

of the film using UV light and heat. Such a ‘smart surface’ is especially suitable for the development of the photo-responsive microfluidic channel, which could be spatially controlled by optical elements from the environment. The theoretical studies of the optical isomerism of photochromic compounds and experimental studies for the development of a multifunctional photoresponsive polymer also have been carried out by Yu et al. [17], Harris et al. [34], Priimagi et al. [35], and Brömmel et al. [36].

(a)



(b)



(c)

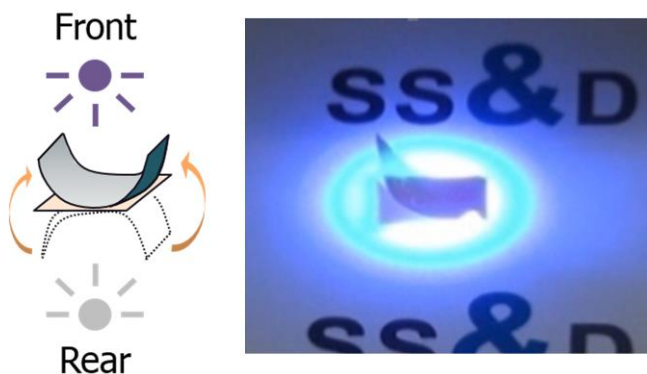


**Figure 1.1.** Mechanism of bending of a photoresponsive liquid crystal: (a) Photoisomerization reaction of azobenzene molecules, (b) change of polymer microstructure during the photo-isomerization, and (c) macroscopic bending deformation of the PRP material

## 1.2. PRP reinforced with nanoparticles

One important step in the development of PRP materials and structures is that the sufficient level of mechanical strength and thermal stability must be maintained for their useful mechanical design. Accordingly, two approaches have been mainly considered for the fabrication of stable and multi-components' reactive PRP material. One approach involves the formation of densely crosslinked, glassy photo-responsive networks having a preferred deformation axis created by the local director orientation of a liquid crystalline network [30,34,37], and the other approach involves the use of multifunctional nano-sized particles [38-40]. The former approach has been adopted to achieve the complex macroscopic shape such as spiral ribbons and helicoids, by controlling the chiral arrangement of liquid crystal mesogens. This concept is certainly beneficial to the design of complex mechanical systems – the synthesized material shows various states of deformation only by the alignment of the internal microstructures. However, handling of the homogeneous phase of the material is insufficient to overcome intrinsic weaknesses of the PRP material (high brittleness, low thermal stability, and slow response time), thus an investigation regarding the PRP nanocomposites system must be accompanied.

The insertion of nanoparticle induces multi-functionality of the material as well as the enhancement of its structural property. For more than 20 years, the development of polymer nanocomposites containing functional organic or inorganic nanoparticles in the host polymer networks have attracted attention due to their superior thermomechanical



properties to those of microcomposites under the same loading conditions [41-45]. As the size of the filler particle decreases to the nanoscale, the strong non-bonding interaction between the nanoparticle surface and the polymer segments in the vicinity of the particle significantly affects the properties of the overall composites due to the massive surface-to-volume ratio of the nanoparticles. The significant enlargement of the particle/matrix interface area forces the polymer chain around the particle surface to wrap tightly to form an interphase layer in the vicinity of the interface. Especially, when the diameter of a nanoparticle even remotely approaches the radius of gyration of typical polymers, the surrounding polymer near the surface of the nanoparticle is critically immobilized and strongly adsorbed on the surface of the nanoparticle.

To systematically design the mechanical behavior of the above-mentioned methods with mechanical rigor, analyses are needed for opto-mechanical and thermo-mechanical properties of the PRP material. Hence, these analyses must be preceded by sub-continuum scale level analyses because the origin of the opto-thermal actuation of the PRP material is strongly related to the photo-isomerization of the photoactive molecules and the thermal phase transition of the liquid crystalline microstructures. Furthermore, to predict the effective material properties of PRP composites structure reinforced by nanoparticles, the interfacial effects and their role in nanocomposites need to be verified. However, while numerous experimental studies have been devoted to the measurement of net deformation of the specimen, until recently, little attempt has been made to comprehend the intrinsic molecular structure both in the bulk and interfaces of the stimulus field.

### **1.3. Characterization of effective interphases formed in polymer nanocomposites**

The characterization of the effective mechanical properties and geometry of the interphase in a heterogeneous material is a key issue for the design of polymer nanocomposites due to the dominant effect of the interphase on the overall behavior of the composites. The interphase region in a composite possesses properties that are distinct from those of a host polymer, and it directly plays an important role in the structural stability of the overall composites. As the nanoparticle size decreases for a given volume fraction, the effect of the nano-reinforcement of the phase is exhibited more remarkably. Recent experimental and computational works have revealed that the nanoparticle size clearly effect various material properties such as the Young's and shear moduli [42,44,45], the thermal expansion coefficient [41,44], the thermal conductivity [46], and the electrical conductivity [47]. Particularly, the nano-reinforcement effect on the thermomechanical response is still valid even when the glassy state of the polymer matrix is transformed to a rubbery state in environments with temperatures above the glass transition temperature [42,48].

Many efforts have been made to evaluate the mechanical response of the interphase and characterize its effective stiffness and volume fraction (or thickness) for use as a design parameter for polymer nanocomposites [43-50]. So far, the exact thickness and properties of the interphase region have not been fully understood due to the difficulties in

the experimental visualizations in nanoscale. Thus, most experimental approaches have relied on indirect methods to monitor the effective thickness of the interphase layer in nanocomposites. Mortezaei et al. [51] measured the difference in the glass transition temperature between the host polymer and the interphase by differential scanning calorimetry (DSC). Fragiadakis et al. [52] derived the dielectric strength of the corresponding relaxation of the composite using thermally stimulated depolarization currents (TSDC) and combined the results with the degree of crystallinity of the bulk polymer to calculate the interfacial region. Bhuiyan et al. [53,54] approximated the morphological changes of the densified polymer regions around the particle surface using atomic force microscopy (AFM).

Meanwhile, the mechanical design and modeling of the nanocomposite interphases *in silico* have also been intensively investigated to characterize the reinforcing effect of the intermediate medium between nanoparticles and the surrounding polymer. The nanocomposite structures have been simply regarded as a three phase multi-inclusion based on the continuum model. The densified polymer region of the nanoparticle is considered an independent material that differs from the particle or polymer resin. Thus, the effective properties of the ‘interphase’ in the continuum model should be inversely obtained from the constitutive equation of the micromechanics model or the numerical solution of the finite element analysis via the homogenization method after the overall corresponding properties of the nanocomposites are fully obtained by experiments or molecular simulations.

## **1.4. Nano-continuum bridged multiscale model**

Until now, the concept of the multi-inclusion continuum model for polymer nanocomposites and their associated interphases has continued to develop. Our group developed a scale-bridging multiscale methodology for the elastic, elastoplastic, and thermoelastic mechanical behavior of polymer nanocomposites and explored the effect of nanoparticle size on the corresponding properties [44-46,55,56]. Ayatollahi et al. [57] suggested a finite element based multiscale model for single walled carbon nanotube-reinforced composites. In their study, it was emphasized that an interphase stiffness between the polymer and nanotube significantly affects the overall nanocomposite properties. Otero et al. [58] formulated the serial and parallel rule of mixture for nanotube-reinforced composites by adapting a non-linear constitutive laws to explicitly characterize the mechanical performance of the interphase.

An effort to constitute a delicate inclusion model is also under way to obtain an accurate and realistic internal stress distribution in the nanocomposite structures. Shabana [59] applied the multi-layered interphases concept for the micromechanical modeling of the nanocomposite structures, and predicted the debonding damage of reinforcements during the deformation process under various loading conditions. Recently, Ben et al. [60] presented a nonlinear cohesive model for a nanoparticulate polymer by adapting a functionally graded interphase and estimated the interfacial strength and debonding strain at the interface of the model.

While the interphase modeling in computational surveys seems to be uncomplicated, it has crucial shortcomings to identify the mechanical stress transfer capability at the nanofiller-matrix interface, because the physical properties of the intermediate medium in nanocomposites are strongly dependent on the effective region of the interphase layer. All of the above studies emphasize that defining the interfacial region of the nanocomposites is an important design factor in characterizing their physical behavior. Nevertheless, the quantitative mechanical properties of the adsorbed polymer region in the vicinity of the nanoparticle have so far only been obtained under an assumption of the proper thickness of the layer. From a mechanical viewpoint, an understanding of not only the reinforcing size but also the effective region of the interphase (such as the percolation threshold of the nanofiller or nanocomposite phase separation boundary under an overloaded condition) is a crucial design variable for polymer nanocomposites. Thus, an analytical methodology that can determine the effective mechanical properties and the thickness of the interphase should be developed considering the importance and potential applicability of the interphase analysis.

## **1.5. Outline of the thesis**

The main objective of this thesis is to develop a multiscale mechanical model for the PRP and PRP nanocomposites by combining the all-atom MD simulations with the conventional FE model. The photo-thermal actuation properties of a photo-responsive

network are investigated using MD simulation. For the implementation of the trans-to-cis isomerization of azo compounds, a switchable potential formalism for the diazene group is applied to the crosslinked PRP unit cell model. During the light switch-on and heating-up simulations at a wide range of temperatures, the scalar orientational order parameter for the mesogenic side group molecules, the effective photo-induced strain of the bulk polymer network, and the photo-mechanical properties can be characterized. The correlation between the microstate which belongs to the molecular location and the macroscopically observed photostrain is identified according to the isomerization ratio of the diazene groups.

In addition, to explore the possibility of introducing nanoscale fillers for improving such photo-mechanical properties of the PRP matrix, the above MD modeling method is applied to the case of a PRP nanocomposites system containing spherical gold nanoparticles, and the reinforcing efficacy of the nano-reinforcements are quantified. We particularly examined the effect of nanoparticle size on the photo-thermal actuation by varying the diameter of the nanofiller under the same volume fraction. The results indicated that the insertion of the gold nanoparticles enlarges the photostrain of the material while enhancing its mechanical stiffness and thermal stability. When the diameter of the nanoparticle is similar to or smaller than the length of the mesogen, the interfacial energy between the nanofiller and the surrounding polymer matrix does not significantly affect the alignment of the mesogens; rather, the adsorption energy at the interface generates a stable interphase layer. Hence, these improvements were more effective as the size of the gold nanoparticles was decreased.

Lastly, based on the present findings from MD simulations, we propose a logical approach to characterize the internal mechanical behavior of the intermediate media of PRP nanocomposites in terms of the nanoparticle size as well as the photo-isomerization ratio of the macromolecular unit cell. In addition, the nanophysics of the intermediate media are discussed in detail. The proposed model involves matching the analysis results of molecular dynamics (MD) and finite element (FE) simulations. The intrinsic nanomechanical behavior of polymer nanocomposite models, such as the effect of nanoparticle size on the thermomechanical properties or the particle/matrix interface adhesion characteristics, is demonstrated atomically using MD simulation. Meanwhile, a three-dimensional FE model for determining the mechanical properties of nanocomposites allows us to identify the equivalent continuum model in terms of the internal stress field characteristics of the nanofiller and the hosting matrix, as well as the global stiffness of the composite materials. The unknown mechanical response and geometrical boundaries of the interphase (polymer networks adsorbed on the particle surface) are thus numerically obtained from a continuum model through the matching of the homogenization and deformation energy to a full atomic molecular model. The equivalent continuum models given from the present multiscale method successfully represent the virial local stresses of the interphase region of the full-atomic model in both the before and after photo-isomerization conditions, as well as the particle size dependent stiffness of the nanocomposites. Therefore, the present methodology can facilitate a more accurate and efficient evaluation of a nano-sized filler-dispersed heterogeneous system considering its intrinsic nanoscale nature. This gives a

wider analysis of the nanofiller-reinforced PRP composites and the mechanical design of the PRP actuator system.

The remainder of this work is organized as follows. **Chapter 2** provides results for the evaluation process of the photo-deformation, mechanical properties, and thermal phase transition of PRP material by using all-atom MD simulations. At the end of this chapter, we also discuss some preliminary research on the mechanical application of the glassy PRP material and its experimental evaluation. **Chapter 3** focuses on PRP nanocomposites that are functionalized with gold nanoparticles, especially for their enhancement of photo-mechanical properties. By deriving the photo-thermal actuation properties of the nanocomposites models, the functional role of the non-bonded interface between the nanoparticle and the polymer matrix is explained. Thus, the relation between local disordering of the microstructure and the global deformation behavior of the material is defined. **Chapter 4** gives a multiscale methodology to reproduce the obtained photo-thermal actuation behavior of PRP nanocomposites in continuum mechanics models. Both the shape parameter for the design of the stress-free bending of the specimen and its elastic properties and the thickness of the effective interphase under mechanical loading are examined according to the embedded nanoparticle size and photo-isomerization ratio of the matrix. **Chapter 5** summarizes the concluding remarks and outlines some future challenges.



## 2. Photo-thermal actuation analysis of PRP

### 2.1. Model preparation for the MD simulations

#### 2.1.1. Modeling of nematic liquid crystalline polymer system

With the goal of the multiphysics design and analysis of the photo-responsive structure, densely crosslinked PRPs were modeled *via* MD simulation and their photo-mechanical properties were estimated. The entire crosslinked network structure is represented by a full-atomic description without the assumption of a rigid-body translation of the mesogen or the flexibility of methyl side groups, which have been shown to be well suited to coarse-grained models by Ilnytskyi et al [61,62] and Toshchevikov et al [63]. This allows the quantitative estimation of the structural and energetic properties of the material, including the geometrical illustration of the microstate and the nematic-isotropic (N-I) phase transition of the monodomain structure, as well as its mechanical stability. To examine the correlation between the degrees of photo-isomerization of diazene groups and the macroscopic deformation of the monodomain phase (which currently is not easy to verify using experimental techniques), we adopt a switchable potential formalism for the double bonds of the nitrogen atoms (N=N) in the classical MD simulation.

A highly crosslinked nematic polymer unit cell that possesses azobenzene moieties as photoactive agents was prepared for MD simulations. We selected a liquid

crystalline molecule 6-[4-(4-ethoxyphenylazo)phenoxy]hexyl acrylate and a crosslinking agent 4,4'-di(6-(acryloxy)hexyloxy)azobenzene for the modeling of the polymer structure that was typically used in previously reported experimental surveys [17,64]. Details of the molecular models are presented in **Figure 2.1**. Both molecules contain azobenzene chromophore, in which photo-isomerizes from trans-to-cis form on UV light irradiation and cis-to-trans form on visible light irradiation (or heat). The present PRP model has an advantage due to the many photoactive sites in nanoscale; the entire polymer network structure can be fully described by all-atom MD without the aid of mesoscopic modeling of the molecular system. The modeling of polymer chain molecules and their macromolecular structures with a full atomic representation was carried out with the commercial MD package, Materials Studio 6.0 (Accelrys Inc.) [65]. The opto-thermal actuation of the models was observed and the characterization of their microstructural and mechanical properties described below was carried out by using the open-source MD code, LAMMPS (Sandia Lab.) [66].

The uncrosslinked monomers and diacrylate agents are initially collocated (7:1 molar ratio) into an amorphous unit cell with periodic boundary condition, while each molecule maintains its internal direction along the x-axis. The model was sequentially relaxed using the conjugated gradient method, followed by 5ns of an isothermal dynamic (NVT) ensemble at 300K and 3ns of an isothermal-isobaric (NPT) ensemble at 300K and 0.1MPa. The timestep for the equilibration of the model was 1fs, except where noted. During the equilibration process, the potential energy of the constituent atoms including

their covalent and non-covalent interactions was calculated using a polymer consistent forcefield (PCFF) [67] that satisfactorily describes the thermo-mechanical properties and thermal phase transition of condensed polymer.

A polymer crosslinking procedure was addressed for the equilibrated model. The overall simulation flow is shown in **Figure 2.2**. Because the model studied includes a polycondensation reaction of a liquid crystalline monomer unit as well as a crosslinking reaction of the agent, we separated the procedure for the formation of chemical bonds into two steps. In the first step, the crosslinking agents were linked with the surrounding liquid crystalline monomers in order to build the side branch of the polymer network. The distance cutoff started from 1.0 Å and increased to 5.4 Å with the step increment of 0.2 Å. The energy minimization with conjugated gradient method (convergence cutoff was 10 kcal/mol Å) and NVT ensemble at 400 K for 50 ps were executed for every possible cutoff point to enable all the intramolecular structures of the connected units to relax effectively. Eighty percent of all the reactive sites of the crosslinking agents were crosslinked during the first step. The second step involved the polymerization of the liquid crystalline monomers. Because the distances between crosslink sites on the residual molecules became wider after the first crosslinking step, we applied a longer reaction distance cutoff (7.5 Å) with the increased step increment of 0.5 Å. The potential energy of the model was minimized again for each distance cutoff. It was found that the final crosslink density of the liquid crystalline molecules reaches to 45-% and all the monomers are fully interconnected not only in the unit cell but also across the boundaries of the periodic cell

box. The crosslinked macromolecular structure was equilibrated again by the NVT ensemble at 300 K for 5 ns and the NPT ensemble at 300 K and 0.1 MPa for 10 ns. The proposed crosslinking method partly follows the procedures used in other MD studies [68], guaranteeing that the condensed model shows energetically stable microstates with the associated molecular structure. The completed PRP model contained a total of 5,113 atoms and 85 azobenzene moieties and the model configuration is shown in **Figure 2.3**.

### 2.1.2. Applying trans-to-cis photoswitching potential

The photo-responsibility of the PRP material originated from the isomerization reaction of the photoactive molecules in the system. As shown in **Figure 1.1**, the azobenzene moiety used in this study is representative of the photoactive functional group which changes its molecular conformation upon irradiation with UV light (~365 nm) and with visible light (~520 nm). Because the conventional force fields including PCFF potential do not provide the basis for simulating this type of stimulus, an additional interatomic potential which specifies the change of molecular geometry at the photo reactive sites should be required for the computation in MD simulations.

In the present study, therefore, we treated the dihedral potential parameters for the unit cell models. From a molecular structural point of view, the photo-isomerization of azobenzene is reproduced by changing the equilibrium dihedral angle of the diazene group from 180 ° to 0 ° or *vice versa*. The quartic form of the torsional energy (E) used in a

class II force field is described as

$$E = \sum_{n=1}^3 V_n \left[ 1 - \cos(n\varphi - \varphi_n^0) \right] \quad (2.1.)$$

where  $V_n$  is the dihedral potential and  $\varphi_n^0$  is the equilibrium dihedral angle. **Figure 2.4** shows a schematic of the photo-switching of molecules in MD simulation. The trans to cis (UV light irradiation,  $\varphi^0 = 0$ ) and cis to trans (visible light irradiation or thermal isomerization,  $\varphi^0 = \pi$ ) isomerization of the azobenzene and its peripheral groups was implemented by adapting a switchable N=N dihedral parameter. This rotation potential formalism has been widely employed for an *in silico* model of azobenzene and its derivatives such as the light-driven molecular switching in the DNA [69,70], RNA [71], and peptide [72,73] structures, photoreactive liquid crystal cluster [74], and self-assembled monolayer phase [75]. Similarly, we handled the dihedral potential angle and the corresponding potential coefficients given by Heinz et al. [76] for the diazene group in the PRP model. The parameters of photoactive potential of the azobenzene unit used in this study are shown in **Table 2.1**. For each photoreactive point, the photoexcitation energy was added to the C-N=N-C dihedral component to overcome the thermal conversion barrier (~24 kcal/mol) while the equilibrium angle was reversed.

We validated the steered dihedral potential by comparing the minimized molecular geometry of single azobenzene with the corresponding one derived from density functional theory (DFT) study. As shown in **Table 2.2**, the employed switchable potential [76] has reproduced the geometrical features of the trans- and cis-states of the azobenzene

provided in our DFT result (Gaussian 09 package, HatreeFock; 6-31g basis set) as well as the reported data in the literature [77], both for trans- and cis- isomers.

We modulated the photo-isomerization ratio by selectively adapting the modified dihedral potential described above to the diazene groups of the unit cell. When the light is irradiated on the PRP surface, the photo-isomerization of PRP is partially driven depending on the transparency of the material and the light intensity of the environment. Because the macroscopic deformation performance of the material is strongly correlated with the isomerization ratio of azobenzene, the parameter is essential for its mechanical design. Beginning from all the trans-state, the azobenzene moieties in the equilibrated models were randomly selected and converted to cis-state with the conversion ratios of 0 %, 25 %, 50 %, 75 %, and 100 %, as shown in **Figure 2.5**. The unit cells were then equilibrated for another 3 ns in the NPT ensemble at 300 K and 0.1 MPa.

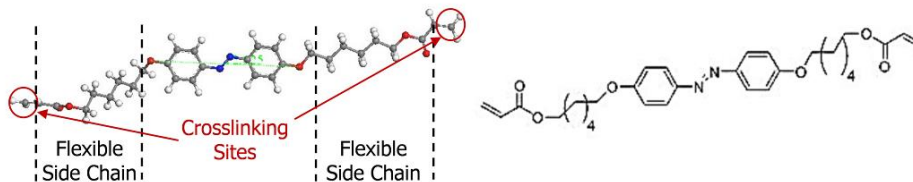
**Table 2.1.** Dihedral force field parameters for the diazene group and its photo-isomerization description

State	Dihedral energy coefficients [76]					
	$V_1$	$\phi_1^0$	$V_2$	$\phi_2^0$	$V_3$	$\phi_3^0$
	(kcal/mol)	(deg)	(kcal/mol)	(deg)	(kcal/mol)	(deg)
Thermal equilibrium	5.2	180	12	0	0	0
trans-Azo	34	180	0	0	0	0
cis-Azo	34	0	5.2	180	0	0

**Table 2.2.** Geometrical properties of trans and cis state azobenzene

Mode	trans state			cis state		
	MD	DFT	DFT [77]	MD	DFT	DFT [77]
NN (Å)	1.283	1.264	1.253	1.270	1.253	1.242
NC (Å)	1.394	1.412	1.366	1.460	1.433	1.435
NNC (deg)	123.7	115.0	128.8	129.0	124.4	122.9
NCC (deg)	121.2	120.5	120.3	118.4	120.1	119.8
CNNC (deg)	180.0	180.0	180.0	0.0	11.0	4.2

**Compound 4** (Crosslinker) 6-[4-(4-Ethoxyphenylazo)phenoxy]hexyl Acrylate



**Compound 6** (Host LC resin) 4,4'-Di(6-(acryloxy)hexyloxy)azobenzene

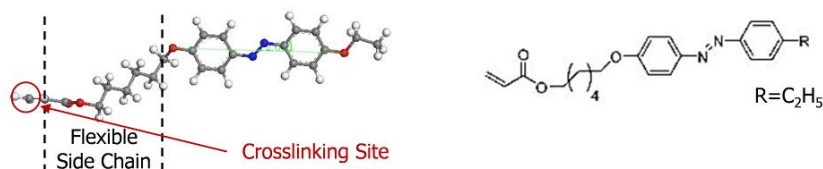


**Figure 2.1.** Azobenzene derivatives used in this study

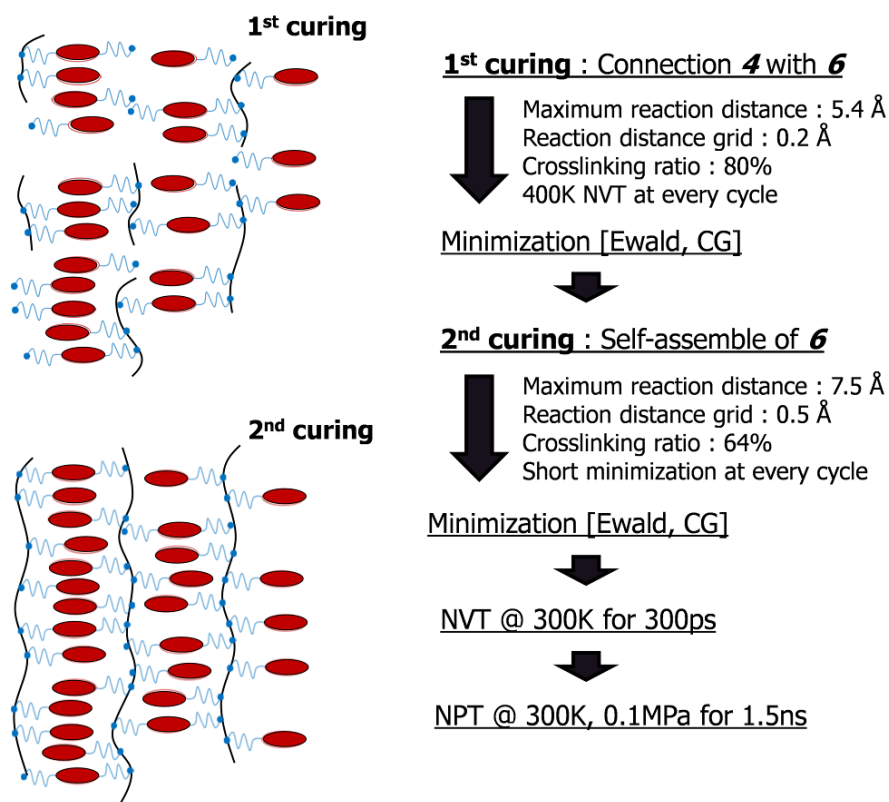
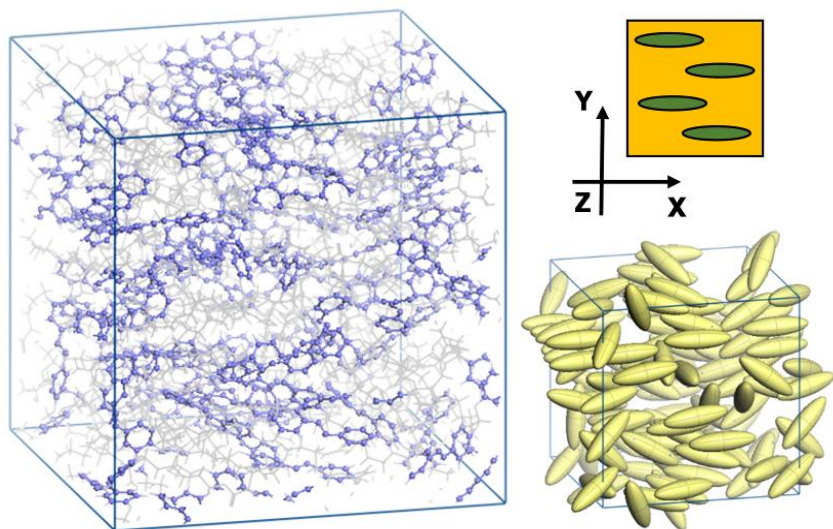


**Figure 2.2.** A two-step crosslinking process to prepare glassy liquid crystalline polymer networks in MD simulation





✓ **Front view (XY plane)**

✓ **Side view (YZ plane)**

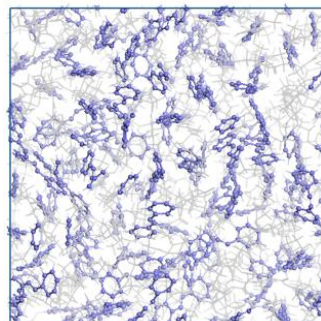
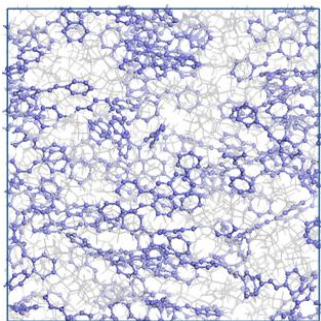


**Figure 2.3.** Modeled PRP material using MD simulation. Diazene groups were highlighted to show that the host liquid crystal molecules were aligned in the x direction of the unit cell.

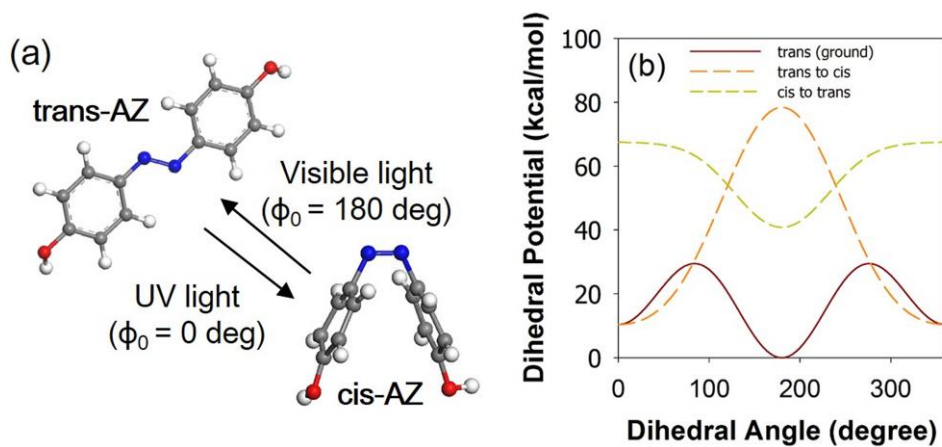


**Figure 2.4.** Trans-cis photo-isomerization of azobenzene in MD simulation: (a) schematic of the conformation change of diazene group and (b) dihedral potential energy functions for the reproduction of tran-cis transition of the azobenzene.

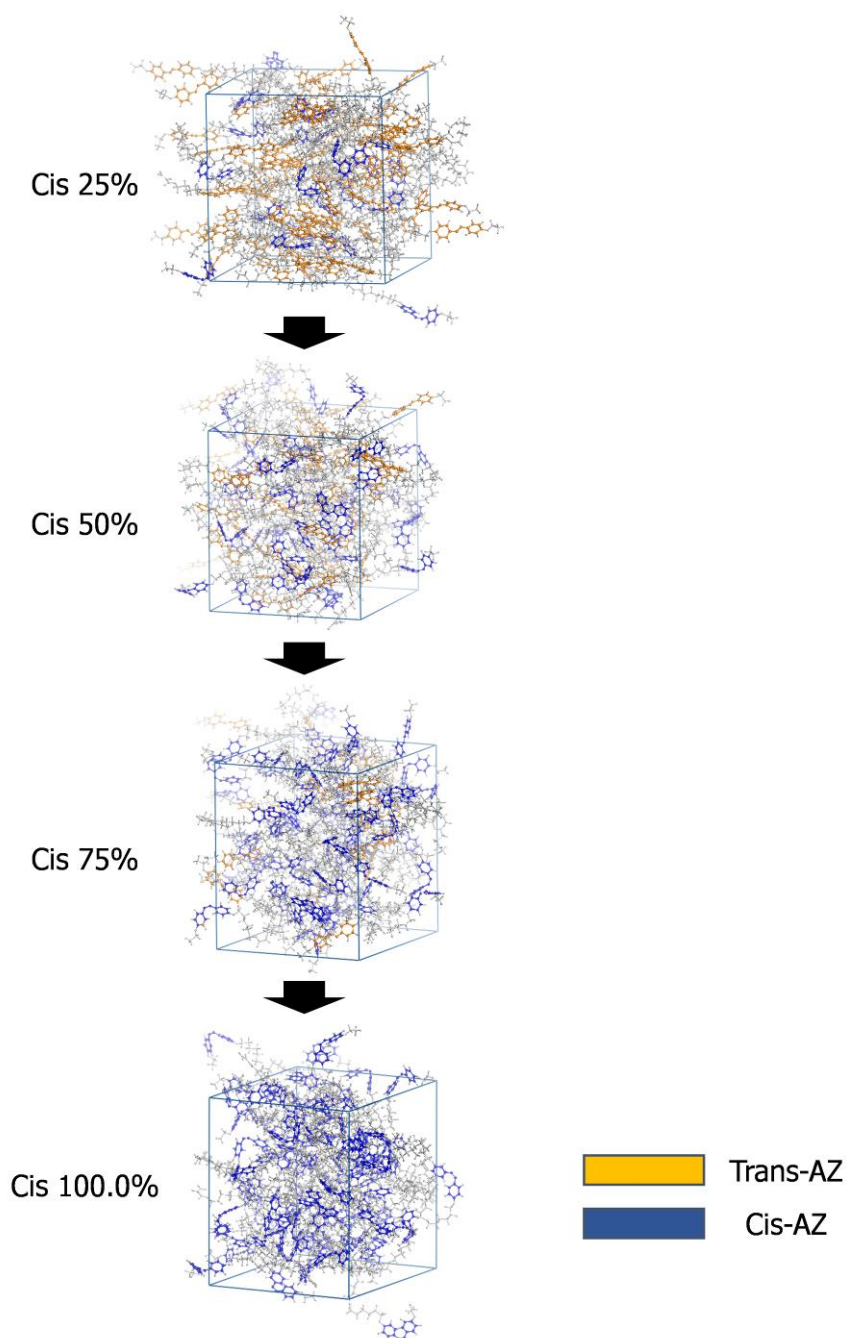


**Figure 2.5.** Trans-to-cis photo-isomerization simulation for the modeled PRP unit cell. As the isomerization reaction was progressed, both the disorder of the alignment of polymer molecules and the shrinkage of the system along the x direction were observed.

## 2.2. Characterization of the material properties during the photo-isomerization reaction

### 2.2.1. Macroscopic bulk lattice change with incompressibility

For the equilibrated model, the trans- to cis-mode switchable potential was applied and equilibrated again with an NPT ensemble for 3ns with a timestep of 0.2 fs. The photoactive sites were randomly selected among the diazene group in the PRP model and the time evolution of the unit cell length  $l_x$  (which is perpendicular to the nematic direction (x-axis)) was derived. During the MD run the modified potential field significantly changed the bulk properties of the system as well as the geometry of the microstructure. Whereas the unit cell length along all three axes was updated at the same rate for the pre-equilibration process, each unit cell length was controlled independently at the photoswitching stage. Therefore, the conformational change of the polymer network and the corresponding anisotropy of the material provoked a variation of the unit cell length during the simulation. As illustrated in **Figure 2.5**, this verifies that the constructed PRP model represents the macroscopic photo-shrinkage of the polymer network system as well as the collapse of the internal molecular order.

For a series of partly isomerized PRP models, as depicted in **Figure 2.6 (a)**, a linear dependence of the photo-deformation of the material on the conversion ratio of the cis form can be found: The degree of disorder of the microstate induced by the photo-

isomerization of the azo compounds contributes to the effective photostrain of the material at a given temperature.

The modeled PRPs showed incompressible behavior during the photo-deformation, whereas their internal network conformation underwent extreme changes. The contraction of the cell length along the x-axis was fully compensated by the expansions of the other two directions, while the density of the model retained its initial value regardless of the isomerization ratio, as shown in **Figure 2.6 (b)**. In terms of atomic structure, this result demonstrates the limited role of the azo derivatives in the macromolecular structure: the bent-core shape of the diazene molecules loses its directionality and significantly affects the orientation order of the overall material. However, the intermolecular interaction energy of polymer chains does not change during the isomerization, but realigns in the bulk material. Thus, the cis-isomers only affect the local geometry and direction of the polymer molecules while maintaining their total free volume in the model.

### **2.2.2. Mechanical properties**

These conformation changes are also strongly related to the transformation of the mechanical properties of the material. To further research the structure-property relationships, we examined the elastic property for all the considered PRP models by applying uniaxial strain. The length of the unit cell is elongated during the NVT ensemble

run at 0.1K, with the true strain rate of  $10^6/\text{ps}$ . Maintaining the total strain of less than 0.3%, the elastic stiffness components in both the axial ( $C_{11}$ ) and transverse directions ( $C_{22}$  and  $C_{33}$ ) were calculated and the results are presented in **Figure 2.7**. Under the trans state, the PRP shows transversely isotropic characteristics and has the highest stiffness in the nematic direction since all the polymer backbone segments are aligned along that direction. However, such strong structural anisotropy is significantly reduced as the isomerization occurs and the stiffness ratio between the axial and lateral stiffness of the PRP reaches close to 1, which indicates that the PRP structure becomes nearly isotropic. When the macromolecular complex was constructed, most monomers were preferably reacted along the nematic director axis and the translational motion was restrained in that direction by the periodic boundary condition of the modeled unit cell. Nevertheless, the disordering of the nematic and reconfiguration of the associated polymer chain due to the isomerization remarkably influence the mechanical characteristics of the material.

### **2.2.3. Microstate order parameter change during heating-up simulation**

The conformational changes of the molecular structure also affect the thermal N-I phase transition of the material. To characterize the thermo-optical properties, each model was heated up in the NPT ensemble run and scalar orientational order ( $S$ ) profile was measured to estimate how well the mesogen components sustain their alignment along the

nematic director. For each given atomic configuration, the value can be calculated as follows:

$$S = \left\langle \frac{3 \cos^2 \theta - 1}{2} \right\rangle \quad (2.2)$$

where  $(\theta)$  is the angle between the x-axis of the unit cell and the straight-line segment joining both ends of the azobenzene phenyl rings, and the bracket symbol,  $\langle \bullet \rangle$  denotes the ensemble average over all atoms in the system. Starting from 300 K, the temperature increased gradually with the heating rate of 5 K/ns until it reached the melting temperature ( $T_{iso}$ ), where the mesogens rotated vigorously and the alignments had fully collapsed ( $S < 0.05$ ), as shown in **Figure 2.8**. The melting temperature is significantly lowered according to the isomerization reaction because the pre-collapsed microstructure accelerates the thermal phase transition. However, simultaneously, the cis-isomers suppress the thermal response of the system so the transition temperature range broadens and the decreasing rate of the melting temperature reduces. We also performed simulations of the cooling-down of the unit cell models (from 300K to 200K) and found that the reduction of the orientation induced by photo-isomerization cannot be recovered thermally near room temperature.

#### 2.2.4. Quantification of the photo-thermal deformation of PRP

The results obtained so far provide important information for the design of the

effective photostrain of the material in accordance with the isomerization ratio and the thermal condition of the system. The quantified photostrain  $\varepsilon^{ph}$  could be derived by dividing the deformation along the director by the length of the all-trans model as,

$$\varepsilon^{ph} = \left\langle \frac{l_{cis} - l_{trans}}{l_{trans}} \right\rangle_x \quad (2.3)$$

Similarly, the spontaneous stretching ratio at a certain temperature  $\lambda_T$  can be simply derived from the ratio between the bulk length at a given temperature (300K) and the corresponding ratio at a melting temperature, defined as,

$$\lambda_T = \left\langle \frac{l_T}{l_{T_{iso}}} \right\rangle_x. \quad (2.4)$$

All the results are summarized in **Table 2.3**. The experimental data from the literatures [18,78], in which azobenzene containing liquid crystal homopolymers were considered, are also included. According to the results, the current computational study shows good prediction of the structural deformation quantity under both thermal and light stimuli. Compared with the experiment, the current model has its own advantage, in that it exhibits quantitative values both for the change of bulk material properties and the associated microstate distributions during the light irradiation, and hence can be an efficient design and analysis tool for the photoresponsive polymer and its applications.



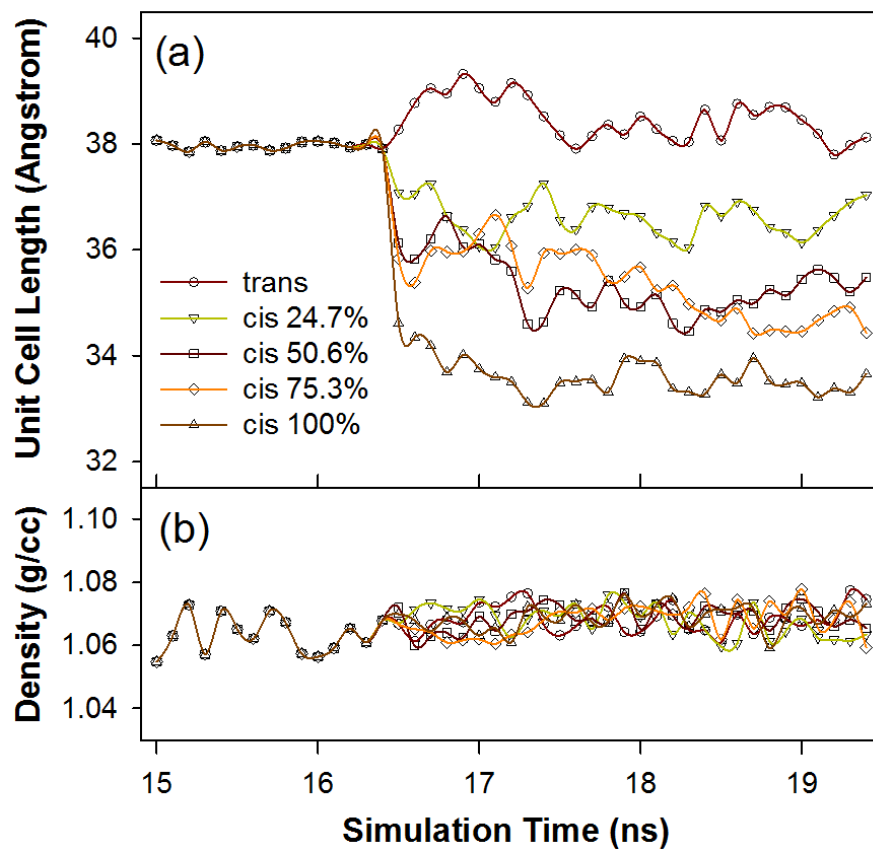


**Figure 2.6.** (a) Unit cell lengths along the director axis and (b) densities of the PRP models during the photo-isomerization. Photo-switching potential was applied at 16.4 ns.

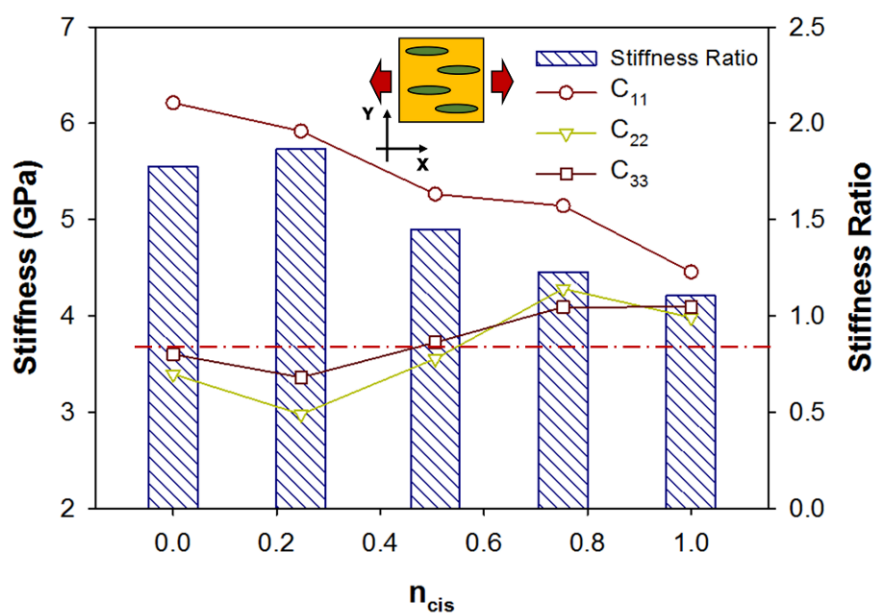


**Figure 2.7.** Elastic stiffness components and their ratio according to the cis-isomerization ratio

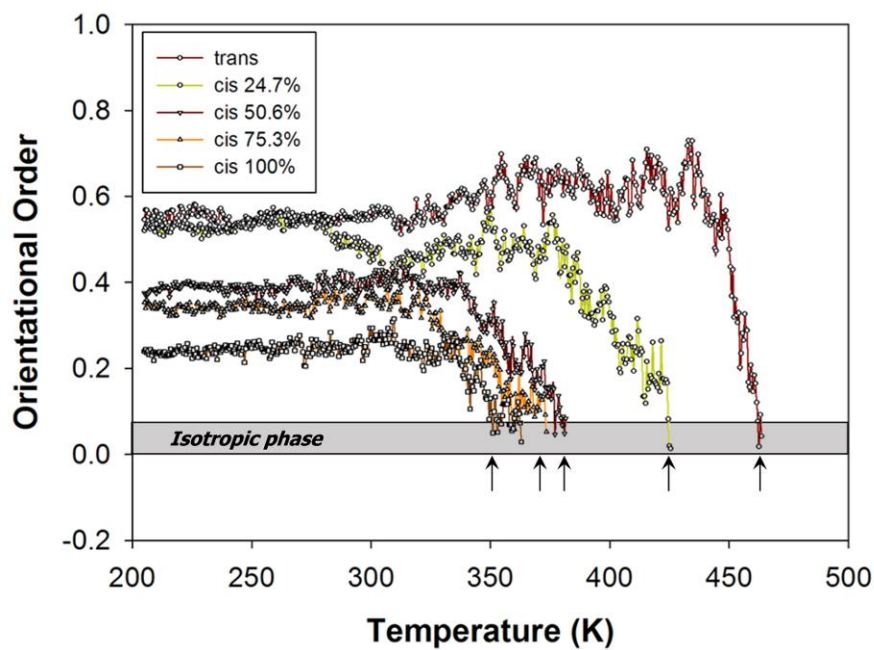


**Figure 2.8.** Scalar orientational order parameter at a wide range of temperature (photo-switching potential was applied at 300K prior to the heating-up simulation).

**Table 2.3.** Photo-mechanical properties of the PRP materials. Regarding the partly isomerized models, the photostrain calculation was repeated 4 times and averaged with random selection of isomerization sites. S.D. is standard deviation of the model.

System	$n_{cis}$	$T_{iso}$ (K)	$\epsilon^{ph}$ (S.D.) (%)	$\lambda_T$
trans	0.000	462.0	0.00	1.59
cis-24.7%	0.247	425.0	-3.47 (1.32)	1.52
cis-50.6%	0.506	381.5	-7.65 (0.93)	1.30
cis-75.3%	0.753	373.5	-10.54 (1.38)	1.31
cis-100%	1.000	363.5	-11.62	1.15
Exp. (thermally) [78]	0.000	394.0	N/A	1.57
Exp. (optically) [18]	1.000	388.0	-13.00	N/A

## **2.3. Suggestion of a mechanical application: A light-driven PRP strand**

### **2.3.1. Motivation**

The photo-mechanical behavior of the PRP system has considerable potential as the self-sensing actuator. The material is driven by a specific wavelength of light and its actuation capacity is sufficient to deform the workpiece device. The most striking feature is that contact-less, localized control is possible without the aid of electrical circuit elements. Furthermore, the photo-sensitive behavior of the PRP material implies good reversibility and that it can be repeatedly used in practical applications. Also, the actuation performance of the PRP material is comparable to that of other types of self-adaptive material. For example, the normal strain along the nematic axis of the PRP material estimated in the present all-atom study and in the literature [18,76,78] is significantly larger than that for shape memory alloys [79] or ionic polymer-metal composites [80]. Accordingly, it is expected that the PRP material considerably widens the application field of sensor/actuator devices and soft robotics.

Despite such considerable advantages, the PRP material has a number of drawbacks. The material behaves similar to glass and is easily broken by the external loading environment. Simultaneously, the photo-sensitive behavior of the material only appears when the thickness of the operation layer is below the millimeter-scale due to the

short penetration depth of the ray. For the mechanical engineer, this severely restricts the design space because the maximum strength of the PRP device is strictly limited to only a few MPa. Thus, the effective load carrying capability of the material is not sufficient to support heavy objects or to be used as a linkage part connecting adjacent bodies. Another drawback is the cost of the product; the syntheses of azobenzene derivatives have only been at the laboratory level and are very expensive for application to the large-scale system.

Accordingly, as White and Broer emphasized in their recent review [28], the bottleneck in the development of the PRP device lies in the need for mechanical implementations that will meet the requirements for practical applications of small amounts of material. Therefore, exploring a ‘creative mechanical design’ for the PRP material is an important subject in this research. In this regard, we proposed a light-driven PRP strand which contains a single layer of PRP composites, consisting of a polymer-fiber matrix and glassy PRP. From a structural viewpoint, the high aspect ratio of the strand induces the strand to deform elastically and it allows flexible and adaptive deformation to the PRP strand. Also, by attaching transparent thin films on both sides of the PRP composites, the strand fabricated in this study showed sufficiently high mechanical strength to sustain substantial tensile stress without fracture. We examined the performance of the PRP strand by threading a maze-like obstacle, which cannot be passed by conventional methods, with UV-light sources.

### **2.3.2. Experimental section**

### **Preparation of a PRP strand**

The PRP material was prepared by the thermal polymerization of 6-[4-(4-ethoxyphenylazo)phenoxy]hexyl acrylate. The crosslinker 4,4'-di(6-(acryloxy)hexyloxy)azobenzene was mixed with the resin as a dry powder with a molar ratio of 4.4:1. The two azobenzene derivatives were purchased from BEAM Co. (USA). The powdered mixture of resin and crosslinker was stirred in the minimum amount of ethyl acetate at room temperature and then heated to dry on a hot plate at 60 °C for 30 minutes. The thermal initiator 1,1'-azobis(cyclohexane-1-carbonitrile) purchased from Wako (Japan) was added 1 mol.-% and stirred at room temperature. A meshed multidirectional polymeric fabric tape with ~120 micrometer thickness (a conventional iron-on fusible interfacing) was prepared as a skeletal frame, and the mixture in solution-state flowed into the polymer frame in a glass cell. The material was then heated at 90 °C for 24 hours for polymerization. Both sides of the soaked frame were coated with a poly ethylene terephthalate adhesive layer of 23 micrometer thickness provided by Kookje La-Tech (Korea). Typically, the layered film was cut parallel to the long axis to fabricate a strand-like structure (length: 75 mm, width: 3 mm).

### **Material characterization**

The alignment of the mesogen at room temperature was measured by polarized optical microscopy (Olympus BX51M, Japan). The alignment of the PRP strand immersed in the

skeletal matrix was compared with the corresponding strand of the pure PRP coated on a cellophane tape, as shown in **Figure 2.9**. It was found that the azobenzene derivatives were self-assembled very well on the polymer substrate, even when the mechanical rubbing was not performed. In the case of the PRP in a fibrous polymer scaffold, the orientations of mesogens were randomly distributed on the surface of each fiber bundle. However, the liquid crystal phase was clearly observed and thus the resulting composites could be deformed at the site of irradiation.

### **Preparation of a maze-like obstacle**

The maze component was drawn using SolidWorks® (Dassault Systemes, USA). The body component was fabricated using a 3D printer (ROKIT 3DISON Plus, Korea) with acrylonitrile poly-butadiene styrene (ABS) filaments. The size of the maze was  $30 \times 16 \times 15$  (mm<sup>3</sup>). Transparent glass sheets of 2 mm thickness were attached to both sides and to the top of the component to seal other passages except the inlet and the outlet.

### **UV light irradiation to allow light-driven motion of a PRP strand in a maze**

An LED type UV light source (wavelength: 365 nm, light intensity: 7200 mW/cm<sup>2</sup>; UVSMT SUV2010-S, Korea) was used to control the photo-bending of the free-standing PRP strand. Because the intensity of the light source beam is sufficient to produce the desired amount of strain, the experiment was carried out under room temperature condition. Two light-source channels were prepared which have a spot size of  $\varnothing 3$  and the light was

irradiated on the PRP strand sequentially or simultaneously beyond the glass wall of the maze.

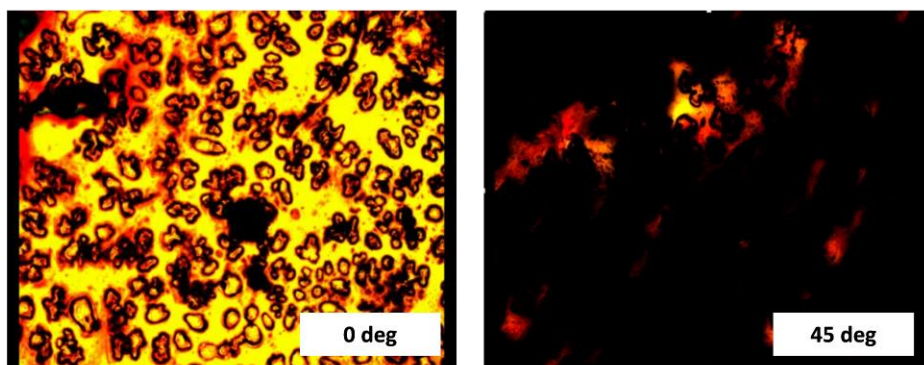
### **2.3.3. Threading the physical maze with a PRP strand**

To assess the performance of the fabricated PRP strand, we considered a simple path-finding problem as described in **Figure 2.10**. The PRP strand was placed into a closed ‘maze’ that cannot be passed by the conventional straight-line strand. We set two UV-LED spot lights outside of the maze box with their positions fixed in order to focus on the stationary points on the moving pathway of the PRP strand. With the pulling-in of the PRP strand, we controlled the UV-LED spots beyond the glass walls of the maze to deform the strand.

The schematic representation of the desired pathway and the test result are shown in **Figure 2.11**. The result verified that the strand completely threaded its way through the maze box, successfully avoiding the obstacles. Such dynamic modulation can be further extended if the number of UV-spot channels is increased and the length of the strand is prolonged. In addition, the PRP strand fabricated in this study has even greater strength than the pure PRP film and significantly less PRP material is used than that for the pure PRP film of the same size. In summary, the PRP strand suggested in this work may overcome the main drawbacks of the PRP material (high cost and low tensile strength) and enable the practical design of the PRP devices.



**(a)**



**(b)**

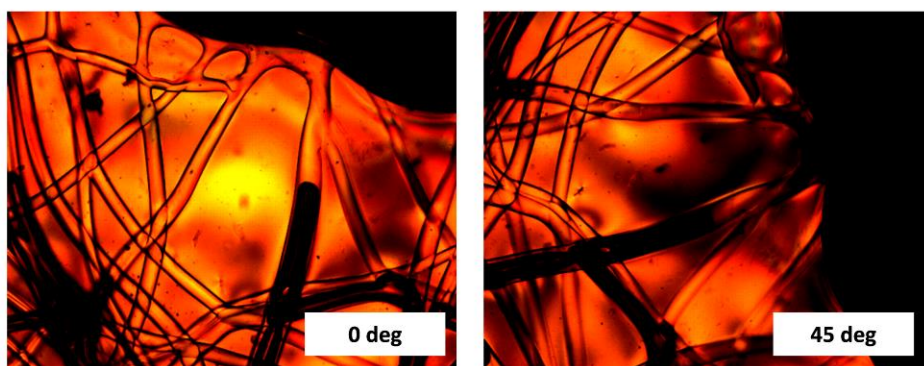
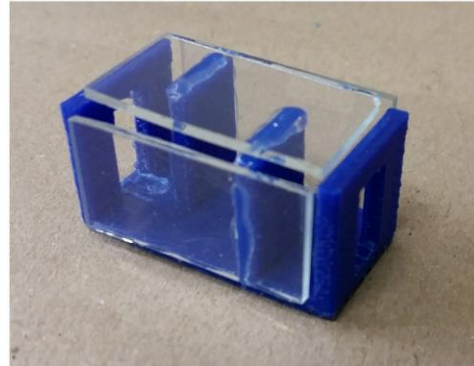
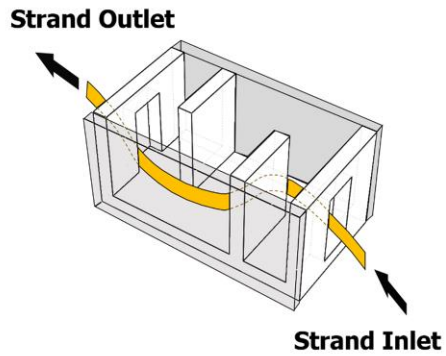


**Figure 2.9.** POM images of (a) the neat PRP material coated with cellophane and (b) the PRP immersed in the fusible interfacing under 100X magnification.

(a)



(b)

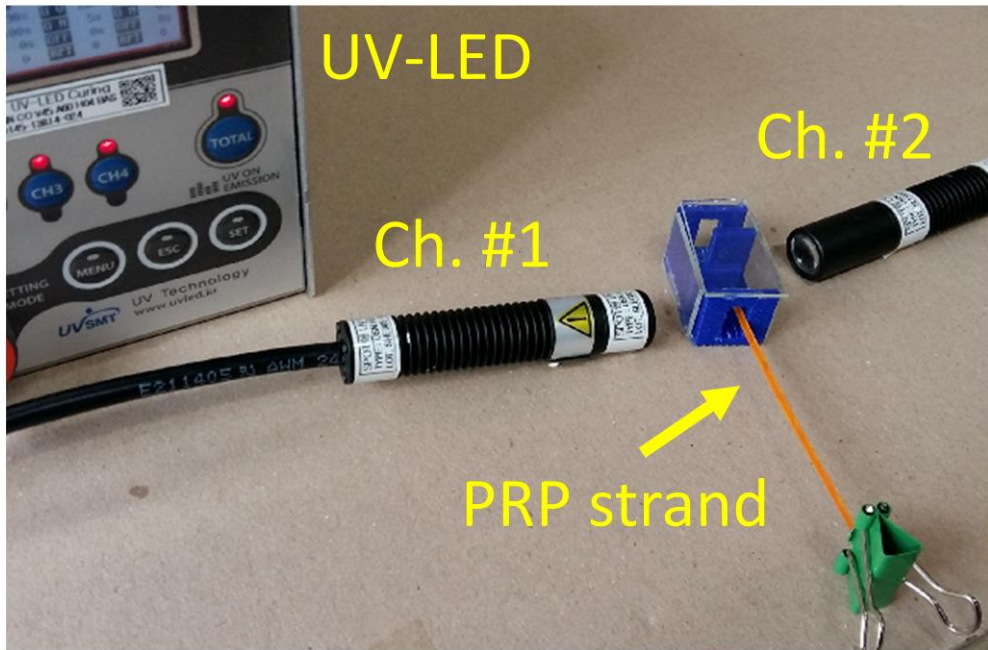


**Figure 2.10.** (a) The maze component modeled in the CAD apparatus and produced by the 3D printer, and (b) the experimental setup.

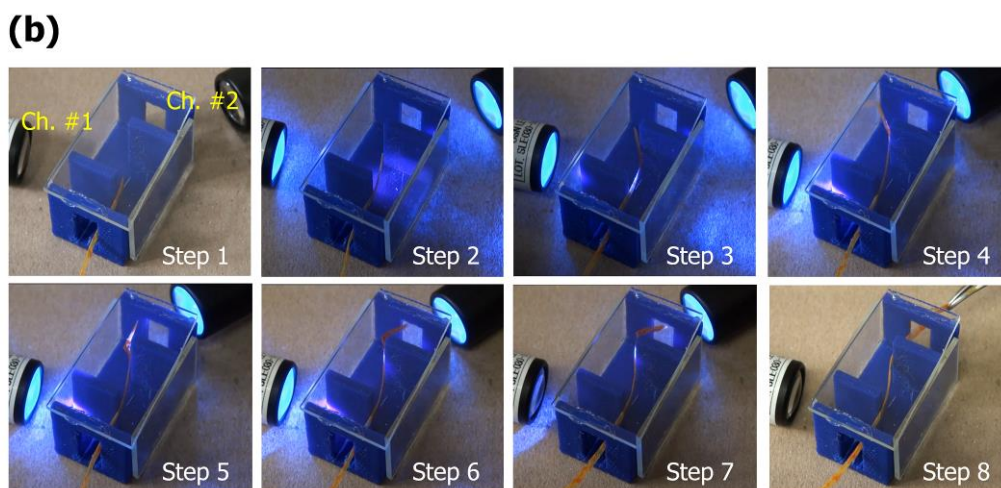
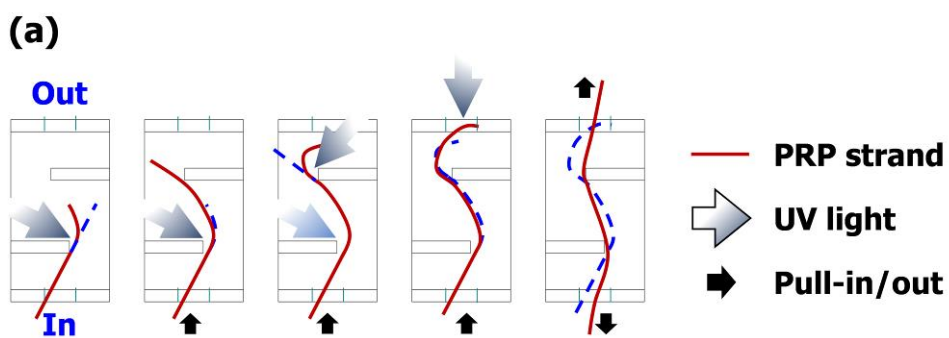


**Figure 2.11.** (a) Schematic view of the PRP strand passing through the maze guided by UV-light and (b) snapshots of the path-finding behavior of the PRP strand in the maze

## 2.4. Chapter summary and conclusions

In **Chapter 2**, we evaluated the photo-deformation, mechanical properties, and thermal N-I transition of the PRP structure by using all-atom MD simulations. The photo-isomerization reaction of azobenzene caused by light exposure was represented by applying the photo-excitation energy absorbed by the azobenzene moiety to the dihedral potential for diazene groups in the unit cell. The contribution of the molecular motion to the macroscopic transformation of the crosslinked polymer network were presented and the corresponding various isomerization ratios were characterized. The obtained results contribute to the development of a multiscale methodology that integrates the molecular analysis with that of the continuum mechanics that will be shown in **Chapter 4**. This chapter also discusses a simple experiment we performed that maximizes the mechanical capabilities of the PRP material in a real environment. The PRP monomers were cured in a fibrous polymer scaffold and a PRP composites strand was fabricated, having high aspect ratio and high tensile strength. By controlling the position and irradiation sequence of UV-light sources, the PRP strand successfully passed a closed maze box. The experimental result demonstrated the potential uses of the PRP composites in a wider range of applications.

### **3. An all-atom analysis of PRP nanocomposites**

#### **3.1. Modeling of PRP/gold nanocomposites using MD simulations**

The PRP nanocomposites reinforced with gold (PRP/gold) were prepared by MD simulations. To examine the effect of the nanofiller addition on the thermal and mechanical properties of the PRP, we selected PRP nanocomposite structures by embedding spherical gold nanoparticles. It is well known that the incorporation of nanoparticles in a polymer matrix leads to the desired functions based on the properties inherent in the nanoparticles, as well as enhancing the mechanical properties. The gold nanoparticle used in this study is one of the promising nanoscale materials because the diameter can be controlled with nanometer precision [81] and has multifunctional properties such as good conductivity [82,83], non-toxicity [84,85], and high mechanical stability [86]. The material is especially suitable as a reinforcement in PRP matrix composites because the nematic phase of liquid crystal molecules enables the spatial arrangement of nanoparticles [87,88]. Some experiments and theoretical analyses have thus been performed for the PRP/gold nanocomposites or nanofilm system and proved the potential applicability of the system [74,89-91].

The most important design variable for the multifunctional polymer nanocomposites is the size of the nanoparticle. The effective material properties of nanocomposites are dominated by the localized polymer-rich phase around the nanoparticle

surface and its interfacial behavior. Nevertheless, the size effect of the nanoparticle on the whole PRP system has not been characterized until now due to the difficulty of quantifying the nanoscale architecture of the material. Accordingly, we prepared four different nanocomposite unit cells with different-sized gold nanoparticles (10 to 20 Å in diameter) under a constant volume fraction to systematically compute the bulk property of the system, and therefore to characterize the effect of nanoparticle size on the opto-thermal actuation of the PRP material. The configurations of polymer molecules and spherical gold nanoclusters used in this study are shown in **Figure 3.1**. We selected PRP compositions same with the ones described in **Chapter 2** for the modeling of matrix structure (a liquid crystalline molecule 6-[4-(4-ethoxyphenylazo)phenoxy]hexyl acrylate and a crosslinking agent 4,4'-di(6-(acryloxy)hexyloxy)azobenzene). The detailed material composition for the neat PRP and PRP/gold nanocomposite models is given in **Table 3.1**.

The model equilibration process for PRP/gold nanocomposite systems was the same as that of the neat PRP model described above, except that the spherical gold nanoparticle was positioned in the center of the unit cell. To avoid the interference between the nanoparticle and the uncrosslinked PRP compounds, the initial positioning of the molecules in the unit cell box was conducted under very low density (< 0.1 g/cc). The numbers of liquid crystalline monomers and crosslinker molecules were determined, in which the volume fraction of the gold nanoparticle becomes 1.62-%. To meet the consistency of the polymer structure, in all cases the crosslink density of the liquid crystalline molecules was fixed as 0.45 by suitably varying the maximum distance cutoff

for the crosslinking simulations. After the oriented PRP molecules and a gold nanoparticle were constituted, the unit cell box was hydrostatically compressed until the density reached that of the neat PRP material (1.07 g/cc). During the compression, the total internal energy of the system was minimized by the conjugated gradient method. Next, another NVT run at 300 K for 3 ns and NPT run at 300 K and 0.1 MPa for 5 ns were applied for equilibration. As shown in **Table 3.1**, the nanocomposite models were further compressed during the NPT run and had a much higher density than the neat PRP structure. Especially, the density of the nanocomposites increased further when the size of the filler was decreased, suggesting that a dense and richly structured polymer layer was spontaneously formed around the nanoparticle surface during the equilibration period.

The equilibrated PRP/gold nanocomposites unit cell model used in this study is shown in **Figure 3.2**. Due to the dense crosslinking simulation, all the polymer molecules are interconnected and represent a macromolecular network. The methyl side chain units are randomly dispersed in the simulation cell while the azobenzene moieties within the crosslinked polymer are aligned along the nematic director. To better understand the microstructural behavior of the matrix phase in the vicinity of the nanoparticle, the structural properties of the azobenzene liquid crystal and methyl side groups in the polymers will be further discussed in the next subchapter.

**Table 3.1.** Neat PRP and PRP/gold nanocomposite systems studied.

System	Gold diameter (Å)	Nanoparticle volume fraction (%)	Crosslink density (%)	Cubic cell length (Å)	No. of photoactive sites	Total no. of atoms	Density (g/cc)
Neat PRP	-	-	45	37.91	85	5,113	1.07
PRP+10Å Au	10	1.62		29.56	34	2,103	1.58
PRP+13Å Au	13			40.91	102	6,349	1.40
PRP+16Å Au	16			51.07	204	12,755	1.38
PRP+20Å Au	20			64.20	408	25,001	1.36



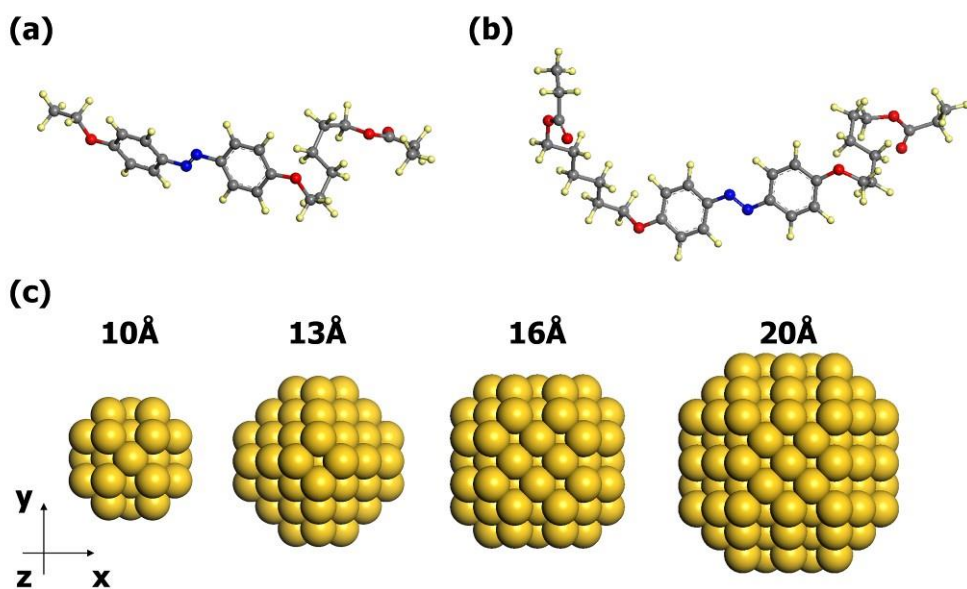


**Figure 3.1.** Molecular structure of the components contained in photo-responsive polymer and its nanocomposites. (a) Liquid crystal monomer compound, (b) diacrylate crosslinking agent and (c) gold nanoparticles.

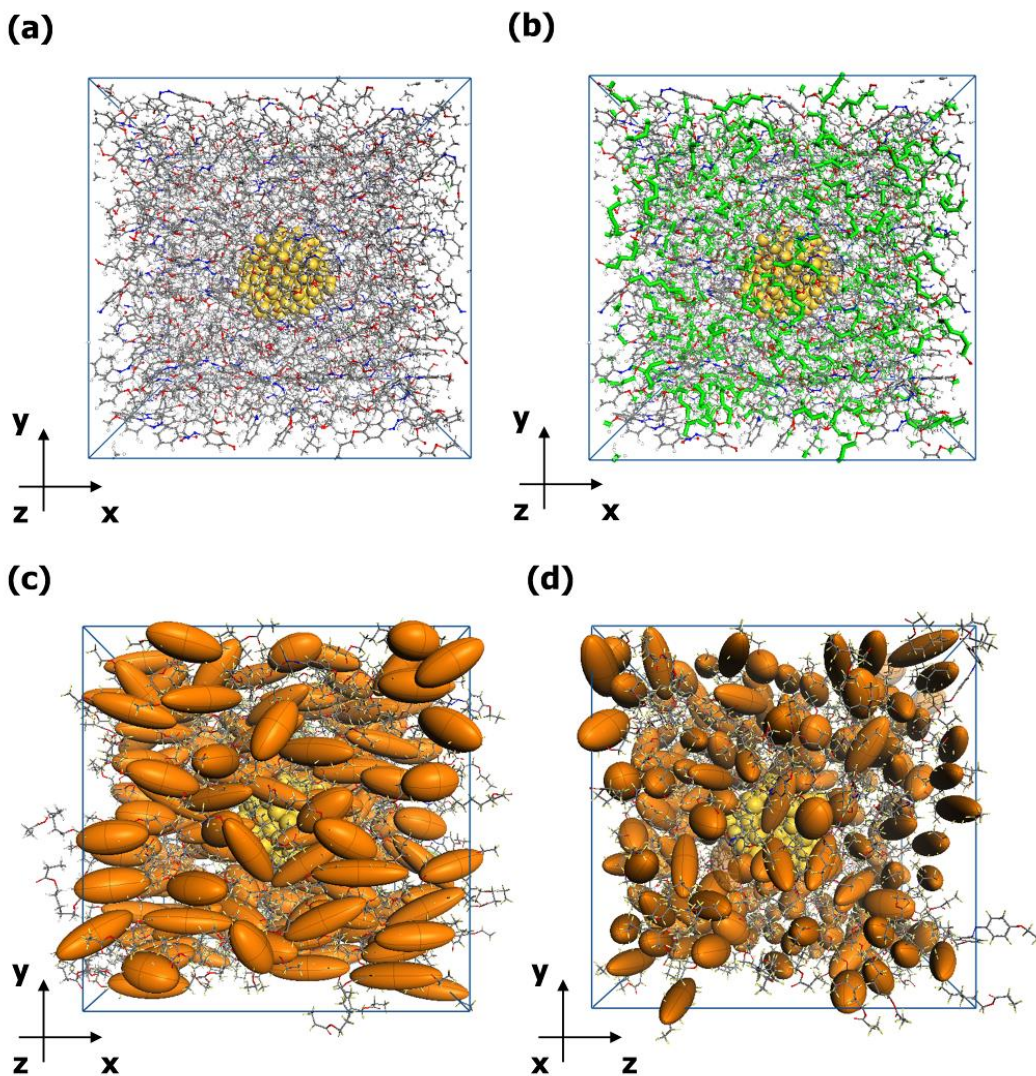


**Figure 3.2.** Configuration of the modeled PRP/gold nanocomposites' periodic unit cell. (a) Front view of the original configuration, (b) highlighted view of crosslinked polymer chains in green, (c) highlighted view of photoactive mesogens as ellipsoidal inclusions, and (d) side-view of the configuration of (c)

### 3.2. Characterization of the effective material properties of the PRP/gold nanocomposites

During the photo-isomerization reaction, not only the mesogen alignment but also the density distribution of the crosslinked side chains was varied due to the polymer relaxation. In particular, the polymer conformation of the PRP/gold nanocomposites also significantly changes with the interfacial features between the reinforcements and the matrices, i.e., generating interphase layers distinguished with the neat polymer on the nanoparticle surfaces [87,92-96]. Therefore, to comprehend the effect of the photo-reaction on material properties and the associated microstructures, we derived the structural, mechanical, and thermal properties of the prepared PRP/gold nanocomposites models as follows.

♦ Photostain ( $\mathcal{E}^{ph}$ ):

Here, to estimate the effective strain of the models during the photo-isomerization simulation, the x, y, and z dimensions of the unit cell box were independently controlled. The effective photostrain ( $\mathcal{E}^{ph}$ ) of the modeled system can be simply defined by the change in the length of the unit cell ( $l$ ) along the x direction described as,

$$\mathcal{E}^{ph} = \left\langle \frac{l_{cis} - l_{trans}}{l_{trans}} \right\rangle_x \quad (3.1.)$$

where the bracket  $\langle \bullet \rangle$  refers to the ensemble average of the last 500 ps of simulation. To

reduce the uncertainty caused by the sampling of the reactive constituent, the photostrain calculation was repeated 9 times with randomly chosen sets of isomerization reaction locations and the results were averaged.

♦ Scalar orientational order of the mesogen ( $S$ ):

To estimate the directionality of the PRP matrices during the MD simulations, artificial line segments joining both ends of the azobenzene phenyl rings were considered. By measuring the angle ( $\theta$ ) between the defined line segment and the x-axis (desired molecular orientation), the alignment of the mesogen could be computed. The scalar orientational order of the PRP material was therefore derived as,

$$S = \left\langle \frac{3 \cos^2 \theta - 1}{2} \right\rangle. \quad (3.2)$$

where the bracket symbol  $\langle \bullet \rangle$  is the ensemble average over all molecules in the system. When the photo-isomerization or thermal phase transition occurs, the uniaxial nematic phase of the modeled structure converts to the isotropic phase and the value of  $S$  is close to zero. Thus eq. (3.2) is able to estimate how the polymer molecules react to the external stimuli.

♦ Elastic stiffness ( $C_{ij}$ ):

After the photo-isomerization process was completed, we calculated the elastic mechanical properties in all modeled cases by applying a longitudinal uniaxial tensile strain

of up to 0.3 % with engineering strain rates of 10<sup>6</sup>/s. Based on the virial theorem, the atomic stress tensor ( $\sigma$ ) during the mechanical loading can be computed as [97],

$$\sigma = \frac{1}{V} \left( - \sum_i^N m_i (\mathbf{v}_i \mathbf{v}_i^T) + \frac{1}{2} \sum_i^N \sum_{j \neq i}^N \mathbf{r}_{ij} \mathbf{F}_{ij} \right) \quad (3.3)$$

where  $V$  is the volume of the unit cell,  $N$  is the number of atoms in the unit cell,  $m_i$  and  $\mathbf{v}_i$  are the mass and the thermal velocity of the  $i$ -th atom,  $\mathbf{r}_{ij}$  and  $\mathbf{F}_{ij}$  are the interatomic distance and the force between the  $i$ -th and  $j$ -th atoms, respectively. In order to derive the equivalent continuum stress, the tensile simulations were carried out using the NVT ensemble at 0.1K and the kinetic effects were excluded [98]. The remaining potential part of  $\sigma$  is therefore expressed as a summation of the interatomic pair, bond, angle, torsional angle, and out-of-plane angle as,

$$\begin{aligned} \sigma_{ij} = -\frac{1}{V} & \left[ \frac{1}{2} \sum_{Pair} (r_{1i} F_{1j} + r_{2i} F_{2j}) + \frac{1}{2} \sum_{Bond} (r_{1i} F_{1j} + r_{2i} F_{2j}) + \right. \\ & \frac{1}{3} \sum_{Angle} (r_{1i} F_{1j} + r_{2i} F_{2j} + r_{3i} F_{3j}) + \frac{1}{4} \sum_{Dihedral} (r_{1i} F_{1j} + r_{2i} F_{2j} + r_{3i} F_{3j} + r_{4i} F_{4j}) + \\ & \left. \frac{1}{4} \sum_{oop} (r_{1i} F_{1j} + r_{2i} F_{2j} + r_{3i} F_{3j} + r_{4i} F_{4j}) \right]. \end{aligned} \quad (3.4)$$

For transversely isotropic material (both for the neat PRP and PRP/gold nanocomposites considered in this study), the axial stress components which are normal to the nematic director (yz-plane) are averaged, as shown in Eqs. (3.5) and (3.6).

$$\sigma = \begin{pmatrix} \sigma_{xx} & \sigma_{xy} & \sigma_{xz} \\ \sigma_{yx} & \sigma_{yy} & \sigma_{yz} \\ \sigma_{zx} & \sigma_{zy} & \sigma_{zz} \end{pmatrix} \equiv \begin{pmatrix} \hat{\sigma}_{11} & \hat{\sigma}_{12} & \hat{\sigma}_{12} \\ \hat{\sigma}_{12} & \hat{\sigma}_{22} & \hat{\sigma}_{23} \\ \hat{\sigma}_{12} & \hat{\sigma}_{23} & \hat{\sigma}_{22} \end{pmatrix} \quad (3.5)$$

where

$$\begin{aligned}\hat{\sigma}_{12} &= \frac{1}{4}(\sigma_{xy} + \sigma_{xz} + \sigma_{yx} + \sigma_{zx}), \\ \hat{\sigma}_{22} &= \frac{1}{2}(\sigma_{yy} + \sigma_{zz}), \quad \hat{\sigma}_{23} = \frac{1}{2}(\sigma_{yz} + \sigma_{zy}).\end{aligned}\tag{3.6}$$

The elastic stiffness tensor written in Voigt's notation can be simply derived under Hooke's law:

$$\sigma_i = C_{ij} \varepsilon_j \quad (i, j = 1, \dots, 6)\tag{3.7}$$

The obtained mechanical stresses include uncertainties depending on the relaxed conformation of the partially or fully photo-isomerized polymer networks. Therefore, in order to guarantee computational accuracy, the tensile loading simulations were carried out 15 times (5 times for each loading direction) for each condition and the elastic constants were averaged.

♦ Thermal phase transition and corresponding thermal stretching ratio ( $\lambda_T$ ):

To estimate the thermal stability of the PRP/gold nanocomposites, the heating up simulations from 250 K to melting temperature ( $T_{iso}$ ) at a rate of 5 K/ns were carried out in all cases under the isobaric conditions at 0.1 MPa. The melting temperature was defined in which the alignments of the mesogen were fully disordered ( $S < 0.05$ ) and had no preferential orientation. During the heating up simulations, the change of length of the unit cells along the x axis and the associated orientational order parameter of the mesogen were recorded simultaneously. The ratio of unit cell length ( $l_T$ ) at a given temperature to the corresponding value at a melting temperature ( $l_{T_{iso}}$ ) describes the thermal stretching ratio

of the material, as

$$\lambda_T = \left\langle \frac{l_T}{l_{T_{iso}}} \right\rangle_x. \quad (3.8)$$

By monitoring the correlation between  $\lambda_T$  and  $S$  during the heating up simulation, we examined whether the phase transition of the liquid-crystalline structure is sufficient to address the macroscopic deformation of the solid nanocomposites.

The characterization of the material properties of PRP nanocomposites is particularly important for the design and analysis of the smart material in mechanical terms because the intrinsic multifunctionality that arises from the polymer architecture and the interfaces determines the photo-thermal actuation performance of the material. For the convenience, the overall workflow of the simulation procedures described above are summarized and presented in **Figure 3.3**.

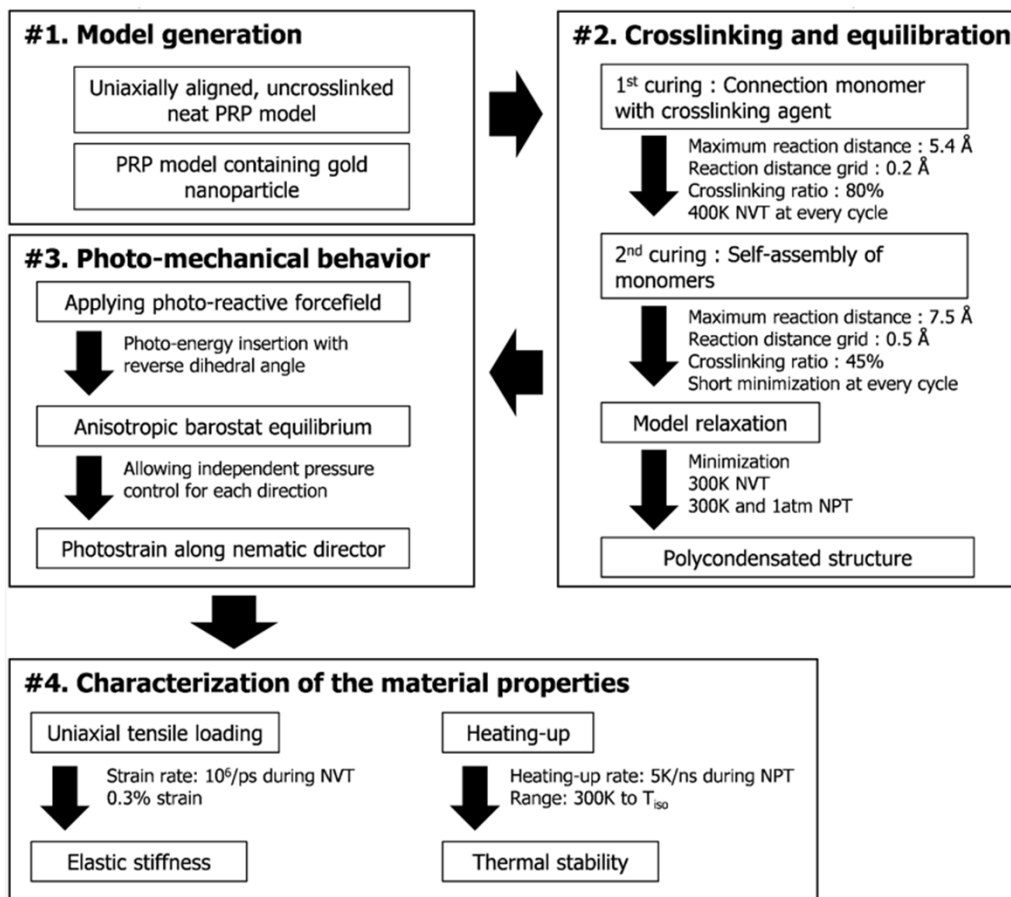


**Figure 3.3.** Overall workflow of the present MD simulations for the neat PRP and the PRP/gold nanocomposites models



### **3.3. Role of the interfacial layer during the photo-isomerization reactions**

#### **3.3.1. Structural characteristics of the PRP molecules around the nanoparticle**

The length distribution of the azobenzene molecules in the equilibrated system after the photo-reactive dihedral potential applied to the model is shown in **Figure 3.4**. When trans-azobenzene is converted to cis-azobenzene, the effective length of the molecules reduces by 25%. In all cases, the conversion ratio of the azobenzene molecules in the unit cell reached the desired photo-isomerization ratio; it is thus verified that the provided photo-reactive potential energy for the diazene moiety is sufficient to overcome the energy barrier required for the kink motion in the crystalline glassy polymer phase. One aspect of the result is that the deviation of the length distribution of cis-azobenzene is significantly larger than the corresponding length distribution of trans-azobenzene. This deviation indicates that the molecules converted to the cis-form lose their rod-like rigidity and bridging ability and thus the width of the angular amplitude of oscillation of the kinked moieties increases. The effect of the molecular structural mechanics of azobenzene groups on the structural properties and stabilities of the bulk PRP and PRP nanocomposites materials will be further discussed in the following section.

Regarding the PRP/gold nanocomposite models, the radial density distribution

profile of the polymer matrix surrounding the nanoparticle is obtained and shown in **Figure 3.5 (a)**. The crosslinked polymer networks in the vicinity of the nanoparticle surface strongly interacted with the gold atoms and the local density in that region would be higher than that of the pure polymer. As the result indicated, the radial density of the PRP phase is not uniform but depends on the distance from the nanoparticle surface; the peak density point is observed at the nearest surface of the particle, and the value gradually converges to the density of the bulk system as the radial distance increases. Such morphological change of polymer chains caused by the non-bonded interaction with the nanoparticle is well known in the polymer nanocomposites field [43,44,99-101]. The tightly coated polymer chains at the interface, the so-called interphase, renders the matrix phase more stable and enhances the mechanical properties of the material. The result shown in **Figure 3.5 (a)** also indicates that the interfacial characteristics plays an important role in the microstructure and the relevant physical properties of highly crosslinked nematic networks. When the components were mixed before crosslinking, the interaction energy between the flexible fragments of the polymer chains and the nanoparticle generated the interphase layer, and the melt was then solidified during thermal curing.

One interesting aspect is that the morphological stability of PRP around the nanoparticle was sustained even after the trans-azobenzene was fully transformed to cis-azobenzene, as shown in **Figure 3.5 (b)**. When the isomerization occurs due to the light irradiation, the rod-like features of the azobenzene molecules disappeared and the direct mesogen-mesogen interactions did not hold the alignment of the polymer chains. On the

other hand, the adsorption characteristics of the flexible methyl side chains are not associated with the structural change of the azobenzene and thus the interphase around the filler particles clearly remain. Instead, because there is less mesogen-mesogen ordering under cis configuration, the structural interference during the photo-isomerization of the azobenzene becomes weaker and the interfacial energy of the polymer chains with the nanoparticle dominates the relaxation kinetics of the atoms. Accordingly, the first peak of the radial density is slightly shifted toward the nanoparticle surface with higher local density in all the considered cases.

The issue whereby the alignment feature of the liquid crystalline polymer networks are also substantially affected by the shape and size of the filler might appear to be a concern. However, the change of the local orientation of the nematic azobenzene polymers surrounding the nanoparticle is not significant in this study because the size of the filler is in the order of only a few nanometers. In order to visualize the relation between the nanoparticle diameter and the mesogen alignment, we prepared additional PRP/gold nanocomposites models containing larger diameter gold particles (up to 5 nm) and measured their scalar orientational order of the matrix phase. In spite of the same equilibration process, the result depicted in **Figure 3.6** showed that the majority of the mesogen molecules lost their initial orientation but were adsorbed on the curved surface of the nanoparticle. As the nanoparticle diameter increased, this disorder became obvious and most polymer chains could no longer sustain a nematic phase. However, as the diameter of the embedded nanoparticle became smaller (less than 2 nm), the order parameter of the

matrix phase was fully recovered: the alignment characteristics of the mesogen molecules were not affected by their adsorption behavior on the nanoparticle surface.

Indeed, as described in **Figure 3.7**, the local orientation of the azobenzene does not show a distinct change even for the largest nanocomposites model (PRP/20Å gold). This result is strongly consistent with the reported results [92,93], demonstrating that the influence of the nanoparticle on the orientation of the liquid crystalline director is short ranged. As the size of the filler reaches nanometer scale and becomes comparable to the length of the mesogen, the planar anchoring effect of the particle appears only at the near-interface layer. Meanwhile, because the polymer matrix considered in this study was fully crosslinked in nematic states, the alignment change of mesogens caused by the insertion of nanoparticles was rather restricted in the present model.

While the nano-architecture of the macromolecular polymer system did not induce a significant change in the orientation of the matrix, the photo-isomerization of the azobenzene exerted a significant effect for that trait. As the photo-isomerization occurred, the orientational order of the matrix was drastically decreased regardless of the radial distance from the nanoparticle surface even under the low isomerization ratio. Because the isomerization sites were randomly selected and sparsely dispersed at low isomerization ratio, the result depicted in **Figure 3.7** shows that the trans to cis isomerization ratio of the isomers mainly determines the structural features and properties of the material. Therefore, the photo-isomerization ratio is an important design variable for understanding the photo-mechanical behavior of the PRP nanocomposites.

### 3.3.2. Nanoparticle size effect on photostrain and mechanical properties

To further investigate the effect of nanoparticle size on the vicinity of the interface during the photo-isomerization, we characterized the photostrain and the mechanical properties of the considered nanocomposites models as well as of the neat PRP model. Using Eq. (3.1), we derived the photostrain of the modeled unit cells according to the photo-isomerization ratio of the azobenzene molecules and depicted the result in **Figure 3.8**. In all cases, the uniaxial strain along the nematic director steadily increases as the trans-to-cis isomerization ratio reaches 1. Note that the maximum deformation of the PRP obtained by experiments (the material was composed only of azobenzene moieties so the composition is almost identical to the neat PRP model) is about 13% [102], which is very close to the photostrain value of the completely isomerized model in the present study. In comparison, the estimated photostrains in the PRP/gold nanocomposites models are remarkably higher (from 31 % to 47 %) than those of the neat PRP model, regardless of the photo-isomerization ratio and the size of the nanoparticle. The reason for the higher photostrain of the PRP/gold nanocomposites than the neat PRP is the dense interphase formed by the flexible methyl groups in the polymer. As mentioned in **Figure 3.5**, the polymer chains were wrapped on the nanoparticle surface while keeping the alignment of the azobenzene groups. They inhibit the spontaneous rotation of the molecules in a random direction while assisting the compressive deformation of the microstructure along the pre-aligned direction.

Another important feature in **Figure 3.8** is that the photostrain of the nanocomposites material continuously increases as the inserted nanoparticle size decreases when the trans-to-cis conversion ratio of the unit cell does not exceed 75%. The main cause of the nanoparticle size dependence on the photostrain is the clearance at the interface between the nanoparticle and the polymer matrix. While the photo-isomerized molecules and their surrounding matrix environment were covalently crosslinked, the isomers around the nanoparticle surface were connected with the particle only by non-bonded contacts. Therefore, the isomers in the interphase had sufficient spatial freedom for shrinkage of the structure along the nematic director during the isomerization. Because such effect mainly occurs in the interphase region, a more distinct photo-shrinkage activity of the material can be observed as the size of the nanoparticle decreases and the associated interface has a larger surface-to-volume ratio. Especially, this size effect is clearly observed under low photo-isomerization ratio and then fades out as the photo-isomerization ratio reaches 50%. The result indicates that, under the high photo-isomerization ratio condition, the converted azobenzene groups gain sufficient energy to transform the entire matrix region and thus the measured photostrain is saturated.

Note that the increase of the photostrain of the material under partially photo-isomerized condition is particularly important in the mechanical design of the PRP device. Generally, the entire thickness of the PRP specimen in the experiment reported in the literature is a few micrometers and thus, only the surface of the material would be completely exposed to the light stimuli, while the intensity gradually decreases below the

surface. Again, the finite penetration depth of the light characterizes a certain profile for the effective photo-isomerization ratio according to the thickness of the material [103]. Because the present MD study systematically identifies the deformation range of the PRP nanocomposites structure according to the effective isomerization ratio inside the microstructure, the results are able to be adapted to the nano-continuum bridged multiscale mechanical model suggested in a previous study [104].

In order to better discuss the implications of the morphological change of the polymer, we derived the overall mechanical properties of the modeled structure from the tensile loading simulations. **Figure 3.9** shows the obtained anisotropic elastic stiffness of the neat PRP and PRP/gold nanocomposites along the nematic axis and normal plane. As the particle size decreases to nanoscale, the effective volume fraction of the interfacial region is significantly large that the interphase directly affects the overall material properties. Since the polymer interphase formed by the attractive interaction with the nanoparticle has better structural stability and higher local density, in all the considered cases the PRP/gold nanocomposites models show higher normal and transverse stiffness components than the corresponding components of the neat PRP model, regardless of the particle size or photo-isomerization ratio of the azobenzene. Also, the nanoparticle size effect on the mechanical properties is observed under low photo-isomerization ratio condition: the elastic stiffness of the PRP/gold nanocomposites becomes increased as the embedded nanoparticle size is decreased because the fraction of the occupied volume of the interphase in the matrix is increased. Such enhancement features are sustained after the

azobenzene groups in the matrix are changed from trans- to cis- state, as mentioned in detail above.

### **3.3.3. Linear correlation between micro-macro deformation phenomena explained with photo-thermal phase transition**

The nematic-isotropic phase transition of conventional liquid crystal also occurs when the thermal energy is sufficient to overcome the orientational forces of the molecular field. Both the photo-isomerization and the thermal isomerization induce the macroscopic mechanical motion of the stimuli-responsive polymer material as well as the change in its microstructure. Even though the outward appearances of the deformation are similar, the intrinsic mechanism evolved by the microstructure significantly differ. In the case of the thermal isomerization, the liquid crystalline molecules lose their alignment due to the large kinetic energy while maintaining their rod-like shape. In comparison, the photo-isomerization directly changes the molecular conformation of the azobenzene so the isomers affect the arrangement of the surrounding molecules, independent of the thermal effects.

To thoroughly examine the multi-stimuli responsive effect, we therefore carried out heating-up simulations in MD for the PRP nanocomposites models in all photo-isomerization ratio conditions and plotted the orientational order profiles in **Figure 3.10**. When the photo-isomerization progresses prior to the heating-up, the initial orientational



order of the azobenzene molecules is reduced by more than 50% and the results concur with the structural and mechanical characteristics of the matrix phase in the nanocomposites mentioned above. The remaining orientation gradually collapses and the material becomes isotropic when the given temperature reaches the melting point of the unit cell. One noticeable difference of the photo-thermal behavior of PRP/gold nanocomposites compared to the corresponding behavior of the neat PRP is that the collapse of the orientation is considerably retarded and hence the melting temperature of the material is increased. Because of the non-bond interaction energy between the nanoparticle and the surrounding matrix, the local liquid crystalline polymer chains near the nanoparticle sustain their alignment until the bulk matrix region outside the interphase has undergone thermal isomerization. The improvement of the thermal stability of the liquid crystal alignment according to the nanoparticle additive is a good agreement previous theoretical and experimental results [104-107].

Another interesting feature seen in **Figure 3.10** is that the change of the microstructure of the PRP/gold nanocomposites during the heating-up simulation is not abrupt but occurs gradually over a wide range of temperature whereas the pure, non-isomerized PRP shows a sudden drop at the transition temperature. In the case of neat PRP material with non-isomerized azobenzene, the polymer chains were closely packed and all the microstructures showed uniform distribution. Accordingly, all the mesogen molecules in the unit cell sustain their alignment directly before the temperature reaches melting point and the transition occurs immediately over the entire domain. On the other hand, free space

surrounds the matrix containing the nanoparticle or cis-isomers. The associated PRP participant around the free space has local material characteristics regarding the structure and kinetics of the crosslinked polymer; thus, the alignment parameter of the molecules has a continuous variation. To examine the correlation between the disordering of the polymer microstructure and the macroscopic deformation of the material, we plotted the compressive normal strain along the x-axis of the unit cell in **Figure 3.11** with respect to the orientational order parameter during the heating-up simulations. While the deformation quantity of the non-isomerized PRP model without nano-reinforcements is severely scattered and shows low correlation with the orientation of the microstructure, the photo-isomerized and other PRP/gold nanocomposites models show a clearly linear trend with the orientation of the microstructure. Therefore, the result in **Figure 3.11** implies that the insertion of the gold nanoparticle has a positive role in widening the transitional state of the polymer, while the photo-thermal actuation features of the material are guaranteed in accordance with the conditions of temperature and light.

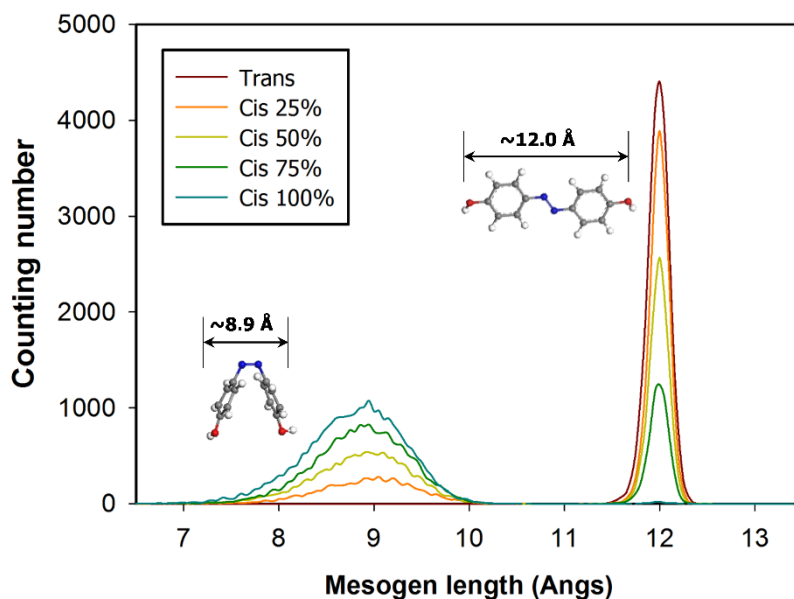


**Figure 3.4.** Length distribution of the azobenzene moieties in the neat PRP unit cell according to the photo-isomerization ratio

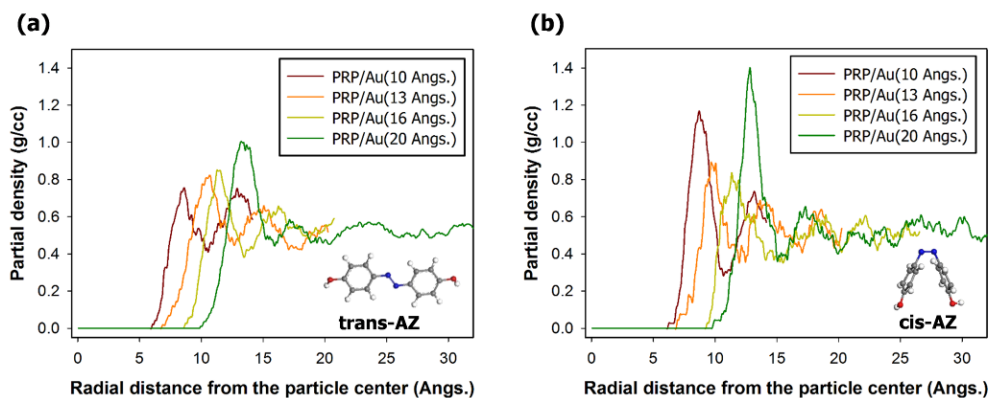
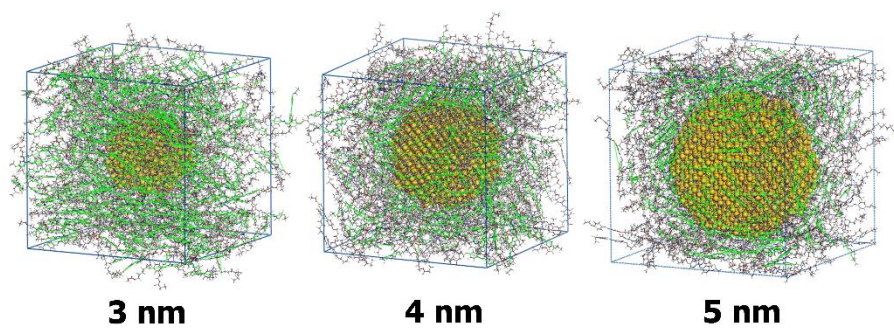


**Figure 3.5.** Radial density distribution of the polymer backbone constituents according to the size of the nanoparticle: (a) non-isomerized PRP/gold models and (b) fully isomerized PRP/gold models.

**(a)**



**(b)**

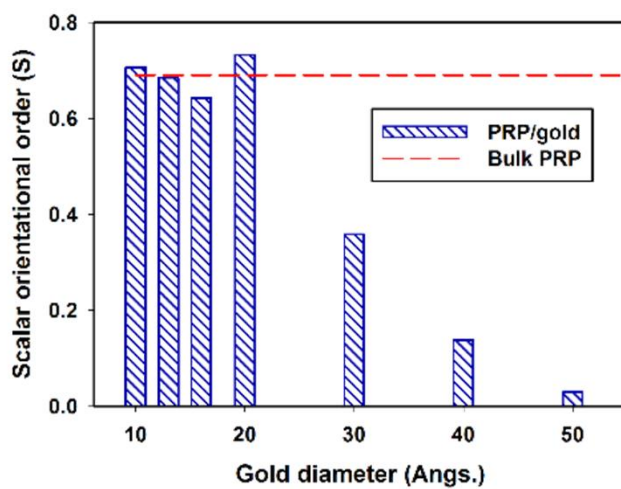


**Figure 3.6.** (a) Configurations of the additional equilibrated models with larger nanoparticle sizes (alignments of the mesogen fragments are highlighted in green) and (b) averaged order parameter of the PRP matrix in the considered nanocomposites models.

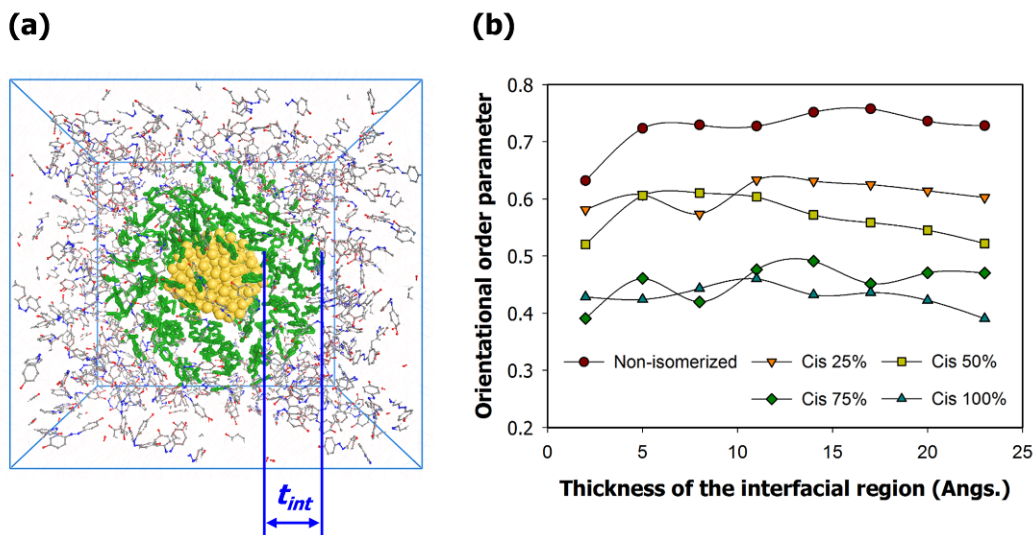


**Figure 3.7.** Radial distribution of the scalar orientational order parameter of the PRP/gold (20Å) nanocomposites according to the photo-isomerization ratio of the azobenzene. (a) Local orientation of the azobeznene was measured from the arbitrarily defined spherical shell around the nanoparticle with given thickness ( $t_{int}$ ). (b) Obtained distributions of the orientational order of azobenzene molecules along the nematic director.

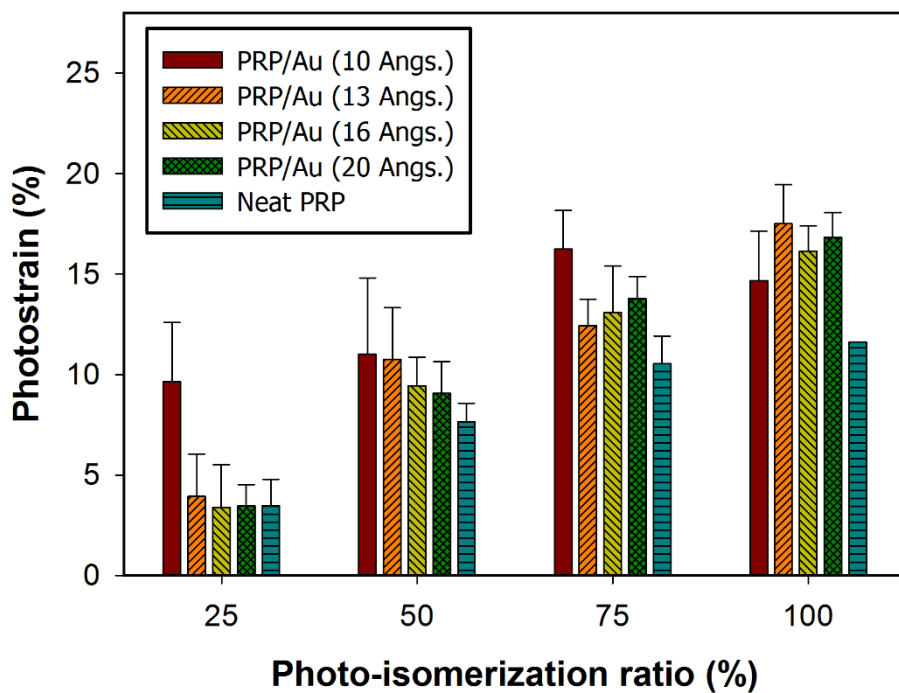


**Figure 3.8.** Calculated photostrain of the neat PRP and the PRP/gold nanocomposites models according to the photo-isomerization ratio. Because the trans-to-cis isomerization simulation induced the shrinkage of the unit cell, we plotted the compressive strain as positive. Error bars for the nanocomposites models represent one standard deviation around the mean value.

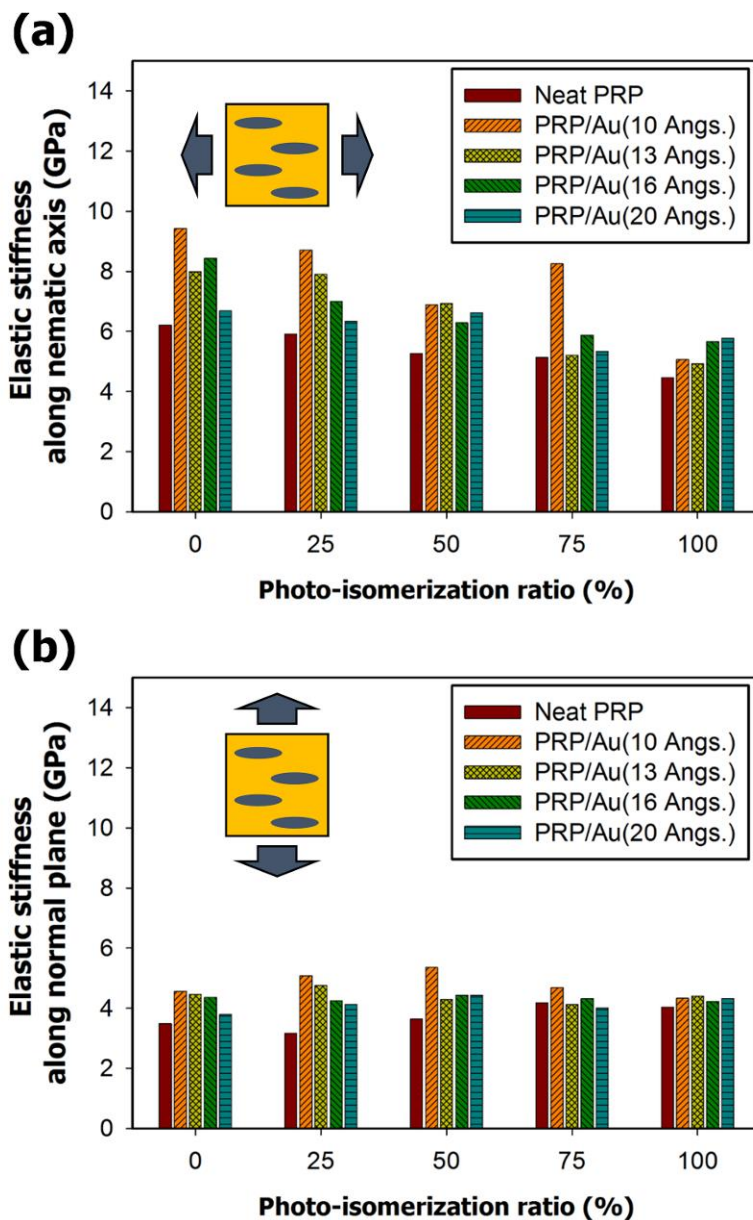


**Figure 3.9.** Elastic stiffness components of the PRP/gold nanocomposites according to the photo-isomerization of the azobenzene molecules inside of the structure. (a) Normal (x-axis) and (b) transverse (y- and z-axes) stiffness along the nematic axis of the azobenzene.

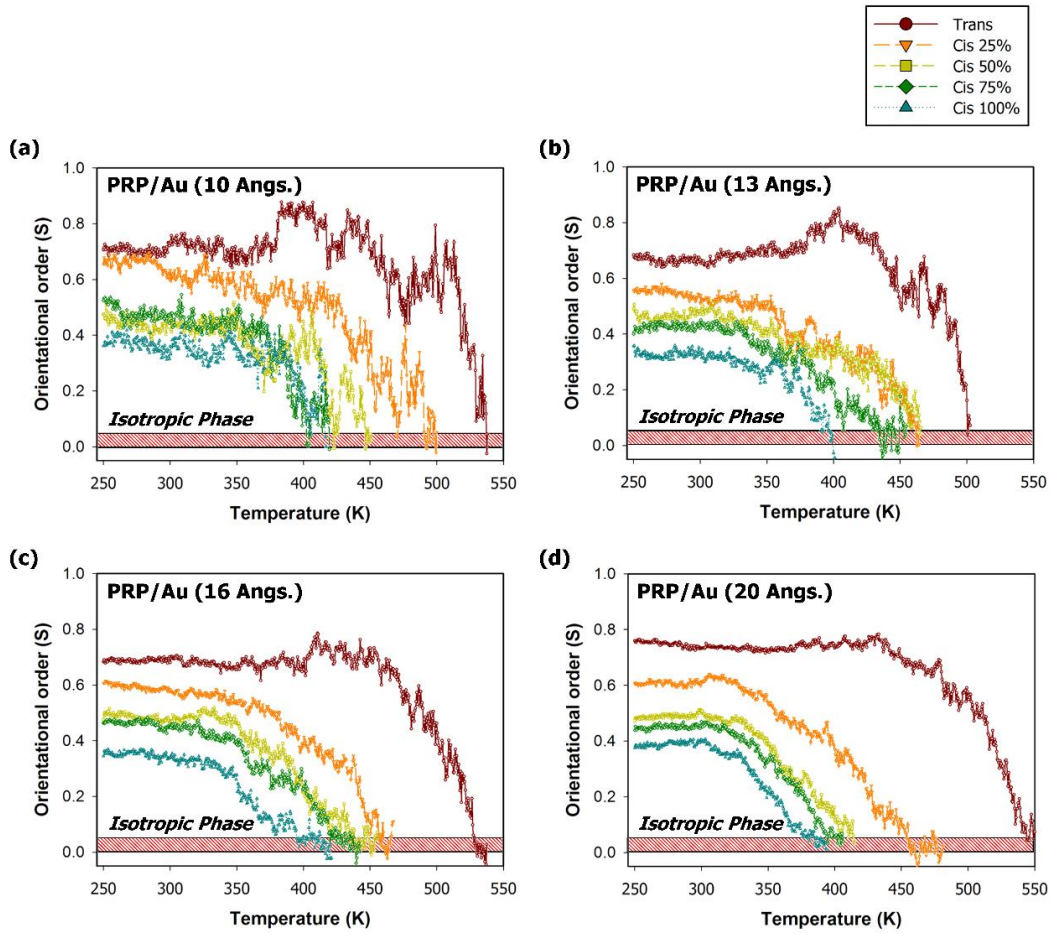


**Figure 3.10.** Thermal phase transition profile of the PRP/gold nanocomposites according to the photo-isomerization ratio of the azobenzene. We defined the melting point of the material where the averaged orientational order of the microstructure is lower than 0.05.



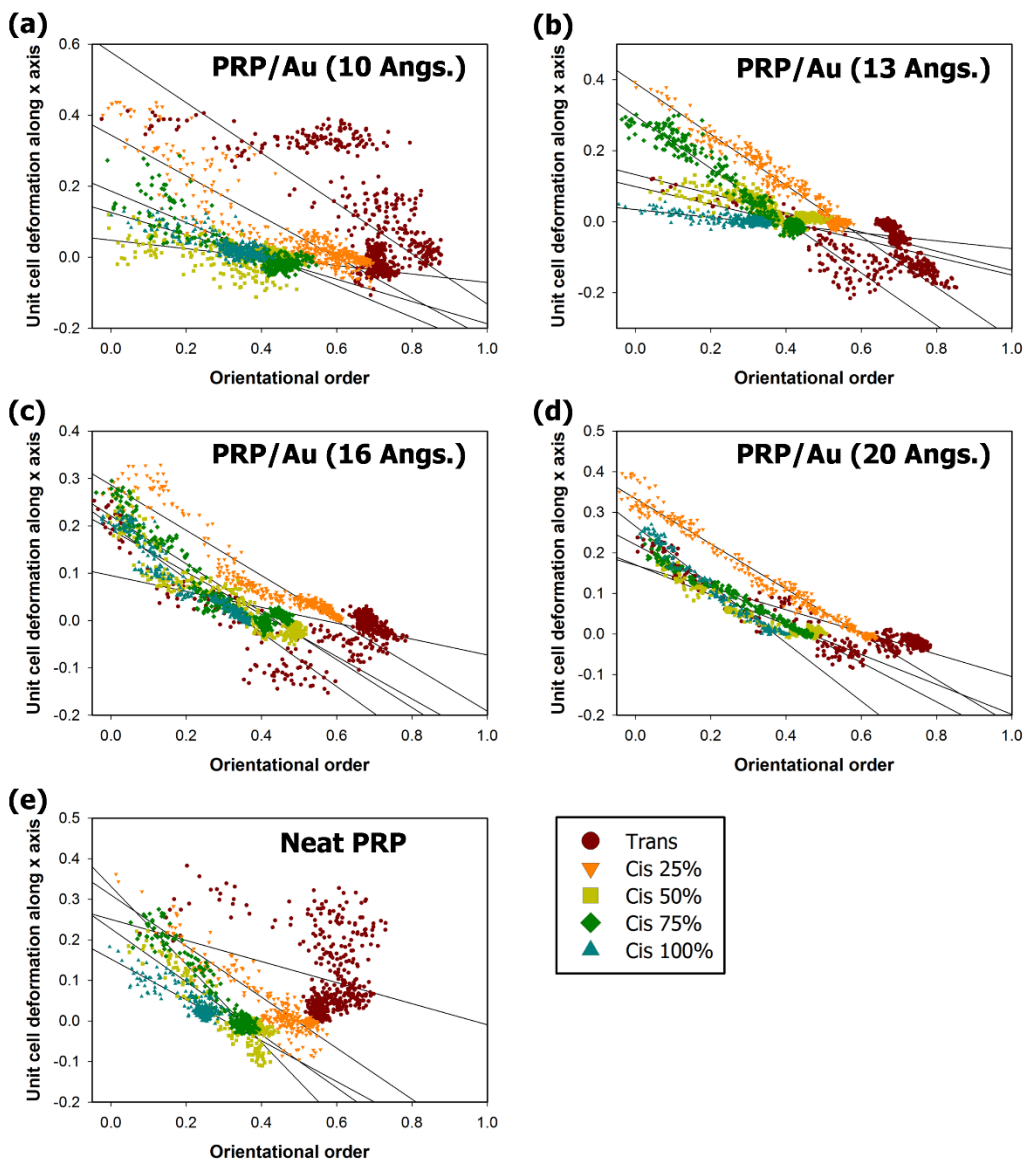


**Figure 3.11.** Linear correlation between the macroscopic deformation of the modeled unit cell and the microscopic orientational order of the internal molecules according to the diameter of gold nanoparticle in the unit cell. The final graph in (e) was obtained from the previous simulation data introduced in **Chapter 2**. We defined the compressive strain as positive.

### 3.4. Chapter summary and conclusions

In **Chapter 3**, MD simulations were carried out to investigate the photo-thermal actuation behavior of the PRP/gold nanocomposites. According to the photo-isomerization ratio of the azobenzene isomers and the size of the embedded gold nanoparticle under constant volume fraction, we obtained the bulk properties including the photostrain, elastic modulus, and thermal phase transition of the considered material. During the simulation, the internal microstructure of the polymer phase as well as the interfacial region between the particle and the matrix were also examined to clarify the origin of the photo-induced characteristics.

The results indicated that the nano-sized reinforcement not only increases the thermo-mechanical properties of the liquid crystalline polymer, but also increases the photostrain of the microstructure. The strong non-bond interactions between the particle and the matrix generate the densely packed local structure at the interfacial region and enhances the overall properties of the material. Nevertheless, the degradation of the preferred orientation caused by the reinforcement is observed only at sites close to the surface of the nanoparticle. Also, the vacuum level at the interface allows a conformational mobility of the crosslinked polymer along the alignment direction during the photo-isomerization reaction. Accordingly, this improvement of the multi-functionality becomes more significant as the nanoparticle size decreases owing to the increase of the effective area occupied by the interphase.

Based on the current numerical results, we reached two crucial conclusions regarding a way to improve the mechanical stability of the PRP material by using the reinforcements while maintaining the material's photo-deformation behavior. First, provided the size of the nanofiller is comparable or smaller than the length of the mesogen molecules, the nanofiller only slightly changes the alignment of the nematic phase and the multifunctional behavior of the PRP material would be preserved. Secondly, if an attractive interaction develops between the filler and the matrix, the polymer matrices around the nanoparticles form the interphase which strengthens the overall composites structure and assists the prompt deformation response to the light stimuli. Therefore, the results obtained thus provide important insight into the mechanical design of the stiff but resiliently deformable PRP nanocomposites materials and enables quantitative analysis of their mechanical properties at a given temperature and light exposure conditions.

## **4. Multiscale design model for PRP nanocomposites and their associated interphases**

### **4.1. Shape parameter under stress-free conditions**

#### **4.1.1. Basic background**

So far, we have discussed the photo-thermal actuation behavior of the neat PRP and the PRP nanocomposites reinforced with gold nanoparticles by the steered MD simulations. Comparing with the neat PRP, the PRP/gold nanocomposites show enhanced thermo-mechanical properties due to the formation of the physically adsorbed polymer networks around the nanoparticle surface. In particular, the photostrain measured from the PRP/gold nanocomposites models is comparable or even larger than the one of the neat PRP because the alignment of the mesogen phase of PRP matrix is not hindered by inhomogeneity interactions. Such non-intrusive behavior of the nano-reinforcements brings a valuable multifunctionality, in that the nanocomposites material can be deformed more than the neat PRP by the UV-light irradiation while keeping its rigid structure. In **Chapter 2** and **Chapter 3**, the photo-mechanical behavior of the PRP and PRP/gold nanocomposites has been characterized with respect to the nanoparticle size and the photo-isomerization ratio of the PRP matrix.

The two important parameters for the design of PRP nanocomposites material are

‘shape parameter’ according to the conditions of environment and ‘quantified interphase properties’ in the vicinity of the nanoparticle surface. The former is an essential variable in the continuum interpretation for photo-bending behavior of the material under stress free conditions, and the latter is a key to discovering the role of interfacial layer between the nanoparticle surface and the surrounding polymer networks under mechanical loading conditions. As mentioned in **Chapter 1**, the main application of the PRP material is in mechanical engineering and thus both of these studies are strongly necessary.

In this section, we deal with the method which predicts the photo-deformation behavior of the PRP nanocomposites under stress-free conditions. The obtained microstructural behavior in MD simulations was represented as continuous functions in terms of photo-isomerization ratio as well as the particle diameter. It provides the information on the design variables relevant with the photo-deformation to the continuum model such as non-linear FE analysis models [104,108]. Hence the outcome of this work can be efficiently utilized for the specific particle diameter and photo-irradiation conditions where we are interested to design PRP nanocomposites system.

As depicted in **Figure 2.8** and **Figure 3.9**, the modeled PRP and PRP nanocomposites behave as a kind of liquid-crystalline polymer, so the thermal phase transition is not 1<sup>st</sup> or 2<sup>nd</sup> order but is laid in between them [78,109,110]. The simple form of the order parameter is given as [78],

$$S = \begin{cases} \left| 1 - \frac{T}{T_c} \right|^\zeta & \text{if } T < T_c \\ 0 & \text{otherwise} \end{cases} \quad (4.1)$$

where  $T_c$  is the clearing temperature and  $\zeta$  is the adjustable exponent parameter giving the optimum fit for the order parameter for the thermal phase transition. Physically,  $T_c$  denotes the temperature where all the internal participants of the mesogen lose their directionality and the system becomes an isotropic. And  $\zeta$  indicates how long the material persist against the internal collapse of the microstructure after the temperature rises to the nematic-isotropic phase transition point of the system. Thus the function can be directly applied to the neat PRP system and the effect of photo-isomerization reaction on the thermal phase transition can be explained with the two coefficients. But in case of the PRP nanocomposites system, there is inhomogeneity in the system and hence the temperature-independent parameter should be considered to the equation as well as the exponent parameter. To properly consider the external field effect, Haller [110] suggested a modified equation given by,

$$S = \begin{cases} k \left| 1 - \frac{T}{T_c} \right|^\zeta & \text{if } T < T_c \\ 0 & \text{otherwise} \end{cases} \quad (4.2)$$

where  $k$  is the temperature-independent characteristic coefficient. Although the theoretical foundation is quite limited, he emphasized the usefulness and the wide applicability of the equation and ascertained that most of the nematic liquid crystalline phase could be fitted excellently over a wide range of temperatures.

Meanwhile, the actual deformation behavior of the material induced by the phase transition of the liquid crystal has a linear relation to the magnitude of order parameter as,

$$\lambda = 1 + \tilde{\alpha} \cdot S = 1 + \alpha \cdot T_c^\zeta \cdot S \quad (4.3)$$

where  $\lambda$  is the macroscopic, spontaneous stretching ratio of the material in response to heat and light stimuli and  $\alpha$  is the opto-mechanical coupling parameter specified in the material. Finally, the shape parameter  $r$  simply can be derived from the cubic of the stretching ratio as [108],

$$r \cong \lambda^3 = \left(1 + \alpha \cdot k \left|T_c - T\right|^\zeta\right)^3. \quad (4.4)$$

#### **4.1.2. Influence of the nanoparticle and photo-isomerization reaction**

Using the profiles of local orientational order parameter of the liquid crystalline system obtained from all-atom MD simulations, the characteristic coefficients  $k$  and  $\zeta$  for the PRP nanocomposites system and their parametrical dependence on the external environment is elucidated. In **Chapter 2** and **Chapter 3**, we have found that the two most important design factors to control the actuation of the material are ratio of the trans-to-cis isomerization reaction and the size of gold nanoparticle. The order parameter described in Eq. (4.2) thus can be formulated in terms of the two variables as,

$$S = k \left| 1 - \frac{T}{T_c} \right|^\zeta = k(d_p, n_{cis}) \left| 1 - \frac{T}{T_c(n_{cis})} \right|^{\zeta(d_p)}. \quad (4.5)$$

where  $d_p$  is the diameter of gold nanoparticle and  $n_{cis}$  is the percent of cis-isomers in the matrix. To interpret the microstructural changes in the matrix in a wide range of temperature, firstly the estimated clearance temperature of each nanocomposites is averaged over the considered nanoparticle size and listed in **Table 4.1**, with the corresponding value of the neat PRP. As can be expected, the PRP nanocomposites models shows an enhanced thermal stability regardless of the ratio of the isomerization reaction. Next, we fitted the raw MD data for the last 50 K below the clearance temperature and derived the model coefficients by least squares and listed them in **Table 4.2**. The results showed there was a clear difference in the measured temperature-independent characteristic coefficients between the neat PRP and the PRP nanocomposites. Particularly, the coefficients for PRP nanocomposites were depending on the diameter of the nanoparticle - as the nanoparticle size decreases, the  $\zeta$  and the  $k$  decrease consistently. It is because the vacuum layer at the interface between the nanoparticle and the matrix let the liquid crystalline mesogen disordered continuously over the entire high-temperature region and the fraction of the vacuum field becomes more salient as the nanoparticle size decreases. Meanwhile, the ratio of photo-isomerization reaction also influenced the decrease in the  $k$  and  $T_c$  of the PRP system because the local order of the mesogen was destroyed in the initial state due to the significant conformational change of cis-isomers.

Accordingly, such strong dependence of the order parameter plays a major role in



the specification of the mechanical behavior of the PRP nanocomposites system and their design of the continuum structures. The main point of the present result was that the intrinsic properties of PRP matrix could be well described by the conventional phase transition model suggested by Haller. In the next section, the description method of the order parameter as a continuous function of the photo-isomerization ratio and nanoparticle size would be presented.

#### **4.1.3. Description of the order parameter and shape parameter under photo-thermal stimuli**

In the previous chapter, the photostrain of the PRP material was estimated in MD simulations by measuring the change of the lattice parameter along the nematic director axis. The approach has its own advantages in that the effective deformation quantity of the microstructure purely induced by photo-irradiation effect without the involvement of the thermal-driven phase transition. However, it should be noted that the actual photo-deformation behavior of the PRP material in macroscale system highly depends on the operation temperature. In order to comprehend the underlying continuum of interest, therefore, it is strongly required to provide the order parameter profile in a wide range of operation temperature as well as the other two design variables. In this section, we propose continuous functions with respect to the shape parameter as well as the corresponding order parameter of the modeled PRP nanocomposites system. Because the continuous functions

can provide the information on the particle size and photo-isomerization dependence on the equivalent continuum model, we can utilize the functions to the specific particle size and the light irradiation conditions in which we are interested to design nanocomposites.

To describe all the base coefficients as dimensionless parameters, firstly we set dimensionless coefficients  $T_c^*$  and  $d_p^*$  as below:

$$T_c^* = \frac{T_c}{T_c^0} \quad \text{and} \quad d_p^* = \frac{d_p}{d_a} \quad (4.6)$$

where  $T_c^0$  is 462.52 K (the clearance temperature of the PRP matrix without reinforcements) and  $d_a$  is 3.495 Å (the first peak of the radial density profile of adsorbed polymer layer around the nanoparticle), respectively. All the least square approximations were carried out with these dimensionless quantities. As shown in the **Table 4.2**, the exponent value ( $\zeta$ ) for PRP nanocomposites is similar to that obtained from the neat PRP only in the case of extremely small diameter of the gold particle and the value decreases further as the size of particle increases. Accordingly, the functional form of the  $\zeta$  is simply given as,

$$\zeta(d_p^*) = \zeta_1 \exp(d_p^*) + \zeta_2 \quad (4.7)$$

where  $\zeta_1$  and  $\zeta_2$  are the regression coefficients. Meanwhile, the temperature-independent factor ( $k$ ) is influenced by both of the diameter of the particle and the isomerization ratio. The value decays exponentially with the decreasing size of the inserted nanoparticle or with the increasing ratio of the trans-to-cis isomerization reaction. Hence the functional form of  $k$  is described as,

$$k(d_p^*, n_{cis}) = (k_1 \cdot d_p^* + k_2) \exp\{(k_3 \cdot d_p^* + k_4) \cdot n_{cis}\} \quad (4.8)$$

where  $k_1 - k_4$  are the regression coefficients. Lastly, the clearance temperature of the PRP nanocomposites ( $T_c$ ) during the photo-isomerization reaction is formulated by the summation of decaying rate of the neat PRP and improvement effect of thermal stability of the matrix phase due to the reinforcements as,

$$T_c^*(n_{cis}) = (1 - \beta^* \cdot n_{cis}) + \{T_1 \cdot \exp(-T_2 \cdot n_{cis})\} \quad (4.9)$$

where  $\beta^*$  is 88.8 which estimated from the neat PRP model in MD simulations and  $T_1$  and  $T_2$  are the regression coefficients. All the obtained coefficients and their R square values were listed in **Table 4.3** and plotted in **Figure 4.1**. It was clearly found that the fitted curves successfully describe all of the characteristic features of the MD data. Using the Eq. (4.5), we directly predicted the orientational order parameter of the PRP nanocomposites at various particle diameters under wide range of temperatures through the modeled functions themselves, as shown in **Figure 4.2**.

Meanwhile, in **Chapter 3** (in **Figure 3.10**) we showed that the linear correlation between the order parameter and the thermal shrinkage of the matrix phase was significant, especially for the PRP nanocomposites models. According to Eq. (4.3), the opto-mechanical coupling term ( $\tilde{\alpha}$ ) can be directly computed from the slope of the linear regression line and depicted the results in **Figure 4.1 (d)**. It is clearly found that the PRP nanocomposites have higher response rates than those with the neat PRP. Also, the value is mainly depending on the photo-isomerization ratio both for the neat PRP and the PRP nanocomposites; the coefficients are consistently reduced during the isomerization reaction,

indicating that a potential capacity of the material to be deformed by light irradiation is substantially reduced. Hence, as discussed in the previously reported literature [78,104,111], the maximum quantity of the photo-deformation can be achieved near the N-I phase transition temperature with sufficient amount of the UV-light intensity. Lastly, as introduced in Eq. (4.4), the final solution for shape parameter of the PRP nanocomposites was derived from the order parameter and the polynomial fitted  $\tilde{\alpha}$  and depicted in **Figure 4.3**.

**Table 4.1** Clearance temperature of the neat PRP and the PRP/gold nanocomposites according to the ratio of isomerization reaction

$n_{cis}$	Neat PRP (K)	PRP/gold (K)
Trans	462.5	519.6
Cis 25%	425.2	453.0
Cis 50%	392.5	426.5
Cis 75%	373.7	404.5
Cis 100%	363.0	383.6

**Table 4.2** Temperature-independent characteristic coefficients of the neat PRP and the PRP/gold nanocomposites for Haller's extrapolation model

$n_{cis}$ (%)	Neat PRP		PRP/10Å gold		PRP/13Å gold		PRP/16Å gold		PRP/20Å gold	
	$\zeta$	$k$	$\zeta$	$k$	$\zeta$	$k$	$\zeta$	$k$	$\zeta$	$k$
0		1.40		0.99		1.20		1.17		1.20
25		1.00		0.92		0.76		0.84		1.08
50	0.38	0.92	0.40	0.41	0.36	0.57	0.29	0.93	0.16	0.93
75		0.91		0.67		0.72		0.67		0.77
100		0.90		0.39		0.41		0.64		0.78

**Table 4.3** Dimensionless fitting coefficients obtained from the MD results

Coefficients	Value	R <sup>2</sup>
$\zeta_1$	-8.161e-4	0.9688
$\zeta_2$	0.3978	
$k_1$	0.0614	0.8306
$k_2$	0.8477	
$k_3$	0.1678	
$k_4$	-1.436	
$T_1$	0.1212	0.9850
$T_2$	-4.618	

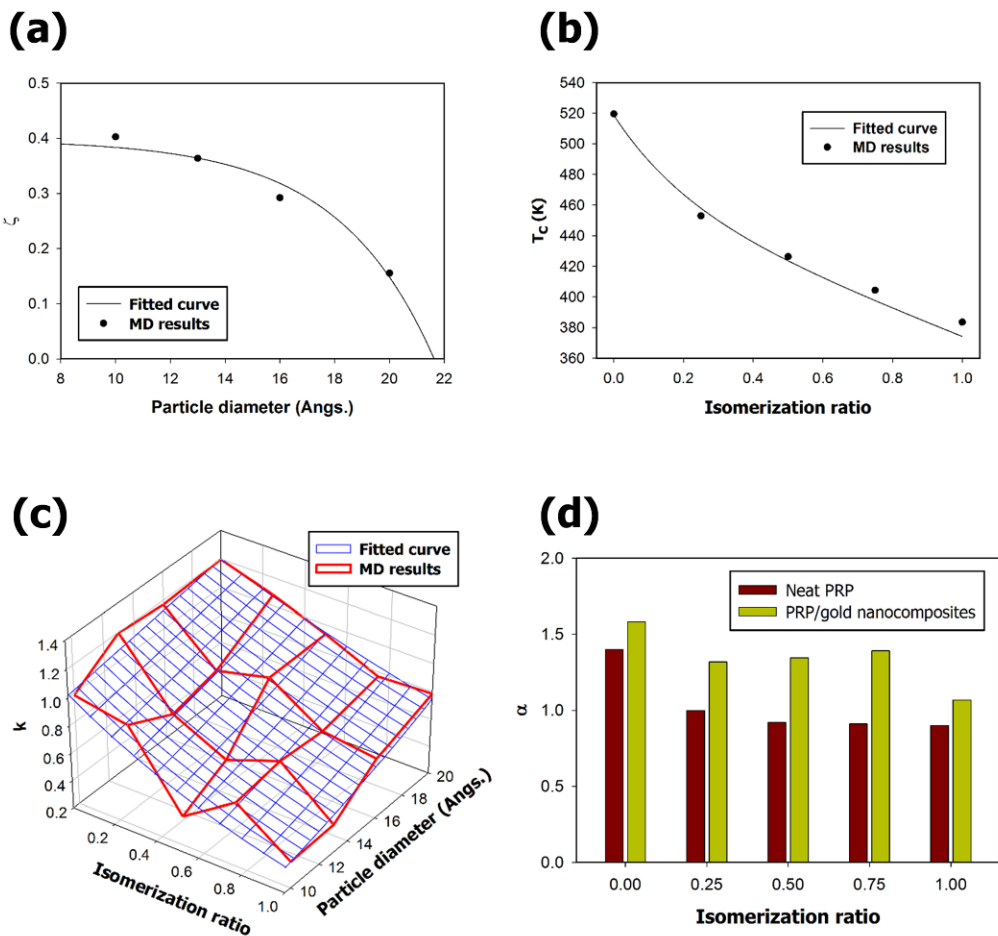


**Figure 4.1.** Exponent dependence of the characteristic coefficients of the PRP nanocomposites models and their fitting curves.

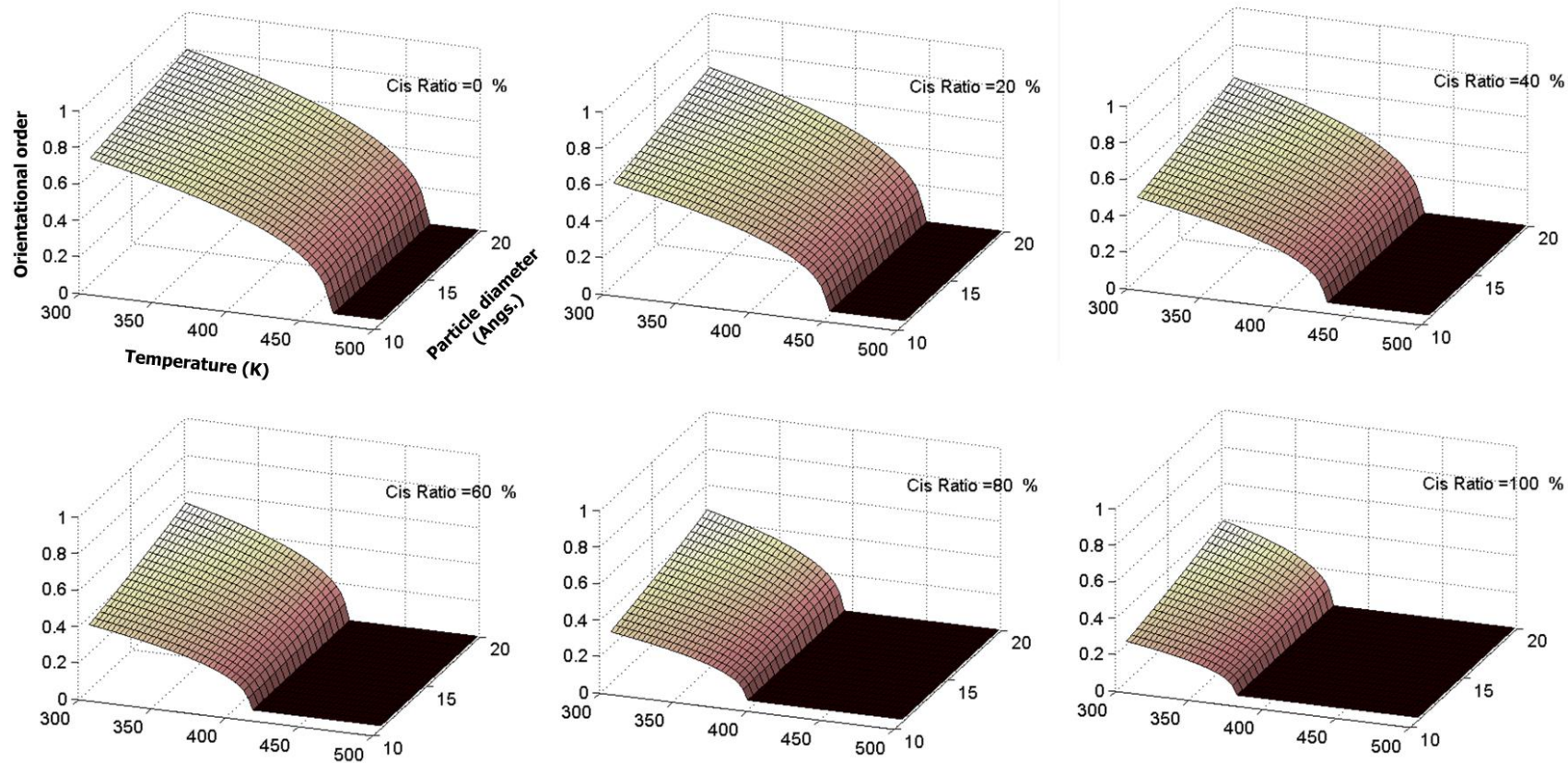


**Figure 4.2.** The continuous function for orientational order parameter of the PRP/gold nanocomposites according to the nanoparticle size and the photo-isomerization ratio



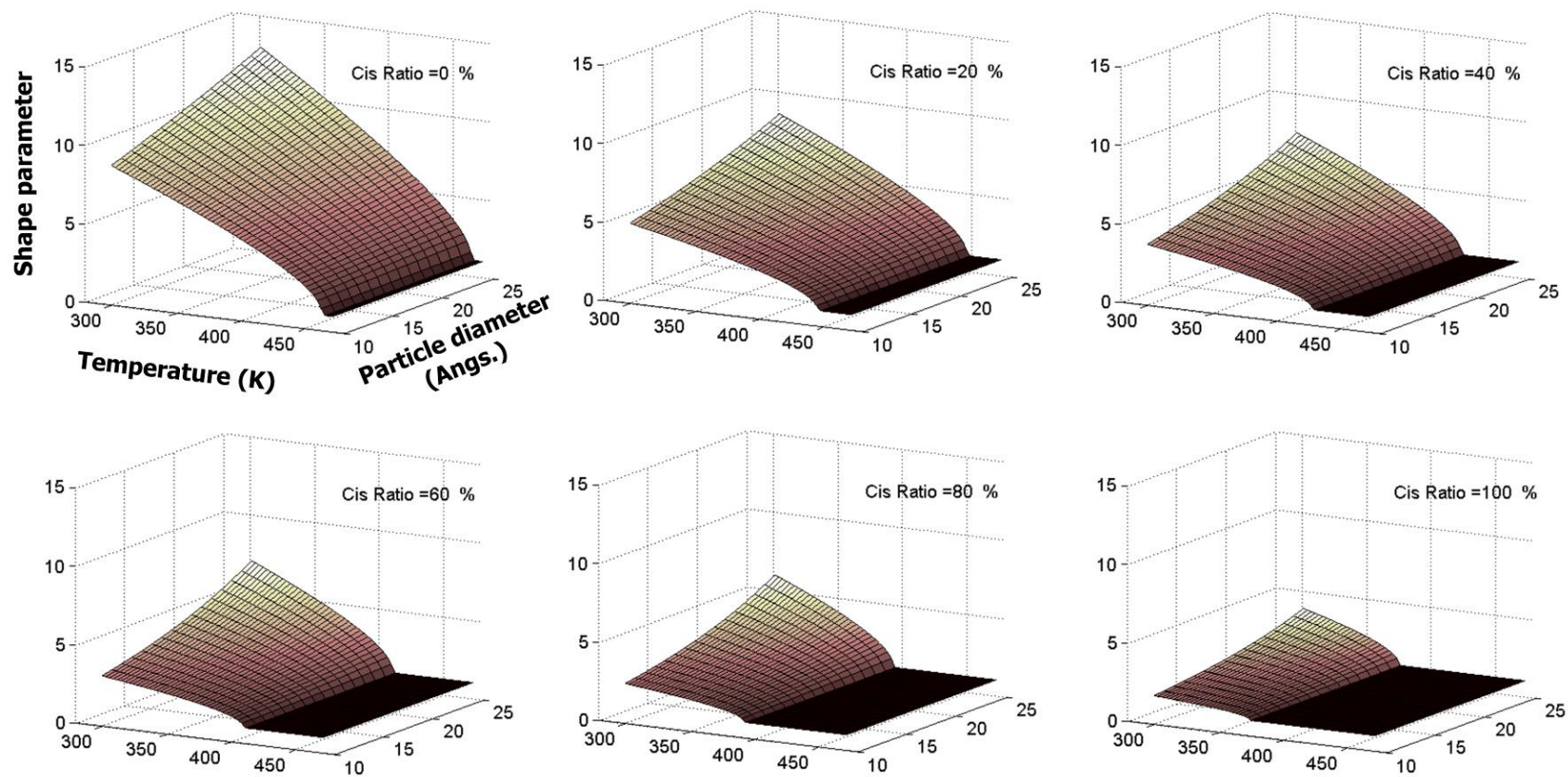


**Figure 4.3.** The continuous function for shape parameter of the PRP/gold nanocomposites according to the nanoparticle size and the photo-isomerization ratio.

## 4.2. Characterization of the interfacial behavior during mechanical loading

### 4.2.1. Local stress distributions at the interfacial layer

In this section, we address the multiscale mechanical analysis for the response of the PRP nanocomposites structure to an external mechanical loading. In the above chapter, we verified that the thermo-mechanical properties of the bulk material is remarkably improved as the nano-sized reinforcements are dispersed in the matrix. Such beneficial effect is mainly originated from the extremely high surface-to-volume ratio of gold nanoparticles and thus the nanoparticle ‘size effect’ was observed because the effective volume fraction and properties of the interfacial region generated by the adsorbed polymer chains around the nanoparticle were dominated by the size of the reinforcements.

To explicitly characterize the independent properties and thicknesses of the interfacial region with respect to the nanoparticle size and photo-isomerization ratio of the material, we carried out uniaxial tensile loading simulations for each modeled unit cell. The considered PRP and PRP/gold nanocomposites models introduced in **Chapter 2** and **Chapter 3** were relaxed at extremely low temperatures (10 K) and at 1 atm for 5 ns within the NPT ensemble. Energy minimization was performed to remove the effect of temperature on the kinetic energy of the molecules in the unit cell. The elastic mechanical response and the load transfer efficiency of the pure polymer and polymer nanocomposite

models are estimated along the x, y, and z directions through uniaxial tensile loading simulations. The tensile simulations for the cases considered were carried out using the Large-Scale Atomic/Molecular Massively Parallel Simulator, an open source code (LAMMPS, Sandia Lab). The lattice length of the unit cell is elongated during the NVT ensemble run at 0.1 K with the true strain rate of  $10^{-6}$ /ps. In this work, we only focus on the linear elastic behavior of the models considered, so the total strain does not exceed 0.3% in the simulation.

According to the tensile tests, stresses for each atom in both the axial and transverse directions can be obtained. From an atomic viewpoint, the potential energy increase can be explained with an atomic stress tensor  $\boldsymbol{\sigma}$  based on the virial theorem defined in Eq. (4.10) [97],

$$\boldsymbol{\sigma} = \frac{1}{V} \left( -\sum_i^N m_i (\mathbf{v}_i \mathbf{v}_i^T) + \frac{1}{2} \sum_i^N \sum_{j \neq i}^N \mathbf{r}_{ij} \mathbf{F}_{ij} \right) \quad (4.10)$$

where  $V$  is the atomic volume,  $N$  is the total number of atoms,  $\mathbf{v}_i$  and  $m_i$  are the thermal excitation velocity and the mass of atom  $i$ , respectively,  $\mathbf{r}_{ij}$  is the relative position between atoms  $i$  and  $j$ , and  $\mathbf{F}_{ij}$  is the atomic force on atom  $i$  due to atom  $j$ . Because the kinetic part in Eq. (4.10) can be excluded near 0K, only the potential part of  $\boldsymbol{\sigma}$  is involved in the deformation energy of the considered model, and it directly indicates the equivalent continuum (Cauchy) stress [98]. Therefore, the atomic stress tensor for a polymer and polymer nanocomposite structure can be computed from a summation of the interatomic pair, bond, angle, and dihedral angle potentials between the atoms in the

system, as shown in Eq. (4.11) [97]:

$$\sigma_{ij}^V = -\frac{1}{V} \left[ \frac{1}{2} \sum_{n=1}^{Pair} (r_{1i} F_{1j} + r_{2i} F_{2j}) + \frac{1}{2} \sum_{n=1}^{Bond} (r_{1i} F_{1j} + r_{2i} F_{2j}) + \frac{1}{3} \sum_{n=1}^{Angle} (r_{1i} F_{1j} + r_{2i} F_{2j} + r_{3i} F_{3j}) + \frac{1}{4} \sum_{n=1}^{Dihedral} (r_{1i} F_{1j} + r_{2i} F_{2j} + r_{3i} F_{3j} + r_{4i} F_{4j}) \right] \quad (4.11)$$

where the subscript number indicates an arbitrary label of the atom included in the interaction cutoff distance (9.5 Å), and  $V$  is the designated atomic volume of a local group of the model considered. The assignment of the effective  $V$  raises an important issue regarding the molecular and atomic analysis of nano-sized structures such as nanorod/nanowire arrays or nanofilms, because the effective atomic volume at the surface domain might be significantly changed by surface relaxation and reconstruction. However, for a nanocomposite with low volume fraction (~2 %), it is clear that the effective atomic volume in any region in the lattice unit is nearly the same as the geometrical volume of the initially designated region when a periodic boundary condition and tightly packed morphology of the model are considered.

To derive the local stress transfer characteristics in the interphase region around the nanoparticle, for each unit cell model we set artificial groups which have a hollow-sphere shell shape and are concentric with the center of the gold nanoparticle, as shown in **Figure 4.4**. The deformation energy density of the group ( $W^{MD}$ ) according to the distance from the nanoparticle surface  $d$  is calculated as:

$$W^{MD}(d) = \frac{U_{total} - U_{Au} - U_{Bulk}(d)}{(4/3)\pi \left\{ (R_{Au} + d)^3 - R_{Au}^3 \right\}} \quad (4.12)$$

where  $U_{Au}$  and  $U_{Bulk}$  are the changes of potential energy of the inner and outer regions

of the designated group due to the strain and  $R_{Au}$  is the radius of the gold nanoparticle.  $W_{MD}$  expresses the isolated load transfer capacity on the adsorbed polymer matrix within the given radial distance from the particle surface; the resulting profiles are therefore used for the energy matching procedure of the current multiscale method, which will be explained in the next section.

The calculated strain energy density distributions of the PRP/gold nanocomposites are shown in **Figure 4.5** (mechanical loading in the x direction) and **Figure 4.6** (mechanical loading in the y and z directions), respectively. It is clearly seen that the energy density distribution is not uniform but highly variable according to the distance from the nanoparticle surface. During the axial loading, the energy density has higher value near the nanoparticle surface than the farfield parts of the matrix, indicating that the interfacial region has unstable structural responses. Such unstable behavior might come from the inhibition of the crosslink formation of methyl side groups as well as the misalignment of mesogen. When the chemically untreated nanoparticle occupies the position of the matrix, the crosslink reaction is inhibited and it locally degrades the material [112,113]. Also, the mesogen disordering around the nanoparticle is involved in the formation of unstable interfacial region, though the effect is expected to be not significant because of the small size of the nanoparticle (we discussed it earlier in **Chapter 3.3**). However, simultaneously, the strong non-bond interaction between the gold nanoparticle and the polymer constituents still affects the strengthening effect of interfacial region. So the overall energy density is increased comparing with that of neat PRP model (not shown

in the graph). Accordingly, the effect of the interfacial behavior at the nanofiller-matrix interface on the local load transfer in the nanocomposites system is still ambiguous in the present situation. This only can be achieved with the combination of the current data obtained from MD simulations with numerical continuum, which will be fully discussed in the next section.

An important aspect shown in **Figure 4.5** and **Figure 4.6** is that the cis-isomerization ratio in the nanocomposites system is a critical variable in the design and analysis of PRP nanocomposites. As shown in **Figure 4.5**, the deformation energy density gradually decreased as the photo-isomerization reaction is progressed, i.e., the stiffness of the material in the director axis would be degraded. On the other hand, the corresponding value under transverse loading shown in **Figure 4.6** does not reduce but rather slightly enhances with cis-isomerization. The results demonstrate that the phase changes from transversely isotropic to isotropic during the UV-light exposure. Note that the result is also in line with findings observed from the elastic stiffness components of the material (the reader is again referred to **Figure 2.7** and **Figure 3.8**.)

#### **4.2.2. Modeling an equivalent multiscale unit using energy method and homogenization**

**Figure 4.7** shows a schematic of the multiscale method developed in this study. For continuum analysis, although both a micromechanics-based analytical methodology

and a numerical calculation using the three-dimensional FE model are applicable to the characterization of the effective interphase, here we introduce the described numerical calculation method to achieve general and intuitive analysis of the effective deformation on the interphase. The model consists of three phases (the particle, the interphase layer, and the matrix), which are represented as concentric spheres meshed with a 10-node tetrahedral element. The mechanical properties of the gold nanoparticle (Young's modulus: 79 GPa and shear modulus: 27 GPa) was adopted in the particle phase of the FE model.

In order to describe the mechanical behavior of a heterogeneous material including the interphase layer with periodic microstructure via mathematical formulation, the two-scale asymptotic homogenization method is adopted in the model [114-116]. Two scale coordinates,  $\mathbf{X}$  and  $\mathbf{y}$ , are defined to conveniently describe both the macroscopic and microscopic behaviors, respectively.  $\mathbf{X}$  is the macroscopic coordinate defined at the entire body level, and  $\mathbf{y}$  is the microscopic coordinate defined at the local microstructure level. The non-dimensional scale parameter  $\alpha$  ( $\ll 1$ ) is defined as the ratio of the microscopic length to the macroscopic length, which is given as [114,115]:

$$\mathbf{X} = \mathbf{X}(\mathbf{x}, \mathbf{y}), \quad \mathbf{x} = \mathbf{X} \text{ and } \mathbf{y} = \mathbf{X} / \alpha. \quad (4.13)$$

The displacement field in the macroscopic domain  $\mathbf{u}$  is then asymptotically expanded as:

$$\mathbf{u}(X) = \mathbf{u}^0(\mathbf{x}, \mathbf{y}) + \alpha \mathbf{u}^1(\mathbf{x}, \mathbf{y}) + \alpha^2 \mathbf{u}^2(\mathbf{x}, \mathbf{y}) + \dots. \quad (4.14)$$

Meanwhile, the principle of virtual displacement subjected to traction is given as follows [114,115]:

$$\int_V C_{ijkl} \frac{\partial u_k}{\partial X_i} \frac{\partial v_i}{\partial X_j} dV = \int_A t_i v_i dA \quad (4.15)$$

where  $\mathbf{u}$  and  $\mathbf{v}$  are the real and virtual displacements, respectively,  $\mathbf{t}$  is the traction, and  $\mathbf{C}$  is the fourth-order elasticity tensor of the nanocomposites. By applying Eq. (4.14), Eq. (4.15) could be arranged about the power of the scale parameter as follows:

$$o(\alpha^{-1}): \int_{\bar{Y}} C_{ijml} \frac{\partial \chi_m^{kl}}{\partial y_n} \frac{\partial \delta v_i}{\partial y_j} dV_y = \int_{\bar{Y}} C_{ijml} \frac{\partial v_i}{\partial y_j} dV_y \quad (4.16a)$$

$$o(\alpha^0): \int_V C_{ijkl}^H \frac{\partial u_k}{\partial X_i} \frac{\partial v_i}{\partial X_j} dV = \int_A t_i \delta u_i^0 dA. \quad (4.16b)$$

where the characteristic function  $\chi(\mathbf{x}, \mathbf{y})$  describes the mechanical behavior of the microstructure under the unit macroscopic strain. Finally, the homogenized elastic stiffness tensor of the nanostructure can be computed as follows:

$$C_{ijkl}^H = \frac{1}{|\bar{Y}|} \int_{\bar{Y}} (C_{ijkl} - C_{ijmn} \frac{\partial \chi_m^{kl}}{\partial y_n}) dV_y \quad (4.17)$$

The characteristic function  $\chi(\mathbf{x}, \mathbf{y})$  and the homogenized elasticity of the nanostructure can be obtained numerically from FE equations. Eq. (4.16a) and Eq. (4.17) can be discretized as follows:

$$\int_Y [\mathbf{B}]^T [\mathbf{C}] [\mathbf{B}] [\chi] dV_y = \int_Y [\mathbf{B}]^T [\mathbf{C}] dV_y \quad (4.18a)$$

$$\mathbf{C}^H = \frac{1}{|Y|} \int_Y ([\mathbf{C}] - [\mathbf{C}] [\mathbf{B}] [\chi]) dV_y \quad (4.18b)$$

Note that because the homogenization method uses a unit cell of the periodic microstructure, the periodic boundary condition is imposed in solving Eq. (4.18a). In order to obtain the



isotropic properties from the fourth-order stiffness tensor, the Hill's model is employed [116].

Fundamental schemes for the nano-continuum bridging technique were proposed by Odegard et al. [117], Tsai and Tzeng [50], Figiel [118], and Cho et al. [56]. Among these, Cho et al. [56] proposed a procedure to obtain the elastic properties of the effective interphase using the homogenization-based multiscale approach. The unknown properties of the interphase with assumed thickness could be solved exactly in continuum mechanics by the inverse identification method (a homogenization technique) when the microscopic behavior of the composites is fully understood via MD simulation. In addition to the precedent multiscale model, in this study we subjoin the deformation energy density comparison procedure in order to determine the geometric boundary at which the strain energy density of the interphase in the continuum model has the same value as that of the full atomic model. The homogenization solution for the unknown mechanical properties of the interphase is derived under various interphase thickness conditions. In the FE model, the elongation of the unit cell lattice in MD simulation is imposed as the enforcing displacement fields, considering periodicity. The discretized equation for the strain energy density of the effective interphase is as follows:

$$W_{\text{int}}^{FE} = \frac{1}{2V_{\text{int}}} \{\mathbf{d}\}^T \int_{V_{\text{int}}} [\mathbf{B}]^T [\mathbf{C}] [\mathbf{B}] dV_y \{\mathbf{d}\} \quad (4.19)$$

where  $\{\mathbf{d}\}$  is the resultant displacement field of the interphase.

A brief summary of the methodology is provided as follows. **Figure 4.8** denotes

the entire process of the established multiscale model as a flowchart. In MD simulation, the overall mechanical properties of the polymer nanocomposites were obtained according to the nanoparticle radius by adapting uniaxial tensile tests. During the static loading along the nematic axis, the atomic potential density increment curve of the adsorbed polymer layer was obtained in terms of the distance from the nanoparticle surface. Meanwhile, the elastic stiffness of the overall nanocomposite models was transferred as an input of the multi-inclusion model in FE analysis. Through the homogenization, the Young's and shear moduli of the interphase were numerically obtained until the continuum model had the same global stiffness as that of the atomic unit cell. After the interphase modulus found under the assumed interphase thickness condition, the strain energy density of the FE model was derived and whether the strain energy density matches the potential energy increment derived in the MD model under the same interphase thickness condition was determined. This optimization algorithm was performed until both the global stiffness and the strain energy density of the interphase converge to those extracted from the MD model.

As a consequence, the proposed equivalent continuum model meets two unknown parameters for the interphase (layer thickness and elastic properties) with the atomic model simultaneously. Thus, it guarantees the consistency of both the global elastic behavior and the effective reinforcing range of the adsorbed polymer region. It is worth noting that this work is the first attempt to characterize the mechanical behavior of the nanocomposite interphases with the credibility of considering mechanical energy. As mentioned above, the reinforcing size of the interphases and their individual mechanical behavior are crucial

design factors for the polymer nanocomposites. Furthermore, the geometry-related challenges in interphase design (such as a phase separation in a mechanical deformation or a rheological percolation threshold of the nanoparticle) can also be overcome.

### **4.2.3. Estimation and validation of the obtained interphase models**

The thickness and elastic properties of the effective interphase of the PRP/gold nanocomposites characterized by the multiscale analysis are listed in **Table 4.4**. In all cases, we revealed that the interphase has stronger mechanical properties than the neat PRP, indicating the strengthening of the adsorbed polymer layers around the nanoparticles. It is noteworthy to mention that the independent mechanical characteristics of the interphase only can be obtained from the nano-continuum integrated multiscale method developed in this study. As discussed in the above section, the mechanical response of the interphase layer would be determined both by the filler-matrix interfacial energy and by the conformation of the polymer matrix around the nanoparticle. In the present nanocomposites models, the polymer networks properly formed densely packed morphology during the relaxation (see the radial density distributions depicted in **Figure 3.5**) and were to generate a strengthened phase – but simultaneously the imperfect bonding condition in gold nanoparticle-reinforced polymer also appeared in the deformation energy density distribution posted in **Figure 4.5**. Thus, the two characters are competed with each other and the net behavior at the interfacial region only can be estimated by the quantitative

multiscale method.

Since the bulk PRP matrix is transversely isotropic, the effective interphase also shows an anisotropic mechanical properties; the  $C_{11}$  has ~2 times higher stiffness than the  $C_{22}$ . In common with the results obtained with neat PRP model shown in **Figure 2.7**, the  $C_{11}$  of the effective interphase becomes decreased gradually as the photo-isomerization reaction is progressed due to the phase transformation (from transversely isotropic to isotropic) of the matrix.

Another important finding in the analyzed results is the change of thickness of the effective interphase according to the nanoparticle size. The thickness of the effective interphase is reduced as the embedded nanoparticle size increases. The main cause of the change of interphase thickness with the nanoparticle diameter is the change of the number of non-bond interaction pairs at the interfacial layer. Even though the variation of diameter of the nanotubes modeled in this study was extremely small, the change of corresponding curvature was significant due to the small size of the nanoparticle. In a geometric view, the interaction region of a matrix constituent atom around the nanotube becomes enlarged as the diameter of the nanotube increases, i.e., the maximal effective length from the polymer constituents to the nanoparticle surface required for the generation of an interphase becomes larger. To clarify this, we calculated the number of non-bond pairs between an arbitrary polymer constituent in the interfacial region and a gold surface and depicted the result in **Figure 4.9**. It supports that the effective distance from the nanoparticle surface to the outer boundary of the adsorbed polymer layer should be increased as the inserted gold

surface becomes flattened to achieve an equilibrium state.

Meanwhile, the interphase thickness also is influenced by the UV-light irradiation. We depicted the estimated interphase thickness and the associated deformation energy during the mechanical loading in nematic axis in **Figure 4.10** and tabulated them in **Table 4.5**. When we focus on the thickness dependency on the photo-isomerization ratio, it can be concluded that the effective thickness of the interfacial layer is consistently decreased as the trans-to-cis isomerization reaction of the matrix is progressed. This sort of dependency is non-trivial but straightforward in principle. As predicted from the deformation energy curves of the nanocomposites (the results are depicted in **Figure 4.5**), the gold nanoparticle formed a long-ranged interaction effect in the polymer matrix. Accompanying with this, the deformation energy at the interphase calculated from the FE model slowly converges with increasing of the interphase thickness (not shown in the graph). Therefore, the intersection point between the two curves derived from the MD simulation and the FE model homogenization is located quite far apart from the nanoparticle surface – the measured volume fraction of the interphase in the nanocomposites system is around 30 to 60%, depending on the model considered. Since the deformation energy curves derived from the MD simulations are considerably decayed during the photo-isomerization, the intersection points with the corresponding ones of FE model is forwarded. In a structural view, such behavior is acceptable in that the local polymer structure around the nanoparticle surface loses its directionality during the event hence the isolated stress transfer capacity along the director axis should be reduced. In

practice, the results shown in **Figure 4.10** clearly demonstrate that the effective deformation energy at the interphase is consistently decreased as the isomerization reaction is progressed.

For the validation of the obtained interphase model, firstly we remodeled three phase multi-inclusion FE models with the conditions suggested by the present multiscale analysis and compared their deformation energy density of the interphase with the corresponding one calculated by MD simulations. As shown in **Figure 4.11** and **Table 4.5**, in all the considered cases the value is successfully reproduced with the error of 5 percent. Note that the elastic stiffness components of the overall nanocomposites predicted by the remodeled units were very accurate (the error is in range of  $10^{-5}$ ) since the homogenization method was implicitly used.

Another validation study for the present model is estimation of the local stress in the interphase. As shown in **Figure 4.12**, we considered rectangular-shaped artificial blocks ( $4 \times 10 \times 10 \text{ \AA}^3$ ) in the PRP/gold ( $16 \text{ \AA}$ ) nanocomposites model in MD and calculated its local virial stress inside of the regions during the tensile loading simulations. The blocks were located across the middle of the interphase layer to represent the interfacial behavior. The obtained virial stresses were averaged over five different loading simulations to reduce the uncertainty that might arise from the limited number of atoms participated. According to the result, it can be noticed that the interfacial stress along the nematic director (x-axis) has  $\sim 2$  times higher than the one in the transversal directions (y- and z-axes). However, as the photo-isomerization is fully progressed and the material changes to a near-isotropic phase,

the gap of the two stresses becomes narrower. The present equivalent continuum unit predicted such findings with a reasonable accuracy. The main cause of the subtle error between the two is that the local stress in the MD model should be derived from very small, simple-box-shaped groups with a limited numbers of atoms, whereas that in a continuum model can be simply obtained with a smooth nature without the volume average effect.

Finally, we derived the internal stress distribution of the effective interphase region considering with the nanoparticle size as well as the photo-isomerization ratio of the matrix and plot the results in **Figure 4.13**. The material anisotropy on the mechanical response of interfacial region under mechanical loading is clearly found. When the UV-light is irradiated and azobenzene molecules in the PRP matrix lose their directionality, the mechanical stress along the nematic axis of the mesogen is drastically reduced. On the other hand, the distribution of interfacial stress along transversal axes of the mesogen does not show significant change under identical condition.

**Table 4.4** Effective thickness and properties of the interphase of PRP/gold nanocomposites obtained from the equivalent multiscale model

System	$n_{cis}$ (%)	$t_{int}$ (Å)	Interphase stiffness (GPa)				
			$C_{11}$	$C_{12}$	$C_{22}$	$C_{23}$	$C_{44}$
PRP/gold (10 Å)	0	10.50	14.32	4.27	5.77	2.40	2.90
	25	9.30	16.75	10.54	16.23	13.40	2.34
	50	8.97	10.84	3.63	12.28	8.65	2.69
	75	9.00	22.50	6.13	5.72	2.17	2.63
	100	8.62	6.40	1.29	4.77	2.89	0.97
PRP/gold (13 Å)	0	16.48	8.69	3.39	4.80	2.75	1.09
	25	14.36	10.14	4.63	7.17	5.07	1.13
	50	12.56	9.90	3.49	5.36	4.09	0.63
	75	13.19	5.02	2.21	3.87	1.53	1.30
	100	11.56	5.51	2.73	4.80	2.39	1.30
PRP/gold (16 Å)	0.0	19.00	9.85	2.89	4.79	2.30	1.41
	25	21.69	7.33	3.02	4.73	2.97	0.89
	50	13.42	8.79	3.04	6.56	3.82	1.59
	75	19.14	6.14	2.67	4.23	2.68	0.77
	100	16.77	7.00	3.03	4.23	2.65	0.78
PRP/gold (20 Å)	0.0	27.23	6.71	2.20	3.80	2.28	0.79
	25	24.63	6.36	2.90	4.59	2.87	0.86
	50	19.30	8.78	3.08	5.62	3.56	1.10
	75	16.53	5.49	1.93	3.52	0.70	1.81
	100	16.40	10.98	2.27	4.60	2.12	1.30



**Table 4.5** Deformation energy density of the effective interphase during the tensile loading (in x-axis). The value predicted by the present multiscale method was reproduced by the remeshed FE model for the model validation.

System	$n_{cis}$ (%)	$t_{int}$ (Å)	Energy density (Multiscale, kJ/m <sup>3</sup> )	Energy density (Reproduce, kJ/m <sup>3</sup> )	Error (%)
PRP/gold (10 Å)	0	10.50	40.34	40.18	0.40
	25	9.30	30.42	30.40	0.04
	50	8.97	29.64	29.34	1.01
	75	9.00	26.75	25.29	5.48
	100	8.62	25.34	25.26	0.34
PRP/gold (13 Å)	0	16.48	36.44	36.41	0.07
	25	14.36	34.12	34.19	0.22
	50	12.56	30.91	30.77	0.46
	75	13.19	25.31	25.30	0.02
	100	11.56	23.41	23.39	0.11
PRP/gold (16 Å)	0	19.00	39.06	38.80	0.65
	25	21.69	32.00	32.01	0.03
	50	13.42	28.35	28.24	0.38
	75	19.14	27.55	27.63	0.27
	100	16.77	26.39	26.42	0.12
PRP/gold (20 Å)	0	27.23	31.39	31.18	0.67
	25	24.63	29.00	28.93	0.25
	50	19.30	30.40	30.30	0.33
	75	16.53	27.01	27.03	0.07
	100	16.40	24.64	24.47	0.66

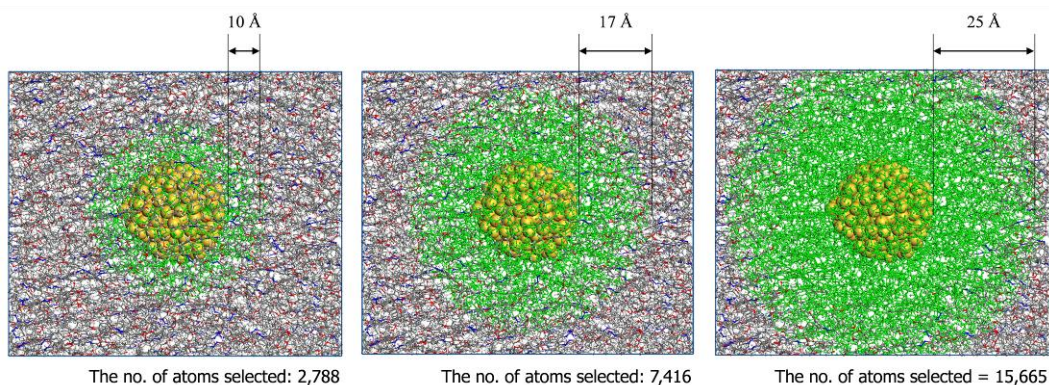


**Figure 4.4** The polymer networks in the vicinity of the nanoparticle were selected by the arbitrarily defined local shell group (highlighted in green) to calculate the deformation energy distribution at the interfacial region.

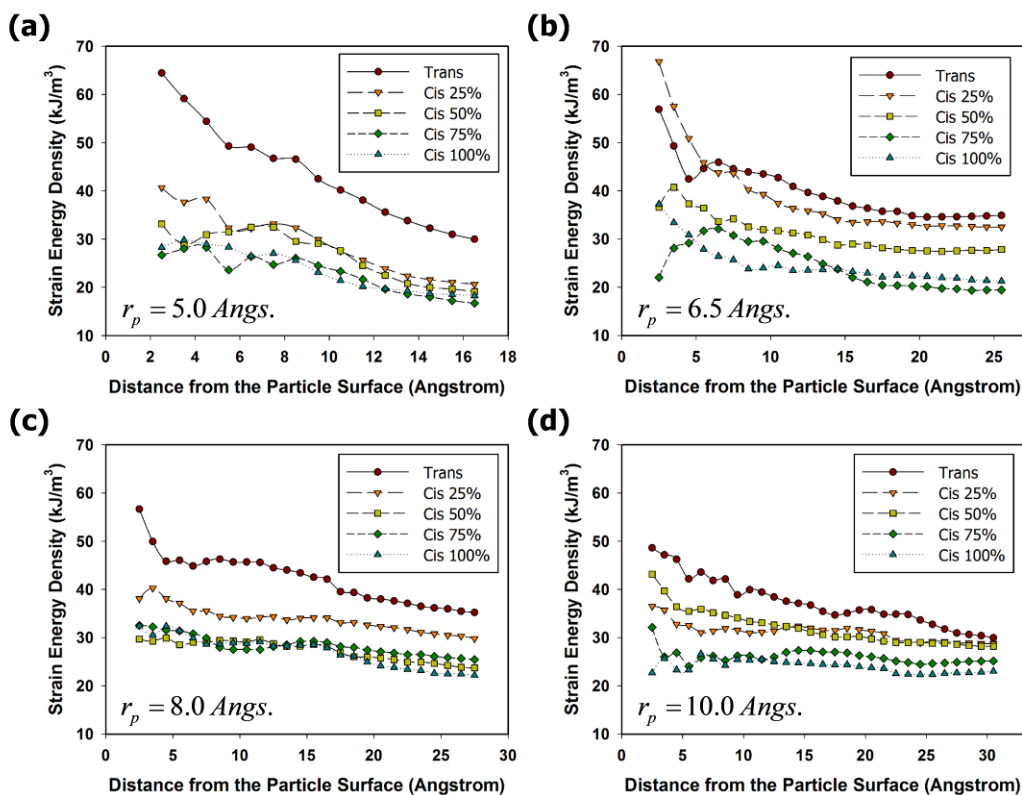


**Figure 4.5** Deformation energy density distribution in normal (x-axis) direction.

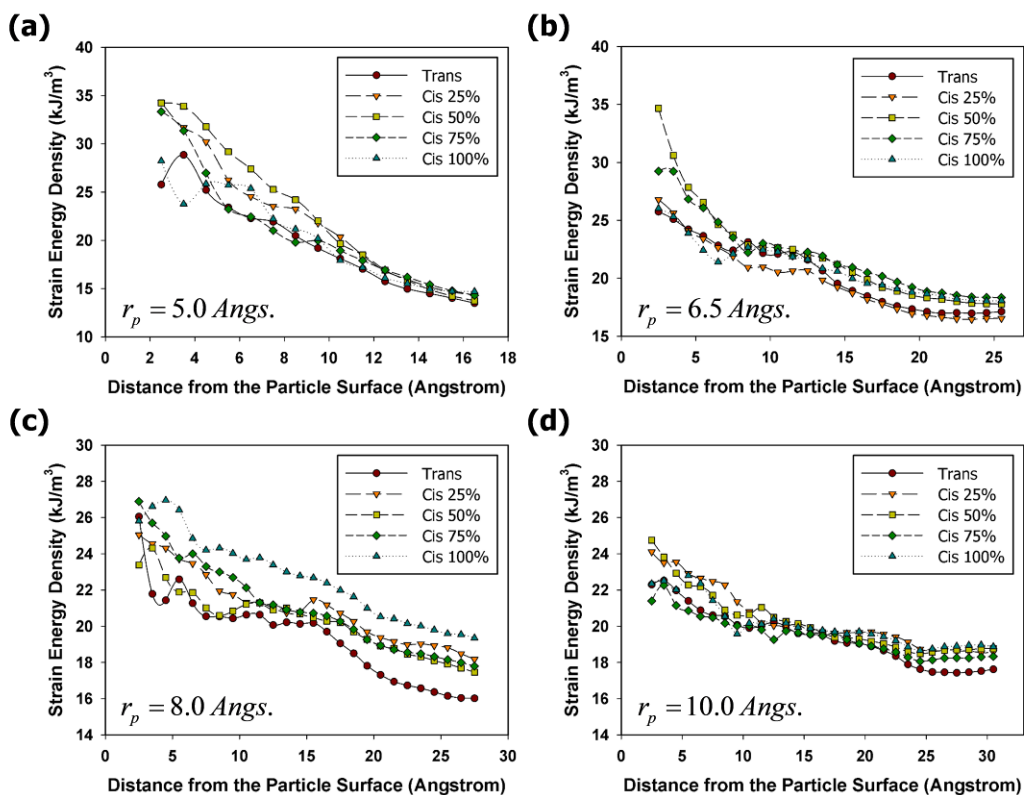


**Figure 4.6** Deformation energy density distribution in transversal (y- and z-axes) direction.

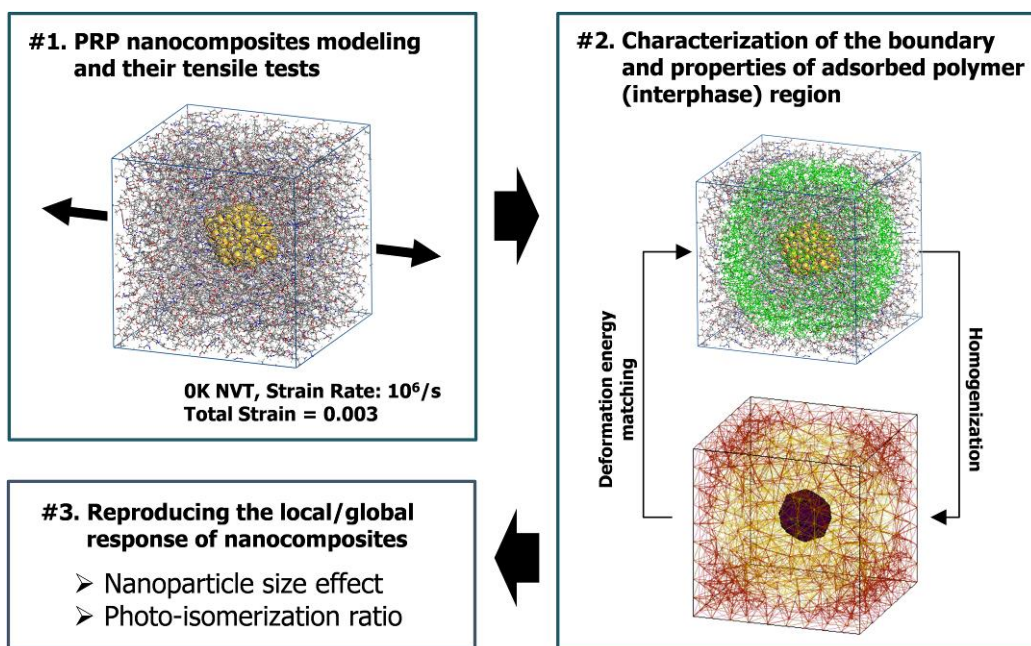


**Figure 4.7** A schematic view of the present multiscale mechanical analysis for the effective interphase formed in PRP/gold nanocomposites considering with the nanoparticle size effect, as well as trans-to-cis photo-isomerization reaction.

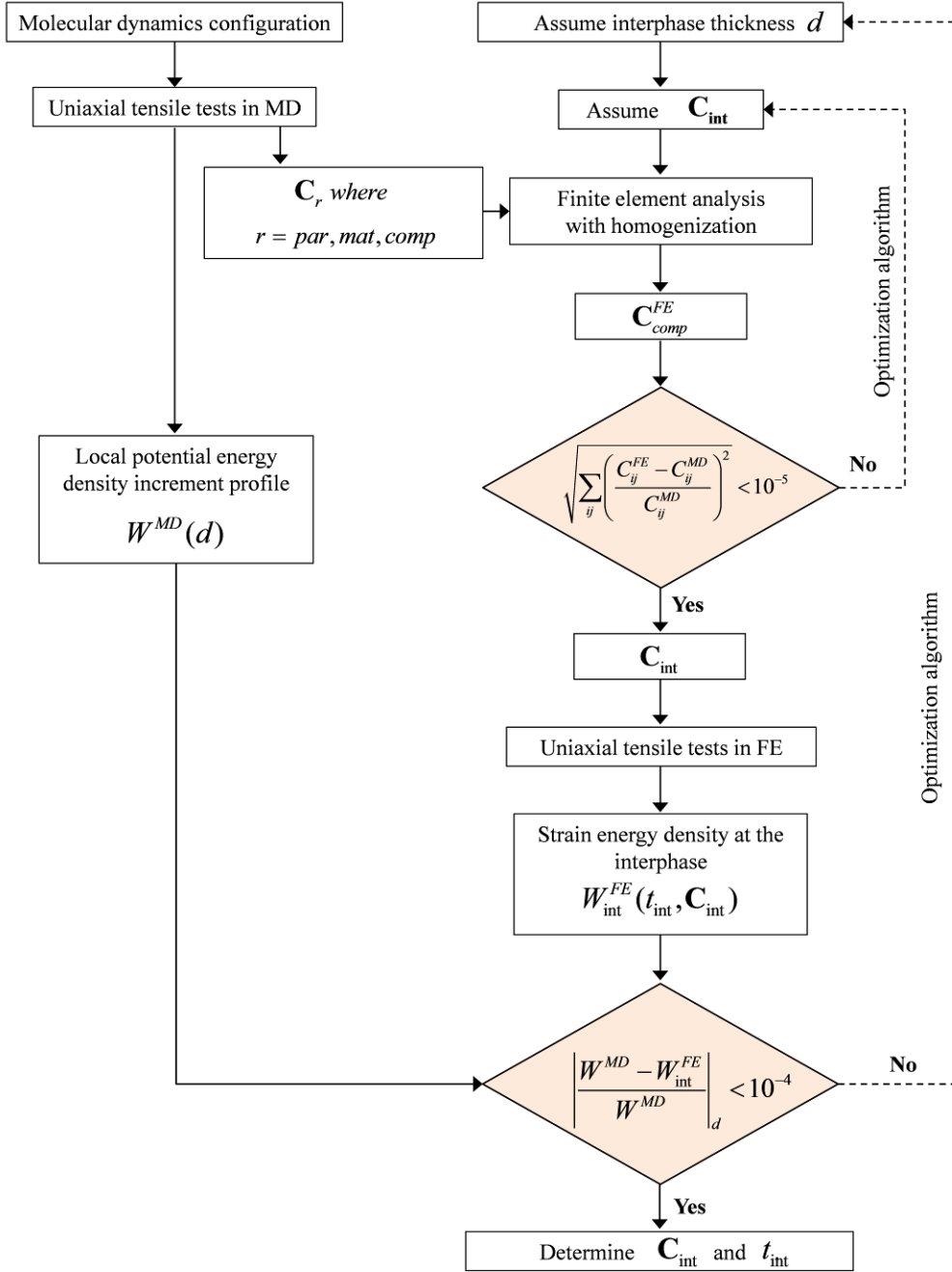


**Figure 4.8** Flowchart for obtaining the effective thickness and properties of the interphase, integrating the MD simulation with FE analysis.

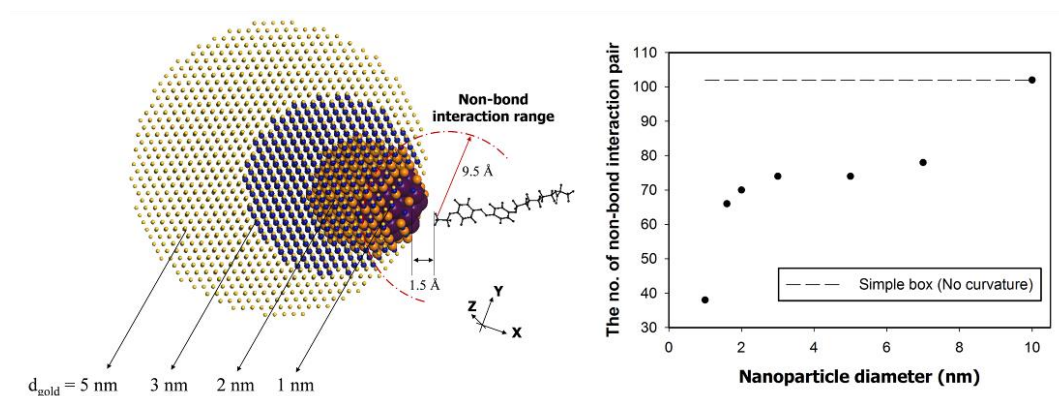


**Figure 4.9** The number of non-bond pairs between the gold nanoparticle and the nearest polymer chain with respect to the size of the nanoparticle. The corresponding value for gold cluster is also drawn as dash line to specify the saturation point.

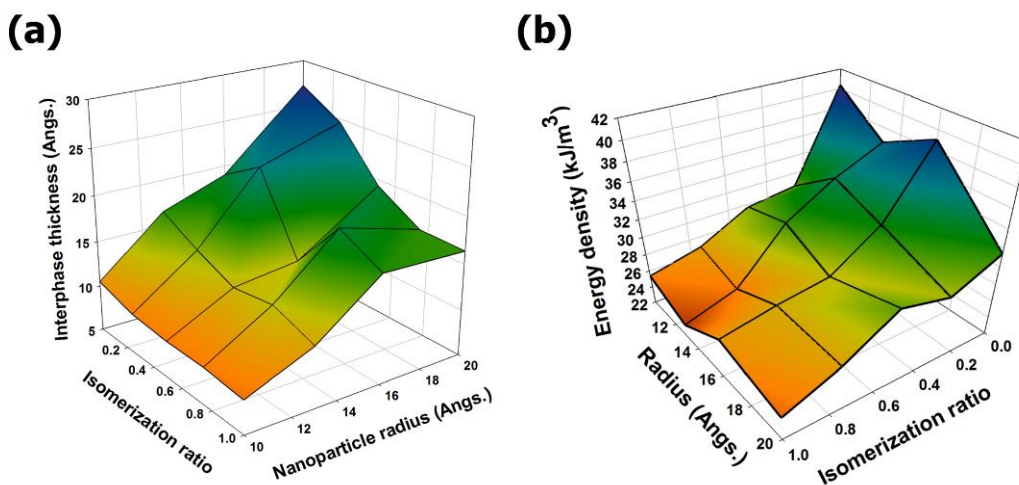


**Figure 4.10** (a) Estimated interphase thickness and (b) the corresponding value of the energy density according to nanoparticle size and photo-isomerization ratio of the system.

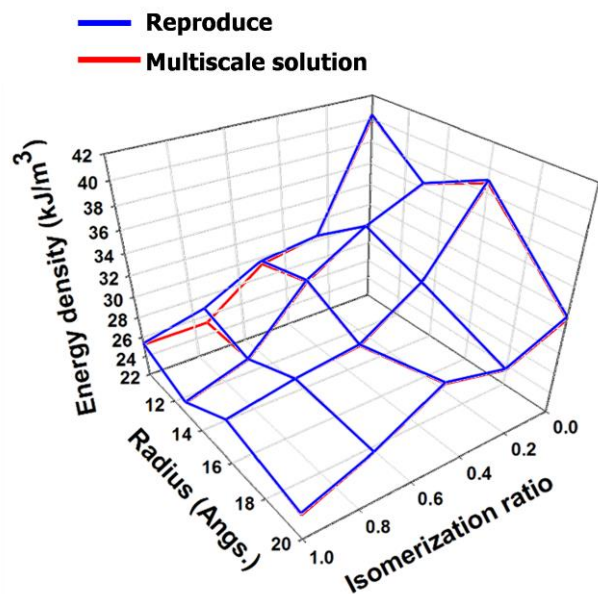


**Figure 4.11** Comparison between the predicted multiscale solution and the MD simulation model in terms of the nanoparticle radius and photo-isomerization ratio.



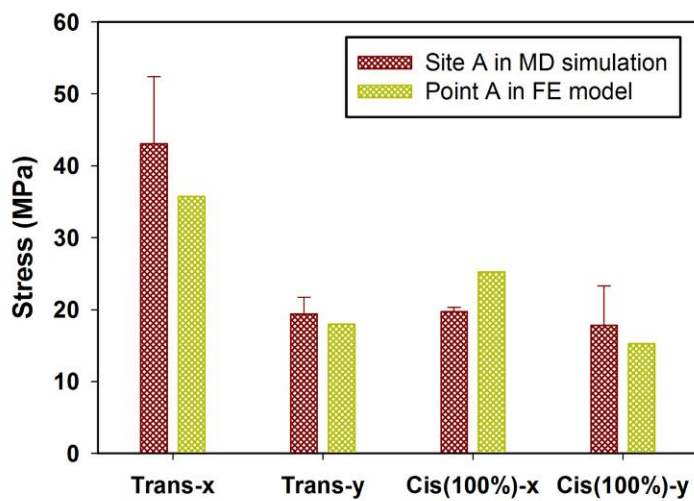
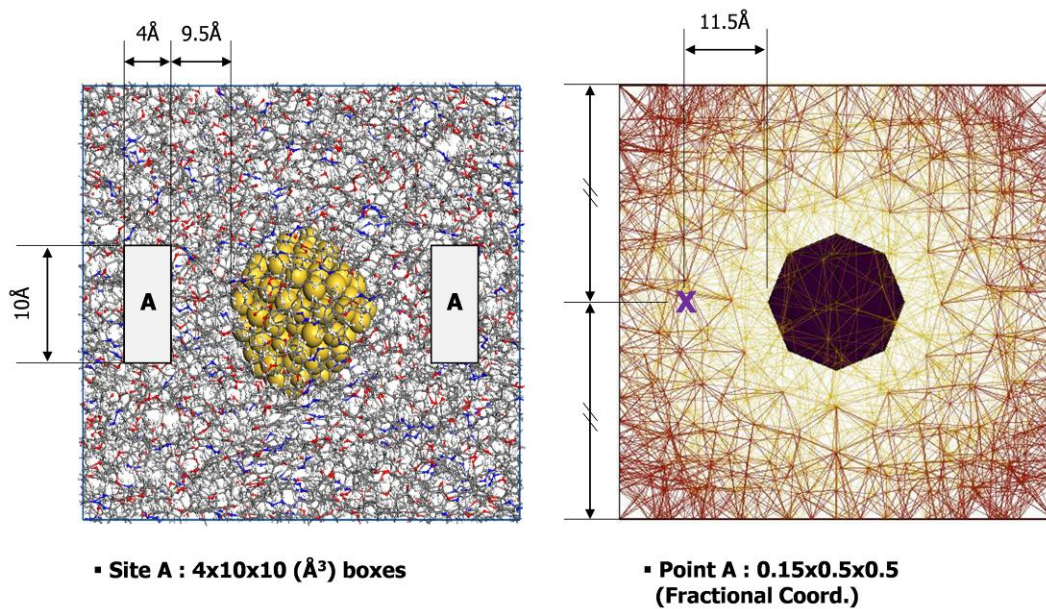


**Figure 4.12** Model validation with the comparison of the local virial stresses of the PRP nanocomposites reinforced with 16Å-gold nanoparticles obtained from the MD model with the corresponding ones predicted by the equivalent multiscale model.



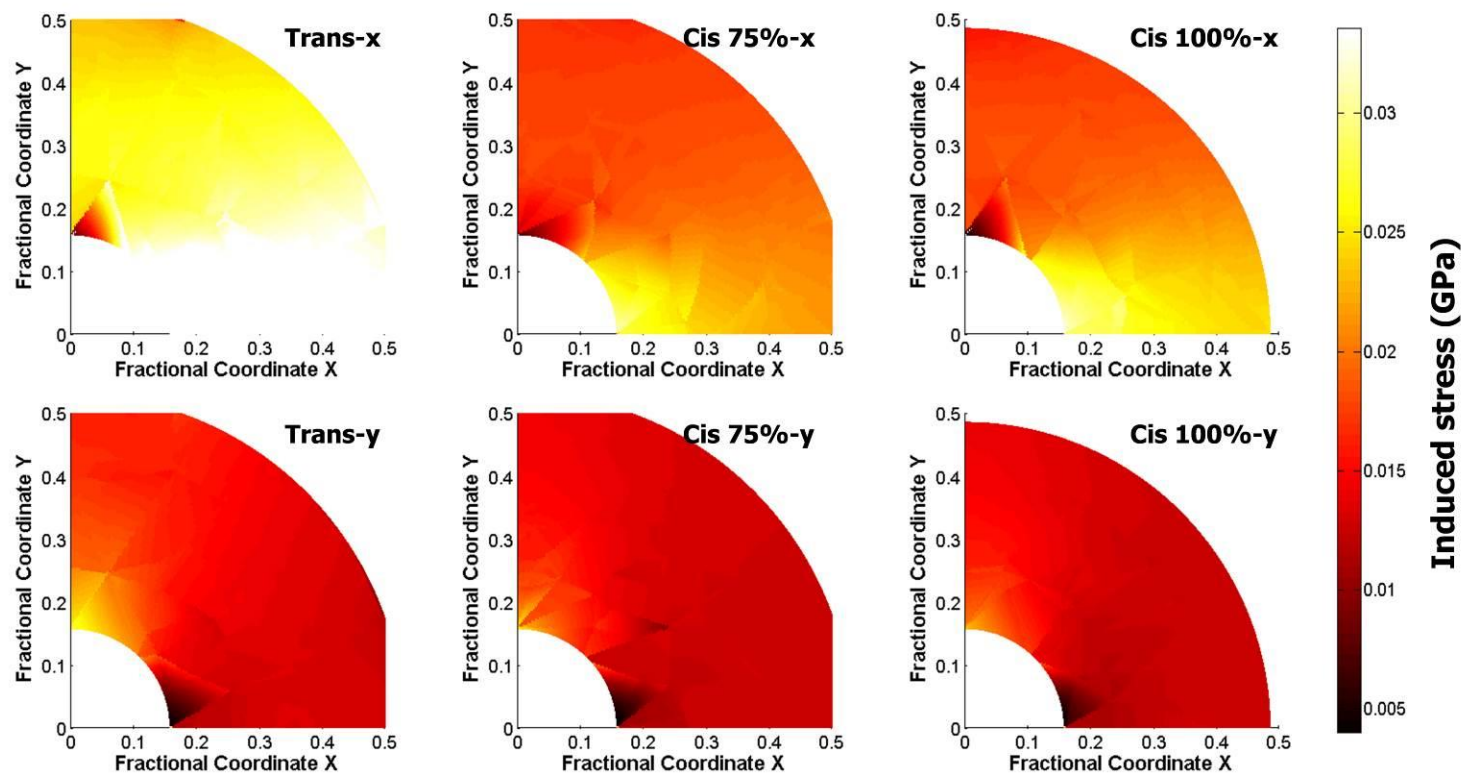


**Figure 4.13** Local stress distribution of the interphase of PRP nanocomposites reinforced with 16 Å-gold nanoparticles during the light irradiation under mechanical loading condition.

### 4.3. Chapter summary and conclusions

In **Chapter 4**, we introduced the multiscale method for the PRP nanocomposites which integrates the all-atom MD simulations with continuum mechanics. The aim of the study is to perform a continuum characterization of the photo-thermal actuation of the PRP system under stress-free condition and to determine the inherent role of interfaces between the particle and the matrix under mechanical loading. In the MD simulations, we found that the material changes from transversely isotropic to isotropic with reduced order of orientation of the matrix and with decreased thermal stretching ratio as the trans-to-cis isomerization reaction of the azobenzene progressed. On the other hand, the adsorption feature of the side polymer chains in the vicinity of the nanoparticle was maintained and hence the thermo-mechanical stability of the PRP would be enhanced, regardless of the isomerization state. Hence, it should be noted that such a multiphysics system must be fully included in the multiscale model.

Regarding the stress-free condition, we suggested continuous functional forms for the opto-mechanical behavior of the material in a wide range of temperatures including the N-I phase transition of the liquid crystals. The orientational order profiles obtained from MD simulations were fitted using the Haller's extrapolation method and the related characteristic coefficients were derived. Each coefficient depends on the conditions of the individual nanoparticle diameter and photo-isomerization ratio and thus its value could be successfully derived with simple exponential functions. By using this relationship, we

obtained the continuous data set for the order parameter as well as the shape parameter of the PRP nanocomposites.

Furthermore, to interpret the strong interfacial bonding characteristics on the nanofiller surface and the associated re-conformation of polymer networks at the interfacial region, we considered the 3-phase multi inclusion model using the FE method. We then determined the effective stiffness and the spatial range of the interphase layer of the material through the deformation energy matching process and homogenization of the phases. The present multiscale model quantitatively revealed the influence of photo-isomerization reaction on the effective mechanical behavior of the effective interphases in the PRP nanocomposites as follows.

Firstly, the interfacial region has higher stiffness than the bulk matrix region where the polymer does not interact with the nanoparticle. Secondly, the orientation feature of the mesogen molecules makes the anisotropy in the interphase region as well as the bulk matrix; hence, the interphase has exceptionally higher stiffness in the nematic direction than in the other two directions. However, similar to the neat PRP material and bulk matrix region of the PRP nanocomposites, such anisotropy is significantly reduced during the photo-isomerization reaction of the material, even though the strengthened effect of the interphase is still valid because of the remaining adsorption characteristics of the polymer chains around the nanoparticle. Accordingly, the photo-isomerization reaction causes a decrease in the effective deformation energy density as well as local stress in the interphase under mechanical loading. Thirdly, the volume fraction (or thickness) of the interphase is

influenced by both the nanoparticle size and the ratio of the photo-isomerization reaction. This finding is particularly important for the mechanical design of the polymer nanocomposites system because the quality of the estimated local stress field and the effective deformation energy in the interphase strongly rely on the thickness of the interphase. It is verified that the present multiscale model is able to obtain an equivalent continuum model which predicts the local stress field and the deformation energy quantity in the interphase with accuracy that can be obtained from the corresponding all-atom computation results. In brief, the multiscale model developed in this study can efficiently and accurately predict the photo-mechanical properties of the PRP nanocomposites system according to the important design variables, as well as the identification of inherent mechanical load transfer behavior.

We expect that the present multiscale method can be further progressed and refined in the near future if efforts are concentrated on examining the photonic and thermo-mechanical properties of the nanocomposites material. For example, regarding the photo-bending analysis of the PRP nanocomposites, the light penetration depth beneath the surface is an important factor because it affects the deformation quantity of the considered body. The gold nanoparticles partly absorb the light energy and reduce the effective intensity of the incident UV light; more specifically, the transmittance of the gold nanoparticle is significantly changed by the size of the nanoparticle [119]. Therefore, numerous experimental observations or precise *ab initio* calculation data would be required for the quantitative evaluation of the light transmittance of the PRP nanocomposites.

Regarding this topic, the population dynamics model which combines the non-linear Beer's law with the stimulated Raman adiabatic passage we formulated in previous work [120] can be adapted to trace the intensity distribution across the depth of the actuator.

Another unexplored aspect of the multiscale analysis for the PRP nanocomposites is the effective photostrain of the interphase during the isomerization reaction. In this current study, we characterized the effective thickness and mechanical properties of the interphase using numerical simulations, but an analytical micromechanics formulation for the photo-thermal strain of the interphase has not yet been developed. To evaluate the internal displacement and strain fields inside the nanocomposites during the photo-isomerization, both of the photoelastic and thermoelastic properties of the PRP nanocomposites must be fully characterized in a wide range of temperature conditions. This can be achieved by using a large set of PRP/gold nanocomposites models with very different temperature and isomerization ratio conditions in MD simulations or experiments. The analytical photostrain of the interphase can then be obtained from the scale-bridging micromechanics model first proposed by Yang and Cho [121], by expanding the formulation to include phase transition and associated 'negative' thermal expansion at the critical temperature.

Finally, although this dissertation focuses on multiscale design and analysis for the PRP and the PRP nanocomposites material, it should be emphasized that the multiscale model can be generalized for all heterogeneous systems to reveal the mechanical role of the interfacial layer in the system. Regarding this, we intensively investigated the

conventional polymer (crosslinked epoxy) reinforced with nanoparticles/nanotubes by applying the current multiscale analysis. The results of this investigation are provided in **Appendix A** and **Appendix B**.

## 5. Conclusions and recommendations

In this study, we examined the methodology of multiscale mechanical design for the multiphysics analysis of the PRP and its nanocomposites. Crosslinked macromolecular polymer models incorporating photo-sensitive molecules as well as nano-reinforcements were simulated *in silico* and in a series using all-atom MD simulations, and their micro-macro correlations were studied. This work represents the first computational attempt to predict the photo-reaction dynamics and their influence on the structural properties of the glassy PRP system. The morphology of the micro/nanostructures and the associated order parameter of the mesogen molecules during the photo-isomerization reaction were quantitatively characterized. The bulk properties were also characterized, including the thermal phase transition and the elastic stiffness. Therefore, the simulation result provided a key to the exploration of the intrinsic physics of the functional liquid crystalline polymer.

In this final chapter, we discuss important but unresolved issues in the future of multiscale mechanical design technology for multifunctional materials. The concept of the integration method of the photoactive potential of azo dyes with a classical force field in MD simulation is not only limited to the analysis of PRP structures, but also to all other materials that the bulk properties are strongly influenced by the photo-induced reaction kinetics of individual molecules. Considering this, the present MD simulation method will be applied to other unexplored areas such as the nano-lithography process, self-healing polymer (or gel), polymer curing and ageing, and protein-folding/unfolding for future investigations. With the rapid development of polymer-based nanodevices and nanotechnology applications, the importance of these all-atom level analyses is increasingly being highlighted in many engineering fields.

As a mechanical application of the PRP material, we also developed a light-driven PRP strand, as a new mechanical threading device operated by UV light. The layered film structure fabricated in this study showed that the main drawbacks of the pure PRP material (high brittleness and low toughness) can be easily overcome by this simple structural design while keeping the original advantages of the material. The potential applicability of the structure is truly unlimited because the deformation pattern and path of the strand structure can be freely designed by selecting the number of UV-light sources, the light irradiation sequence, the location, and the time. Particularly, since the opto-mechanical behavior of the PRP strand is derived from the conformational change of the microstructure at the molecular-level, the work can be further progressed toward a microscale threading system.

Meanwhile, we also examined the opto-thermal actuation behavior of PRP nanocomposites containing gold nanoparticles using MD simulations. In addition to the reinforcing effect of the nanoparticle in the PRP material, we verified the nanoparticle size effect on the opto-mechanical properties and the photostrain. The mesogen-mesogen interactions and the adsorption of the polymer networks around the nanoparticle coexisted in the modeled PRP nanocomposites system and it was verified that the photonic actuation was improved, with enhanced thermo-mechanical properties. For future development, other nanomaterials such as nanocarbon (fullerene, carbon nanotube, and graphene) can be incorporated as the filler. In fact, a number of researchers have recently focused their attention on the significant functionality of photo-responsive materials and obtained some meaningful conclusions, e.g. a multi-stimuli (heat/UV/near-infrared) responsive liquid crystalline polymer nanocomposites with multi-deformation modes [122], the design of a reconfiguration of the film with patterned white light illumination [123, 124], hydrogen-bonded carbon nanotube/polymer nanocomposites with higher mechanical strength and



stability [38], etc. Therefore, the next step in multiscale design and analysis should be to examine the quantitative effect of nanoparticles on the actuation of PRP and to reveal the intrinsic mechanism with atomic detail. Especially, this problem should be more carefully studied for the case of non-spherical nano-reinforcements, e.g. nanotubes, nanowires, nanosheets, and nanoplatelets, because their relative orientation to the mesogen molecules might also affect the opto-mechanical behavior as well as the interfacial characteristics of the nanocomposites system [125, 126].

Lastly, we developed a nano-continuum bridged multiscale method for PRP nanocomposites which characterizes the actuation performance of the bulk material as well as the local mechanical response of the microstructure. To provide the efficient design guidelines for the control of the photo-bending behavior of the PRP system under a free boundary condition, we proposed an empirical model which could be used to represent the shape parameter of the system under conditions of varying photo-isomerization reaction, temperature, and nanoparticle diameter. Particularly, because the occupied volume fraction of the interfacial layer between the nanoparticles and the polymeric matrix was significant and played a major role in the overall opto-thermo-mechanical response of the entire system, we explicitly characterized the effective thickness and the effective elastic stiffness of the interphase in the nanocomposites system using the energy method and homogenization theory.

The multiscale method developed in this study is not limited to the mechanical design of the PRP actuator system; rather, it encompasses the interfacial behavior of all heterogeneous groups including reinforcement for polymeric composites, phase adhesion/separation in polymer blends, and the micro-/nano-encapsulated organic phase, etc. Accordingly, for development in the near future, various suggestions have been made

to examine the interfacial morphologies and the corresponding properties of the nanocomposites by surface treatment of the filler particles [43,127], the agglomeration or cluster behavior of the interphase [128,129], and the self-diffusion behavior of the polymer in a viscoelastic media influenced by its crosslinking density [113,130]. Also, the proposed multiscale concept will be extended further for other physical properties of the effective interphase such as yield strength and hardening rate under large deformation, thermoelastic properties in a wide range of temperatures including phase transition region and thermal conductivity.

# **Appendix A. Multiscale analysis for the effective thickness and mechanical properties of interphase in polymer nanocomposites**

## **A.1. Overview**

So far, it was not clear how to identify the mechanical behavior of the interphase layer in nanocomposites structure quantitatively, because the properties highly depend on the assumptions for the interphase geometry condition. In the **Appendix A**, a multiscale model which integrates molecular dynamics (MD) simulation and finite element (FE) analysis has been developed to design nanofiller-reinforced epoxy nanocomposites and their effective interphase. Both the global stiffness of the polymer nanocomposite model and the internal stress distribution on the nanofiller surface during mechanical loadings were quantitatively characterized. Through MD simulations, crosslinked epoxy resin (crosslinking ratio: 0.45) and nano-sized filler (spherical SiC and zig-zag single walled carbon nanotube) embedded epoxy nanocomposite models were prepared with full atomistic detail. For each model, uniaxial tensile tests were carried out to obtain the elastic behavior of the nanocomposites and the strain energy distribution in the vicinity of a nanofiller surface. Meanwhile, a three-dimensional FE model of a three-phase was prepared, consisting of a nanofiller, polymer networks adsorbed on the nanofiller surface (interphase), and polymer networks non-adsorbed on the nanofiller surface (bulk matrix).

The unknown mechanical response and thickness of the interphase were numerically characterized through homogenization and deformation energy matching to that of the full atomic molecular model, respectively. The present multiscale method, therefore, yields an effective region of the interphase as well as its mechanical properties. The suggested multiscale model accurately predicts virial local stresses at both the interphase and bulk matrix regions of the full-atomic model and explains the reinforcing mechanism at the interphase region.

The current model has its own advantage in that the local load transfer characteristics between the inhomogeneities can be designed in accordance with the atomic view. Various kinds of other design parameters which are closely related with the interphase such as a resin crosslinking density, a polymer-particle grafting ratio, and an aggregation phenomenon of nanoparticles can also be characterized by the present methodology with the understanding of their intrinsic nanophysics.

## **A.2. Revealing strengthened interphase formed in crosslinked epoxy/SiC nanocomposites**

### **A.2.1. Modeling of crosslinked nanocomposites system in MD**

**Figure A.1** shows the molecular models of an epoxy resin (EPON 862<sup>®</sup>) compound and a hardener (TETA<sup>®</sup>) compound for curing the resin considered as a host

polymer in this study. The idealized uncrosslinked polymer unit cell that contains the resin and hardener molecules is initially constructed in an amorphous state with periodic boundary conditions. The ratio of resin to hardener in the modeled unit cell is 3:1 in order to provide a satisfactory number of chemical reactive sites for the two molecules available for crosslinking (four nitrogen atoms in the single hardener molecule can be reacted with up to six carbon atoms of the epoxide rings). Modeling the complex atomic structures and energy relaxation processes of the present atomic models is carried out using the commercial MD simulation package, Materials Studio 5.5 (Accelrys® Inc.). Both the bonding and non-bonding interactions between the adjacent atoms are represented by the polymer-consistent force field (PCFF) potential [67].

The uncrosslinked state model minimizes its total potential energy by using a conjugated gradient method with an energy deviation convergence cutoff of 0.1 kcal/mol·Å, followed by an NVT (isothermal) ensemble simulation at 300K for 500 ps and NPT (isothermal-isobaric) ensemble simulation at 300K and 1 atm for 2 ns. For the efficient calculation of the electrostatic potential energy, the distance-dependent dielectric method with a constant of 1.6 is applied in order ensure that the values of the mechanical response of the current model are similar to those in the literature [44]. For simulation of the crosslinking reaction, all the interatomic distances between the reactive sites of the resin and the hardener molecules in a given unit cell are calculated. If the distance between the reactive sites is within the designated cutoff, a new covalent bond is artificially created between the sites, as shown in **Figure A.2**. The reaction cutoff distance starts at the value

of 1 Å, and gradually increases with the step size increment of 0.5 Å until the final crosslinking ratio reaches 45%. The maximum distance cutoff for a crosslinking ratio of 45% does not exceed 6.5 Å for the considered model, which has a similar value to the chemical reaction distance [44,50,101]. The atomic structure is repeatedly minimized using a conjugated gradient method with refreshed potential energy components, while the reaction cutoff distance is iteratively updated. After the crosslinking procedure is completed, final equilibration runs are executed in an NVT ensemble simulation at 300K for 2 ns, followed by an NPT ensemble at 300K and 1 atm for 3 ns.

The modeling procedure of the polymer nanocomposites (crosslinked epoxy/SiC) is the same as that of a pure crosslinked epoxy system, except that an untreated spherical SiC nanoparticle is inserted in the unit cell with the uncrosslinked resin and hardener. In this study, a total of five different nanocomposite unit cells which have SiC nanoparticles of differing sizes are inserted, while the volume fraction of the particles is fixed at 5.95%, irrespective of the size of the particles, in order to revisit the nanoparticle reinforcing effect on the stress distribution in the polymer networks. An example of the fully equilibrated model of a crosslinked epoxy/SiC unit cell is depicted in **Figure A.3**.

**Table A.1** lists the six simulation systems and their detailed compositions examined in this work. The volume fraction of the nanoparticles of each atomic model underwent slight alteration during the NPT ensemble, while the target condition remained constant. These changes mainly involve an interfacial non-bonding space between the nanoparticle surface and the internal wall of the polymer chains. The percentage of the

interfacial space should be increased as the model size decreases because in all the considered models, the thickness of the vacuum-layer is retained, regardless of the particle radius. Thus, the difference of the nanoparticle volume fraction (around 0.5 percent) was neglected in the current multiscale model, assuming that the composition changes are indwelling in the nanostructured material.

It is worth noting that many other methods can be used for the modeling of the crosslink distribution in epoxy resin in the MD simulation, such as representative network element generation [44,101] and real-time observation of the chemical reaction in a dynamic ensemble [68]. None of these models are perfect, each having its own merits and demerits and being limited only to the targeted properties under specific conditions. Nevertheless, it is generally known that these methods are all well correlated to the experimental methods on the thermal and mechanical behavior of the crosslinked epoxy.

### **A.2.2. Global elastic response of the nanocomposites**

The equilibrated models were then relaxed at extremely low temperatures (10K) and at 1 atm for 2 ns within the NPT ensemble. Energy minimization was performed to remove the effect of temperature on the kinetic energy of the molecules in the unit cell. The elastic mechanical response and the load transfer efficiency of the pure polymer and polymer nanocomposite models are estimated along the x, y, and z directions through uniaxial tensile loading simulations. The tensile simulations for the cases considered were

carried out using the open source code, LAMMPS. The lattice length of the unit cell is elongated during the NVT ensemble run at 0.1K with the true strain rate of  $10^{-6}/\text{ps}$ . In this work, we only focus on the linear elastic behavior of the models considered, so the total strain does not exceed 0.3% in the simulation.

According to the tensile tests, stresses for each atom in both the axial and transverse directions can be obtained. From an atomic viewpoint, the potential energy increase can be explained with an atomic stress tensor  $\boldsymbol{\sigma}$  based on the virial theorem defined in Eq. (A.1) [97],

$$\boldsymbol{\sigma} = \frac{1}{V} \left( - \sum_i^N m_i (\mathbf{v}_i \mathbf{v}_i^T) + \frac{1}{2} \sum_i^N \sum_{j \neq i}^N \mathbf{r}_{ij} \mathbf{F}_{ij} \right) \quad (\text{A.1})$$

where  $V$  is the atomic volume,  $N$  is the total number of atoms,  $\mathbf{v}_i$  and  $m_i$  are the thermal excitation velocity and the mass of atom  $i$ , respectively,  $\mathbf{r}_{ij}$  is the relative position between atoms  $i$  and  $j$ , and  $\mathbf{F}_{ij}$  is the atomic force on atom  $i$  due to atom  $j$ . Because the kinetic part in Eq. (A.1) can be excluded near 0K, only the potential part of  $\boldsymbol{\sigma}$  is involved in the deformation energy of the considered model, and it directly indicates the equivalent continuum (Cauchy) stress [98]. Therefore, the atomic stress tensor for a polymer and polymer nanocomposite structure can be computed from a summation of the interatomic pair, bond, angle, and dihedral angle potentials between the atoms in the system, as shown in Eq. (A.2) [97]:

$$\sigma_{ij}^V = -\frac{1}{V} \left[ \frac{1}{2} \sum_{n=1}^{Pair} (r_{1i} F_{1j} + r_{2i} F_{2j}) + \frac{1}{2} \sum_{n=1}^{Bond} (r_{1i} F_{1j} + r_{2i} F_{2j}) + \right. \\ \left. \frac{1}{3} \sum_{n=1}^{Angle} (r_{1i} F_{1j} + r_{2i} F_{2j} + r_{3i} F_{3j}) + \frac{1}{4} \sum_{n=1}^{Dihedral} (r_{1i} F_{1j} + r_{2i} F_{2j} + r_{3i} F_{3j} + r_{4i} F_{4j}) \right] \quad (\text{A.2})$$



where the subscript number indicates an arbitrary label of the atom included in the interaction cutoff distance (9.5 Å), and  $V$  is the designated atomic volume of a local group of the model considered. The assignment of the effective  $V$  raises an important issue regarding the molecular and atomic analysis of nano-sized structures such as nanorod/nanowire arrays or nanofilms, because the effective atomic volume at the surface domain might be significantly changed by surface relaxation and reconstruction. However, for a nanocomposite with low volume fraction (<10%), it is clear that the effective atomic volume in any region in the lattice unit is nearly the same as the geometrical volume of the initially designated region when a periodic boundary condition and tightly packed morphology of the model are considered.

To derive the Young's and shear moduli of the models, the virial stress for all constituent atoms in the unit cell is calculated. During tensile simulation, a total of nine averaged stress components can be obtained, each of which are averaged in the axial and transversal directions to remove the morphological uncertainties in atomic models, as shown in Eq. (A.3):

$$\sigma_{ij}^{global} = \left[ \begin{array}{ccc} \sigma_{xx} & \sigma_{xy} & \sigma_{xz} \\ \sigma_{yx} & \sigma_{yy} & \sigma_{yz} \\ \sigma_{zx} & \sigma_{zy} & \sigma_{zz} \end{array} \right]_{global} \cong \left[ \begin{array}{ccc} \hat{\sigma}_1 & \hat{\sigma}_2 & \hat{\sigma}_2 \\ \hat{\sigma}_2 & \hat{\sigma}_1 & \hat{\sigma}_2 \\ \hat{\sigma}_2 & \hat{\sigma}_2 & \hat{\sigma}_1 \end{array} \right]_{global} \quad (A.3)$$

where

$$\hat{\sigma}_1 = \frac{1}{3}(\sigma_{xx} + \sigma_{yy} + \sigma_{zz}), \quad \hat{\sigma}_2 = \frac{1}{6}(\sigma_{xy} + \sigma_{xz} + \sigma_{yx} + \sigma_{yz} + \sigma_{zx} + \sigma_{zy}). \quad (A.4)$$

Under linear elastic deformation, the material obeys Hooke's law:

$$\hat{\sigma}_i = C_{ij} \varepsilon_j \quad (i, j = 1, 2, 3) \quad (\text{A.5})$$

where  $C_{ij}$  is the simple three-dimensional stiffness tensor and  $\varepsilon_j$  is the normal strain.

The Young's modulus  $E$  and shear modulus  $G$  can then be derived as [131]:

$$E = \frac{(C_{11} - C_{12})(C_{11} + 2C_{12})}{C_{11} + C_{12}}, \quad G = \frac{C_{11} - C_{12}}{2}. \quad (\text{A.6})$$

The results of the tensile loading of the nanocomposite model are depicted in **Figure A.4**. The model exhibits fully linear elastic behavior along all three axes of the 0.3% strain. **Table A.2** shows the global elastic properties of the models. The reinforcing effect of the nanoparticle in the polymer nanocomposites is clearly observed throughout all the considered cases. Both the Young's and shear moduli of the nanocomposite systems are significantly higher than those of a pure epoxy system, while keeping their Poisson's ratios of about 0.37, which is within the common range of the Poisson's ratio of 0.3-0.4 of conventional polymers. In particular, a nanoparticle size dependency on the elastic properties of the nanocomposites has also been well verified; the Young's and shear moduli are significantly increased as the radius of the reinforcement is decreased. The current nano-size effect on the mechanical properties is supported by previous studies [44,45].

We assume that the proposed method has material structure parameters of the polymer nanocomposites, such as crosslinking ratio, nanoparticle radius, and uniform dispersion of the nanoparticle. Thus, a direct comparison or validation of the results with those of experiments is not possible; rather, the current results can be a quantitative guideline for the design or manufacture of polymer nanocomposites.

### A.2.3. Local stress distribution under tensile loading

The effective strain energy density for local regions in the unit cell can be computed when the atomic stress of individual atoms in the unit cell are partly grouped and summed. By dividing the total strain energy in the unit cell into multiple phases with their effective volumes, the local deformation energy density of the unit cell is obtained during the tensile simulation. To obtain the local load transfer characteristics at the nanoparticle/matrix interface, arbitrary local groups which have a spherical shell shape with 1-Å thickness and are concentric with the inserted nanoparticle are considered, as described in **Figure A.5**. In terms of the group, one can consider a total of three different types of local energy, as follows.

(a) *The total sphere group* includes all atoms in a designated cutoff radial distance. The effective volume of the group is the same as the volume of the sphere. Atomic stresses from the exterior of the spherical group are subtracted. The energy density of the total sphere group ( $W_T$ ) can be computed as:

$$W_T = \frac{U_{par+1+2+3} - U_3}{(4/3)\pi(R_l + d)^3} \quad (A.7)$$

where  $U$  is the change of potential energy due to the strain,  $R$  is the radial distance from the nanoparticle surface,  $d$  is the shell thickness constant (1-Å), and subscripts ‘par’, ‘1’, ‘2’, and ‘3’ are the separated local regions denoted in **Figure A.5**.

(b) *The particle-excluded hollow-sphere group* excludes the energetic contribution of

the nanoparticle and the non-bonding interaction between the nanoparticle surface and the vicinity of the polymer chain from the total sphere group. The energy density of the group ( $W_H$ ) can be calculated as:

$$W_H = \frac{U_{par+1+2+3} - U_{par} - U_3}{(4/3)\pi \left\{ (R_1 + d)^3 - R_{par}^3 \right\}} . \quad (A.8)$$

$W_H$  expresses the isolated load transfer capacity on the adsorbed matrix within the given radial distance from the particle surface; the resulting profiles are therefore used for the energy matching procedure of the current multiscale method, which is explained in the next section.

(c) *The spherical shell with 1-Å thickness group* is a shell-shaped subdivision of group (b) that has a constant thickness (1-Å) and is concentric with the nanoparticle. According to the local energy density distribution of this group with respect to the radial distance from the particle surface, the energetic adsorption characteristics of the crosslinked epoxy to the SiC nanoparticle can be observed in the profile. The energy density of the local shell group ( $W_S$ ) can be calculated from Eq. (A.9):

$$W_S = \frac{U_{par+1+2+3} - U_{par} - U_1 - U_3}{(4/3)\pi \left\{ (R_1 + d)^3 - R_1^3 \right\}} . \quad (A.9)$$

The local stress distribution in the nanocomposite and pure epoxy system at the atomic level is depicted in **Figure A.6**. While the local stress distribution in the pure epoxy is almost uniform regardless of the local energy group that in the nanocomposites shows clear variations along the radial direction from the particle core. According to the local stress-strain profile of the modeled nanocomposites, the strain energy density profile of the

‘local shell group’ can be calculated, and the results are shown in **Figure A.7**. It has a clear peak around the nanoparticle surface and quickly converges to a specific value. The ‘total sphere group’ and the ‘particle-excluded hollow-sphere group’ can be derived in a similar manner, and the results are also depicted in **Figure A.7**.

An interesting feature of the result is that the energy density of the ‘particle-excluded hollow-sphere group’ retains its profile regardless of the nanoparticle size, as shown in **Figure A.8 (a)**. The consistency of the energy density profile in the matrix around the spherical dispersed phase signifies that the internal stress field distribution of the polymer matrix in the nanocomposites is not affected by the size of the nanoparticle. Accordingly, the effect of nanoparticle size on mechanical properties is not only caused by the conformation difference of the adsorbed region of the polymer, but by the change of the non-bonding interaction energy feature between the nanoparticle and the adsorbed polymer. **Figure A.8 (b)** describes the strain energy density profiles of the effective interphase under various thickness conditions. Unlike the atomic results, the effective strain energy density of the interphase layer in a three-phase continuum model shows a clear particle size dependency among the models, because the interphase layer in the FE model is perfectly bonded to the adjacent nanoparticle layer, and the non-bonding interaction energy between them is implicitly considered.

#### **A.2.4. Derivation of the equivalent interphase using multiscale model**

For continuum analysis, although both a micromechanics-based analytical methodology and a numerical calculation using the three-dimensional FE model are applicable to the characterization of the effective interphase [43], we introduce the described numerical calculation method to achieve general and intuitive analysis of the effective deformation on the interphase. The model consists of three phases (the particle, the interphase layer, and the matrix), which are represented as concentric spheres meshed with a 10-node tetrahedral element.

The multiscale model used in this study is same with the one introduced in **Chapter 4**, so in the appendix we only provide the whole multiscale flowchart in **Figure A.9**. In MD simulation, the overall mechanical properties of the polymer nanocomposites were obtained according to the nanoparticle radius by adapting uniaxial tensile tests. During the static loading, the atomic potential density increment curve (  $W_H$  ) of the adsorbed polymer layer was obtained in terms of the distance from the nanoparticle surface. Meanwhile, the elastic stiffness of the overall nanocomposite models was transferred as an input of the multi-inclusion model in FE analysis. The mechanical properties of the SiC nanoparticle (Young's modulus: 451.6 GPa and shear modulus: 182.5 GPa) and bulk epoxy (Young's modulus: 3.65 GPa and shear modulus: 1.33 GPa – obtained by current MD simulation) were used in the particle and matrix phases of the FE model, respectively.

As shown in **Figure A.10**, the effective thickness of the interphase which predicts both the global elastic behavior and the local load transfer efficiency on the adsorbed

polymer layer of the nanocomposites can be derived by comparing the energy density curves of the interphase with those of the '*particle-excluded hollow-sphere group*' in the MD simulation. The mechanical properties, interphase thickness, and volume fraction of the equivalent FE models demonstrated in the condition of the energy density balance and homogenization are shown in **Table A.3**, which indicates that the effective elastic stiffness of the interphase is higher than that of the pure epoxy due to the morphological change and densification of the polymer microstructure.

A noticeable aspect of **Table A.3** is the relation between the predicted thickness of the interphase and the inserted particle radius. The increase of the thickness occurs gradually until 9 Å, but it does not increase any further with particle size larger than 10 Å. **Figure A.11** shows a geometric view of the number of non-bond pairs between single polymer constituent atoms laid on a particle surface. The particle constituent atoms within the employed cutoff radius are indicated. The non-bond pair number is inversely proportional to the particle curvature, which means that the effective distance from the particle surface to the outer boundary of the adsorbed polymer layer should be decreased as the particle curvature is increased to achieve an equilibrium state in the system.

A number of studies [2-4,9,12-22] have reported methods of characterizing the effective thickness of the interphase layer for the mechanical analysis of polymer nanocomposites, as listed in **Table A.4**. As is shown in **Table A.4**, the range of thicknesses of the interphase layer obtained from the current work is 4.5–9.1 Å, which is close to the value of the interphase thickness suggested by the references via MD simulations.

Another key aspect is that even though the volume fraction of the interphase is identified using the energy method, a particle size dependency on the interphase modulus remains. The obtained interphase moduli have a deviation according to the particle size due to the small number of the polymer constituent atoms around the particle and their conformational uncertainty. However, the modulus not only fluctuates around a constant value, but also decreases as the particle size is increased. The relationship between the particle size and the interphase modulus could be due to the structuring influence on the polymer according to the nanoparticle curvature. For small nanoparticles, the surface curvature is extremely high and each atom at the particle surface has a broad non-bond interaction region with polymer constituent molecules. As the particle size is increased, however, the surface of the particle becomes flatter and the adsorbed polymer chains have less space to interact with the particle surface. Therefore, the adsorbed polymer layer around the small nanoparticles achieves higher structural stability than that around the larger nanoparticles, resulting in an improvement of the mechanical properties of the interphase. This particle curvature effect on the structural stability of the polymer matrix had been discussed earlier in [43,100].

However, the curvature effect appears only with an extremely small particle radius and is rapidly diminished after the particle radius becomes larger than 10 nm, although the system still has nano-reinforcement features. From this result, it is expected that the effective volume fraction of the interphase region with a saturated layer thickness would be a dominant design factor for polymer nanocomposites in a real environment. In other



words, one can apply the saturated interphase thickness and its mechanical properties under a given volume fraction according to the particle radius for the design of polymer nanocomposites in manufacturing.

Even though the difference of thickness does not seem to be an important factor, it crucially affects the local energy density of the composite material, especially for the adsorbed polymer phase. We constrainedly applied the interphase thickness to the FE model as the methods suggested by [44,50], to compare the effective strain energy density at the interphase with that obtained from the current model. The deformation energy density of a hollow-sphere group which has the same thickness as that of the interphase layer determined by the current method was calculated and arranged in **Table A.5**. The current multiscale model clearly follows the local energy density of full-atomic models. On the other hand, the local energy density provided by the other two methods cannot agree with that of the full atomic model, but overestimates the deformation energy at the adsorbed polymer phase. A geometrically determined interphase region such as that given in the radial density distribution or inter-atomic distance between filler and matrix does not correctly represent the reinforcing effect between the adsorbed and non-adsorbed polymer matrices; rather, it stores most of the deformation energy of the overall composites structure unrealistically. Therefore, the stress transfer characteristics of the nanocomposite unit cell can be reflected in the FE model only if the volume fraction of the interphase region is determined by the current multiscale method.

For the validation of the current multiscale model, we directly compare the local stress

distribution of the equivalent continuum model with that of the atomic model, both at the adsorbed polymer region (the interphase layer) and the non-adsorbed polymer region (the host matrix phase), as shown in **Figure A.12**. The local stress in the adsorbed polymer region in the MD model is higher than two times that of the non-adsorbed polymer region, and the equivalent continuum model clearly follows these atomic results.

**Table A.1.** Chemical composition of crosslinked epoxy and crosslinked epoxy/SiC nanocomposites in MD simulation. The effective particle volume fractions and the unit cell densities after equilibration with isothermal-isobaric (NPT) ensemble are also described.

System	SiC nanoparticle radius (Å)	No. of EPON862® resin molecule	No. of TETA® hardener molecule	No. of crosslinking (ratio)	Cubic cell length (Å)	Target volume fraction (%)	Equilibrated volume fraction (%)	Equilibrated density (g/cm <sup>3</sup> )
Epoxy	-	90	30	81 (0.45)	36.21	-	-	1.14
Epoxy+5.18Å SiC	5.18	18	6	17 (0.47)	21.79		5.63	1.20
Epoxy+7.80Å SiC	7.80	60	20	56 (0.47)	32.57		5.75	1.23
Epoxy+9.00Å SiC	9.00	90	30	81 (0.45)	37.07	5.95	5.99	1.26
Epoxy+10.0Å SiC	10.00	126	42	113 (0.45)	41.39		5.91	1.26
Epoxy+11.5Å SiC	11.50	189	63	170 (0.45)	47.27		6.03	1.27

**Table A.2.** The elastic mechanical properties of the molecular models

System	E (GPa)	G (GPa)	Poisson's ratio
Epoxy	3.65	1.33	0.37
Epoxy+5.18Å SiC	5.61	2.06	0.36
Epoxy+7.80Å SiC	5.38	1.99	0.35
Epoxy+9.00Å SiC	5.24	1.90	0.38
Epoxy+10.0Å SiC	5.07	1.83	0.38
Epoxy+11.5Å SiC	5.09	1.84	0.38

**Table A.3.** The effective Young's moduli and volume fractions for the equivalent interphase

System	$E_{\text{int}}$ (GPa)	$G_{\text{int}}$ (GPa)	$Vof_{\text{int}}$ (%)	$t_{\text{int}}$ (Å)	$E^{FEA}$ (GPa)	$G^{FEA}$ (GPa)
Epoxy+5.18Å SiC	8.68	3.22	30.85	4.48	5.61	2.06
Epoxy+7.80Å SiC	9.85	3.64	25.46	5.90	5.38	1.99
Epoxy+9.00Å SiC	7.29	2.64	29.80	7.33	5.24	1.90
Epoxy+10.0Å SiC	5.81	2.10	35.12	9.08	5.07	1.83
Epoxy+11.5Å SiC	7.11	2.59	26.99	8.77	5.09	1.84

**Table A.4.** Comparison the interphase thickness result with related references

Approach	Researchers	Composition	Filler loading (%)	Chemical Treatment	Methodology & Technique	Interphase thickness (Å)
Multiscale	Choi et al.	Epoxy/SiC	5.95 vol%	X	Current study	4.5 - 9.1
MD	Yu et al. [44]	Epoxy/Al <sub>2</sub> O <sub>3</sub>	5.5 vol%	X	Matrix adsorption layer with the constant outer thickness	6.8
MD	Yang and Cho [45]	SiO <sub>2</sub> /PI	3.0 vol%	X	Same above	6.9 - 7.1
MD	Tsai and Tzeng [50]	SiO <sub>2</sub> /PI	3.4-6.1 vol%	X	Inter-atomic distance between the filler and matrix	3.2 - 4.1
MD with Exp.	Hadden et al. [101]	Epoxy/graphite	5.8 vol%	X	Matrix density distribution (MD) and TEM (Exp.)	~10
Exp.	Jang et al. [49]	SiO <sub>2</sub> /Epoxy	0.6 vol%	X	FEM inverse problem	187.5 - 525.2
Exp.	Bhuiyan et al. [53,54]	CNT/PP	0.1wt%	X	AFM phase image	200 - 300
Exp.	Mortezaei et al. [51]	SiO <sub>2</sub> /PS	0.5-5.0 vol%	X	Thermodynamic work of adhesion	55
Exp.	Mortezaei et al. [51]	SiO <sub>2</sub> PS	0.5-5.0 vol%	O	Same above	44
Exp.	Fragiadakis et al. [52]	PDMS/SiO <sub>2</sub>	9.7-23.5 wt%	O	Differential scanning calorimetry	21 - 24
Exp.	Arrighi et al. [132]	SBR/SiO <sub>2</sub>	20-50 wt%	X	Dynamic mechanical analysis	16 - 21

**Table A.5.** Comparison of the strain energy density at the interphase layer with that of full atomic model

System	$t_{\text{int}}$ (Å)	Energy density of multiscale model (kJ/m <sup>3</sup> )	Energy density of full atomic model (kJ/m <sup>3</sup> )	Inter-atomic distance between filler and matrix [50]		Radial density distribution [44]	
				$t_{\text{int}}$ (Å)	Energy density (kJ/m <sup>3</sup> )	$t_{\text{int}}$ (Å)	Energy density (kJ/m <sup>3</sup> )
Epoxy + 5.18 Å SiC	4.48	42.37	42.79	3.03	268.89	7.67	109.38
Epoxy + 7.80 Å SiC	5.90	38.71	38.12	3.03	373.05	8.25	78.12
Epoxy + 9.00 Å SiC	7.33	40.83	40.10	2.82	3703.29	7.85	47.61
Epoxy + 10.0 Å SiC	9.08	41.92	43.20	2.72	3252.59	7.85	47.27
Epoxy + 11.5 Å SiC	8.77	40.11	39.94	2.56	4673.78	7.45	47.53

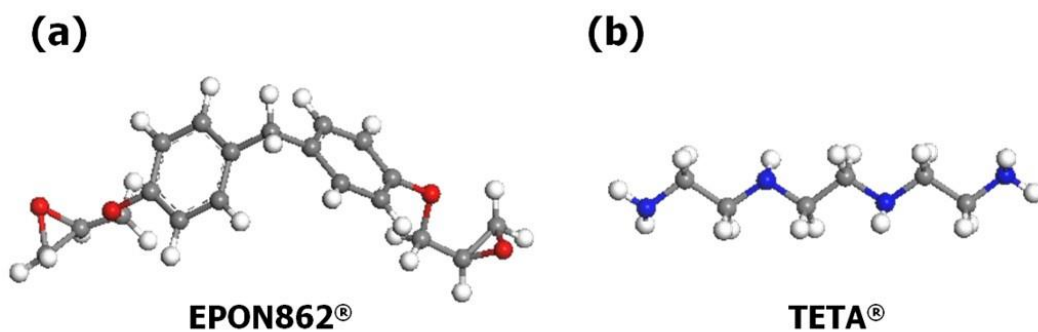


**Figure A.1.** Molecular structure images of (a) an epoxy resin (EPON 862<sup>®</sup>) and (b) a crosslinker (TETA<sup>®</sup>)

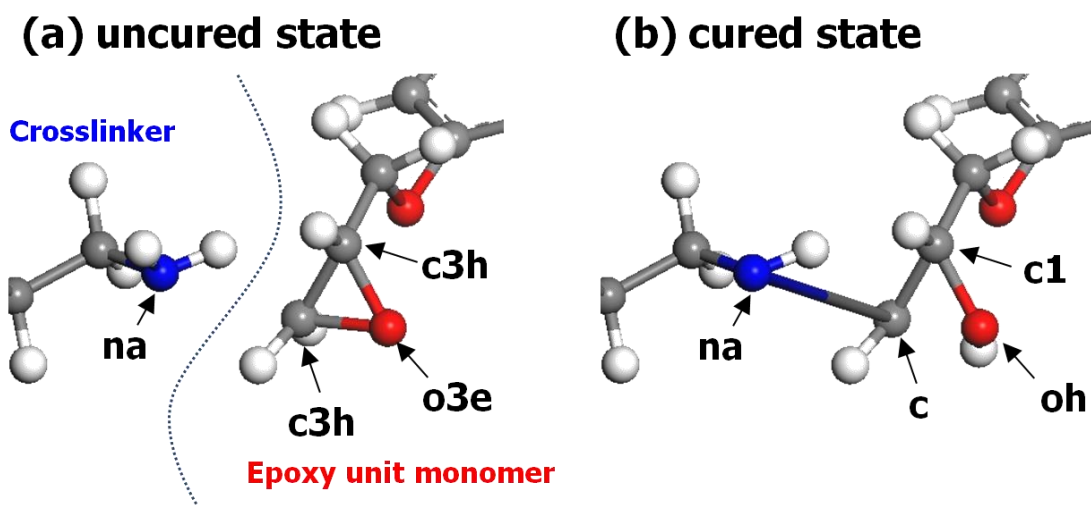


**Figure A.2.** Snapshots of the (a) uncured and (b) cured state of epoxy resin. Force field types change during the crosslinking reaction is also stated. When the epoxide triangular ring-opening occurs, a new covalent bonding is formed with a nitrogen atom in the hardener molecule within the cutoff distance.

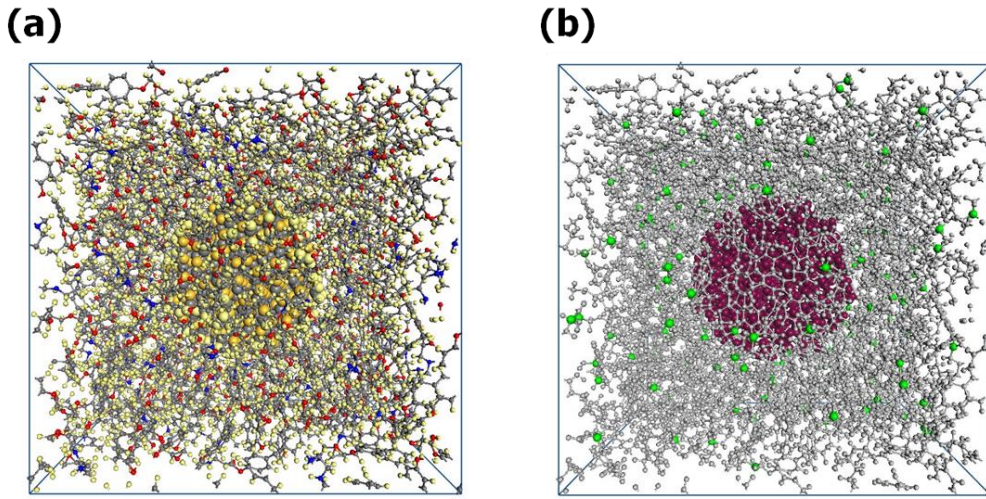


**Figure A.3.** (a) Crosslinked epoxy/SiC nanocomposites unit cell model and (b) highlighted view of nanoparticle and crosslinked points

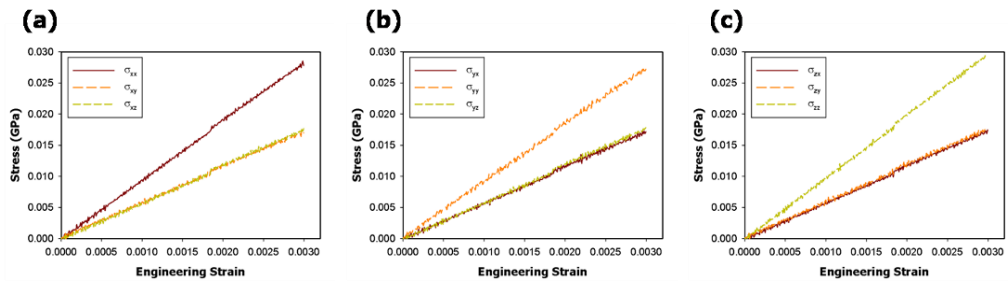


**Figure A.4.** Linear elastic behaviors of the nanocomposites ( $r_p = 10.00 \text{ \AA}$ ) along the three axes



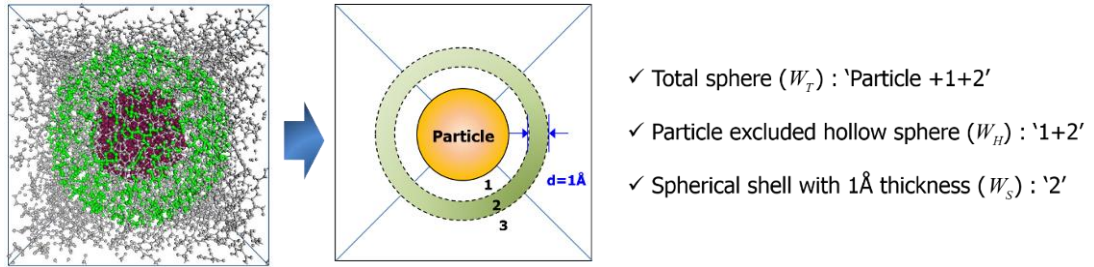


**Figure A.5.** Arbitrarily defined local group for the observation of effective deformation energy on interphase layer. The distance between the particle surface and the inner boundary of the spherical surface is varied while maintaining the thickness of the local group.

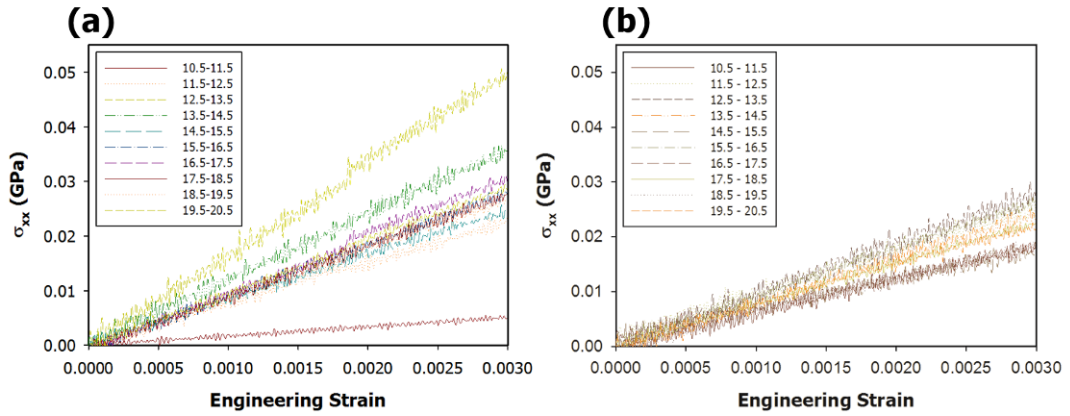


**Figure A.6.** Elastic behavior of the locally isolated polymer matrix domain for (a) nanocomposites ( $r_p = 10.00 \text{ \AA}$ ) and (b) pure epoxy systems with respect to the same spherical shell energy group. The legend describes the inner and outer distances of the energy group from the center of the unit cell.

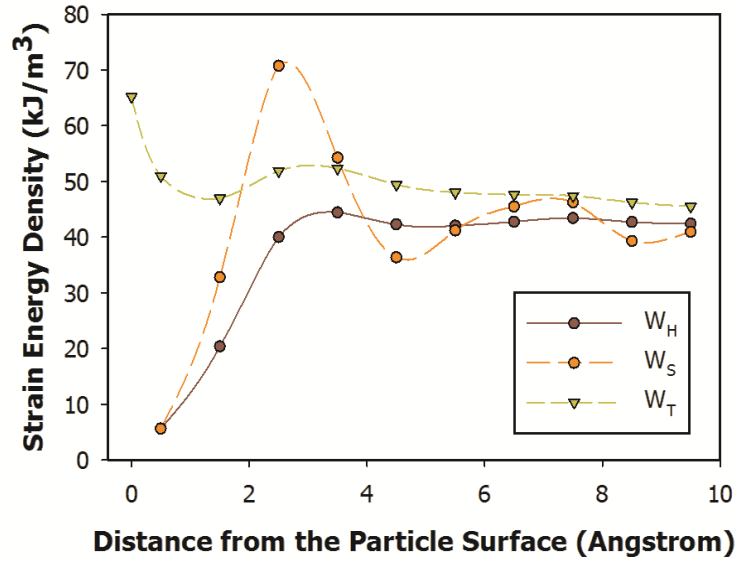


**Figure A.7.** Local strain energy density distribution of the nanocomposites ( $r_p = 10.00 \text{ Å}$ ) regarding the kinds of energy groups.

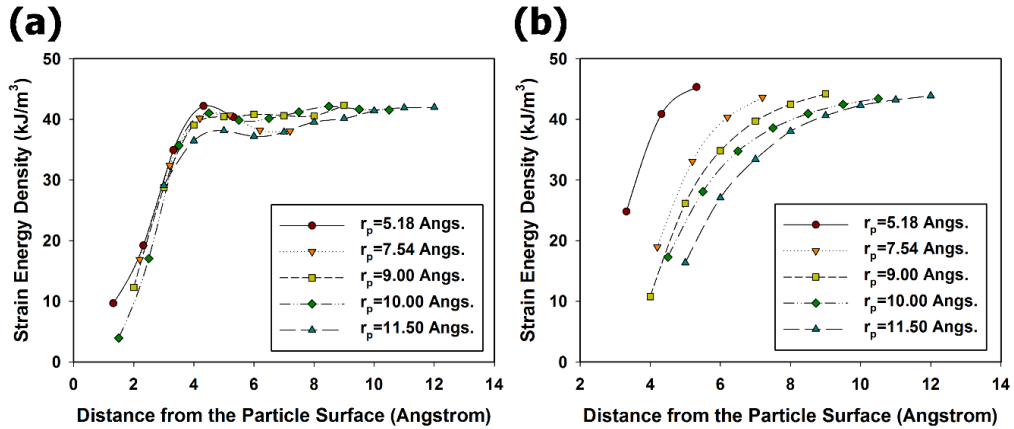


**Figure A.8.** Strain energy density profile of (a) 'particle-excluded hollow-sphere group' and for (b) the interphase in continuum basis obtained by homogenization process under various thickness conditions

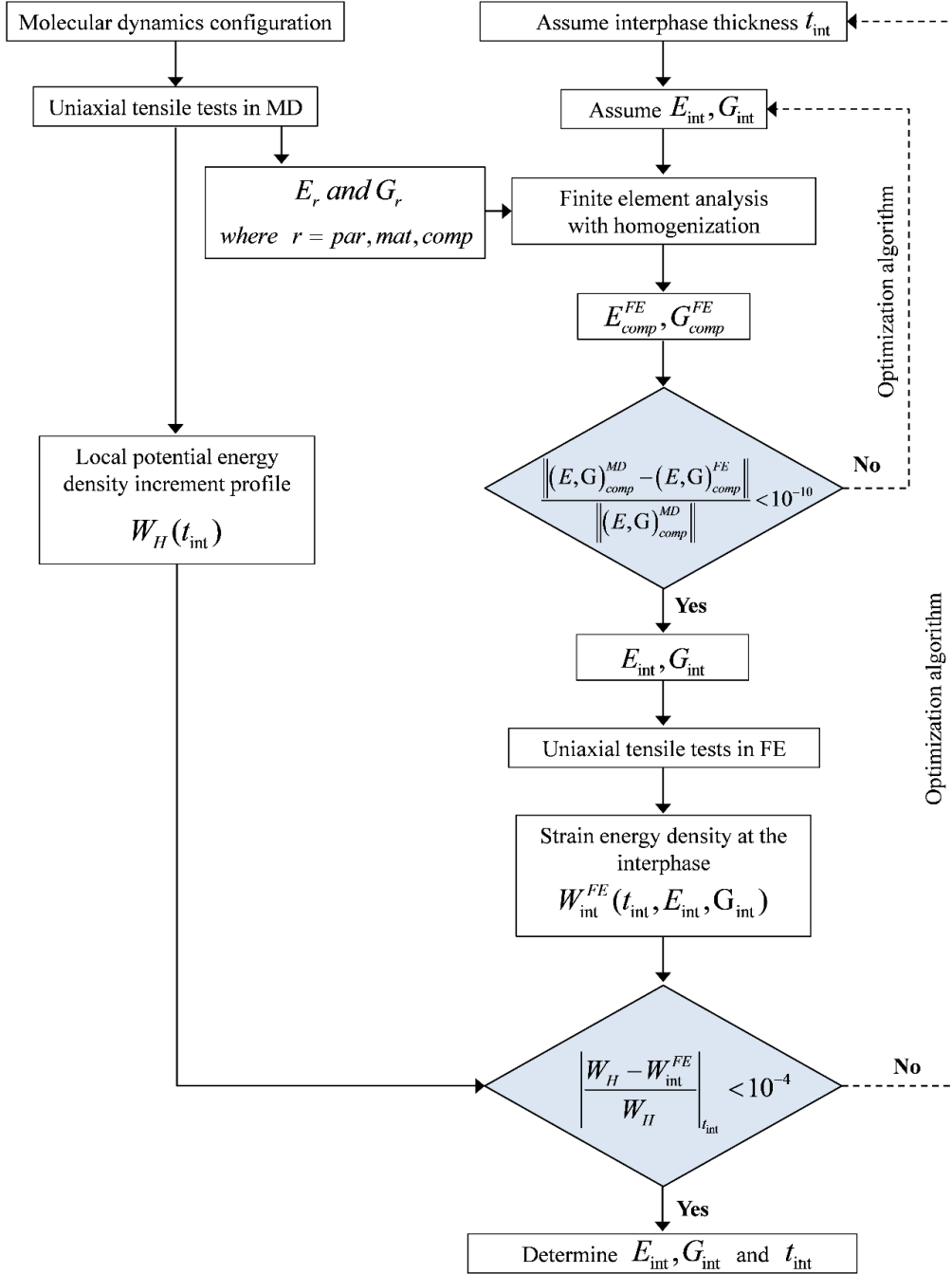


**Figure A.9.** A flowchart for the derivation of interfacial mechanical properties and geometry of the interphase by using the multiscale approach.

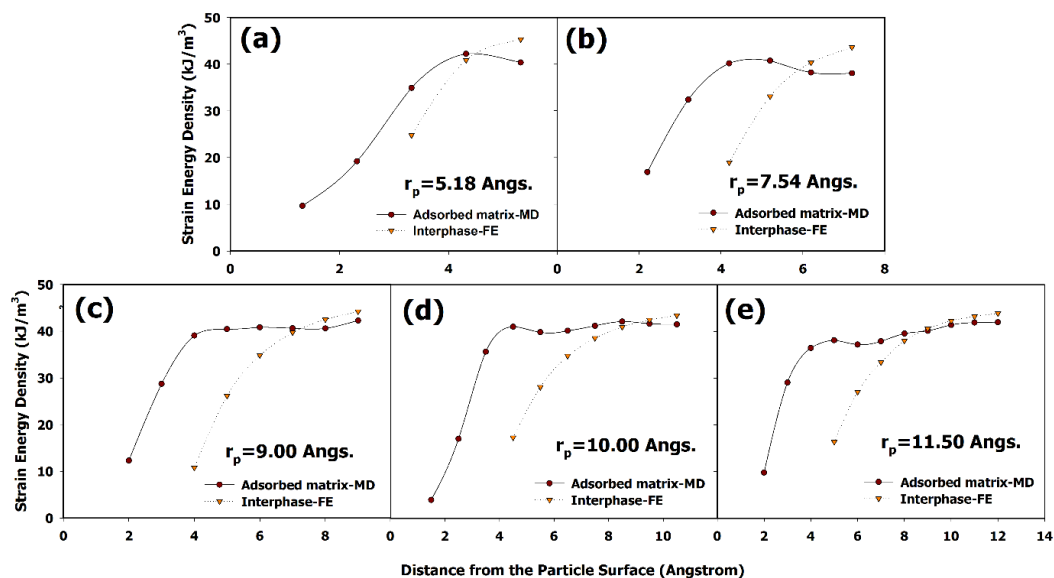


**Figure A.10.** Comparison of the strain energy density profiles of the interphase in the FE model and the local energy density profiles of the particle-excluded hollow-sphere group in MD

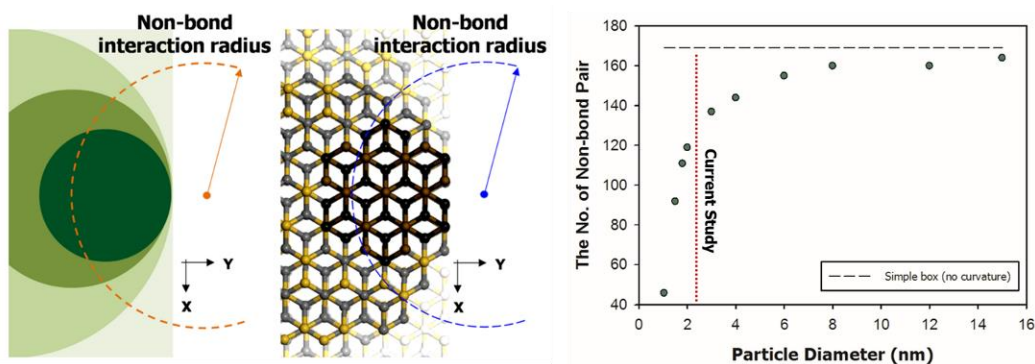
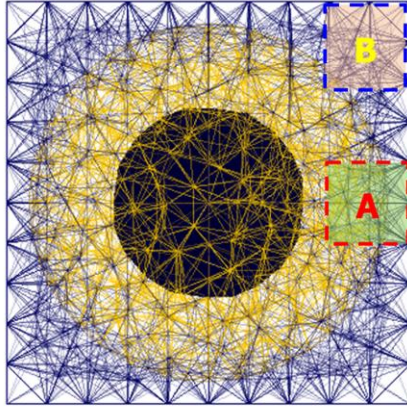
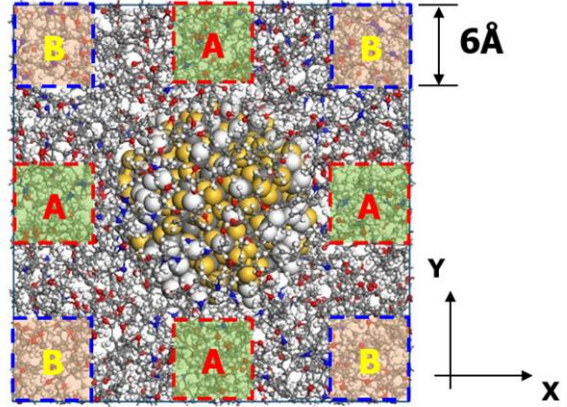


**Figure A.11.** Relationship between the nanoparticle curvature and the effective number of non-bond pairs

**(a)**

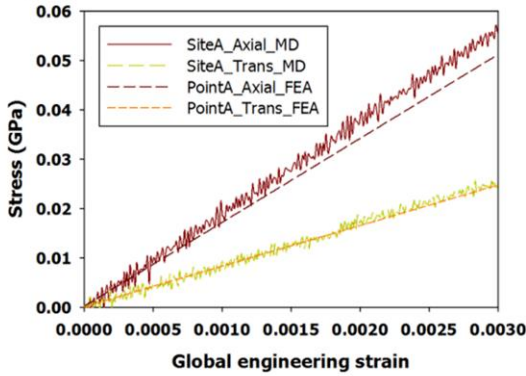


- Point A :  $0.75 \times 0.5 \times 0.5$
- Point B :  $0.75 \times 0.75 \times 0.75$   
(Fractional Coord.)



- Site A :  $6\text{Å}$  simple box (# of sites : 6)
- Site B :  $6\text{Å}$  simple box (# of sites : 8)

**(b)**



**(c)**

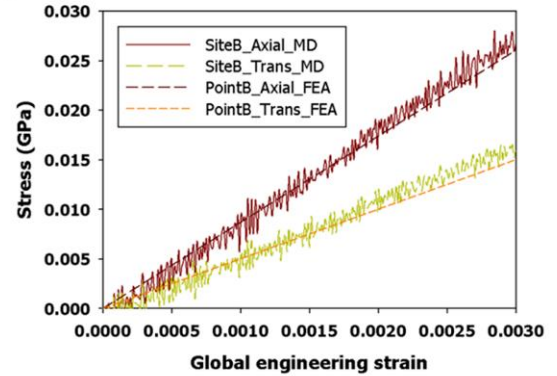


**Figure A.12.** Model validation with the comparison of the local stress-strain curves predicted by the equivalent continuum model with the averaged virial stress calculated from the molecular model: (a) validation sites description, (b) comparison result of the site A (adsorbed matrix region), and (c) comparison result of the site B (non-adsorbed matrix region)

### **A.3. Revealing weakened interphase formed in polymer nanocomposites reinforced with carbon nanotubes**

#### **A.3.1. Brief review on polymer/carbon nanotube nanocomposites**

The mechanical design of nanocarbon fiber-reinforced polymer composites is an important subject in polymer science and technology. Numerous investigations have indicated that single or multi-walled carbon nanotubes (CNTs) [133,134] are the most promising fiber material as reinforcement filler of composite materials on account of their extraordinary properties, in particular, high stiffness [135] and excellent thermal conductivity [136]. Such multi-functionality of CNT clearly presents itself even with a low weight fraction (<1.0 wt.%) in the polymer matrix [137,138] because the nanocarbon fibers possess a huge aspect ratio in nanoscale and the interfacial area between the filler surface and the polymer matrix is extremely large.

However, the applicability of CNT as reinforcement in polymer composites is very limited due to its poor interfacial bonding strength between the nanofiber and the matrix polymer. Both experimental and computational studies have found that the mechanical stiffness and strength of the CNT-reinforced polymer composites is very weak, contrary to usual expectations [55,139-141]. To overcome the weak-interface problem of CNT/polymer nanocomposites, chemical oxidation of CNTs [142,143] or *in-situ* grafting of the polymer chain onto the surface of the CNT [144,145] are commonly adopted. These

surface treatment methods are the next best way because all of the prominent features of CNT mainly originate from the hexagonal lattice of  $sp^2$  carbon atoms. The surface treatment or chemical reforming process would distort and locally collapse the pristine atomic structure of the nanofiber and severely sacrifice its effective mechanical properties. Hence, the development of quantitative estimation methods for the effect of interfacial adhesion on bulk mechanical properties of CNT/polymer nanocomposites is one of the crucial issues for the manufacturing technology of multifunctional polymer composites.

Understanding the mechanical behavior of interfaces at the molecular level, with evaluation of their independent structures and properties, must precede the modeling of multi-functional polymer nanocomposites. A comprehension of the internal stress and stress gradients at the CNT/polymer interface in composite structures is only possible if the interfacial characteristics are fully quantified on the sub-micrometer scale. In order to visualize and characterize the interfacial region and mechanical behavior of CNT-polymer nanocomposites, some experimental surveys measured the interphase layer using high-sensitivity differential scanning calorimetry (DSC) [42,146] or transmission electron microscopy (TEM) [53,54]. These experimental measurements serve to define the extents of the interfacial region. Not only experiments, but also theoretical and computational studies have been performed to analyze the mechanical properties of the interphase and to derive nanoscale design variables for the nanocomposite structures. To define the interphase region, all-atom or coarse-grained molecular dynamics (MD) simulations of nanoparticle-filled polymer composites were carried out, and the density distribution of the

polymer network in the vicinity of the nanoparticle was derived [40,44,55,147,148]. The mechanical properties of the effective interphase were then solely derived by matching the behavior of bulk nanocomposite materials obtained in MD simulations with the counterpart from a homogenized continuum mechanics model such as a finite element (FE) or multi-inclusion micromechanics model [48,58,149-152].

The models of the effective interphase obtained from the above-mentioned methods are certainly well founded. It is no doubt that they successfully reproduce the bulk elastic/plastic mechanical response of the nanocomposite material. However, these effective interphase models are still only partially acceptable because they only explain the bulk response of the nanomaterial and are not complete enough to properly represent the local stress transfer at the non-bonded interface area. Because such models determine the effective thickness of the interfacial region from a thermodynamically equilibrated snapshot of the nanocomposite model, the deformation energy at the interphase and its corresponding stress cannot be estimated with mechanical rigorousness. This limitation is particularly stringent for the analysis of the interphase of CNT/thermoset polymer nanocomposites because the conformation and effective properties of filler-adsorbed polymer segments might be significantly changed due to the interaction energy with the nanocarbon fibers [153,154] as well as the crosslink kinetics [44,101,113,155] of the thermoset resin. Therefore, to systematically identify the origin of the poor mechanical behavior of the interfaces between nanocarbon reinforcements and thermoset polymers, the



effect of the crosslink distribution of polymer networks on the mechanical stability of the nanocomposites and their associated interphases should be also comprehended.

### A.3.2. MD simulations and results

To derive the bulk and interfacial properties of pristine single walled carbon nanotube (SWNT)-reinforced epoxy composites, we constructed SWNT/epoxy nanocomposite unit cells using MD simulations. The molecular configurations of the SWNT and the epoxy resin (EPON 862<sup>®</sup>) and its hardener (TETA<sup>®</sup>) compounds are shown in **Figure A.13**. The resin and hardener molecule models were disposed in the unit cell in an amorphous state with the ratio of 3:1, which satisfies the number of chemical crosslink sites between the two molecules. The pristine zigzag SWNT aligned along z-axis was located in the center of the unit cell. Because the simulation cell was periodically bounded and both ends of the nanotube model were interconnected to each other, the length of the embedded nanotube was regarded as infinite. The initial density of the overall unit cell was set as 1.0 g/cc ahead of the crosslinking reaction among the polymer matrix constituents. The interatomic potential energy of the modeled unit cells was minimized using the conjugated gradient method with an energy deviation convergence cutoff of 0.1 kcal/mol·Å, followed by an isothermal (NVT) ensemble at 300K for 500 ps and an isothermal-isobaric (NPT) ensemble at 300K and 1 atm for 900 ps. The dynamics timestep used was 1 fs.

In order to obtain the cured thermoset network model, an *in-situ* crosslinking

method introduced in above **Section A.2** was applied. The crosslink distance cutoff was gradually tuned from 3.0 Å to 5.5 Å with the fixed step size of 0.5 Å. We targeted a total of 45% of all resin molecules to be cured with hardener molecules in the unit cell. It is noted that the targeted density of crosslinks is quite lower than that of an ordinary epoxy network (up to 70% under 5.5 Å cutoff interatomic length) because the centered SWNT nanofiller put some distance between the reactive sites of the polymer molecules and geometrically inhibits the crosslink reaction between them [112]. To directly compare the mechanical properties of the considered nanocomposite model with those of the bulk polymer matrix, we also prepared a control unit cell for a neat epoxy model that had the same crosslink density as the resin without nanotube reinforcements. After the crosslink density reached 45%, the cells were equilibrated again with an NVT ensemble run at 300K for 3 ns, followed by an NPT ensemble run at 300K and 1 atm for 5 ns.

With this way of MD modeling, we prepared four different SWNT/epoxy nanocomposite unit cells that contain zigzag SWNT models of different diameters under the same volume fraction and the same crosslinking ratio of the resin, to systematically examine the nanotube curvature effect on the interfacial characteristics of the nanocomposite material. The detailed composition and equilibrated sizes and densities of the structures are introduced in **Table A.6**. All the configurations of the equilibrated SWNT/epoxy nanocomposite unit cells are depicted in **Figure A.14**.

In all MD simulations, polymer-consistent force field (PCFF) potential [67] was used to describe both covalent and non-covalent interactions between the constituent atoms.

Constructing the three-dimensional nanostructures including the crosslinking process of the polymer networks were performed using commercial MD simulation software, Materials Studio (Accelrys Inc.).

**Figure A.15** shows the radial density distribution profiles of the nanotube and matrix phase in the nanocomposites. Starting from the concentric position of the nanotube, the local density at each point in the unit cell was measured on the cylindrical shell with 0.01 Å thickness. According to the structural feature of the SWNT, the highest density peak appears on the surface of nanotube, followed by a vacuum layer existing between the nanotube and the surrounding matrix. One notable thing is the density profile of the matrix phase is not uniform but localized in interfacial regions, indicating that a densely packed morphology was formed in all the nanocomposites models during the relaxation. Hence it is appropriate to regard the interfacial region exhibits totally different mechanical behavior compared to the neat epoxy resin. Such morphological change of the polymeric matrix in nanocomposites has been quite well known and demonstrated with both experimental [42,53,54,146] and computational [101,147,148,156] approaches.

The elastic stiffness matrices of neat epoxy and SWNT/epoxy nanocomposites were derived from the fluctuation method suggested by Parrinello and Rahman [157,158] combined with the isothermal-isostress ( $N\sigma T$ ) ensemble. For each equilibrated model, an additional  $N\sigma T$  ensemble run was executed at 300K and 1 atm for 600 ps and a sufficiently large number of trajectories of the lattice (10,000) were obtained from the last 100 ps of simulation. During the flexible unit cell simulations, the distortion and volumetric change

of the lattice box ( $\Delta\epsilon$ ) was allowed and the elastic properties of the considered model can be calculated as follows [158]:

$$C_{ijkl}^{MD} = \frac{kT}{\langle V \rangle} \langle \Delta\epsilon_{ij} \Delta\epsilon_{kl} \rangle^{-1} \quad (\text{A.10})$$

where  $k$  is the Boltzmann constant,  $T$  is the temperature,  $V$  is the volume of the unit cell box, and the brackets  $\langle \bullet \rangle$  denote the ensemble average. To reduce the numerical uncertainty of the calculation that originates from the resort to an assumed initial velocity distribution of the atoms, the NVT ensemble runs and fluctuation analyses were performed over five times for each considered cell, and the obtained elastic constants were averaged. We also carried out uniaxial tensile tests for each equilibrated model along three axes to estimate the local stress distribution between the SWNT and crosslinked epoxy in the nanocomposite. During an NVT ensemble run at a very low temperature (0.1K) with the true strain rate of  $10^6/\text{sec}$ , the lattice box was uniaxially elongated by 0.3% while keeping the lengths of the other two sides, as introduced in **Chapter 4** and **Section A.2**, respectively.

The obtained elastic stiffness components of the modeled neat epoxy and SWNT/epoxy nanocomposites from MD simulations are arranged in **Table A.7**. Unlike the neat epoxy, the SWNT/epoxy nanocomposite shows strong anisotropy in alignment with the nanotube. The axial stiffness of the SWNT/epoxy nanocomposite in the nanotube alignment is estimated to be more than 10 times that of the transverse axial stiffness because the uniform displacements were imposed on the unit cell structure in all directions while keeping periodic boundaries. Without considering the debonding of interfaces between the

ends of the nanotube tips and the polymer chains, most of the strain energy of the unit cell would be accumulated in the nanotube constituent atoms (sp<sup>2</sup> carbon). Hence the atoms generated a huge amount of mechanical stress during the displacement in the z direction. Note that the stiffness anisotropy of the unit cell of SWNT-reinforced polymer is in line with previously reported MD results [53,55,140,148,156].

Secondly, regarding the role of nanotube size on the mechanical reinforcement of polymers, it can be noticed that the elastic constants of SWNT/epoxy nanocomposite are significantly degraded as the diameter of SWNT is increased. While the radius of curvature of the nanotube is changed from 7 Å to 14 Å, the  $C_{33}$  component of the modeled SWNT/epoxy nanocomposite is almost halved and the  $C_{11}$  (and  $C_{22}$ ) component is reduced by 5.5%. Not only the tensile stiffness of the nanocomposite, but also the values of bending and torsional stiffness along the nanotube direction ( $C_{13}$ ,  $C_{23}$  and  $C_{66}$ ) depend on the nanotube curvature. The main cause of such degradation of the nanocomposite is due to the size-dependency of the cylinder rigidity of the nanotube. Since there is no internal support layer inside of the carbon wall, the roundness of the SWNT is decreased during the interaction with the surrounding epoxy chains when the diameter of the nanotube is increased and its surface is flattened. These geometric changes weaken the structural stability of the nanotube because the covalently bonded carbon wall cannot sustain external force along the off-axis direction of the carbon atomic sheet. Thus, the reinforcing value of the nanofiber is also decreased with increasing diameter.

The most important fact in **Table A.7** is that the enhancement of the mechanical properties of SWNT/epoxy nanocomposites is much less than expected. Except along the nanofiber orientation, the effective mechanical properties of composites were not improved but rather worsened comparing to the neat epoxy model. Besides, due to the effect of nanoparticle curvature described above, the elastic constants of the nanocomposites decreased further as larger nanotubes were embedded in the matrix. Recent experimental reports have shown that the nanotube bundles cannot remain straight but form tangled webs in the polymer matrix and have random orientation and arbitrary shape. Due to the high aspect ratio of nanotubes, the transversely normal and shear components play a dominant role due to the local load transfer of the interfacial layer between SWNT and epoxy networks when the external load is applied to the composites [55]. As it can be seen in **Table A.7**, however, both the transverse ( $C_{11}$  and  $C_{22}$ ) and shear ( $C_{44}$  and  $C_{55}$ ) stiffness components of SWNT/epoxy nanocomposites are lower than those of pure epoxy without reinforcement. Therefore, the present results indicate that the SWNT should be regarded rather as a defect in the transverse direction of the polymer even if the nanotube bundles are fully dispersed in the matrix and physically interlocked.

### **A.3.3. Quantification of deformation energy at the epoxy/carbon nanotube interface**

To seek the origin of the weak interfacial load transfer in SWNT/epoxy nanocomposites, in this section we further examine the characteristics of the interfacial layer in the nanocomposites unit cell by deriving the deformation energy and local stress distributions under transverse loading. By adapting the MD-FE linked multiscale analysis developed in this study, we elucidate the role of filler-matrix interaction on the morphology of the polymer segments in the vicinity of the nanotube. The surface effect of nanotubes exhibited by the sp<sup>2</sup> carbon atomic sheet on the mechanical stress distribution at interfacial layer is also in consideration, at an atomic level of detail.

To observe the load transfer capacity at the interphase (adsorbed polymer networks in the vicinity of the nanotube), we considered an artificial region in the unit cell that has a hollow cylindrical shape concentric to the nanotube but with the occupied volume of the reinforcement excluded. The deformation energy density of the group  $W^{MD}$  is computed as a function of its radial thickness as:

$$W^{MD}(r) = \frac{U_{total} - \{U_{SWNT} + U_{Bulk}(r)\}}{z\pi(r^2 + rd)} \quad (A.11)$$

where  $U_{SWNT}$  and  $U_{Bulk}$  are the potential energy increments of the inner and outer regions of the interphase group during the tensile loading,  $r$  is the radial distance from the nanotube surface,  $z$  is the cell length along z-direction, and  $d$  is the diameter of the SWNT. Since the energy contributions that come from the outside of the region are subtracted, Eq. (A.11) describes the effective strain energy density of the interphase according to the distance from the nanotube surface. We calculated the deformation energy

density of the interphase group at 1 Å intervals. All the uniaxial tensile tests and calculations of the effective deformation energy in the vicinity of the nanotube were carried out using the open source MD code, LAMMPS (Sandia Lab.).

During the transverse loading of the nanocomposite unit cell with uniform displacement boundary conditions, all the atomic structures inside of the unit cell were relaxed freely and the elastic energy of the nanocomposite under deformation was distributed to satisfy the thermodynamic equilibrium condition. The local strain energy density of the nanofiller-interacted polymer components at varying radial distance from the nanotube surface was calculated using Eq. (A.11) and the results are depicted in **Figure A.16**. One important aspect of the results is that there is a thin but still distinct region of high deformation energy close to the surface of the nanotube for all of the considered models. Because the strain energy was computed under a constant displacement condition, high deformation energy points out that the corresponding region is mechanically ductile and inhibits an efficient stress transfer between heterogeneous phases. Such a soft region however disappears quickly as the radial distance is increased since well-densified epoxy networks that are tightly adsorbed on the surface of SWNT appear next to the soft interface layer. As the computed region is sufficiently extended, the value of the deformation energy density converges to a certain value. In other words, the polymer matrix reinforced with SWNT has three distinct regions: i) a soft and ductile interfacial layer around the nanotube surface, ii) an adsorbed polymer layer interacted with the nanotube and iii) the bulk matrix which does not participate in the generation of the interphase. It is important to note that



the first region (soft interfacial layer laid on the SWNT surface) is the main cause of the weakened interfacial properties and it has unique and characteristics distinct from those of other polymer nanocomposites reinforced with ceramic or metallic nanoparticles that exhibit strong interaction with polymer constituents and in which only tightly packed adsorption layers can be formed on the nanoparticle surface [44,113].

Meanwhile, the FE model used is a multi-layered unit cell which consists of three perfectly bonded homogeneous phases: solid fiber (SWNT), interphase (polymer networks interacted with SWNT), and matrix (non-adsorbed polymer networks). All the phases are concentric meshed with a 10-node tetrahedral element. The material properties of SWNT were assumed to be orthotropic and the corresponding mechanical properties are listed in **Table A.8**. Tsai et al. [156] systematically estimated the mechanical properties of zigzag-SWNT using a molecular mechanics calculation according to the diameter of nanotube. It was claimed that all the stiffness constants are linearly decayed in semi-log space as the diameter of the nanotube increases. Thus we interpolated the data reported in the literature [156] with a semi-log function and determined the mechanical properties of zigzag-SWNT with given diameters. Similarly, the interphase layers were assumed to be orthotropic, to correctly describe a considerable load transfer of the nanotube along its axial direction. The mechanical properties in the other two directions were regarded to be the same owing to the centrosymmetry of the structure. The stiffness matrices of the nanotube reinforcement and interphase are therefore given as,

$$\mathbf{C}_{SWNT} = \begin{bmatrix} C_{11} & C_{12} & C_{13} & 0 & 0 & 0 \\ C_{12} & C_{22} & C_{23} & 0 & 0 & 0 \\ C_{13} & C_{23} & C_{33} & 0 & 0 & 0 \\ 0 & 0 & 0 & C_{44} & 0 & 0 \\ 0 & 0 & 0 & 0 & C_{55} & 0 \\ 0 & 0 & 0 & 0 & 0 & C_{66} \end{bmatrix} \text{ and } \mathbf{C}_{\text{int}} = \begin{bmatrix} C_{11} & C_{12} & C_{13} & 0 & 0 & 0 \\ C_{12} & C_{11} & C_{13} & 0 & 0 & 0 \\ C_{13} & C_{13} & C_{33} & 0 & 0 & 0 \\ 0 & 0 & 0 & C_{44} & 0 & 0 \\ 0 & 0 & 0 & 0 & C_{44} & 0 \\ 0 & 0 & 0 & 0 & 0 & \frac{(C_{11}-C_{12})}{2} \end{bmatrix}. \quad (\text{A.12})$$

The homogenized elastic constants of the nanocomposite of FE model were then compared with the corresponding ones of the MD simulation results as,

$$\frac{\|(C_{33}, C_{11})^{MD} - (C_{33}, C_{11})^{FE}\|}{\|(C_{33}, C_{11})^{MD}\|} < 10^{-2}. \quad (\text{A.13})$$

More detailed formulation procedures for the homogenization method and the fundamental concept for the scale-bridging between the continuum analysis and the MD simulations are introduced in **Chapter 4.2**.

The bold lines shown in **Figure A.16** denote the effective strain energy density at the interphase of the FE model according to the assumed interphase thickness conditions. For all of the cases, the strain energy density at the interphase of FE model is decreased as the interphase layer thickness is increased. This inversely proportional relationship is opposite to that observed for nanocomposites reinforced with ceramic nanoparticles presented in **Section A.2** because the effective stiffness at the interphase is weaker than the one at the bulk matrix region due to the influence of the aforementioned soft interfacial layer. Because the mechanical properties of the interphase were derived by the homogenization method, all the FE based nanocomposites models on each bold line have an equivalent elastic stiffness to that obtained from MD model. However, when the strain energy density curves of the FE model are compared with those of the MD model, we can

clarify that there is a unique solution for the effective thickness of the interphase that satisfies the global elastic properties of the nanocomposites as well as the local deformation energy at the interphase layer. The MD-FE linked multiscale model developed in this study yields the effective thickness of the interphase at the intersection of the two curves in **Figure A.16**, and thus quantitatively determines the equivalent mechanical properties of the interphase simultaneously.

### **A.3.4. Multiscale mechanical analysis of the nanocomposites and their effective interphase model**

A simplified flowchart of the current multiscale bridging model is illustrated in **Figure A.17**. The radial thickness of the interphase ( $l'$ ) in FE model was changed and the model meshing and homogenization were repeated until the difference of the deformation energy density with the corresponding one in MD was below  $10^{-4}$ . The obtained mechanical properties and layer thicknesses of the interphase models that exactly reproduce the corresponding elastic stiffness of the SWNT/epoxy nanocomposites derived by MD simulations are arranged in **Table A.9**.

Due to the significant anisotropy of the nanotube and the large difference of mechanical properties between filler and matrix, the elastic constants of the interphase obtained by the homogenization process also show a strong anisotropy. The axial stiffness of the interphase along the nanotube alignment direction is 8 to 12 times higher than the

corresponding transverse axial stiffness. Unfortunately, the obtained  $C_{33}$  values of the interphase do not represent real macroscale environments of polymer nanocomposites because they were derived from uniform displacement of the SWNT/epoxy unit cell without considering the slippage of crosslinked polymer networks at the ends of the nanotube. The main concern of this work, however, is focused on the transverse axial and shear components ( $C_{11}$  and  $C_{12}$ ) since they are essential for the multiscale design and analysis of the nanocomposite structure to determine the effective regions of filler-matrix interaction and to extract the intrinsic mechanical properties of the intermediate region. The  $C_{11}$  and  $C_{12}$  results in **Table A.9** illustrate that the transverse axial and shear stiffness of the SWNT/epoxy interphase are weaker than those of bulk matrix because of the poor interfacial bonding feature that was revealed by the MD simulations.

Another remarkable aspect is that the effective thickness of the interphase layer shows a clear dependency on the diameter of the incorporated nanotubes. The smallest SWNT contained in the nanocomposite forms an adsorbed layer of 1 nm thickness but the layer grows to a thickness of 2 nm as the radius of curvature of the nanotube is increased from 7 Å to 14 Å. The proportional relationship of interphase thickness with nanotube diameter is predominantly caused by the effective number of atomic interaction pairs between the carbon atoms at the nanotube rim and the polymer surface atoms. As the diameter of the nanotube is increased and the surface becomes flattened, the effective interaction range of the matrix can extend further along the radial direction of the nanotube.

To explain this in a geometric way, we simply prepared various zigzag SWNTs with sizes ranging from 7.05 to 78.29 Å in diameter as shown in **Figure A.18**. With the 9.5 Å non-bond cutoff distance, we set an arbitrary single atom which was 4.5 Å from the surface of the modeled nanotubes and then counted the number of non-bond interaction pairs at the interfacial layer with respect to the diameter of the nanotube. The results shows that even though the variation of diameter of the nanotubes modeled in this study is extremely small, the change of corresponding curvature is significant and it directly affects to the interaction region of a matrix constituent atom. As the diameter of the nanotube increases, the interaction region around the nanotube becomes enlarged and hence the maximal effective length from the polymer constituents to the nanoparticle surface required for the generation of an interphase becomes larger. In other word, the effective distance from the nanotube surface to the outer boundary of the adsorbed polymer layer should be increased as the inserted nanotube becomes thickened. The orders of magnitude of the predicted interphase thicknesses are in line with the experiment results for the case of nanocarbon-reinforced thermoset polymer in reference [101]. Also note that such nanotube size dependency on the effective interphase thickness of the nanocomposites is consistent with that shown by our previous work on the PRP nanocomposites as well as ceramic-reinforced polymer nanocomposites.

### **A.3.5. Strain energy and local stress at the interphase**

For the validation of the present multiscale analysis, the local stress and strain energy of the interphase that is predicted from the equivalent model is directly compared with the same quantities for the adsorbed polymer network region from the MD simulations. We placed artificial blocks ( $6 \times 6 \times 63.51 \text{ \AA}^3$ ) as validation sites for the MD unit cell model in which the center of the block was laid across the middle of the interphase layer obtained from the multiscale analysis, as shown in **Figure A.19**. Uniaxial static tensile tests were conducted for both the full atomic and the equivalent multiscale models and the local stresses at the assigned site were estimated. Regarding the stress calculation in the MD simulation, the volume averages of the local virial stress calculated from the MD simulations is properly converged when a sufficient number of atoms exists in the blocked group. Therefore, to overcome the small volume of the block, four blocks were positioned centro-symmetrically and all of the derived virial stresses in the blocks during the tensile loadings were averaged.

The prediction results for the effective deformation energy density of the interphase and the local stress at the site are presented in **Table A.10** and **Table A.11**, respectively. The values are compared with those obtained from MD simulations and we see that the present effective interphase model exactly reproduces the local mechanical behavior of the matrix at the adsorbed interface layer observed in the corresponding molecular unit cell. Exceptionally, the deformation energy of the effective interphase in the (9,0) SWNT reinforced model was slightly overestimated because the predicted layer thickness of the interphase exceeded the bound of the FE unit cell model.

To assess the legitimacy of the present scale-bridging method, we also obtained the deformation energy density of interphase region for the same MD model under different thickness conditions determined by the previous research [48,148,156] and compared the results in **Table A.10**. Qiao and Brinson [48] suggested the nanotube size-dependent interphase thickness: the interphase was modeled as 1.5 times thicker than the inserted nanotube diameter for the dilute loading condition. Tsai et al. [156] and Herasati et al. [148] calculated the free space between the filler and the matrix from the equilibrated MD simulation models to define the interfacial region of the nanocomposite. We applied the above-mentioned two approaches to the current MD models and derived the effective mechanical properties of the interphase using a homogenization method in the FE model. The results in **Table A.10** indicate that even if the overall elastic stiffness of the FE model is equivalent with that of the corresponding MD simulation (not shown in the table), the local deformation energy at the adsorbed polymer layer around the nanofiller cannot be properly reproduced but is overestimated in all of the cases. In other words, the mechanical energy transfer and dissipation in polymer nanocomposites can only be quantitatively legitimate through the prediction of the present multiscale model.

Meanwhile, as shown in **Table A.11**, the averaged local stress on designated sites in the MD model is also reproduced with fair accuracy (the difference of the stress value between the MD and multiscale models is from 4 to 7 MPa). But in greater detail, the stress values predicted by the multiscale analysis are consistently lower. There are two main causes accounting for this shift. First, the stress in atomic scale is described as an averaged

value for the finite volume of the sites and it does not provide the internal stress distribution at each point in the volume. Due to the conformational uncertainty of polymer networks around the nanoscale filler material, neither experimental nor atomic computational approaches could derive the deterministic point stress in the infinitesimal matrix region of the nanocomposite. To the contrary, the equivalent FE model numerically yields the stress tensor from nodal displacement of the element and depicts the internal stress distribution of the unit cell. Such differences of local stresses between the MD unit cell and the equivalent continuum model were also shown for ceramic nanoparticle/polymer nanocomposites in previous studies introduced in **Section A.2**. However, it should be remembered that the margin of error of the reproduced local stress in **Section A.2** is less than 10%, so this effect partially explains the differences of the local stresses estimated in the present study. The second cause of the difference is related to the fact that the soft and slippery interfacial layer on the surface of the nanotube generates imperfect bonding between the constituents [58,141,159]. Whereas the ceramic nanoparticle in **Section A.2** has strong nonbond interactions with the surrounding polymer at the interfacial region and forms the desired anchoring effect, the SWNT is at ease to translate or rotate inside of the soft matrix without the need of additional work due to not only its weak interaction energy [141,160] but also the high aspect ratio of the nanotube. For the convenience of the reader, we illustrate a schematic of mechanical loading system of a nanocomposite unit in **Figure A.20**. In the real environment, the nanotube surface behaves as very soft spring with a small elastic constant and the adsorbed polymer molecules have functionally graded properties



according to the distance from the nanotube surface. Compared to that, the present multiscale model presumes the adsorbed matrix to be a single independent material and the boundaries of the phase plane are perfectly bonded with the nanotube and bulk matrix. Therefore, as the external force is applied to both systems in **Figure A.20** the latter one has lower local stress value in the middle of the interphase domain under the same displacement of the unit cell.

One noteworthy feature in **Table A.11** is the dependence of the stress in the middle of the interphase domain on the nanotube diameter. As the size of the nanotube increases, the measured local stress in the interphase region increases gradually until the nanotube diameter reaches 1.2 nm and then it drops down again. This result indicates that both the imperfect bonding condition at the interface and the reinforcing capabilities of adsorbed polymer layer in the vicinity of the nanotube surface are affected by the curvature of nanotube. As discussed by Ndoro et al. [43,100] and in our previous study for polymer nanocomposites doped with ceramic-based nanoparticles, the effective interaction area becomes enlarged as the nanoparticle size decreases and it generates a thin but stiff polymer layer around the nanoparticle. And such a tendency can also be clearly shown for SWNT/polymer nanocomposites, as in **Table A.9**. Meanwhile, the extremely large curvature of the nanotube increases its structural rigidity (concentricity) at the same time and the imperfect bonding feature at the interface appears more significantly. Therefore, along the direction transverse to the nanotube, the mechanical stress transfer from the external medium to the interface in composites becomes decreased. Such soft and slippery

contact characteristics of the nanotube are mainly due to the short-range nonbond interaction [141,160] so the effect only occurs in a few angstroms. In summary, results in **Table A.11** imply that with the smaller diameters of the nanotube, the internal stress in the effective interphase region increases as the nanotube size increases— but the value might be decreased again when the diameter of the embedded nanotube is over 1.2 nm because the softening effect due to the imperfectly bonded interface is reduced and the internal stress depends dominantly on an adsorbed polymer layer.

The present multiscale model accurately predicts the deformation energy at the interfacial area where the matrix interacts with the nanotube, and quantifies its effective thickness and the corresponding mechanical properties. Besides, the local stress inside the interphase shows reasonable agreement with the volume-averaged virial stress obtained from the MD simulations. The small difference of the local stress can be fully explained by the conformation uncertainty of polymer networks in nanoscale volumes and the weakened stiffness of the effective interphase induced by imperfect bonding of the polymer with the nanotube. This work is the first quantitative mechanical modeling considering the unique intrinsic properties of imperfect bonding of the nanocarbon surface with thermoset polymer. As shown in **Figure A.21**, the equivalent continuum model provides the size and properties of the interfacial layer with mechanical rigorousness and reasonably predicts the internal stress of the phase according to the embedded nanotube size.

**Table A.6.** Composition of bulk epoxy and SWNT/epoxy nanocomposite unit cell systems.

System	SWNT diameter (Å)	Crosslinking density of the resin	Filler volume fraction (%)	Cell length (Å)		Density (g/cm <sup>3</sup> )
	(Chirality)			x and y	z	
Neat epoxy	- (-)	0.45	-	36.21	36.21	1.14
Epoxy + (9,0) SWNT	7.05 (9,0)			27.30		1.26
Epoxy + (12,0) SWNT	9.39 (12,0)		5.95	36.44	63.51	1.27
Epoxy + (15,0) SWNT	11.74 (15,0)			46.13		1.20
Epoxy + (18,0) SWNT	14.09 (18,0)			55.22		1.20

**Table A.7.** Elastic constants of neat epoxy and SWNT/epoxy nanocomposite models derived using MD simulations (units: GPa).

System	C <sub>11</sub> and C <sub>22</sub>	C <sub>33</sub>	C <sub>12</sub>	C <sub>13</sub> and C <sub>23</sub>	C <sub>44</sub> and C <sub>55</sub>	C <sub>66</sub>
Neat epoxy	6.53	6.53	3.87	3.87	1.33	1.33
SWNT (9,0)	6.29	116.80	4.46	6.89	0.68	0.91
SWNT (12,0)	6.25	87.63	4.67	6.03	0.84	0.79
SWNT (15,0)	6.03	71.90	4.42	5.97	0.74	0.80
SWNT (18,0)	5.95	58.78	4.55	5.30	0.76	0.70

**Table A.8.** Elastic properties of zigzag-SWNT according to the tube diameter used for the FE models in this study (units: GPa).

Type (Chirality)	C <sub>11</sub> and C <sub>22</sub>	C <sub>12</sub>	C <sub>13</sub>	C <sub>23</sub>	C <sub>33</sub>	C <sub>44</sub> and C <sub>55</sub>	C <sub>66</sub>
SWNT (9,0)	755.43	181.49	255.77	255.77	1641.90	1222.68	286.19
SWNT (12,0)	625.71	151.16	210.97	210.97	1275.04	930.89	236.32
SWNT (15,0)	531.92	129.36	179.06	179.06	1010.79	722.83	200.11
SWNT (18,0)	474.70	116.25	160.26	160.26	850.95	599.92	177.82

**Table A.9.** The effective layer thickness and mechanical properties of the equivalent interphase predicted by MD-FE linked multiscale model.

System	$r_{\text{int}}$ (Å)	Interphase stiffness (units: GPa)			
		$C_{11}$	$C_{12}$	$C_{33}$	$C_{44}$
Epoxy + (9,0) SWNT	11.4*	5.80	3.44	70.89	1.19
Epoxy + (12,0) SWNT	15.4	5.55	3.29	52.95	1.13
Epoxy + (15,0) SWNT	17.4	5.27	3.13	46.11	1.08
Epoxy + (18,0) SWNT	19.2	4.85	2.88	39.33	0.99

\*Obtained interphase thickness exceeds the box lattice length of the unit cell in MD simulation

**Table A.10.** Prediction of deformation energy density and their comparison results with the ones derived from the other previous methods.

System	$t_{\text{int}}$ (Å)	Deformation energy ensity (kJ/m <sup>3</sup> )			
		MD	Multiscale	Interphase layers is set to be 1.5 times the SWNT diameter** (phase thickness. Å) [48]	Non-bonded distance at the interface (phase thickness. Å) [148,156]
Epoxy + (9,0) SWNT	11.4*	28.72	31.71*	36.36 (10.58)	367.4 (2.18)
Epoxy + (12,0) SWNT	15.4	30.04	29.70	35.05 (14.09)	462.2 (2.40)
Epoxy + (15,0) SWNT	17.4	28.64	29.34	34.36 (17.61)	595.9 (2.45)
Epoxy + (18,0) SWNT	19.2	29.60	28.40	31.75 (21.14)	831.2 (2.19)

\*Obtained interphase thickness exceeds the box lattice length of the unit cell in MD simulation

\*\*The energy density is measured assuming the same thickness condition as for the current multiscale model.

**Table A.11.** Local stress prediction results for the validation sites (the ‘site A’ depicted in **Figure A.19**).

System	SWNT diameter (Å)	$t_{\text{int}}$ (Å)	Stress prediction in the middle of interphase tube, site A ( $\sigma_x$ , MPa)	
			MD	Multiscale
Epoxy + (9,0) SWNT	7.05	11.4*	18.46	18.68*
Epoxy + (12,0) SWNT	9.39	15.4	24.97	20.18
Epoxy + (15,0) SWNT	11.74	17.4	30.38	23.02
Epoxy + (18,0) SWNT	14.09	19.2	22.05	18.10

\*Obtained interphase thickness exceeds the box lattice length of the unit cell in MD simulation

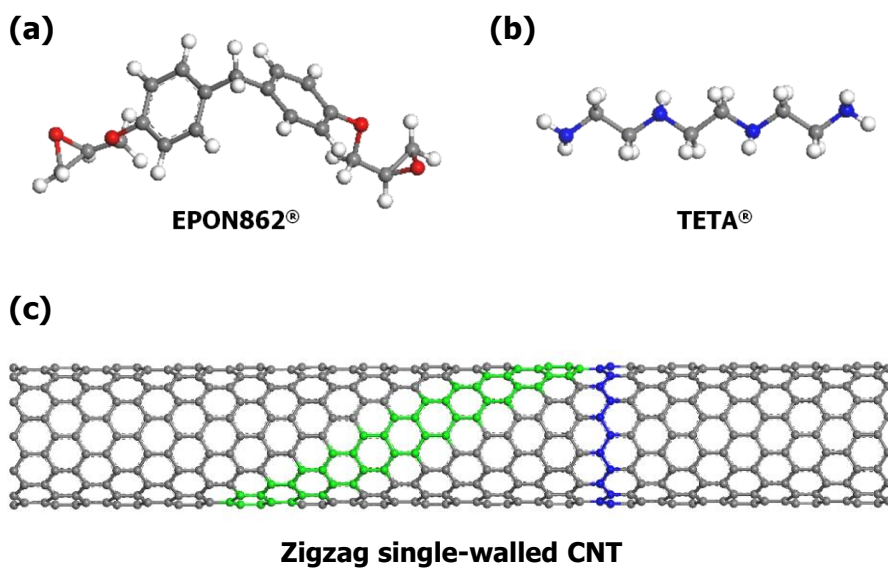


**Figure A.13.** Molecular structure images of (a) an epoxy resin (EPON 862<sup>®</sup>), (b) a hardener (TETA<sup>®</sup>) and (c) a nano-reinforcement (zigzag single-walled carbon nanotube).



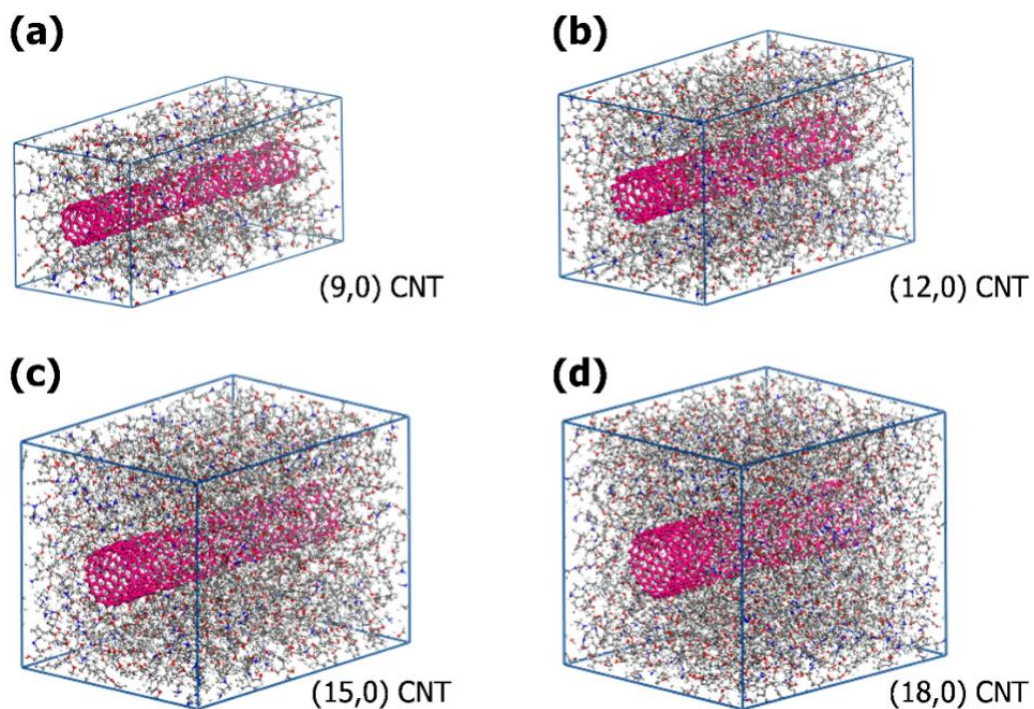


**Figure A.14.** The SWNT/epoxy nanocomposite unit cells modeled in MD simulations. A total of four different sizes of unit cells with the same volume fraction of reinforcement (5.95 vol.%) were prepared. According to the unit cell size, the dispersed zigzag-SWNT model changed its chirality as follows: (a) (9,0) (b) (12,0) (c) (15,0) and (d) (18,0).

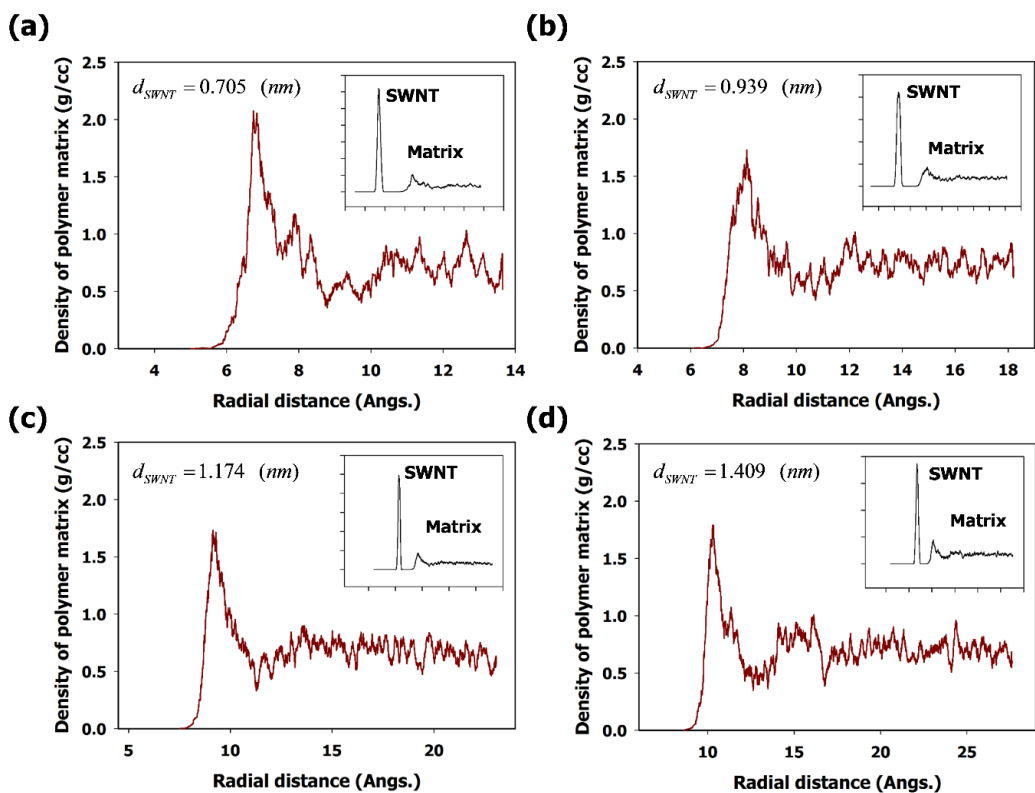


**Figure A.15.** Radial density distributions of epoxy matrix in the nanocomposites unit cells.

Each curve was derived at the room temperature condition after equilibrated by the NPT ensemble. The inset in each subfigure describes the overall density distribution profile of the unit cell including the nanofiber.

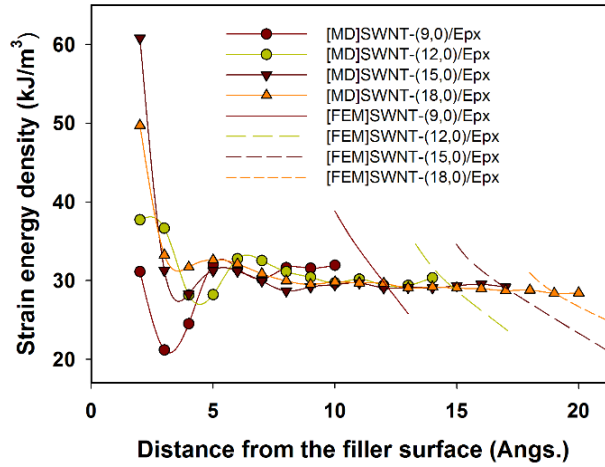


**Figure A.16.** Strain energy density curves at the interfacial layer according to the distance from the nanotube surface (solid lines with symbols) derived using MD simulations and the strain energy density of the FE based interphase models under various layer thickness conditions (bold lines without symbols).

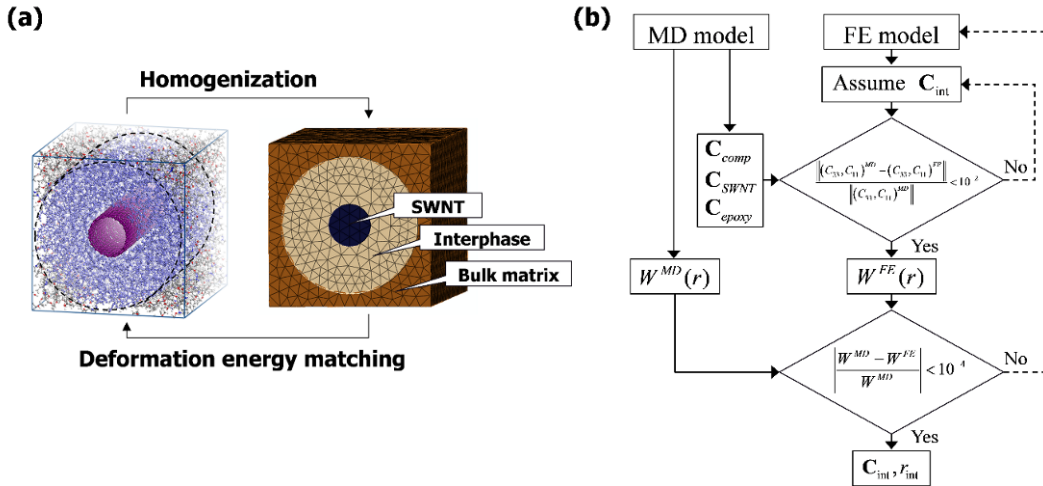


**Figure A.17.** (a) A scheme of the MD-FE bridged multiscale method which characterizes the thickness and strain energy density of the effective interphases of the SWNT/epoxy nanocomposite and (b) its flowchart.

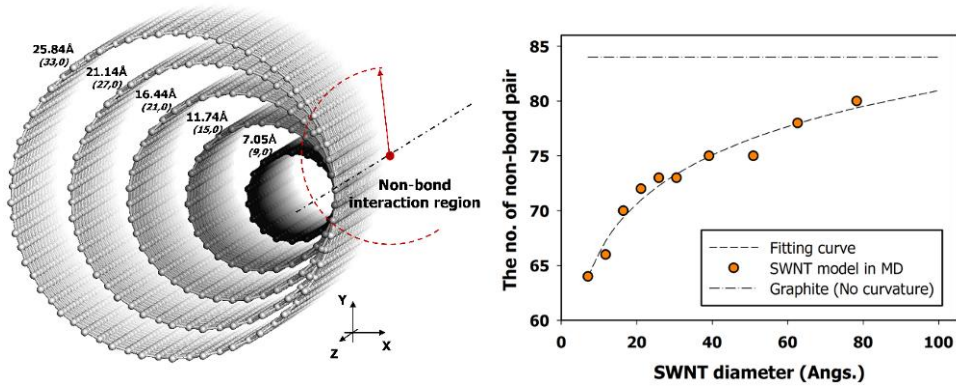


**Figure A.18.** The number of non-bond pairs between the nanotube and the adjacent polymer constituents according to the diameter of the nanotube. The corresponding value for single-layered graphite (graphene) is also depicted as dash-dot line to show that the number of non-bond pairs gradually saturates to the value as nanotube diameter increases.

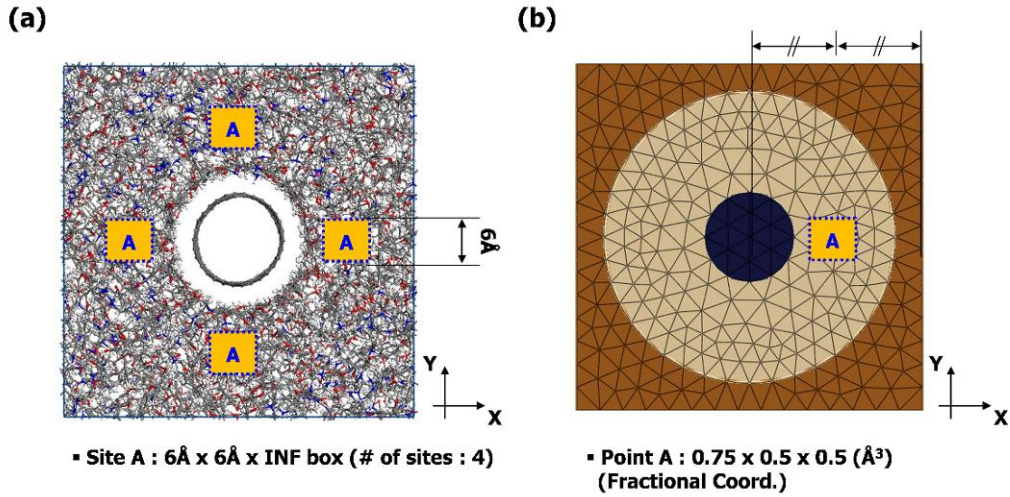


**Figure A.19.** Model validation with the comparison of the local stress-strain curves predicted by the equivalent continuum model with the averaged virial stress calculated from the molecular model at the validation site (marked as 'A'): (a) MD simulation model, (b) FE model obtained by the present analysis.

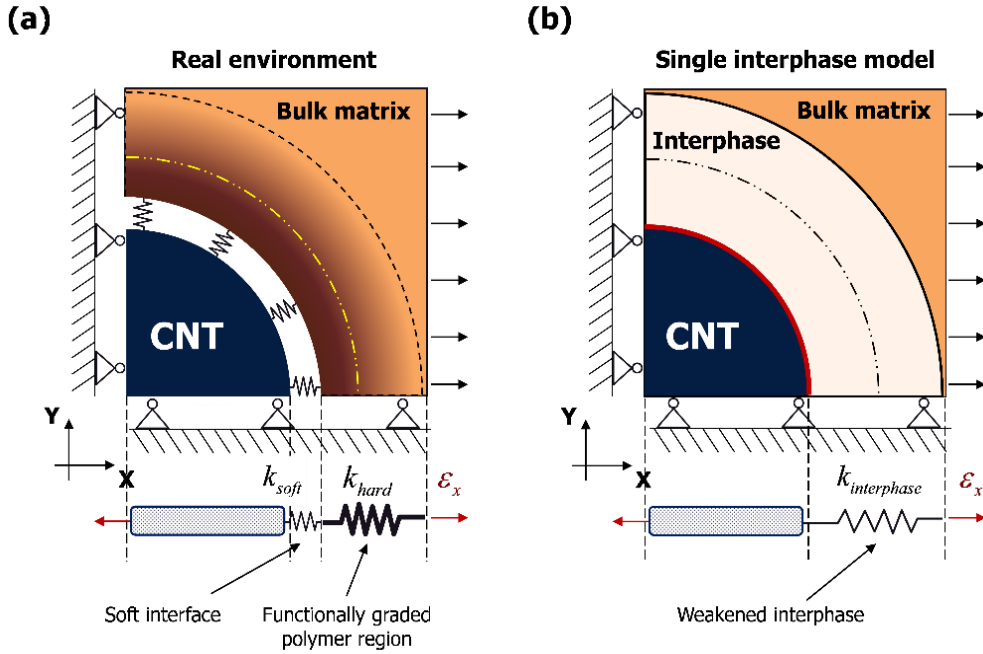


**Figure A.20.** A schematic comparison of internal force distribution in the nanocomposite structure during the external loading: (a) a real environment where both of the soft interface and the functionally graded polymer region exist and (b) a single interphase model that the adsorbed polymer region interacting with the nanotube is treated as an independent material and perfectly bonded to the two opposing surfaces.

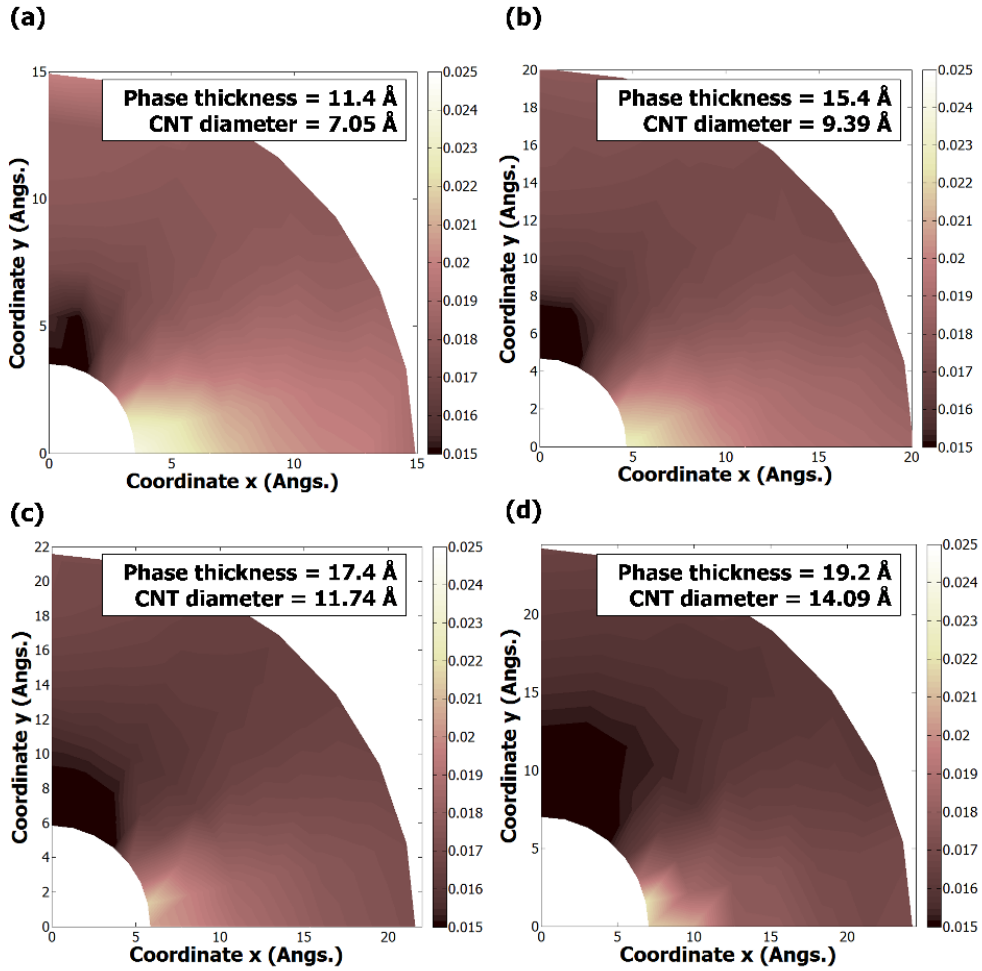


**Figure A.21.** Local stress distribution of the effective interphase during the tensile loading along x direction predicted by the proposed multiscale models: (a) Epoxy + (9,0) SWNT, (b) Epoxy + (12,0) SWNT, (c) Epoxy + (15,0) SWNT, and (d) Epoxy + (18,0) SWNT nanocomposite (colormap units: GPa)

## A.4. Summary of Appendix A

Using the developed multiscale model, we explicitly obtained the individual mechanical properties and the layer thickness of the effective interphase for crosslinked epoxy nanocomposites in **Appendix A**. For the crosslinked epoxy reinforced with SiC nanoparticles, we examined the influence of the nanoparticle size on the overall mechanical behavior of composites and the associated interphase region through the model. Three major conclusions were drawn:

- The methodology yields an effective volume fraction and mechanical properties of the interphase in a nanocomposite system based on the mechanics of elasticity. The effective interphase thickness of the equivalent continuum model increases with the particle radius scale, because the extremely high curvature of the nanoparticle inhibits the formation of the saturated number of non-bond pairs between the reinforcement and matrix constituent atoms. On the other hand, the increase of the nanoparticle curvature also leads to a larger non-bond interaction space and generates a stiffer interphase layer. Hence, the mechanical properties of the interphase are improved as the particle size is decreased, while the layer thickness is reduced. However, the curvature effect is rapidly diminished and can be neglected as the radius of the particle increases to over 10 nm.
- Through the tensile loading simulation for full atomistic models, the nanoparticle size effect on the global elastic stiffness is clearly observed. We found that the morphological change of the polymer chains generated in the vicinity of the particle

surface is not affected by the embedded particle size. Hence, the nano-reinforcement effect only originates from the non-bonding interaction energies between the particle constituent atom and the vicinity of the polymer chains.

- Together with the global elastic stiffness, the internal local stress distribution of the atomic model can be clearly followed by the equivalent continuum model, both at the adsorbed polymer layer and the non-adsorbed polymer regions. In particular, the equivalent continuum model realistically represents the reinforcing effect between the adsorbed and non-adsorbed polymer matrices, whereas the other precedent equivalent model [44,50] overestimates the deformation energy at the interphase.

Meanwhile, mechanical properties of the interfacial regions of epoxy nanocomposites reinforced with SWNT were also examined through the present multiscale model. Similar with the epoxy/SiC nanocomposites, the results showed a clear size effect: as the diameter of the SWNT is decreased, the elastic constants of the nanocomposite system are significantly increased— especially along the nanofiber orientation due to the enhancement of the structural stability of the nanotube. However, the improvement of effective mechanical properties of all the nanocomposite models considered is far less than would have been expected from the results of many other experimental and theoretical studies.

To further examine the origin of the weak interfacial load transfer of the SWNT reinforced polymer, the deformation energy density around the nanotube surface during tensile loading was obtained, with respect to the distance from the nanotube surface, using



MD models. Here we discovered the presence of a very thin and soft interfacial layer on the nanotube surface that cannot be observed in the ceramic- or the metallic-nanoparticle-reinforced polymers. Furthermore, it is verified that the  $sp^2$  carbon structures of SWNT have slippery interfacial characteristics with their associated polymer matrices and severely degrade the overall mechanical behavior of the composites structure as well. Hence, the current multiscale mechanical work is mainly focused on the comprehension of the structural and energetic properties of the nanotube and the surrounding polymer networks. The proposed method has the advantage of predicting the stress distribution inside the polymer/SWNT composites and of reproducing the interfacial behavior in a continuum in accordance with the inherent nanoscale properties of the materials.

# **Appendix B. Multiscale analysis for the thermoelastic behavior of polymer nanocomposites in a wide range of temperatures**

## **B.1. Overview**

In the **Appendix B**, the glass transition and thermoelastic properties of cross-linked epoxy-based nanocomposites and their filler-size dependency are introduced. In order to verify the size effect of nanoparticles, five different unit cells with different-sized silicon carbide (SiC) nanoparticles are considered under the same volume fraction. By considering a wide range of temperatures in isobaric ensemble simulations, the glass transition temperature is obtained from the specific volume-temperature relationship from the cooling-down simulation. In addition, the coefficient of thermal expansion (CTE) and the elastic stiffness of the nanocomposites at each temperature are predicted and compared with one another. As a result, the glass transition and thermoelastic properties of pure epoxy are found to be improved by embedding the SiC nanoparticles. Especially regarding the CTE and elastic moduli of nanocomposites, the particle size-dependency is clearly observed below and above the glass transition temperature.

Based on the MD results, we propose a sequential multiscale modeling approach to describe the thermoelastic behavior of the considered nanocomposites through a continuum micromechanics constitutive model. In the equivalent continuum model, an

interphase is defined between the particle and the matrix to account for the contribution of the polymer densification in the vicinity of the nanoparticle to the size-dependent CTE and elastic modulus at each temperature. Based on the thermal strain field defined in the micromechanics constitutive model, a physically meaningful description of the thermal expansion behavior of the interphase is obtained to reproduce the MD simulation results from fully continuum-based approaches for nanocomposites in rubbery state as well as in glassy state. Finally, the accuracy of the proposed multiscale approach is confirmed from finite element analysis.

## **B.2. MD simulations and results**

### **B.2.1. Modeling of representative unit cell system**

To investigate the reinforcing effect of nanoparticles, two kinds of unit cells were prepared: one was a pure epoxy unit cell and the other was an epoxy-based nanocomposite unit cell. The epoxy chain used in the unit cells was made up of nine chains of EPON862<sup>®</sup> and three chains of TETA<sup>®</sup>, and the curing ratio between EPON862<sup>®</sup> and TETA<sup>®</sup> was set at 61%, as depicted in **Figure B.1**. To characterize the size effect, five SiC particles of differing sizes were embedded in the nanocomposite unit cells, while the volume fraction of the particles was fixed at 5.8%, irrespective of the size of the fillers. For isotropic unit cells, the epoxy matrix was constructed as an amorphous structure, and the spherical SiC

was centered on the nanocomposite unit cell. The cross-linking methodology and the representative cross-linked molecule modeling process followed the approach employed in previous work [44]. Periodic boundary conditions were applied to the systems to reflect the bulk effect to obtain the macroscopic properties. The configurations of the modeled unit cells are shown in **Figure B.2**.

The COMPASS (Condensed-phase Optimized Molecular potentials for Atomistic Simulation Studies) forcefield [161] was adopted for the interactions between atoms. The COMPASS forcefield is based on an ab initio potential that enables us to calculate not only the atomic valence interactions but also non-bonded interactions such as the Coulomb and van der Waals interactions; thus, it enables a highly accurate prediction of the molecular behaviors and properties of various materials such as polymers or polymer-based composites. In this study, the van der Waals and Coulomb potential energies were calculated through atom-based summations, and the cutoff radius of non-bonded interactions was fixed at 9Å. In the computation of the Coulomb potential, the distance-dependent dielectric method with a dielectric constant of 1.6 was applied to let the thermoelastic properties of the atomistic model show similar values as the literature [44,162,163]. The details of the systems are presented in **Table B.1**.

To minimize the total potential energy of the initial system, the conjugate gradient method was applied until the energy difference between the steps was equal to or less than 10kcal/mol. Then, to equilibrate the structures, an NVT (isothermal) ensemble simulation at 300K for 500ps was followed by an NPT (isothermal-isobaric) ensemble simulation at

300K and 1 atm for 900ps. During the equilibrating process, the volume fraction of particles may vary a little from the initial unit cell. However, it has been found that the change in the volume fraction is negligible, as shown in **Table B.1**.

### **B.2.2. Glass transition temperature**

One of the main objectives of the present study was to verify the size effect of SiC nanoparticles on the glass transition temperature ( $T_g$ ) of epoxy-based composites. The value of  $T_g$  was obtained from the specific volume-temperature relationship and the variation of the mean squared displacement (MSD) curve with the temperature during the cooling-down simulation from 550K under the isobaric condition. After the equilibration process at 300K, the temperature of the unit cells was increased to 550K, and the cells were equilibrated again at that temperature at 1 atm for 900ps. Then, a gradual cooling-down simulation was implemented at a constant cooling rate of 10K/500ps until the temperature of the unit cells reached 280K. For relatively smaller systems that include particles whose radii are smaller than 9.0Å, a relatively large fluctuation in the energy and cell density evolution may be encountered in constant ensemble simulations for cooling-down or heating-up simulations. Thus, an NPT simulation was additionally applied to smaller systems for 200ps at each temperature after the cooling-down simulation finished. The specific volume at each temperature was averaged over the last 100ps to generate the specific volume-temperature relationship from 280K to 550K.

During the cooling-down process, the MSD curves of the epoxy and nanocomposite unit cells with respect to various temperatures were generated using the initial 30ps of the NPT simulation at each temperature. The MSD of  $N$  atoms at time  $t$  is given as follows:

$$MSD = \frac{1}{3N} \sum_{i=0}^{N-1} \left\langle \left| \vec{R}_i(t) - \vec{R}_i(0) \right|^2 \right\rangle \quad (\text{B.1})$$

where  $\vec{R}_i(t)$  denotes the current position of the  $i$ -th atom at time  $t$ . Through the variation of the MSD curve with the temperature, the relative diffusivity of a molecular system that undergoes a temperature change can be estimated. When polymers experience a glassy-to-rubbery phase transition, the torsional and rotational motions of molecules combined with the local motion can enable the disentanglement of chains; thus, the polymers experience a sudden increase in the diffusivity. The sudden increase in the diffusivity appears as a sudden jump in the MSD curves plotted with respect to the elapsed time. Thus, by investigating the gap between each MSD curve, an approximate candidate range for the glass transition temperature can be estimated to within 10K. Based on a rough estimation of the glass transition region from the MSD curves, the glass transition temperature was obtained from the intersection point of the two least-square fits of the specific volume-temperature relationship below and above the candidate glass transition region.

The specific volume-temperature relationship and the variation of the MSD curves of pure epoxy and nanocomposites in the set E54 obtained from the cooling-down

simulations are depicted in **Figures B.3** and **B.4**, respectively. The glass transition temperatures of the pure epoxy and epoxy nanocomposites obtained from the breakpoint of the specific volume-temperature relationship and the variation of the MSD curves with respect to the temperature are presented in **Table B.2**. The glass transition temperature of the present epoxy unit cell with a 61% conversion ratio was found to be about 390K, which was quite close to the value from our preceding simulation for the same material and conversion ratio [163]. Through the addition of spherical nanoparticles, it can be confirmed that SiC nanoparticles can increase the glass transition temperature of pure epoxy by 10K~28K. Intuitively, it seems that  $T_g$  depends on the size of nanoparticles. However, one should bear in mind that the breakpoint of the specific volume-temperature relationship determined from linear regression is too sensitive to the slopes of the two linear regressions in **Figure B.4**. Thus, it is natural that there may be some deviations in obtaining the glass transition temperature according to the number of data used in linear regression. Nevertheless, the glass transition temperatures obtained from the specific volume-temperature relationship in each case lie in the candidate area for the glass transition that is predicted from the MSD curve. Again, from the glass transition area estimated from the MSD curves, it can be concluded that there is no clear particle size-dependency in the glass transition temperature. In practice, the unclear tendency of the size dependency on glass transition temperature has been also observed in experimentally measured glass transition temperature of nanosilica reinforced cyanate ester composites [41]. In the reference, the increment of glass transition temperature is no less than 1% regardless of the particle size

or volume fraction.

### B.2.3. Coefficient of thermal expansion

The coefficient of thermal expansion (CTE) was derived through a similar method as the simulation process for  $T_g$ . Using the volume of the unit cells obtained from the cooling-down process, the CTE can be approximated simply as follows:

$$3\alpha \cong \gamma = \frac{1}{V_0} \frac{\partial V}{\partial T} \cong \frac{1}{V_0} \frac{\Delta V}{\Delta T} = \rho_0 \frac{\Delta v}{\Delta T} \quad (\text{B.2})$$

where  $\alpha$  and  $\gamma$  are the linear and volumetric thermal expansion coefficients, respectively,  $V_0$  and  $\rho_0$  respectively are the initial volume and density of a unit cell at the reference temperature, and  $v$  is the specific volume of a unit cell. Thus,  $\Delta v / \Delta T$  denotes the slope of the linear regression of the specific volume-temperature relationship. From the two slopes of the specific volume-temperature relationships, the CTEs in the glassy and rubbery states were estimated from Eq. (B.2).

In predicting the CTE from discrete molecular dynamics simulation results within a certain temperature range, the slope of the linear regression in the specific volume-temperature relationship is quite sensitive to the number of points used in the regression because of the inevitable fluctuation of the thermodynamics properties at a finite temperature. In addition, the concave nature of the specific volume-temperature relationship of typical polymers that undergo a glass transition makes the slope of the linear



regression in glassy and rubbery states show considerable variation according to the number of data points considered. Thus, in this study, the CTE of each state was calculated from two different temperature ranges: one was wider and considered all the data points in each state, while the other was narrow and accounted for an initially small number of data points in each state. The former was obtained from the overall temperature range: from 280K to  $T_g$  (in the glassy state) and from  $T_g$  to 550K (in the rubbery state). Meanwhile, the latter was calculated from an initially short temperature range of 40K: from 280K to 320K (the glassy state) and from 430K to 470K (the rubbery state). As the number of data points used in the linear regression of the latter was smaller than that in the former case, the latter was more likely to encounter the problem of large deviations. Therefore, the CTEs were averaged over three different simulation results in the latter case to minimize the error that might stem from the number of data points.

The CTEs of epoxy and nanocomposites above and below the glass transition temperature are depicted in **Figure B.5** and displayed in **Table B.3**. When SiC nanoparticles are inserted into the epoxy matrix, the CTE of the pure epoxy matrix decreases by more than 20% in the glassy state. Furthermore, it is found that the CTE of nanocomposites decreases as the radius of the nanoparticles decreases, indicating that smaller nanoparticles are superior to larger ones for decreasing the CTE of the pure epoxy matrix. The trend observed from the present MD simulations can be elucidated from the formation of the interface where matrix molecules are immobilized and adsorbed. As smaller nanoparticles can have a greater surface area than larger ones, more atoms of the

surrounding matrix are anchored; thus, this structural change macroscopically appears as a decrease in the CTE. One major finding obtained from the present MD simulation results is that the size effect of nanoparticles still appears even after the nanocomposite unit cells undergo the glassy-to-rubbery phase transition. Thus, it can be concluded that the existence of the interface still is an important structure-property relationship to enable particle size-dependent thermoelastic properties in the rubbery state.

Regarding the results shown in the seventh column of **Table B.3** from our previous work [163] in glassy states that dealt with the same epoxy nanocomposites, all the CTEs obtained from the present MD simulations are larger than those from our previous work. The difference originates from the range of the temperature considered in estimating the CTE of the nanocomposites. In Ref. [163], the CTE of the nanocomposites was obtained from the temperature-volume relationship from 280K to 340K while the present study calculated it from 280K to  $T_g$  in the glassy state. Considering that the typical temperature-volume (specific volume) relationship of polymeric material is convex, the CTE of polymeric material can vary according to the range of the temperature considered in establishing the volume-temperature relationship. As mentioned in the previous section, the CTEs of the nanocomposites obtained from the initial range of 40K are independently compared in **Table B.3** and **Figure B.5** with the CTEs obtained from all the temperature values in the glassy and rubbery states in order to account for the effect of the range of the linear regression. As the range of the temperature to calculate the CTEs of the nanocomposites decreases, the CTEs of the nanocomposites increase. One notable aspect is that no matter

how the range of the temperature is chosen to calculate the CTE, the size effect of the nanoparticles is clearly observed in all the cases compared in **Table B.3**. The embedded particle size effect on the CTE of polymer-based nanocomposites in glassy state has also been demonstrated in experimental results in Ref.[41]. In the reference, it has been reported that the CTE of cyanate ester at glassy state could be lowered up to 27% by embedding 40nm fumed nanosilica while more remarkable decrease of the CTE was observed from 12nm fumed nanosilica reinforced case. In the present MD simulation results, the difference of the CTE between nanocomposites and pure epoxy varies from 21 to 45% according to the size of the embedded nanoparticle.

Considering the size and volume fraction of the nanocomposites considered in the present MD simulation results which are different from those of the Ref. [41], direct quantitative comparison with the experimental result is not allowed. While, the results observed from the present MD simulations qualitatively agree well with the results in Ref. [41]. Meanwhile, the CTE in rubbery state of nanocomposites cannot be compared with the experimental result due to the lack of data. To the author's best knowledge, the size effect observed not only at glassy but also rubbery state in our manuscript is truly believed to be a new finding that can complement thermal design of nanocomposites that experience critical temperature cycles. Thus, current MD simulation results can serve as a useful guideline for thermal design of the nanocomposites.

#### **B.2.4. Elastic modulus**

Within the range of the temperature considered in this study, the elastic moduli of pure epoxy and epoxy nanocomposites were calculated every 50K, from 250K to 550K. After the cooling-down simulations, the trajectories saved at each temperature were used as the initial equilibrium structure to calculate the elastic stiffness. The elastic stiffness was calculated from the Parrinello-Rahman fluctuation method [157] combined with the N $\sigma$ T ensemble simulations. In Parrinello-Rahman's flexible unit cell simulation, volumetric change as well as the distortion of unit cells is allowed. The elastic stiffness of a unit cell is calculated from the following fluctuation formula:

$$C_{ijkl} = \frac{kT}{\langle V \rangle} \langle \Delta \varepsilon_{ij} \Delta \varepsilon_{kl} \rangle^{-1} \quad (\text{B.3})$$

where  $k$  is the Boltzmann constant,  $T$  is the target temperature,  $V$  is the volume of the unit cell, and the brackets  $\langle \bullet \rangle$  denote the ensemble average. As a test run for applying the fluctuation method, an N $\sigma$ T ensemble simulation for a total of 600 ps under an equivalent external pressure of 1atm was executed at each temperature. From the last 100ps of the N $\sigma$ T ensemble, 10,000 strain fluctuation values were saved to calculate the elastic stiffness from Eq. (B.3). In order to guarantee computational accuracy, all the elastic constants were averaged over six different simulation results.

The elastic moduli of epoxy and nanocomposite unit cells (except the largest system of E54) obtained from the Parrinello-Rahman fluctuation methods are shown in **Table B.4**. Similar to the trend in CTEs reported in the previous section, the elastic stiffness

of nanocomposites also shows a particle-size effect even in the rubbery state. In the passage through the glass transition region from the rubbery state to the glassy state, the elastic moduli of the nanocomposites dramatically increase, as shown in **Figure B.6**. The size effect of the nanoparticles, however, is likely to decrease in the rubbery state because the epoxy molecules are less confined in the interface, and the molecules in other regions are easily disentangled as a result of the increased kinetic energy of individual atoms at high temperature.

Meanwhile, the elastic modulus of pure epoxy in this study is higher than that from our previous work. The gap between the two moduli is caused by the different simulation conditions such as the number of molecules in a unit cell (the present epoxy unit cell is larger than the previous one in Refs. [44,163]) and the thermal history, i.e., the present epoxy unit cell undergoes a prolonged cooling-down process before the elastic modulus is calculated at 300K. During a gradual cooling-down simulation, all the atoms in epoxy molecules can have enough time to find an optimal position that minimizes the total energy of the overall system for a well-equilibrated unit cell structure. Thus, the present epoxy unit cell has been more or less finely equilibrated than the unit cell considered in Refs. [44,163]. The effect of the thermal history also can be confirmed from the elastic moduli of the nanocomposites that are slightly higher than those from Ref. [163]; the elastic moduli are displayed and compared in **Table B.5**.

**Table B.1.** Composition of epoxy and epoxy/SiC nanocomposite unit cell systems.

System	Particle radius (Å)	Target volume fraction (%)	Initial volume fraction (%)	Stabilized volume fraction (%)	No. of crosslinked epoxies	Unit cell length (Å)
Epoxy	-	-	-	-	6	36.28
E06	5.18		5.80	5.73	2	21.66
E18	7.54		5.80	5.95	6	31.14
E30	9.00	5.80	5.87	6.08	10	36.89
E42	10.00		5.76	5.96	14	41.26
E54	10.90		5.80	6.02	18	44.84

**Table B.2.** Results of the analysis of the glass transition temperatures of pure epoxy and nanocomposites

System	Radius (Å)	T <sub>g</sub> by regression (K)	T <sub>g</sub> by MSD (K)
Epoxy	-	390.12	380~390
E06	5.18	418.02	410~420
E18	7.54	404.79	400~410
E30	9.00	400.66	400~410
E42	10.00	413.37	400~410
E54	10.90	400.03	400~410

**Table B.3.** Thermal expansion coefficient (CTE) of the modeled system (units:  $10^{-6}/\text{K}$ )

System	Radius ( $\text{\AA}$ )	CTE below $T_g$	CTE below $T_g$	CTE above $T_g$	CTE above $T_g$	Ref. [163] (below $T_g$ , initial 60K)
		(overall range)	(initial 40K)	(overall range)	(initial 40K)	
Epoxy	-	109.72	89.74	187.62	171.12	103.6
E06	5.18	85.31	49.43	155.63	137.31	77.3
E18	7.54	96.94	51.35	165.80	152.18	86.7
E30	9.00	92.07	64.80	171.00	156.69	91.0
E42	10.00	103.47	70.27	168.01	162.47	84.2
E54	10.90	104.53	70.28	169.87	158.74	91.8



**Table B.4.** The elastic modulus of the modeled system at various temperature conditions (units: GPa)

Temp. (K)	E06 (5.18 Å)	E18 (7.54 Å)	E30 (9.00 Å)	E42 (10.00 Å)	Epoxy
250	6.87	6.44	6.11	5.70	4.22
300	5.54	4.96	5.01	4.81	4.08
350	4.72	4.16	4.19	4.23	3.12
400	3.21	2.53	2.93	2.39	2.08
450	1.83	1.72	1.56	1.58	1.09
500	1.61	1.21	1.48	0.95	0.80
550	1.26	0.84	1.11	0.65	0.47
Ref. [4] (at 300K)	5.72	4.59	4.65	3.69	3.16

**Table B.5.** Deviation of the elastic modulus of pure epoxy in relation to the simulation time and comparison with the literature (units: GPa)

Current research	Total 2.5 ns NPT	Total 1 ns NPT	Yang et al. [163]	Yu et al. [44]	Fan et al. [162]
4.08	3.37	2.79	3.16	3.36	3.75

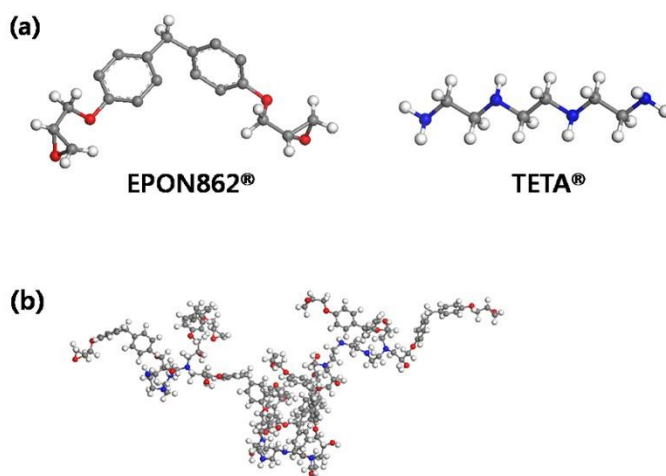


**Figure B.1.** (a) The cross-linked epoxy unit is formed by reaction between the carbon of EPON862<sup>®</sup> and the nitrogen of TETA<sup>®</sup>. (b) The unit chain of the polymer network, which converges to a ratio to 61%; this has been considered in the present study.

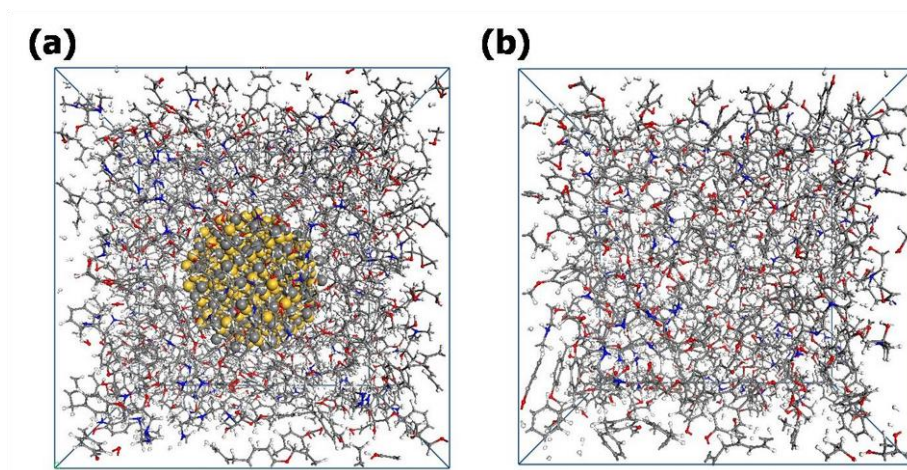


**Figure B.2.** (a) Epoxy/SiC nanocomposites and (b) pure crosslinked epoxy models. A total of five different sizes of unit cells with the same volume fraction regarding nanocomposites were prepared.

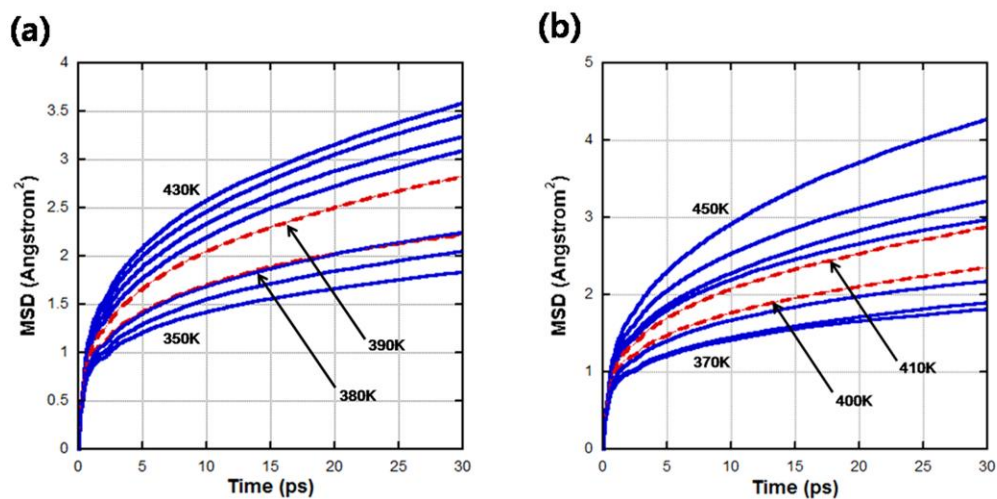


**Figure B.3.** The MSD curves of: (a) pure epoxy and (b) the E54 system.

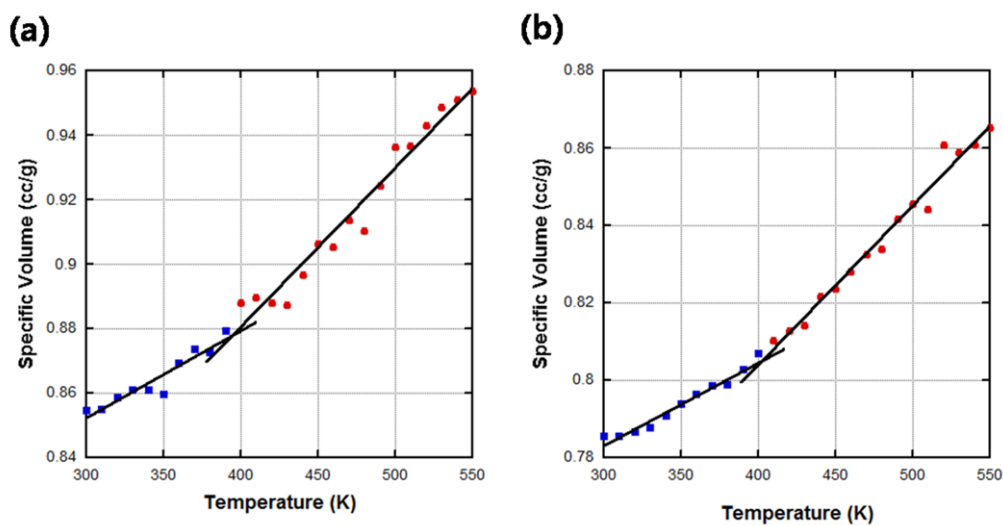


**Figure B.4.** The specific volume-temperature relations of: (a) pure epoxy and (b) the E54 system

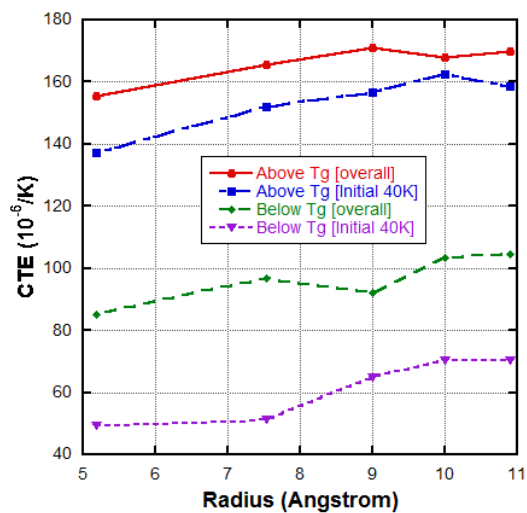


**Figure B.5.** The CTEs increase as the measured temperature range broadens within the same phase region because the specific volume-temperature plot is convex. It is worth noting that the size effect on the CTE could be observed regardless of the phase of the nanocomposites.

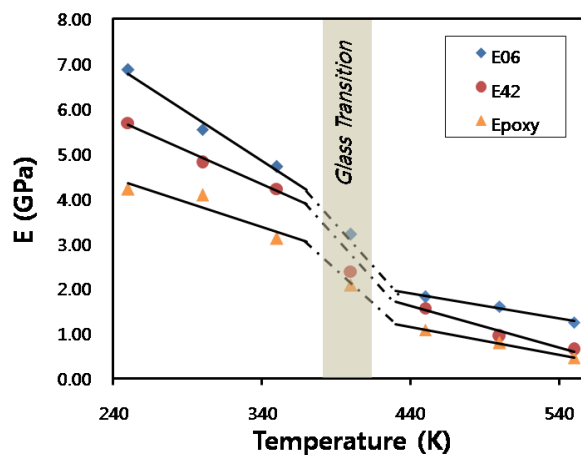


**Figure B.6.** Comparison of the elastic moduli of the smallest-filler-reinforced, the largest-filler-reinforced, and pure epoxy cells under various temperature conditions. The size effect could be observed clearly both below and above the glass transition.

### **B.3. Multi inclusion micromechanics model for thermoelasticity**

As shown in the previous sections, the Young's and shear moduli and the linear CTE of nanocomposites show a clear particle-size dependency both in glassy and rubbery states. A well known structure-property relationship of the size dependency indicates the dominance of the molecular adsorption in the vicinity of the embedded fillers that becomes a highly dense area, which has been neglected in conventional composites. Therefore, the equivalent micromechanics modeling of nanocomposites should define a characteristic phase that describes the variation of the particle-size dependency of the overall thermoelastic properties. In this study, a representative volume element (RVE) of nanocomposites in equivalent continuum modeling is defined as a three-phase structure consisting of the particle, interphase (adsorption layer), and matrix. In order to consider the three-phase RVE, a multi inclusion model [164] is considered as an equivalent micromechanics model to describe the thermoelastic behavior of nanocomposites. Note that the main formulation for the thermoelasticity of nanocomposites was done by Yang and Cho [165] and only essential equation would be provided in this section. The details of the calculation can be found in reference [165].

In the multi inclusion model, it is assumed that a multiple-layered inclusion is embedded into an infinite medium of yet unknown properties. According to the volume fraction of the filler and the degree of filler concentration effect, the property of the infinite medium is properly chosen. As the volume fractions of present nanocomposites are about

6%, which is sufficiently small for ignoring the non-dilute concentration effect, the stiffness of the infinite medium was set to the stiffness of the matrix. The closed form solution of the overall elastic stiffness of composites is given as,

$$\mathbf{C} = \mathbf{C}_{\text{inf}} \left[ \mathbf{I} + (\mathbf{S} - \mathbf{I}) \left( \sum_r f_r \mathbf{\Lambda}_r \right) \right] \left[ \mathbf{I} + \mathbf{S} \left( \sum_r f_r \mathbf{\Lambda}_r \right) \right]^{-1}, \quad (r = p, i, m) \quad (\text{B.4})$$

where  $\mathbf{C}_{\text{inf}}$  is the stiffness of the infinite medium,  $f_r$  is the volume fraction of the  $r$ -th phase ( $p, i, m$  respectively indicate particle, interphase, and matrix),  $\mathbf{S}$  and  $\mathbf{I}$  are the Eshelby tensor [166] and identity tensor, respectively. The fourth-order tensor  $\mathbf{\Lambda}_r$  is the eigenstrain concentration tensor of the  $r$ -th phase given as,

$$\mathbf{\Lambda}_r = \left[ (\mathbf{C}_{\text{inf}} - \mathbf{C}_r)^{-1} \mathbf{C}_{\text{inf}} - \mathbf{S} \right]^{-1} \quad (\text{B.5})$$

where  $\mathbf{C}_r$  is the stiffness of the  $r$ -th phase. Since the elastic field is not coupled with the temperature change, all the stiffness tensors in Eqs. (B.4) and (B.5) are defined at each of the temperature considered in this study.

Contrary to the micromechanics modeling of the elastic field, that of the thermal expansion (thermal residual field) requires detailed description of the thermal strain change of each constituent, especially on the interphase, to calculate the volume fraction changes of the phases at each temperature. Thus, some important formulations of the internal thermal strain field of composites are reviewed for the multi-inclusion modeling of the thermal expansion [167].

For a thermal expansion problem, not only the eigenstrain induced by the mismatch of elastic stiffnesses but also the particle's own eigenstrain due to the mismatch

of CTEs are defined in Eshelby's equivalent inclusion method given as,

$$\mathbf{C}_r \left( \boldsymbol{\varepsilon}^0 + \boldsymbol{\varepsilon}_r^p - \boldsymbol{\varepsilon}_r^T \right) = \mathbf{C}_{\text{inf}} \left( \boldsymbol{\varepsilon}^0 + \boldsymbol{\varepsilon}_r^p - \boldsymbol{\varepsilon}_r^T - \boldsymbol{\varepsilon}_r^{**} \right) = \mathbf{C}_{\text{inf}} \left( \boldsymbol{\varepsilon}^0 + \boldsymbol{\varepsilon}_r^p - \boldsymbol{\varepsilon}_r^* \right) \quad (\text{B.6})$$

where the strain fields  $\boldsymbol{\varepsilon}^0$  and  $\boldsymbol{\varepsilon}_r^p$  are the far field strain and the perturbed strain of the r-th phase respectively, and  $\boldsymbol{\varepsilon}_r^T$  is the thermal eigenstrain caused by the mismatch of CTEs given as,

$$\boldsymbol{\varepsilon}_r^T = -\mathbf{C}_r^{-1} \boldsymbol{\lambda}_r \theta = \boldsymbol{\alpha}_r \theta \quad (\text{B.7})$$

where  $\boldsymbol{\lambda}_r$  is the thermal stress tensor of the r-th phase and  $\theta$  is the temperature change from a reference temperature.  $\boldsymbol{\varepsilon}_r^{**}$  is the eigenstrain caused by the mismatch of elastic stiffness and  $\boldsymbol{\varepsilon}_r^*$  is the effective eigenstrain that includes both eigenstrain fields.

By applying Eshelby's solution, the perturbed strain of the r-th phase is defined as,

$$\boldsymbol{\varepsilon}_r^p = \mathbf{S} \left( \boldsymbol{\varepsilon}_r^T + \boldsymbol{\varepsilon}_r^{**} \right) \quad (\text{B.8})$$

Using Eq.(B.8), the eigenstrain field  $\boldsymbol{\varepsilon}_r^{**}$  can be expressed in terms of the far field strain and the thermal eigenstrain as,

$$\boldsymbol{\varepsilon}_r^{**} = \boldsymbol{\Lambda}_r \boldsymbol{\varepsilon}^0 + \boldsymbol{\Lambda}_r (\mathbf{S} - \mathbf{I}) \boldsymbol{\varepsilon}_r^T. \quad (\text{B.9})$$

Then, using Eq.(B.9), the average strain of the r-th phase caused by a temperature change is given as,

$$\begin{aligned} \boldsymbol{\varepsilon}_r &= \boldsymbol{\varepsilon}^0 + \boldsymbol{\varepsilon}_r^p = \boldsymbol{\varepsilon}^0 + \mathbf{S} \left( \boldsymbol{\varepsilon}_r^T + \boldsymbol{\varepsilon}_r^{**} \right) \\ &= (\mathbf{I} + \mathbf{S} \boldsymbol{\Lambda}_r) \boldsymbol{\varepsilon}^0 + \mathbf{S} \left( \boldsymbol{\Lambda}_r (\mathbf{S} - \mathbf{I}) + \mathbf{I} \right) \boldsymbol{\varepsilon}_r^T. \end{aligned} \quad (\text{B.10})$$

In Eq.(B.10), the thermal eigenstrain  $\boldsymbol{\varepsilon}_r^T$  can be calculated from Eq.(B.7), and the farfield strain  $\boldsymbol{\varepsilon}^0$  can be determined from the boundary conditions of the nanocomposites.

Because the thermal expansion of each phase is the main concern, a free boundary

condition should be used to derive the farfield strain as a function of the given variables and thermal eigenstrain.

Under the free boundary condition, the average thermal stresses of composites due to a temperature change should be zero, thus,

$$\boldsymbol{\sigma}_{\text{comp}} = \mathbf{C}_{\text{inf}} : \left( \boldsymbol{\varepsilon}^0 + \boldsymbol{\varepsilon}_r^p - \boldsymbol{\varepsilon}_r^T - \boldsymbol{\varepsilon}_r^{**} \right) = 0 \quad (\text{B.11})$$

Substituting Eqs.(B.7)-(B.9) into Eq.(B.11), one can derive the farfield strain as a function of the thermal eigenstrain as follow,

$$\boldsymbol{\varepsilon}^0 = - \left[ (\mathbf{I} + \mathbf{S}\boldsymbol{\Lambda}) - \boldsymbol{\Lambda} \right]^{-1} \sum_r f_r (\mathbf{S} - \mathbf{I}) \left[ \boldsymbol{\Lambda}_r (\mathbf{S} - \mathbf{I}) + \mathbf{I} \right] \boldsymbol{\varepsilon}_r^T \quad (r = p, i, m) \quad (\text{B.12})$$

where the fourth order tensor  $\boldsymbol{\Lambda}$  is given as,

$$\boldsymbol{\Lambda} = \sum_r f_r \boldsymbol{\Lambda}_r \quad (r = p, i, m). \quad (\text{B.13})$$

Then, the thermal strain tensor of the r-th phase can be calculated using Eq.(B.7), Eq.(B.10), and Eq.(B.12) for a certain temperature change of  $\theta$ . The overall thermal stresses and CTEs of composites are given as,

$$\boldsymbol{\lambda} = \mathbf{C} : (\mathbf{I} + \boldsymbol{\Lambda} : \mathbf{S})^{-1} : \sum_r f_r \left[ \boldsymbol{\Lambda}_r : (\mathbf{S} - \mathbf{I}) + \mathbf{I} \right] : \mathbf{C} : \boldsymbol{\lambda}_r \quad (\text{B.14})$$

$$\boldsymbol{\alpha} = -\mathbf{D} : \boldsymbol{\lambda} \quad (\text{B.15})$$

where  $\mathbf{D}$  is the overall compliance tensors of composites.

In order to utilize Eqs.(B.4)-(B.5) and Eqs.(B.14)-(B.15) to predict the elastic stiffnesses and CTEs of nanocomposites at various temperature, the volume fraction, stiffness, and the CTE of each phase should be provided. At the reference temperature of



250K, stiffness and CTEs of the matrix and particle, and the volume fraction of the particle are obtained from MD simulation. Thus, the volume fraction, stiffness and CTE of the interphase remain as unknown variables at the reference temperature. Even though these values are provided at the reference temperature, the way to determine the volume fraction of the interphase at a certain elevated temperature should be established. In the next section, the way to determine the interphase properties at the reference state and at a specific temperature is detailed.

## **B.4. Scale-bridging model for thermoelasticity of the interphase**

### **B.4.1. Determination of the volume fraction and thermoelastic properties**

To determine the volume fraction, Young's and shear moduli, and the CTE of the interphase, the following assumptions are applied throughout the micromechanics modeling at the present temperature range.

- (a) The elastic modulus and the CTE of silicon carbide are constant regardless of temperature.
- (b) Dimensional change of the SiC nanoparticle due to temperature change (thermal loading) is negligible; thus, the thermal strain of SiC is set to zero.

Because the thermal expansion coefficient of SiC is one-thirtieth and the Young's modulus

is 120 times that of pure epoxy, these two assumptions are reasonable. Moreover, the melting point of SiC is about 3000 K; thus, a sudden diffusion of carbon and silicon atoms that results in the change of the CTE is not expected in the temperature range considered in this study.

In addition to these assumptions, we used two different sets of definition for the temperature range that applies to thermal expansion and elastic stiffness. Because typical shape of the temperature-specific volume relation of polymeric materials near the glass transition temperature is concave, it is not easy to define the CTEs of epoxy and nanocomposites for the glass transition region. Therefore, we simply divided the temperature domain into two regions-‘glassy’ and ‘rubbery’. The glass transition temperatures of nanocomposites shown in **Table B.2** indicate no clear tendency between the glass transition temperature and the radius of the nanoparticles but the derived glass transition temperatures have deviations in the range between 400K and 420K. As has been briefly mentioned in the previous section on the estimation of the glass transition temperature from MD simulations, the resultant glass transition temperature obtained from the break point of the temperature-specific volume relation can vary to a certain degree according to the number of data used to fit the linear relation between the temperature and the specific volume for glassy and rubbery states. However, the glass transition temperatures in **Table B.2** are within the range obtained from the MSD curves, which can roughly estimate the candidate glass transition region. Thus, the glass transition temperatures of the nanocomposites were representatively set as 410K, regardless of the

particle radius in our bridging model.

While the temperature domain to describe thermal expansion has two regions, the domain for elastic moduli is divided into three ranges. As can be seen from MD simulation results, a rapid degradation of elastic moduli and shear moduli is observed around the glass transition temperature. In order to confirm this, least square fits of the Young's moduli in glassy (250K~350K), transitional (350K~450K), and rubbery (450K~550K) states are independently compared with the MD simulation results. As can be seen in **Figure B.7**, the Young's moduli in each range of the temperature domain show very good linearity regardless of the embedded particle size.

The volume fraction of the interphase can be calculated by defining the thickness of the interphase with the assumption that both the nanoparticle and interphase are coaxial. According to the structural evidence [168] that supports the existence of the interphase, the radial density distribution function (RDF) of the matrix polymer can be used to identify the highly dense area to distinguish the interphase from the pure matrix phase. Thus, at the reference temperature of 250K, which is the lowest temperature considered in this study, the RDF of the epoxy matrix in each unit cell was obtained from the position and mass of the atoms in the unit cell. As depicted in **Figure B.8**, there exist distinguishable peak points in the vicinity around the surface of nanoparticles in RDFs, indicating the formation of a densely packed interphase. Because the elastic stiffness and mobility of a polymeric material are closely related with the density, it is reasonable that the peaks in the RDFs confirm the interphase.

In this research, the thickness of the interphase at 250K is determined by the embedded particle radius  $r_p$ , the peak distance  $r_{peak}$ , and the outer thickness of the interphase  $t_{adsorption}$  as follows,

$$t_i |_{T=250K} = r_{peak} + t_{adsorption} - r_p \quad (B.16)$$

Here, the outer thickness  $t_{adsorption}$  was assumed as 4.8Å regardless of the radius of nanoparticle at 250K because there was no evident variation in the width of the first peak in the RDFs. Even if the outer thickness of the present equivalent continuum model is chosen as a specific value of 4.8 Å in our study, other values larger or smaller than this value can also be used. The thickness values of the interphase are arranged in **Table B.6**. Because there is no evident variation with respect to the radius of the nanoparticle, the initial interphase thickness at 250 K was set as 7.67 Å by averaging the values in **Table B.6**. Meanwhile, from the cell size of the nanocomposites at 250K, the volume fraction of the nanoparticle in each unit cell was calculated and obtained as 5.98% with negligible deviation according to the size of embedded nanoparticle.

After the volume fraction of the interphase was determined, the stiffness and CTE of the interphase was obtained by manipulating the closed form solution Eqs.(B.4)-(B.5) and Eqs.(B.14)-(B.15) with respect to the stiffness of the interphase [163] as,

$$\mathbf{C}_i = \mathbf{C}_{inf} \left[ \mathbf{I} - \left( f_i \mathbf{B}^{-1} \left( \mathbf{C}_{inf}^{-1} \mathbf{C} \mathbf{S} - \mathbf{S} + \mathbf{I} \right) + \mathbf{S} \right)^{-1} \right] \quad (B.17)$$

$$\mathbf{B} = \mathbf{I} + (\mathbf{S} - \mathbf{I})(f_p \mathbf{\Lambda}_p + f_m \mathbf{\Lambda}_m) - \mathbf{C}_{inf}^{-1} \mathbf{C} (\mathbf{I} + \mathbf{S}(f_p \mathbf{\Lambda}_p + f_m \mathbf{\Lambda}_m)) \quad (B.18)$$

$$\alpha_i = -\frac{1}{f_i} \left[ \Lambda_i (\mathbf{S} - \mathbf{I}) + \mathbf{I} \right]^{-1} \left\{ \mathbf{C}^{-1} (\mathbf{I} + \Lambda \mathbf{S}) \lambda \right. \\ \left. - f_p \left[ \Lambda_p (\mathbf{S} - \mathbf{I}) + \mathbf{I} \right] \mathbf{C}_p^{-1} \lambda_p - f_m \left[ \Lambda_m (\mathbf{S} - \mathbf{I}) + \mathbf{I} \right] \mathbf{C}_m^{-1} \lambda_m \right\} \quad (\text{B.19})$$

Before calculating the stiffness and CTE of the interphase, the Young's moduli, shear moduli, and the CTEs of the nanocomposites were semi-log fitted in terms of the particle radius at each temperature to prevent undesirable results due to the fluctuation of the results in MD simulations. For example, because the CTE and stiffness of the interphase are coupled variables as shown in Eq.(B.7), the resultant CTE of the interphase can be obtained as a negative value or extreme value according to the fluctuation of the stiffness of the nanocomposites.

As the MD simulation results at each temperature clearly show the particle-size effect of nanocomposites, and as the size effect gradually diminishes with increasing the size of nanoparticles, it is reasonably assumed that the thermoelastic properties of the nanocomposites approach certain values where the contribution of the interphase is negligible. To reflect this physics into the current bridging model, the fitted curve was targeted to converge to the conventional Mori-Tanaka two phase micromechanics solutions. Thus, the semi-log fitted elastic moduli and CTEs were represented here as  $y$ , which is defined as an exponential function of the particle radius given as,

$$y = y(r_p) = y|_{M-T} + C_2 \times \exp(C_3 \times r_p) \quad (\text{B.20})$$

where the  $r_p$  is the radius of the nanoparticle,  $y|_{M-T}$  means the converged point obtained from Mori-Tanaka method (for the prediction of micromechanical solution which

does not consider the size effect of nanoparticles) [169], and the coefficients  $C_2$  and  $C_3$  are the fitting coefficients. After calculating the coefficients, all the thermoelastic properties of the nanocomposites at the same composition were reproduced from the fitted function and used as input values to Eqs.(B.4)-(B.5) and Eqs.(B.14)-(B.15) to predict interphase properties.

The interphase properties at an elevated temperature can be obtained from the same process that was used to obtain the interphase properties at the reference temperature. However, the thickness (volume fraction) of the interphase at an elevated temperature must be determined carefully as the CTE of the interphase is dependent on the embedded particle size. Therefore, the thermal strain of the interphase induced by thermal loading differs according to the size of the embedded nanoparticle. Consequently, the thickness of the interphase at an elevated temperature is not a constant value but differs with the size of the particle.

Once the CTE of the interphase at the reference temperature is determined, the thermal eigenstrain of the interphase at an elevated temperature can be obtained from Eq.(B.7). Then, both the farfield strain  $\boldsymbol{\varepsilon}^0$  and the thermal strain of the interphase at the elevated temperature can be obtained from Eq.(B.12) and Eq.(B.10) respectively. Then, the linear CTE of the interphase inside the unit cell of a nanocomposite can be obtained from the thermal strain of the interphase as,

$$\boldsymbol{\alpha}_i^{comp} = \frac{\boldsymbol{\varepsilon}_i}{\theta} \quad (\text{B.21})$$

where the superscript ‘comp’ indicates the overall composite domain. Here, it is noticed that  $\alpha_i^{comp}$  is obtained from the real amount of thermal expansion that the interphase experiences inside the nanocomposite. Then, volumetric change of the interphase after  $\theta$  K of thermal loading can be obtained as,

$$V_{(250+\theta)K} = V_{250K} \left(1 + \alpha_i^{comp} \theta\right)^3. \quad (B.22)$$

From the volume change, the volume fraction of the interphase at the elevated temperature can be calculated from the cell length of the nanocomposite at the elevated temperature. Consequently, the Young’s modulus, shear modulus, and the CTE at the elevated temperature can be obtained again from Eqs.(B.4)-(B.5) and Eqs.(B.14)-(B.15). The volume of the nanocomposite at the elevated temperature that is required to calculate the volume fraction of the interphase can be either obtained from the raw MD simulation results or reproduced from the CTE of the nanocomposite given in **Table B.3** and the volume of nanocomposite at the reference state using the same relation shown in Eq.(B.19). In this study, the latter approach is chosen to update the volumes of the nanocomposites in micromechanics modeling.

The CTE of the interphase obtained from the thermal strain at this stage is different from the CTE that is calculated from Eq.(B.19) because the real amount of thermal expansion of the interphase inside of the nanocomposite is different from that of the condition in which the interphase material is thermally expanded without any interaction with other neighboring phase materials. On the other hand, the CTE of the interphase obtained from Eq.(B.19) is the pure CTE of the interphase as a constituent of the

nanocomposite. Likewise, volumetric changes of the embedded particle and matrix in the nanocomposites are not the same as when the particle and the matrix in nanocomposites are solely experience thermal expansion as an individual material.

The flow chart of the proposed micromechanics bridging process to characterize the interphase properties are shown in **Figure B.9**. According to the temperature change from 250K to 550K, all the thermoelastic properties of the interphase are updated every 50K. Because the volume change of the interphase at each temperature can be obtained from Eq.(B.22), the thickness change can also be estimated and is shown in **Figure B.10**. Below the glass transition temperature of 410K, the thickness of the interphase slightly increases as the external temperature increases. Passing through the glass transition temperature, the thickness of the interphase shows more rapid change at the rubbery state than at the glassy state, like the volumetric changes of the nanocomposites and the epoxy matrix. Thus, the thermal behavior of the interphase is similar to the glass transition behavior of the matrix polymer.

Together with the thickness (volumetric) change of the interphase, we can characterize the variation of the thermomechanical properties of the interphase and compare them with those of the pure epoxy matrix phase to elucidate the contribution of the thermomechanical properties of interphase to the overall thermoelastic properties of nanocomposites. The average CTEs of the interphases of the five nanocomposites unit cells calculated from Eq.(B.19) in glassy and rubbery states are compared with those of the pure epoxy matrix in **Figure B.11**. In a glassy state, the CTEs of the interphases were 43% lower



than that of the epoxy matrix, indicating that the interphase act as an intermediate anchor block that prevents the outward diffusion of the individual molecules in the pure matrix region, which is thermally tightly anchored by the nanoparticle as well. Even though the CTE of the interphase is obtained from the micromechanics constitutive relation by combining the MD simulations with the continuum model, the difference between the CTEs of the interphase and matrix suggests an important structure-property relationship that can explain the superiority of the nanoparticles to the conventional fillers, and the filler-size dependency of the CTE of a nanocomposite. Due to the densely packed and subsequent immobilized structure of the interphase, the atoms at the interphase are less diffusive even when their kinetic energy is equally increased to that of the pure matrix region at an elevated temperature. In a rubbery state, the CTE of the interphase is still distinguishably lower than that of the epoxy matrix, although the difference is less than that of the glassy state – only 24% difference between the CTEs of interphase and epoxy matrix in a rubbery state.

#### **B.4.2. Description of the properties as a function of the particle size and temperature**

Once the volume fraction and thermoelastic properties of the interphase at each temperature considered in MD simulations are decided, they were represented as continuous functions in terms of temperature as well as the particle radius to describe their

particle-size dependency and their global thermal behavior. Here, the size-dependent elastic stiffness of the nanocomposites is affected by not only the stiffness but also the volume fraction of the interphase. Therefore, the concept of ‘effective moduli of interphase’  $\phi$ , which are weighted by the their corresponding volume fraction, is defined as,

$$\phi^E = E_i \times f_i \quad \text{and} \quad \phi^G = G_i \times f_i \quad (\text{B.23})$$

where the  $E_i$  and  $G_i$  are the elastic and shear moduli of the interphase, respectively, which can be calculated from the stiffness of the interphase. In addition, the effective moduli  $\phi^E$  and  $\phi^G$  are defined as functions of external temperature to cover ‘glassy’, ‘transitional’, and ‘rubbery’ states in order to describe the size effect at various temperatures. Thus,  $\phi^E$  and  $\phi^G$  are firstly fitted into exponential functions of the particle radius at each temperature. Here, only two end-point temperatures for each temperature domain, for an example, moduli at 250K and 350K in the glassy state are used in least square fit; thus, the moduli at 300K naturally become the validation point to examine the performance of the present bridging process. Then, the coefficients obtained from the previous least square fit are defined as a linear function of the external temperature again and the coefficients are obtained from the same least square approximations. Therefore, functional forms of the  $\phi^E$  and  $\phi^G$  finally obtained from this process are given as,

$$\phi^E = \phi^E(r_p, T) = \exp(e_1 + e_2 \times T) \times r_p^{e_3 + e_4 \times T} \quad (\text{B.24})$$

$$\phi^G = \phi^G(r_p, T) = \exp(g_1 + g_2 \times T) \times r_p^{g_3 + g_4 \times T} \quad (\text{B.25})$$

where  $e_1 \sim e_4$  and  $g_1 \sim g_4$  are the regression coefficients. Similar to the elastic moduli, the

volume fraction of the interphase should also be defined as a function of the particle radius and external temperature given as,

$$f_i = f_i(r_p, T) = \exp(f_1 + f_2 \times T) \times r_p^{f_3 + f_4 \times T} \quad (\text{B.26})$$

where  $f_1 \sim f_4$  are the regression coefficients.

The variations of the Young's moduli of the interphases of the nanocomposites according to temperature change are compared with each other in **Figure B.12**. Similar to the CTEs, the elastic moduli of the interphases derived from Eq. (B.17) and the MD simulation results are higher than that of the pure epoxy. Passing through the glass transition region from rubbery state to glassy state, the slopes of the moduli-temperature relation of the interphases are similar with that of the pure epoxy; thus, a clear filler-size effect appears at the glassy state than at the rubbery state.

As the radii of the embedded nanoparticles decrease, the moduli of the corresponding interphases decrease, unlike the moduli of the nanocomposites. However, this tendency cannot solely explain the particle size effect — smaller nanoparticles are superior to larger ones — because the volume fraction of the interphase which describes the relative contribution of the interphase in the constitutive equations varies according to the radius of the embedded particle, i.e. the volume fraction of the interphase increases as the radius of the nanoparticle decreases. The weighted moduli of the interphases by volume fractions are compared in **Figure B.13**. Contrary to the moduli-temperature relation, the weighted moduli increase as the radii of the nanoparticles decrease, and the moduli of the smaller nanoparticles increase faster than those of the larger ones as the temperature

decreases below the glass transition temperature.

From the assumption that the elastic stiffness and CTE of a nanoparticle are independent of temperature, these properties do not need to be defined as a function of the particle radius. However, because the Young's modulus and shear modulus of epoxy matrix depend on temperature, they should be defined as a function of temperature as,

$$E_m = em_1 \times T + em_2 \quad \text{and} \quad G_m = gm_1 \times T + gm_2 \quad (\text{B.27})$$

where  $em_1 \sim em_2$  and  $gm_1 \sim gm_2$  are the regression coefficients. Similar to the decomposition of the temperature domain into three regions, the Young's modulus and shear modulus of the matrix are defined as a linear function of the temperature in glassy, transitional and rubbery states independently. Hence, a total of six coefficients are obtained from Eq.(B.27). All the coefficients to describe particle-size dependent thermoelastic behavior are arranged in **Table B.7**.

### **B.4.3. Estimation of the thermoelastic properties of nanocomposites with validation**

Once the particle-size dependent thermoelastic properties of the interphase and the thermoelastic properties of the matrix are regressed as functions of particle radius and temperature, the thermoelastic properties of the nanocomposites at various particle radii under wide range of temperatures can be directly obtained from the micromechanics model itself. The elastic moduli of nanocomposites obtained from the present bridging model are

compared with the MD simulation results in **Figure B.14**. In all cases, the particle-size dependent elastic moduli are accurately reproduced from the proposed multiscale bridging model. Especially, the elastic moduli obtained from the proposed bridging model at 300K, 400K, and 500K, which were not used in the fitting process, match very well with the MD simulation results.

To demonstrate the accuracy of the interphase properties and to confirm the current micromechanics based bridging model, a FE analysis is performed to calculate the overall elastic moduli of the nanocomposites at each temperature. In FE analysis, the elastic moduli of the matrix and particle obtained from MD simulation are used while those of the interphase obtained from the micromechanics bridging model are used as input values. At the same time, the thickness of the interphase at each temperature is also extracted from the micromechanics bridging model. In finite element analysis, multi-inclusion unit cell are modeled by MSC Nastran<sup>®</sup> software (See **Figure B.15**) and simple uniaxial tension tests under multi point constraints are performed to calculate the elastic moduli of the nanocomposites.

The elastic moduli calculated from the FE analysis at every temperature considered in this study are depicted in **Figure B.16** and compared with the results from MD simulations and the proposed micromechanics bridging model, and the results match quite well each other. Thus, it can be confirmed that the thermoelastic properties of the interphase are physically accurate and meaningful and that the proposed model can be efficiently used to estimate the overall thermoelastic properties of nanocomposites at any

particle radius and volume fraction, and even at any temperature condition with consideration of the particle size effect and the glass transition behavior of polymer based nanocomposites.

It is worth noting that the particle size dependency in thermoelastic properties of nanocomposites observed from the current multiscale simulation scheme is qualitatively matched with the other closely related references. Together with the precedent reports presented by our research group, many studies have been performed the analyses [44,45,56,163,165] and the experiments [41,49,170,171] to derive the thermoelasticity of polymeric nanocomposites. Especially, Jang et al. [49] successfully derived the size effect and the effective interphase properties of epoxy/silica nanocomposites through the experiment and the finite element analysis which is very similar to multiscale bridging method developed by our research group. However, most of the studies concerning size effect of nanocomposites have discussed the thermoelastic properties and the interphase effect only at glassy state. However, current MD simulation and the present multiscale bridging model prediction consider particle size effect not only at the glassy but at the transitional and rubbery states. Hence, this study makes a meaningful contribution to the extension of the nano-continuum bridging methodology for predicting the thermoelastic behavior of polymeric nanocomposites in wide range of temperature to which the nanocomposites can be exposed in real environment. This model can play a leading role and serve as useful reference in the relevant research field for design and analysis of nanocomposites.

**Table B.6.** Determining the initial interphase thickness by radial density distribution.

System	Radius (Å)	Peak distance (Å)	Interphase thickness (Å)
E06	5.18	8.05	7.67
E18	7.54	10.15	7.41
E30	9.00	11.95	7.75
E42	10.00	13.25	8.05
E54	10.90	13.55	7.45

**Table B.7.** Coefficients of fitted variables

$E_m$		$G_m$		$\phi^E$		$\phi^G$		$f_i$	
em1	-0.0117	gm1	-0.0040	e1	6.4825	g1	5.5324	f1	2.5532
em2	7.2050	gm2	2.5400	e2	-0.0098	g2	-0.0102	f2	0.0001
(a) Glass temp. region				e3	-2.0932	g3	-2.0553	f3	-1.6593
				e4	0.0028	g4	0.0028	f4	-0.0001

$E_m$		$G_m$		$\phi^E$		$\phi^G$		$f_i$	
em1	-0.0202	gm1	-0.0076	e1	5.1209	g1	4.9643	f1	2.5529
em2	10.1800	gm2	3.8000	e2	-0.0059	g2	-0.0086	f2	0.0001
<i>(a) Transition temp. region</i>				e3	-0.6647	g3	-1.1573	f3	-1.6592
				e4	-0.0013	g4	0.0002	f4	-0.0001

$E_m$		$G_m$		$\phi^E$		$\phi^G$		$f_i$	
em1	-0.0055	gm1	-0.0019	e1	-5.8505	g1	-8.1640	f1	2.5914
em2	3.5650	gm2	1.2350	e2	0.0185	g2	0.0206	f2	0.0000
(c) Rubber temp. region				e3	3.9913	g3	4.7890	f3	-1.6519
				e4	-0.0117	g4	-0.0130	f4	-0.0001

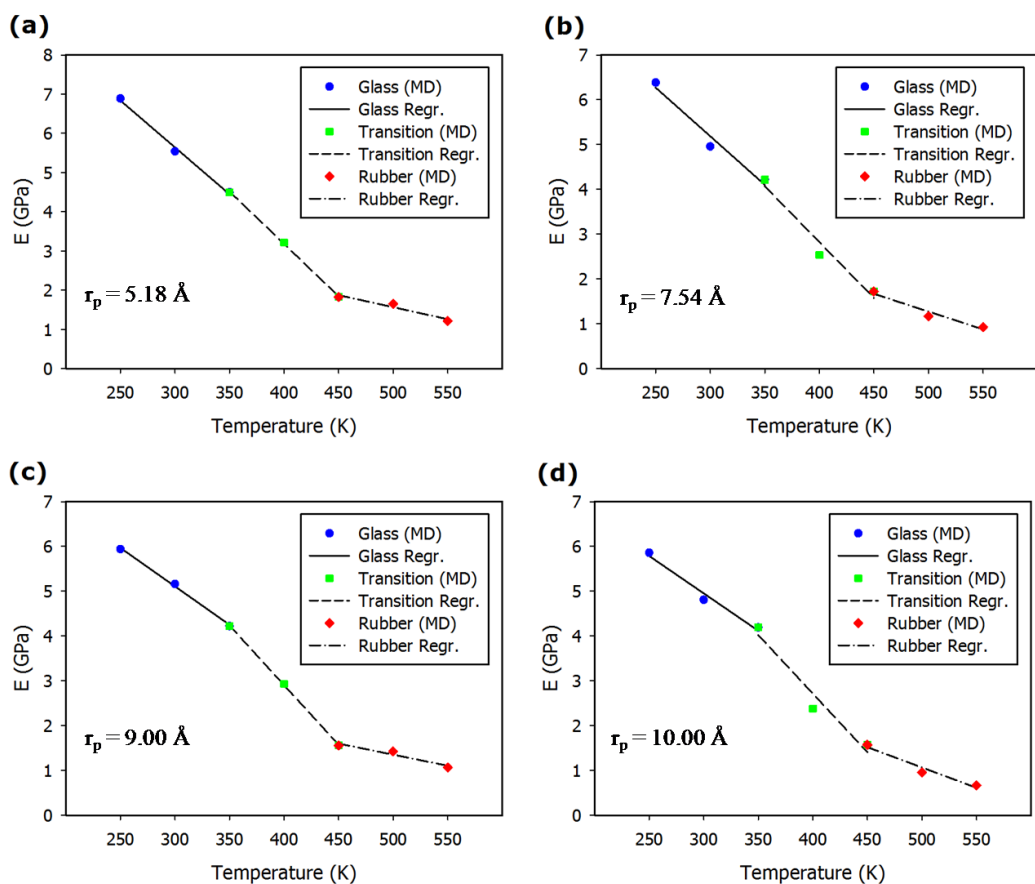


**Figure B.7.** MD results on the thermoelasticity of nanocomposites were linearly regressed for the glass (250K~350K), transition (350K~450K), and rubber (450K~550K) regions. All the cases of nanocomposites showed good linearity in the given temperature ranges of phases.



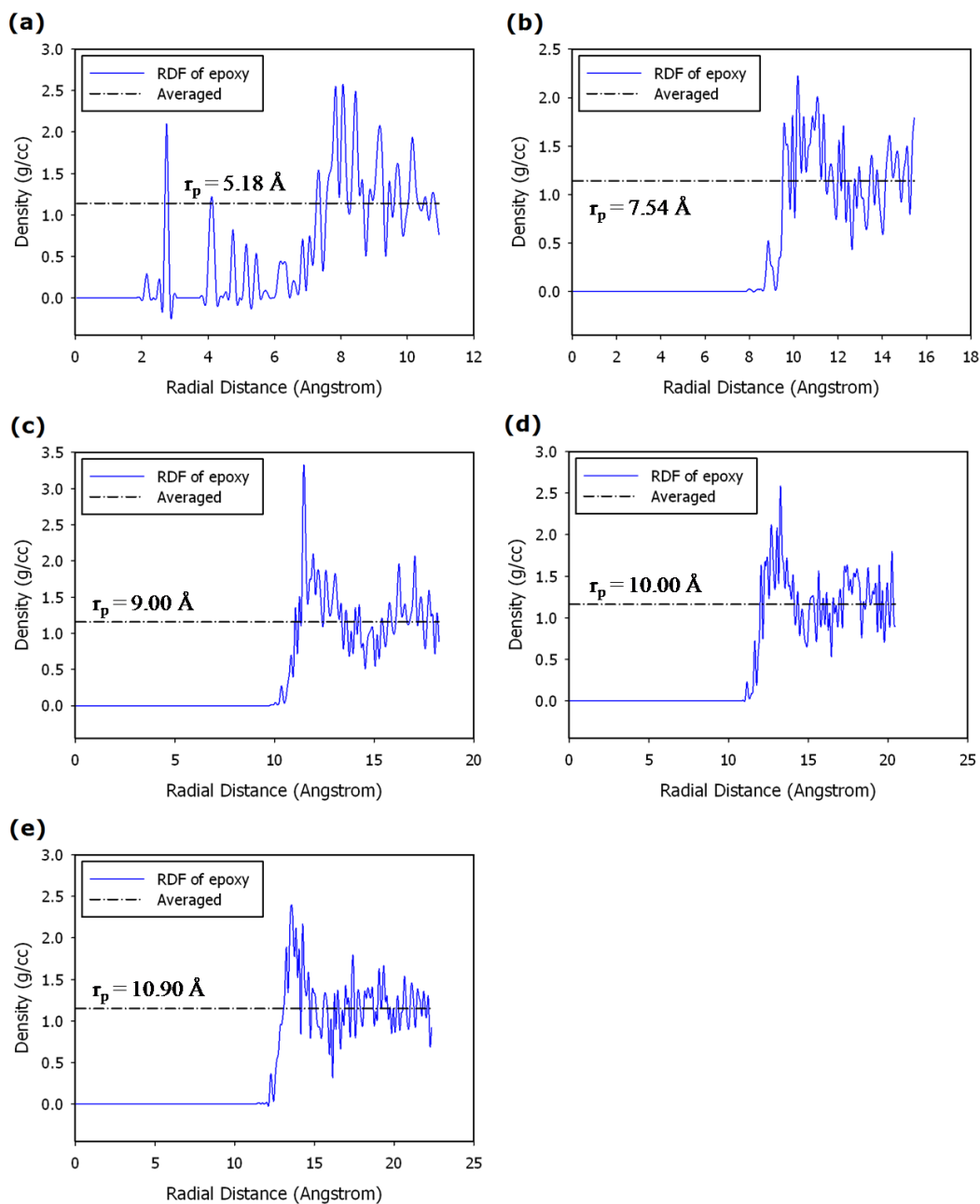


**Figure B.8.** Radial density distribution functions (RDFs) of matrix (epoxy) in modeled unit cells were estimated at the 250K condition, after equilibrated by the NPT ensemble. Both the RDF and averaged density line are depicted until the radial distance reaches the PBC boundary.

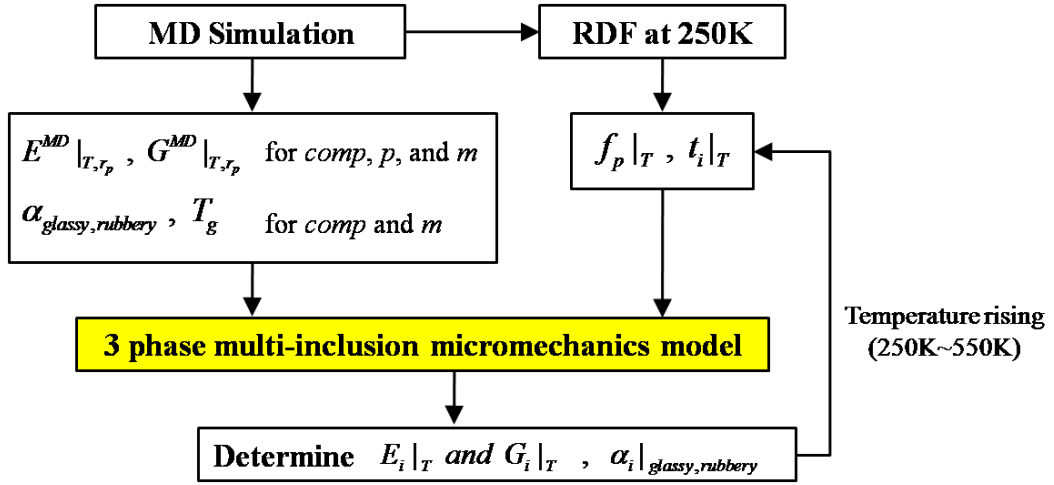


**Figure B.9.** Flowchart for deriving interfacial thermoelastic properties, transferring the MD simulation results into micromechanics model.

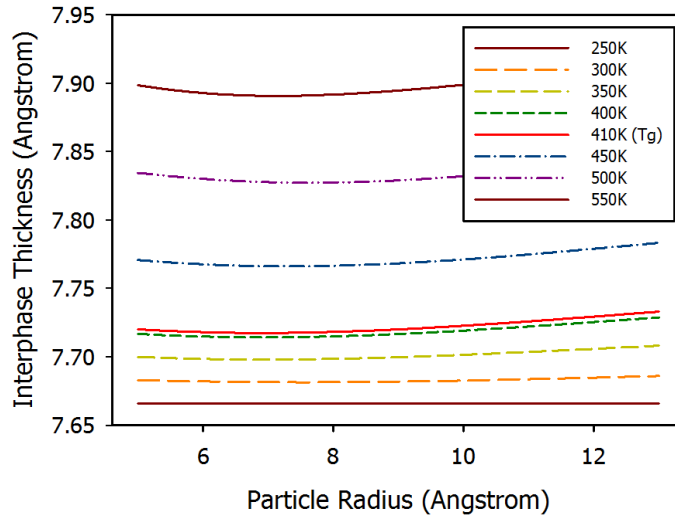


**Figure B.10.** Updated interphase thicknesses by temperature condition

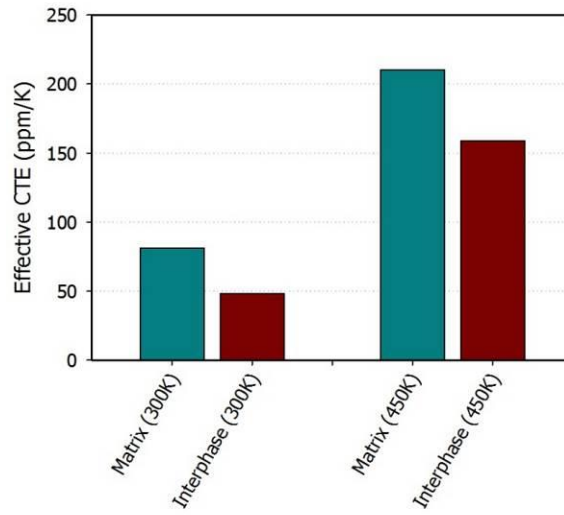


**Figure B.11.** Comparing the CTE between the pure matrix cell and interphase domain in nanocomposite unit cells at room temperature and rubbery state condition.

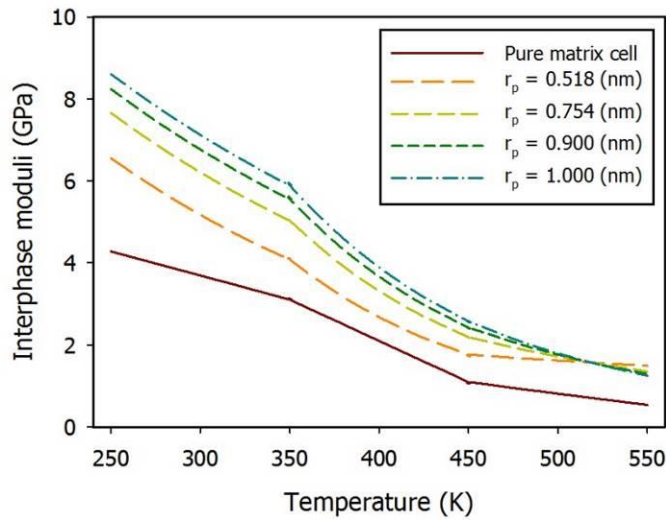


**Figure B.12.** Interphase moduli of nanocomposites derived from three phase multi inclusion micromechanics model.

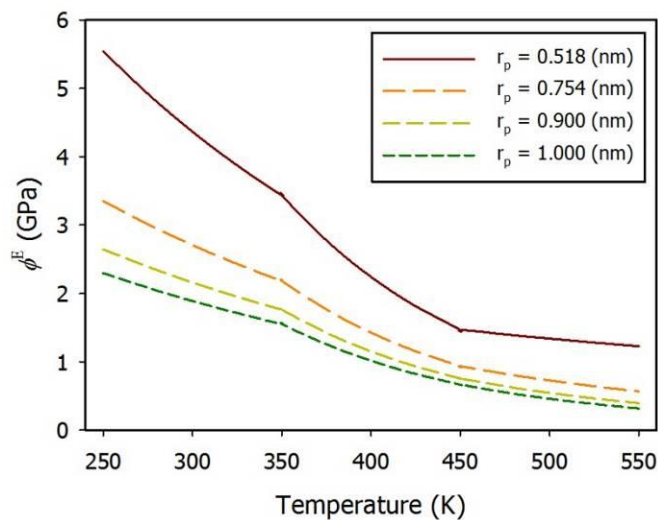


**Figure B.13.** Effective moduli of interphase for a wide range of temperatures

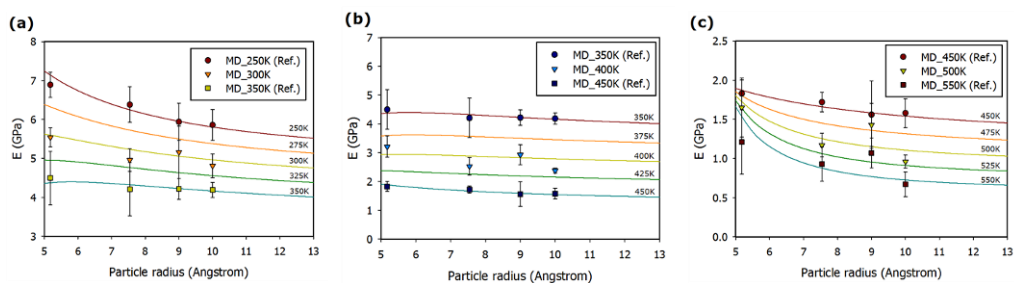


**Figure B.14.** Comparison between the MD simulation and the current bridging model in terms of the embedded particle radius. Here, the error bar on MD results means one deviation of analyzed results (averaged 6 times). Effective moduli of interphase for a wide range of temperatures

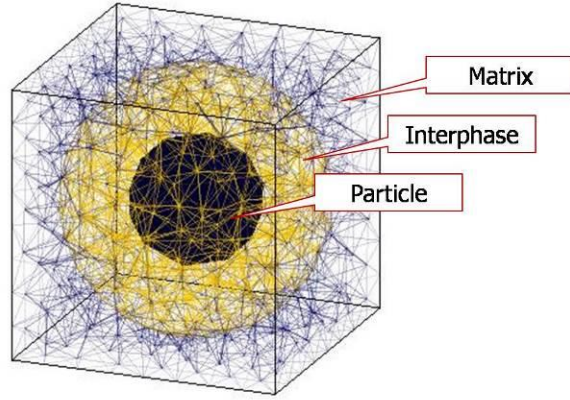


**Figure B.15.** Finite element model to support the feasibility of the thermoelastic property of interphase in nanocomposites derived from the current bridging methodology.

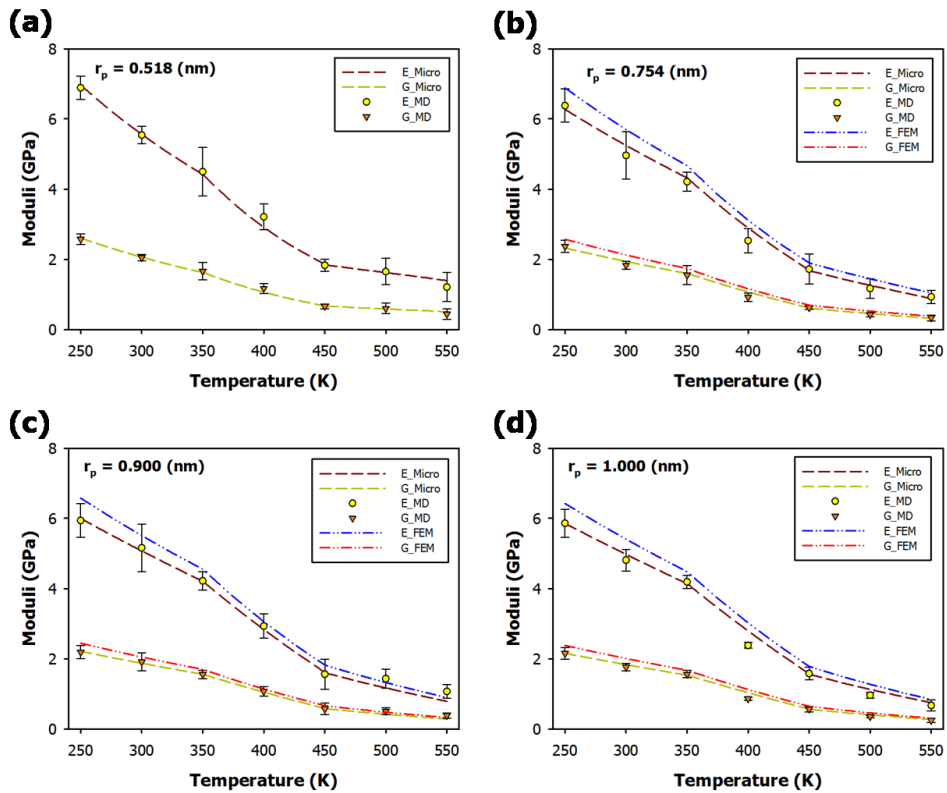


**Figure B.16.** Comparison between the MD simulation results and current bridging model in terms of the temperature condition. The solutions of finite element method are depicted in case of that the diameter of interphase does not exceed the modeled unit cell length.

## **B.5. Summary of Appendix B**

Through this study, the thermoelastic behavior and the particle size effect of epoxy/SiC nanocomposites were verified quantitatively by MD simulations for a wide range of temperatures. From the MD simulations, the unit cells of the modeled nanocomposites showed a glass transition behavior around 410K and drastic changes of the elastic property and CTE through the glassy-to-rubbery transition region. Also, the modeled nanocomposites showed a clear particle size effect not only at the glassy state but also at the rubbery state. The thermomechanical properties and the glass transition behavior obtained from the MD simulations were then parameterized by the multi-inclusion micromechanics model to describe the reinforcing effect of the nanoparticles based on a conventional continuum theory. In the continuum micromechanics model, because the polymer densification around the embedded nanoparticle in a polymeric nanocomposite is the key issue in characterizing the particle size effect on thermomechanical properties of a polymeric nanocomposite, the densified region was defined as an additional phase in constitutive relation of the multi-inclusion model. The thermoelastic properties of the interphase that described the particle size effect were inversely obtained from the closed form solution of the overall thermoelastic properties of nanocomposites with a rigorous consideration of the thermal expansion of the interphase under the free boundary condition. Then, the interphase properties were defined as a function of temperature and embedded particle radius for the micromechanics model to reproduce the glass transition behavior and

the particle size dependent thermoelastic properties that were observed in the MD simulations, and to extrapolate the overall thermoelastic properties at other compositions and temperatures. The proposed bridging methodology efficiently predicted the thermomechanical properties of nanocomposites for a wide range of temperatures with accuracy. Also, the FE analysis of the nanocomposite unit cell model was performed to confirm the accuracy of the thermomechanical properties of the interphase obtained from the proposed bridging methodology. As a result, the derived results from FE showed good agreement with results of the current micromechanics bridging model and the MD simulation.

## References

- [1] Q Zhao, HJ Qi, T Xie. Recent progress in shape memory polymer: New behavior, enabling materials, and mechanistic understanding. *Prog. Polym. Sci.* **2015**, 49-50, 79-120.
- [2] H Meng, G Li. A review of stimuli-responsive shape memory polymer composites. *Polymer* **2013**, 54, 2199-2221.
- [3] MD Hager, S Bode, C Weber, US Shubert. Shape memory polymers: Past, present and future developments. *Prog. Polym. Sci.* **2015**, 49-50, 3-33.
- [4] J Yin, JL Yagüe, MC Boyce, KK Gleason. Biaxially mechanical tuning of 2-D reversible and irreversible surface topologies through simultaneous and sequential wrinkling. *ACS Appl. Mater. Interfaces* **2014**, 6, 2850-2857.
- [5] Y Liu, JK Boyles, J Genzer, MD Dickey, Self-folding of polymer sheets using local light absorption. *Soft Matter* **2012**, 8(6), 1764-1769.
- [6] H Lu, F Liang, Y Yao, J Gou, D Hui. Self-assembled multi-layered carbon nanofiber nanopaper for significantly improving electrical actuation of shape memory polymer nanocomposite. *Compos. B-Eng.* **2014**, 59, 191-195.
- [7] L Sun, WM Huang. Mechanisms of the multi-shape memory effect and temperature memory effect in shape memory polymers. *Soft Matter* **2010**, 6, 4403-4406.
- [8] L Florea, D Diamond, F Benito-Lopez. Photo-responsive polymeric structures



- based on spiropyran. *Macromol. Mater. Eng.* **2012**, 297, 1148-1159.
- [9] T Lan, Y Hu, G Wu, X Tao, W Chen. Wavelength-selective and rebound-able bimorph photoactuator driven by a dynamic mass transport process. *J. Mater. Chem. C* **2015**, 3, 1888-1892.
- [10] H Lu, Y Liu, J Gou, J Leng, S Du. Synergistic effect of carbon nanofiber and carbon nanopaper on shape memory polymer composite. *Appl. Phys. Lett.* **2010**, 96, 084102.
- [11] W Sokolowski, A Metcalfe, S Hayashi, L Yahia, J Raymond. Medical applications of shape memory polymers. *Biomed. Mater.* **2007**, 2(1), S23-S27.
- [12] M Chen, X Xing, Z Liu, Y Zhu, H Liu, Y Yu, F Cheng. Photodeformable polymer material: Towards light-driven micropump applications. *Appl. Phys. A* **2010**, 100, 39-43.
- [13] Y Takashima, S Hatanaka, M Otsubo, M Nakahata, T Kakuta, A Hashidzume, H Yamaguchi, A Harada. Expansion-contraction of photoresponsive artificial muscle regulated by host-guest interactions. *Nat. Commun.* **2012**, 3:1270, 1-8.
- [14] F Cheng, R Yin, Y Zhang, C-C Yen, Y Yu. Fully plastic microrobots which manipulate objects using only visible light. *Soft Matter* **2010**, 6, 3447-3449.
- [15] M Mucha. Polymer as an important component of blends and composites with liquid crystals. *Prog. Polym. Sci.* **2003**, 28, 837-873.
- [16] H Finkelmann, E Nishikawa, GG Pereira, M Warner. A new opto-mechanical effect in solids. *Phys. Rev. Lett.* **2001**, 87(1), 015501.

- [17] Y Yu, M Nakano, T Ikeda. Photomechanics: Directed bending of a polymer film by light. *Nature* **2003**, 425, 145.
- [18] M-H Li, P Keller, B Li, X Wang, M Brunet. Light-driven side-on nematic elastomer actuators. *Adv. Mater.* **2003**, 15 (7-8), 569-572.
- [19] S Fu, Y Zhao. Orientation of azobenzene mesogens in side-chain liquid crystalline polymers: Interplay between effects of mechanical stretching, photoisomerization and thermal annealing. *Macromolecules* **2015**, 48(15), 5088-5098.
- [20] F Cheng, Y Zhang, R Yin, Y Yu. Visible light induced bending and unbending behavior of crosslinked liquid-crystalline polymer films containing azotolane moieties. *J. Mater. Chem.* **2010**, 20, 4888-4896.
- [21] S Kobatake, S Takami, H Muto, T Ishikawa, M Irie. Rapid and reversible shape changes of molecular crystals on photoirradiation. *Nature* **2007**, 446, 778-781.
- [22] J Mamiya, A Kuriyama, N Yokota, M Yamada, T Ikeda. Photomobile polymer materials: Photoresponsive behavior of cross-linked liquid-crystalline polymers with mesomorphic diarylethenes. *Chem. Eur. J.* **2015**, 21, 3174-3177.
- [23] V Shibaev, A Bobrovsky, N Boiko. Photoactive liquid crystalline polymer systems with light-controllable structure and optical properties. *Prog. Polym. Sci.* **2003**, 28, 729-836.
- [24] Y Norikane, E Uchida, S Tanaka, F Fujiwara, E Koyama, R Azumi, H Akiyama, H Kihara, M Yoshida. Photoinduced crystal-to-liquid phase transitions of azobenzene derivatives and their application in photolithography processes

- through a solid-liquid patterning. *Org. Lett.* **2014**, 16, 5012-5015.
- [25] S Xu, Y Li, Y Liu, J Sun, H Ren, S-T Wu. Fast-response liquid crystal microlens *Micromachines* **2014**, 5(2), 300-324.
- [26] Y Choi, J-H Park, J-H Kim, S-D Lee. Fabrication of a focal length variable microlens array based on a nematic liquid crystal. *Opt. Mater.* **2003**, 1-3, 643-646.
- [27] Y Choi, H-R Kim, K-H Lee, Y-M Lee, J-H Kim. A liquid crystalline polymer microlens array with tunable focal intensity by the polarization control of a liquid crystal layer. *Appl. Phys. Lett.* **2007**, 91, 221113.
- [28] TJ White, DJ Broer. Programmable and adaptive mechanics with liquid crystal polymer networks and elastomers. *Nat. Mater.* **2015**, 14, 1087-1098.
- [29] J Iwicky, E Ludwig, M Källäne, J Buck, F Köhler, R Herges, L Kipp, K Rosnagel. Photoswitching of azobenzene multilayers on a layered semiconductor. *Appl. Phys. Lett.* **2010**, 97, 063112.
- [30] S Iamsaard, SJ Aßhoff, B Matt, T Kudernac, JJLM Cornelissen, SP Fletcher, N Katsonis. Conversion of light into macroscopic helical motion. *Nat. Chem.* **2014**, 6, 229-235.
- [31] M Yamada, M Kondo, J Mamiya, Y Yu, M Kinoshita, CJ Barrett, T Ikeda. Photomobile polymer materials: Towards light-driven plastic motors. *Angew. Chem. Int. Ed.* **2008**, 47, 4986-4988.
- [32] D Liu, CWM Bastiaansen, JMJ Toonder, DJ Broer. Photo-switchable surface topologies in chiral nematic coatings. *Angew. Chem. Int. Ed.* **2012**, 51, 892-896.

- [33] D Liu, DJ Broer. New insights into photoactivated volume generation boost surface morphing in liquid crystal coatings. *Nat. Commun.* **2015**, 6, 8334.
- [34] KD Harris, R Cuypers, P Scheibe, CL van Oosten, CWM Bastiaansen, J Lub, DJ Broer. Large amplitude light-induced motion in high elastic modulus polymer actuators. *J. Mater. Chem.* **2005**, 15, 5043-5048.
- [35] A Priimagi, A Shimamura, M Kondo, T Hiraoka, S Kubo, J Mamiya, M Kinoshita, T Ikeda, A Shishido. Location of the azobenzene moieties within the cross-linked liquid crystalline polymers can dictate the direction of photoinduced bending. *ACS Macro Lett.* **2012**, 1, 96-99.
- [36] F Brömmel, W Stille, H Finkelmann, A Hoffmann. Molecular dynamics and biaxiality of nematic polymers and elastomers. *Soft Matter* **2011**, 7, 2387-2401.
- [37] Y Sawa, F Ye, K Urayama, T Takigawa, V Gimenez-Pinto, RLB Selinger, JV Selinger. Shape selection of twist-nematic-elastomer ribbons. *Proc. Natl. Acad. Sci. U.S.A.* **2011**, 108(16), 6364-6368.
- [38] T Ozawa, M Kondo, J Mamiya, T Ikeda. Enhancement of mechanical stability in hydrogen-bonded photomobile materials with chemically modified single-walled carbon nanotubes. *J. Mater. Chem. C* **2014**, 2, 2313-2315.
- [39] L Yu, Z Cheng, Z Dong, Y Zhang, H Yu. Photomechanical response of polymer-dispersed liquid crystals/graphene oxide nanocomposites. *J. Mater. Chem. C* **2014**, 2, 8501-8506.
- [40] M Chambers, H Finkelmann, M Remškar, A Sánchez-Ferrer, B Zalar, S Žumer.

- Liquid crystal elastomer-nanoparticle systems for actuation. *J. Mater. Chem.* **2009**, 19, 1524-1531.
- [41] WK Goertzen, MR Kessler. Thermal expansion of fumed silica/cyanate ester nanocomposites. *J. Appl. Polym. Sci.* **2008**, 109, 647-653.
- [42] SE Harton, SK Kumar, H Yang, T Koga, K Hicks, H Lee, J Mijovic, M Liu, RS Vallery, DW Gidley. Immobilized polymer layers on spherical nanoparticles. *Macromolecules* **2010**, 43, 3415-3421.
- [43] TVM Nodoro, E Voyiatzis, A Ghanbari, DN Theodorou, MC Böhm, F Müller-Plathe. Interface of grafted and ungrafted silica nanoparticles with a polystyrene matrix: Atomistic molecular dynamics simulations. *Macromolecules* **2011**, 44, 2316-2327.
- [44] S Yu, S Yang, M Cho. Multi-scale modeling of cross-linked epoxy nanocomposites. *Polymer* **2009**, 50, 945-952.
- [45] S Yang, M Cho. Scale bridging method to characterize mechanical properties of nanoparticle/polymer nanocomposites. *Appl. Phys. Lett.* **2008**, 93, 043111.
- [46] S Yu, S Yang, M Cho. Multiscale modeling of cross-linked epoxy nanocomposites to characterize the effect of particle size on thermal conductivity. *J. Appl. Phys.* **2011**, 110, 124302.
- [47] J Kratochvíla, A Boudenne, I Krupa. Effect of filler size on thermophysical and electrical behavior of nanocomposites based on expanded graphite nanoparticles filled in low-density polyethylene matrix. *Polym. Composites* **2013**, 34(2), 149-

- [48] R Qiao, LC Brinson. Simulation of interphase percolation and gradients in polymer nanocomposites. *Compos. Sci. Technol.* **2009**, 69, 491-499.
- [49] J-S Jang, B Bouveret, J Suhr, RF Gibson. Combined numerical/experimental investigation of particle diameter and interphase effects on coefficient of thermal expansion and Young's modulus of SiO<sub>2</sub>/Epoxy nanocomposites. *Polym. Composite* **2012**, 33(8), 1415-1423.
- [50] J-L Tsai, S-H Tzeng. Characterizing mechanical properties of particulate nanocomposites using micromechanical approach. *J. Compos. Mater.* **2008**, 42(22), 2345-2361.
- [51] M Mortezaei, MHN Famili, M Kokabi. The role of interfacial interactions on the glass-transition and viscoelastic properties of silica/polystyrene nanocomposite. *Compos. Sci. Technol.* **2011**, 71(8), 1039-1045.
- [52] D Fragiadakis, P Pissis, L Bokobza. Glass transition and molecular dynamics in poly(dimethylsiloxane)/silica nanocomposites. *Polymer* **2005**, 46, 6001-6008.
- [53] MA Bhuiyan, RV Pucha, M Karevan, K Kalaitzidou. Tensile modulus of carbon nanotube/polypropylene composites – A computational study based on experimental characterization. *Comp. Mater. Sci.* **2011**, 50, 2347-2353.
- [54] MA Bhuiyan, RV Pucha, J Worthy, M Karevan, K Kalaitzidou. Defining the lower and upper limit of the effective modulus of CNT/polypropylene composites through integration of modeling and experiments. *Compos. Struct.* **2013**, 95, 80-

87.

- [55] S Yang, S Yu, J Ryu, J-M Cho, W Kyoung, D-S Han, M Cho. Nonlinear multiscale modeling approach to characterize elastoplastic behavior of CNT/polymer nanocomposites considering the interphase and interfacial imperfection. *Int. J. Plasticity* **2013**, 41, 124-146.
- [56] M Cho, S Yang, S Chang, S Yu. A study on the prediction of the mechanical properties of nanoparticulate composites using the homogenization method with the effective interface concept. *Int. J. Numer. Meth Engng.* **2011**, 85(12), 1564-1583.
- [57] MR Ayatollahi, S Shadlou, MM Shokrieh. Multiscale modeling for mechanical properties of carbon nanotube reinforced nanocomposites subjected to different types of loading. *Compos. Struct.* **2011**, 93, 2250-2259.
- [58] F Otero, X Martínez, S Oller, O Salomón. Study and prediction of the mechanical performance of a nanotube-reinforced composite. *Compos. Struct.* **2012**, 94, 2920-2930.
- [59] YM Shabana. A micromechanical model for composites containing multi-layered interphase. *Compos. Struct.* **2013**, 101, 265-273.
- [60] S Ben, J Zhao, T Rabczuk. A theoretical analysis of interface debonding for coated sphere with functionally graded interphase. *Compos. Struct.* **2014**, 117, 288-297.
- [61] JM Ilnytskyi, D Neher, M Sphiannikova. Opposite photo-induced deformations in azobenzene-containing polymers with different molecular architecture: Molecular

- dynamics study. *J. Chem. Phys.* **2011**, 135(4), 044901.
- [62] JM Ilnytskyi, D Neher. Structure and internal dynamics of a side chain liquid crystalline polymer in various phases by molecular dynamics simulations: A step towards coarse graining. *J. Chem. Phys.* **2007**, 126(17), 174905.
- [63] V Toshchevikov, M Saphiannikova, G Heinrich. Light-induced deformation of azobenzene elastomers: A regular cubic network model. *J. Phys. Chem. B* **2012**, 116(3), 913-924.
- [64] C Li, C-W Lo, D Zhu, C Li, Y Liu, H Jiang. Synthesis of a photoresponsive liquid-crystalline polymer containing azobenzene. *Macromol. Rapid Commun.* **2009**, 30, 1928-1935.
- [65] Accelrys Inc. San Diego. <http://www.accelrys.com/>
- [66] Sandia National Laboratories. <http://lammps.sandia.gov/>
- [67] H Sun. Force field for computation of conformational energies, structures, and vibrational frequencies of aromatic polyesters. *J. Comput. Chem.* **1994**, 15(7), 752-768.
- [68] V Varshney, SS Patnaik, AK Roy, BL Farmer. A molecular dynamics study of epoxy-based networks: Cross-linking procedure and prediction of molecular and material properties. *Macromolecules* **2008**, 41, 6837-6842.
- [69] F Zapata, MA Fernández-González, D Rivero, Á Álvarez, M Marazzi, LM Frutos. Toward an optomechanical control of photoswitches by tuning their spectroscopical properties: Structural and dynamical insight into azobenzene. *J.*



- Chem. Theory Comput.* **2014**, 10, 312-323.
- [70] M Biswas, I Burghardt. Azobenzene photoisomerization-induced destabilization of B-DNA. *Biophys. J.* **2014**, 107, 932-940.
- [71] D Rastädter, M Biswas, I Burghardt. Molecular dynamics study of the controlled destabilization of an RNA hairpin structure by a covalently attached azobenzene switch. *J. Phys. Chem. B* **2014**, 118, 8478-8488.
- [72] PH Nguyen, G Stock. Nonequilibrium molecular dynamics simulation of a photoswitchable peptide. *Chem. Phys.* **2006**, 323, 36-44.
- [73] PH Nguyen, S-M Park, G Stock. Nonequilibrium molecular dynamics simulation of the energy transport through a peptide helix. *J. Chem. Phys.* **2010**, 132, 025102.
- [74] Z Tian, J Wen, J Ma. Reactive molecular dynamics simulations of switching processes of azobenzene-based monolayer on surface. *J. Chem. Phys.* **2013**, 139, 014706.
- [75] S Pipolo, S Corni. Wettability of azobenzene self-assembled monolayers. *Langmuir* **2014**, 30(15), 4415-4421.
- [76] H Heinz, RA Vaia, H Koerner, BL Farmer. Photoisomerization of azobenzene grafted to layered silicates: Simulation and experimental challenges. *Chem. Mater.* **2008**, 20(20), 6444-6456.
- [77] A Cembran, F Bernardi, M Garavelli, L Gagliardi, G Orlandi, On the mechanism of the cis-trans isomerization in the lowest electronic states of azobenzene:  $S_0$ ,  $S_1$ , and  $T_1$ . *J. Am. Chem. Soc.* **2004**, 126(10), 3234-3243.

- [78] PM Hogan, AR Tajbakhsh, EM Terentjev. Uv manipulation of order and macroscopic shape in nematic elastomers. *Phys. Rev. E* **2002**, 65(4), 041720.
- [79] T Omori, R Kainuma. Materials science: Alloys with long memories. *Nature* **2013**, 502, 42-44
- [80] V Palmre, D Pugal, KJ Kim, KK Leang, K Asaka, A Aabloo. Nanothorn electrodes for ionic polymer-metal composite artificial muscles. *Sci. Rep.-UK* **2014**, 4, 6176.
- [81] J Song, D Kim, D Lee. Size control in the synthesis of 1-6 nm gold nanoparticles via solvent-controlled nucleation. *Langmuir* **2011**, 27, 13854-13860.
- [82] RJ Tseng, J Huang, J Ouyang, RB Kaner, Y Yang. Polyaniline nanofiber/gold nanoparticle nonvolatile memory. *Nano Lett.* **2005**, 5(6), 1077-1080.
- [83] N Shalkevich, W Escher, T Bürgi, B Michel, L Si-Ahmed, D Poulikakos. On the thermal conductivity of gold nanoparticle colloids. *Langmuir* **2010**, 26(2), 663-670.
- [84] NL Rosi, DA Giljohann, CS Thaxton, AKR Lytton-Jean, MS Han, CA Mirkin. Oligonucleotide-modified gold nanoparticles for intracellular gene regulation. *Science* **2006**, 312(5776), 1027-1030.
- [85] R Shukla, V Bansal, M Chaudhary, A Basu, RR Bhonde, M Sastry. Biocompatibility of gold nanoparticles and their endocytotic fate inside the cellular compartment: A microscopic overview. *Langmuir* **2005**, 21(23), 10644-10654.

- [86] S-T Han, Y Zhou, Z-X Xu, L-B Huang, X-B Yang, VAL Roy. Microcontact printing of ultrahigh density gold nanoparticle monolayer for flexible flash memories. *Adv. Mater.* **2012**, 24(26), 3556-3561.
- [87] J Mirzaei, M Urbanski, H-S Kitzerow, T Hegmann. Synthesis of liquid crystal silane-functionalized gold nanoparticles and their effects on the optical and electro-optic properties of a structurally related nematic liquid crystal. *Chem Phys Chem* **2014**, 15(7), 1381-1394.
- [88] HK Bisoyi, S Kumar. Liquid-crystal nanoscience: An emerging avenue of soft self-assembly. *Chem. Soc. Rev.* **2011**, 40, 306-319.
- [89] R Turanský, M Konôpka, NL Doltsinis, I Štich, D Marx. Optical, mechanical, and opto-mechanical switching of anchored dithioazobenzene bridges. *Chem. Phys. Chem.* **2010**, 11, 345-348.
- [90] SD Evans, SR Johnson, H Ringsdorf, LM Willilams, H Wolf. Photoswitching of azobenzene derivatives formed on planar and colloidal gold surfaces. *Langmuir* **1998**, 14, 6436-6440.
- [91] C Xue, J Xiang, H Nemati, HK Bisoyi, K Gutierrez-Cuevas, L Wang, M Gao, S Zhou, D Yang, OD Lavrentovich, A Urbas, Q Li. Light-driven reversible alignment switching of liquid crystals enabled by azo thiol grafted gold nanoparticles. *Chem. Phys. Chem*, **2015**, 16(9), 1852-1856.
- [92] J Xu, D Bedrov, GD Smith, MA Glaser. Molecular dynamics simulation study of spherical nanoparticles in a nematogenic matrix: Anchoring, interactions, and

- phase behavior. *Phys. Rev. E* **2009**, 79, 011704.
- [93] P Tian, GD Smith, M Glaser. Molecular dynamics simulations studies of nanoparticles in an isotropic liquid crystal matrix: Single particle behavior and pairwise interactions. *J. Chem. Phys.* **2006**, 124, 161101.
- [94] MSS Pereira, AA Canabarro, IN de Oliveira, ML Lyra, LV Mirantsev. A molecular dynamics study of ferroelectric nanoparticles immersed in a nematic liquid crystal. *Eur. Phys. J. E* **2010**, 31, 81-87.
- [95] JA Moreno-Razo, EJ Sambriski, GM Koenig, E Díaz-Herrera, NL Abbott, JJ de Pablo. Effects of anchoring strength on the diffusivity of nanoparticles in model liquid-crystalline fluids. *Soft Matter* **2011**, 7, 6828-6835.
- [96] AZep, MM Wojcik, W Lewandowski, K Sitkowska, A Prominski, J Mieczkowski, D Pocięcha, E Gorecka. Phototunable liquid-crystalline phases made of nanoparticles. *Angew. Chem. Int. Ed.* **2014**, 53, 13725-13728.
- [97] DM Heyes. Pressure tensor of partial-charge and point-dipole lattices with bulk and surface geometries. *Phys. Rev. B* **1994**, 49(2), 755-764.
- [98] AK Subramaniyan, CT Sun. Continuum interpretation of virial stress in molecular simulations. *Int. J. Solids Struct.* **2008**, 45, 4340-4346.
- [99] D Ciprari, K Jacob, R Tannenbaum. Characterization of polymer nanocomposite interphase and its impact on mechanical properties. *Macromolecules* **2006**, 39, 6565-6573.
- [100] TVM Nodoro, MC Böhm, F Müller-Plathe. Interface and interphase dynamics of

- polystyrene chains near grafted and ungrafted silica nanocomposites. *Macromolecules* **2012**, 45(1), 171-179.
- [101] CM Hadden, BD Jensen, A Bandyopadhyay, GM Odegard, A Koo, R Liang. Molecular modeling of EPON-862/graphite composites: Interfaical characteristics for multiple crosslink densities. *Compos. Sci. Technol.* **2013**, 76, 92-99.
- [102] T Ikeda, M Nakano, Y Yu, O Tsutsumi, A Kanazawa. Anisotropic bending and unbending behavior of azobenzene liquid-crystalline gels by light exposure. *Adv. Mater.* **2003**, 15, 201-205.
- [103] J-H Yun, C Li, H Chung, J Choi, M Cho. Photo deformation in azobenzene liquid-crystal network: Multiscale model prediction and its validation. *Polymer* **2015**, 75, 51-56.
- [104] H Chung, J Choi, J-H Yun, M Cho. Nonlinear photomechanics of nematic polymers: Upscaling microscopic behavior to macroscopic deformation. *Sci. Rep.-UK* **2016**, 6, 20026.
- [105] A Acreman, M Kaczmarek, G D'Alessandro. Gold nanoparticle liquid crystal composites as a tunable nonlinear medium. *Phys. Rev. E* **2014**, 90, 012504.
- [106] VM Marx, H Girgis, PA Heiney, T Hegmann. Bent-core liquid crystal (LC) decorated gold nanoclusters: synthesis, self-assembly, and effects in mixtures with bent-core LC hosts. *J. Mater. Chem.* **2008**, 18, 2983-2994.
- [107] M Urbanski, B Kinkead, T Hegmann, H-S Kitzerow. Director field of birefringent stripes in liquid crystal/nanoparticle dispersions. *Liquid Crystals* **2010**, 37(9),

1151-1156.

- [108] H Chung, J Choi, J-H Yun, M Cho. Light and thermal responses of liquid-crystal-network films: A finite element study. *Phys. Rev. E* **2015**, 91, 042503.
- [109] A Buka and WH de Jeu. Diamagnetism and orientational order of nematic liquid crystals. *J. Physique*, **1982**, 43(2), 361-367.
- [110] I Haller. Thermodynamic and static properties of liquid crystals. *Prog. Sol. State Chem.* **1975**, 10(2), 103-118.
- [111] A Sánchez-Ferrer, A Merekalov, H Finkelmann. Opto-mechanical effect in photoactive nematic side-chain liquid-crystalline elastomers. *Macromol. Rapid Commun.* **2011**, 32, 671-678.
- [112] KW Putz, MJ Palmeri, RB Cohn, R Andrews, LC Brinson. Effect of cross-link density on interphase creation in polymer nanocomposites. *Macromolecules* **2008**, 41, 6752-6756.
- [113] B Kim, J Choi, S Yang, S Yu, M Cho. Influence of crosslink density on the interfacial characteristics of epoxy nanocomposites. *Polymer* **2015**, 60, 186-197.
- [114] MP Bendsøe, N Kikuchi. Generating optimal topologies in structural design using a homogenization method. *Comput. Method Appl. M.* **1988**, 71, 197-224.
- [115] JM Guedes, N Kikuchi. Preprocessing and postprocessing for materials based on the homogenization method with adaptive finite element methods. *Comput. Method Appl. M.* **1990**, 83, 143-198.
- [116] R Hill. The elastic behavior of a crystalline aggregate. *P. R. Soc. London* **1952**, 65,

- 349-354.
- [117] GM Odegard, TS Gates, LM Nicholson, KE Wise. Equivalent-continuum modeling of nano-structured materials. *Compos. Sci. Technol.* **2002**, 62(14), 1869-1880.
  - [118] Ł Figiel, CP Buckley. Elastic constants for an intercalated layered-silicate/polymer nanocomposite using the effective particle concept – A parametric study using numerical and analytical continuum approaches. *Comp. Mater. Sci.* **2009**, 44, 1332-1343.
  - [119] A Axelevitch, B Apter, G Golan. Simulation and experimental investigation of optical transparency in gold island films. *Opt. Express* **2013**, 21(4), 4126-4138.
  - [120] J Yun, C Li, H Chung, J Choi, M Cho. Predicting photoisomerization profile of the highly polymerized nematic azobenzene liquid crystal network: First principle calculation. *Chem. Phys. Lett.* **2015**, 627, 20-25.
  - [121] S Yang, M Cho. Scale bridging method to characterize mechanical properties of nanoparticle/polymer nanocomposites. *Appl. Phys. Lett.* **2008**, 93, 043111.
  - [122] M Wang, SM Sayed, L-X Guo, B-P Lin, X-Q Zhang, Y Sun, H Yang. Multi-stimuli responsive carbon nanotube incorporated polysiloxane azobenzene liquid crystalline elastomer composites. *Macromolecules* **2016**, 49, 663-671.
  - [123] AW Hauser, D Liu, KC Bryson, RC Hayward, DJ Broer. Reconfiguring nanocomposite liquid crystal polymer films with visible light. *Macromolecules* **2016**, 49, 1575-1581.

- [124] C Li, Y Liu, C-W Lo, H Jiang. Reversible white-light actuation of carbon nanotube incorporated liquid crystalline elastomer nanocomposites. *Soft Matter* **2011**, 7, 7511-7516.
- [125] W Wang, X Sun, W Wu, H Peng, Y Yu. Photoinduced deformation of crosslinked liquid-crystalline polymer film oriented by a highly aligned carbon nanotube sheet. *Angew. Chem. Int. Ed.* **2012**, 51, 4644-4647.
- [126] X Sun, W Wang, L Qiu, W Guo, Y Yu, H Peng. Unusual reversible photomechanical actuation in polymer/nanotube composites. *Angew. Chem. Int. Ed.* **2012**, 51, 8520-8524.
- [127] S. Yang, J. Choi, M. Cho. Elastic stiffness and filler size effect of covalently grafted nanosilica polyimide composites: Molecular dynamics study. *ACS Appl. Mater. Interfaces* **2012**, 4(9), 4792-4799.
- [128] H. Shin, S. Yang, J. Choi, S. Chang, M. Cho. Effect of interphase percolation on mechanical behavior of nanoparticle-reinforced polymer nanocomposite with filler agglomeration: A multiscale approach. *Chem. Phys. Lett.* **2015**, 635, 80-85.
- [129] J. Liu, Y. Gao, D. Cao, L. Zhang, Z. Guo. Nanoparticle dispersion and aggregation in polymer nanocomposites: Insights from molecular dynamics simulation. *Langmuir* **2011**, 27(12), 7926-7933.
- [130] G.D. Hattemer, G. Arya. Viscoelastic properties of polymer-grafted nanoparticle composites from molecular dynamics simulations. *Macromolecules* **2015**, 48(4), 1240-1255.



- [131] DN Lee. “*Texture and related phenomena*”. The Korean Institute of Metals and Materials, Korea: Hanrimwon Publishing Company, **2006**.
- [132] V Arrighi , IJ McEwen, H Qian, MB Serrano Prieto. The glass transition and interfacial layer in styrene-butadiene rubber containing silica nanofiller. *Polymer* **2003**, 44, 6259-6266.
- [133] S Iijima. Helical microtubules of graphitic carbon. *Nature* **1991**,354,56-58.
- [134] S Iijima, T Ichihashi. Single-shell carbon nanotubes of 1-nm diameter. *Nature* **1993**, 363, 603-605.
- [135] J-P Salvetat, G Andrew, D Briggs, J-M Bonard, RR Bacsá, AJ Kulik, T Stöckli, A Burnham, L Forró. Elastic and shear moduli of single-walled carbon nanotube ropes. *Phys. Rev. Lett.* **1999**, 82, 944-947.
- [136] S Berber, Y-K Kwon, D Tománek. Unusually high thermal conductivity of carbon nanotubes. *Phys. Rev. Lett.* **2000**, 84, 4613-4616.
- [137] JKW Sandler, JE Kirk, IA Kinloch, MSP Shaffer, AH Windle. Ultra-low electrical percolation threshold in carbon-nanotube-epoxy composites. *Polymer* **2003**, 44, 5893-5899.
- [138] A Moisala, Q Li, IA Kinloch, AH Windle. Thermal and electrical conductivity of single- and multi-walled carbon nanotube-epoxy composites. *Compos. Sci. Technol.* **2006**, 66(10), 1285-1288.
- [139] T Tsuda, T Ogasawara, F Deng, N Takeda. Direct measurements of interfacial shear strength of multi-walled carbon nanotube/PEEK composite using a nano-

- pullout method. *Compos. Sci. Technol.* **2011**, 71(10), 1295-1300.
- [140] S Yang, S Yu, M Cho. Influence of Thrower-Stone-Wales defects on the interfacial properties of carbon nanotube/polypropylene composites by a molecular dynamics approach. *Carbon* **2013**, 55, 133-143.
- [141] S Yang, J Choi, M Cho. Intrinsic defect-induced tailoring of interfacial shear strength in CNT/polymer nanocomposites. *Compos. Struct.* **2015**, 127, 108-119.
- [142] V Datsyuk, M Kalyva, K Papagelis, J Parthenios, D Tasis, A Siokou, I Kallitsis, C Galiotis. Chemical oxidation of multiwalled carbon nanotubes. *Carbon* **2008**, 46(6), 833-840.
- [143] Z Spitalsky, D Tasis, K Papagelis, C Galiotis. Carbon nanotube-polymer composites: Chemistry, processing, mechanical and electrical properties. *Prog. Polym. Sci.* **2010**, 35(3), 357-401.
- [144] S Qin, D Qin, WT Ford, DE Resasco, JE Herrera. Functionalization of single-walled carbon nanotubes with polystyrene via grafting to and grafting from methods. *Macromolecules* **2004**, 37(3), 752-757.
- [145] P Liu. Modifications of carbon nanotubes with polymers. *Eur. Polym. J.* **2005**, 41(11), 2693-2703.
- [146] JN Coleman, M Cadek, R Blake, V Nicolosi, KP Ryan, C Belton, A Fonseca, JB Nagy, YK Gun'ko, WJ Blau. High-performance nanotube-reinforced plastics: Understanding the mechanism of strength increase. *Adv. Funct. Mater.* **2004**, 14(8), 791-797.

- [147] Voyiatzis E, Rahimi M, Müller-Plathe F, Böhm MC. How thick is the polymer interphase in nanocomposites? Probing it by local stress anisotropy and gas solubility. *Macromolecules* 2014;47:7878-89.
- [148] S Herasati, LC Zhang, HH Ruan. A new method for characterizing the interphase regions of carbon nanotube composites. *Int. J. Solids Struct.* **2014**, 51, 1781-1791.
- [149] MM Shokrieh, R Rafiee. On the tensile behavior of an embedded carbon nanotube in polymer matrix with non-bonded interphase region. *Compos. Struct.* **2010**, 92, 647-652.
- [150] VA Buryachenko, A Roy, K Lafdi, KL Anderson, S Chellapilla. Multi-scale mechanics of nanocomposites including interface: Experimental and numerical investigation. *Compos. Sci. Technol.* **2005**, 65, 2435-2465.
- [151] KI Tserpes, A Chanteli. Parametric numerical evaluation of the effective elastic properties of carbon nanotube-reinforced polymers. *Compos. Struct.* **2013**, 99, 366-374.
- [152] H Liu, LC Brinson. Reinforcing efficiency of nanoparticles: A simple comparison for polymer nanocomposites. *Compos. Sci. Technol.* **2008**, 68, 1502-1512.
- [153] H Eslami, M Behrouz. Molecular dynamics simulation of a polyamide-66/carbon nanotube nanocomposites. *J. Phys. Chem. C* **2014**, 118, 9841-9851.
- [154] M Hegde, ET Samulski, M Rubinstein, TJ Dingemans. The role of crystallinity in SWCNT-polyetherimide nanocomposites. *Compos. Sci. Technol.* **2015**, 110, 176-187.

- [155] S Masoumi, B Arab, H Valipour. A study of thermo-mechanical properties of the cross-linked epoxy: An atomistic simulation. *Polymer* **2015**, 70, 351-60.
- [156] J-L Tsai, S-H Tzeng, Y-T Chiu. Characterizing elastic properties of carbon nanotubes/polyimide nanocomposites using multi-scale simulation. *Compos. Part B-Eng.* **2010**, 41, 106-115.
- [157] M Parrinello, A Rahman. Crystal structure and pair potentials: A molecular-dynamics study. *Phys Rev Lett* **1980**, 45, 1196-1199.
- [158] M Parrinello, A Rahman. Strain fluctuations and elastic constants. *J. Chem. Phys.* **1982**, 76, 2662-2666.
- [159] S Yang, S Yu, W Kyoung, D-S Han, M Cho. Multiscale modeling of size-dependent elastic properties of carbon nanotube/polymer nanocomposites with interfacial imperfections. *Polymer* **2012**, 53, 623-633.
- [160] LG Zhou, SQ Shi. Adsorption of foreign atoms on Stone-Wales defects in carbon nanotube. *Carbon* **2003**, 41(3), 613-615.
- [161] H Sun. COMPASS: An ab initio force-field optimized for condensed-phase applications – overview with details on alkane and benzene compounds. *J. Phys. Chem. B* **1998**, 102(38), 7338-7364.
- [162] HB Fan, MMF Yuen. Material properties of the cross-linked epoxy resin compound predicted by molecular dynamics simulation. *Polymer* **2007**, 48, 2174-2178.
- [163] S Yang, S Yu, M Cho. Sequential thermoelastic multiscale analysis of

- nanoparticulate composites. *J. Appl. Phys.* **2010**, 108, 056102.
- [164] M Hori, S Nemat-Nasser. Double-inclusion model and overall moduli of multi-phase composites. *Mech. Mater.* **1993**, 14, 189-206.
- [165] S Yang. “*A study on the development of sequential multiscale bridging method for nanocomposites considering the size effect of nanoparticle*” (Doctoral dissertation), **2011**, Seoul National University.
- [166] JD Eshelby. The determination of the elastic field of an ellipsoidal inclusion, and related problems. *Proc. R. Soc. London Ser. A* **1957**, 241(1226), 376-396.
- [167] JY Li. Thermoelastic behavior of composites with functionally graded interphase: A multi-inclusion model. *Int. J. Solids Struct.* **2000**, 37, 5579-5597.
- [168] C Wei, D Srivastava, K Cho. Structural ordering in nanotube polymer composites. *Nano Lett.* **2004**, 4(10), 1949-1952.
- [169] T Mori, K Tanaka. Average stress in matrix and average elastic energy of materials with misfitting inclusions. *Acta Metall.* **1973**, 21, 571-574.
- [170] Y Sun, Z Zhang, CP Wong. Study and characterization on the nanocomposite underfill for flip chip applications. *IEEE T. Compon. Pack. T.* **2006**, 29(1), 190-197.
- [171] RK Goyal, AN Tiwari, UP Mulik, YS Negi. Thermal expansion behaviour of high performance PEEK matrix composites. *J. Phys. D Appl. Phys.* **2008**, 41, 085403.

## 국문 요약

본 논문에서는 외부로부터 조사된 빛과 열에 의해 자가변형 특성을 보이는 광반응 고분자 소재와, 여기에 수 나노미터 급의 직경을 갖는 금 입자를 삽입한 광반응 고분자 나노복합재의 멀티스케일 기계설계 방법론을 다룬다. 재료거동 특성을 원자 수준에서 정량적으로 도출할 수 있는 분자동역학 전산해석법과 연속체 유한요소모델의 균질해법이 본 방법론에 함께 적용되었으며, 이를 통해 광반응 고분자 시스템의 자외선 조사에 따른 광 이성질화 반응률에 의한 재료의 빛-기계 연성거동 특성 변화를 규명하였다. 분자동역학 모델 구성을 위해, 아조벤젠 기를 포함하는 액정 고분자 모델을 네마틱 상을 갖도록 배향하였고 각 고분자 사슬 간에는 가교반응을 수행하였다. 광반응 고분자 나노복합재 모델은 광반응 고분자 모델과 동일한 기지재에 표면처리되지 않은 나노입자를 강화재로써 삽입하여 안정화 과정을 진행하였다. 재료의 광 이성질화 반응 모사를 위해 diazene 결합에 선택적으로 비틀림 평형각을 적용할 수 있는 광반응 포텐셜을 도입하였고, 이로써 광반응 전후의 액정 배향특성 변화와 이에 대동하는 재료물성 변화를 동시 도출하였다.

분자동역학 전산해석 결과 광 이성질화의 진행에 따라 각 액정의 주축 배향특성이 무너지면서 광변형이 발생함은 물론 재료가 횡등방성으로부터 등방성으로 그 내부구조 또한 성질이 크게 변화함을 확인하였다. 재료의 광반응에 의해 액정의 초기배향 질서도는 떨어지게

되는데, 이에 외부온도 상승에 따른 열수축 특성 또한 이성질화 비율에 따라 단조적으로 감소한다. 이러한 광변형 특성과 재료 미시구조의 변화는 직경 2 나노미터 이하의 금 나노입자를 삽입한 모델에서도 동일하게 나타나며, 따라서 빛 조사에 의한 재료의 거시적 기계거동 특성이 나노복합재 시스템에서도 물리적 상사성을 보임을 확인하였다. 특히, 나노복합재의 경우 나노입자 주위에서 입자와 기지재 간의 강한 상호결합력에 의해 고밀화된 흡착 영역을 형성하면서도 네마틱 액정 배향을 저해하지 않아, 기존의 광반응 고분자보다 더 높은 열적·기계적 안정성 및 빛 조사에 따른 더 큰 광변형률을 갖는다. 이러한 긍정적인 효과는 동일 체적분을 조건 하에서 삽입된 입자의 크기가 작을수록 더욱 두드러지는 것으로 나타났다. 즉, 기계설계적 관점에서 시스템 내의 광 이성질화 비율과 나노입자의 크기효과가 중요한 재료설계변수임을 규명하였다.

본 연구에서는 광반응 고분자 나노복합재의 원자 수준 크기로부터 나타나는 다물리, 멀티스케일 현상을 연속체역학 모델로부터 효율적으로 설계하기 위한 멀티스케일 해석 기법을 함께 제안하였다. 광변형 재료의 기계설계에 있어 주요 착안점은 두 가지로, 한 가지는 구속조건이 부여되지 않은 상태에서 빛 조사 방향으로의 시편 굽힘거동을 해석하기 위한 형상 파라미터 설계이며, 다른 한 가지는 재료에 기계적 하중이 가해졌을 때 나노입자 주위의 고밀화된 계면 상의 독립적인 기계적 물성 및 그 영역의 정량적인 크기를 나노스케일에서 규명하는 일이다. 이를 위해 분자동역학 전산해석으로부터 도출된 형상 파라미터를 액정 상전이 모델에 대한 함수로

도시한 결과, 각 계수가 나노입자의 크기와 광 이성질화 반응의 진행도에 따라 뚜렷한 경향성을 나타내었다. 이를 액정의 질서배향도의 함수화에 반영함으로써 광변형 거동 해석 및 설계를 위한 연속체 모델에 직접적으로 활용할 수 있는 형상 파라미터의 설계안을 제시하였다. 한편 기계적 하중 조건 하에서 나노입자와 기지재 사이에 존재하는 계면 상의 독립적인 거동 특성 도출을 위해, 강화재-계면-기지재로 이루어진 3상 복합재료 유한요소 모델을 구성하였다. 안정화된 분자동역학 모델과 동등한 조건에서 일축 인장을 부여하여 계면 상에서 발생하는 변형에너지 밀도의 비교를 통해 계면 상이 전체 시스템에서 차지하는 체적비를 도출하는 동시에 구성된 복합재모델의 균질해로부터 계면의 독립적인 탄성계수를 수치적으로 계산하였다. 이로써 분자동역학 해석법으로부터 규명된 광변형 고분자 나노복합재의 기계적 거동은 물론 입자 주위에서 계면이 차지하는 두께와 그 독립물성을 부가적인 가정이나 제약 없이 제공하는 멀티스케일 모델을 최종적으로 구성하였다. 이로부터 입자 주위의 계면 상은 기지재보다 높은 기계적 물성을 가지며 그 강화효과는 삽입된 입자의 크기가 작을수록 더욱 두드러진다는 사실을 도출하였다. 특히, 재료가 빛을 받아 이성질화가 진행되어감에 따라 계면 상에 위치하는 네마틱 액정의 배향 방향에 대한 인장에너지가 감소함과 동시에 그 계면이 차지하는 두께 또한 줄어들음을 새로이 규명하였다. 제안된 모델의 검증은 멀티스케일 방법론으로부터 구한 유한요소모델의 응력분포와 분자동역학 모델에서의 계면 영역의 비리얼 응력 간의 직접 비교를 통해 이루어졌으며, 이성질화 반응에 의한 계면 상의



응력값 변화, 인장방향에 따른 응력의 비등방성 등이 본 연속체 모델을 통해 예측 가능성을 확인하였다.

한편, 이러한 광반응 고분자 소재의 실제 합성 및 이를 응용한 광반응 작동기의 실험적 제안이 본 연구에서 함께 이루어졌다. 광반응 고분자 소재가 갖는 근본적 한계인 높은 취성 특성과 낮은 기계강도를 극복하고자 실 형상의 적층 복합소재를 고안하였다. 제작된 광반응 고분자 복합구조물은 외부와 격리된 공간 내에서 빛 조사에 따라 장애물을 회피하며 대상을 떼어내는 요소로서의 기능이 가능성을 실험을 통해 검증하였다. 본 연구 결과는 광반응 고분자와 광반응 고분자 나노복합재, 그리고 이를 응용한 기계시스템의 설계 지표로써 그 잠재적 활용 가치가 높다.

**주요어:** 광반응 고분자, 멀티스케일 해석, 고분자 나노복합재, 계면 상, 분자동역학 전산해석, 연속체역학

**학번:** 2010-24076